Nonlinear propagation of ultrasound in microbubble populations

Explore collective dynamics

Matalliotakis, A.

DOI
10.4233/uuid:5d7eefab-a0b4-49aa-b8ae-c0aeabd590da

Publication date
2024

Document Version
Final published version

Citation (APA)
Matalliotakis, A. (2024). *Nonlinear propagation of ultrasound in microbubble populations: Explore collective dynamics*. [Dissertation (TU Delft), Delft University of Technology]. https://doi.org/10.4233/uuid:5d7eefab-a0b4-49aa-b8ae-c0aeabd590da

Nonlinear propagation of ultrasound in microbubble populations

Exploring collective dynamics

Agisilaos Matalliotakis

Nonlinear propagation of ultrasound in microbubble populations

Exploring collective dynamics

Nonlinear propagation of ultrasound in microbubble populations

Exploring collective dynamics

Dissertation

for the purpose of obtaining the degree of doctor

at Delft University of Technology,

by the authority of the Rector Magnificus prof.dr.ir. T.H.J.J. van der Hagen,

chair for the Board of Doctorates,

to be defended publicly

on **Thursday 19 December 2024** at **12:30** o'clock

by

Agisilaos MATALLIOTAKIS

Dipl.-Eng, Mechanical Engineering,
Aristotle University of Technology, Greece

born in Heraklion, Crete, Greece.

The dissertation has been approved by the promotors:

Dr. ir. M. D. Verweij
Prof. dr. ir. N. de Jong

Composition of the doctoral comittee:

Rector Magnificus,	chairperson
Prof. dr. ir. N. de Jong	Delft University of Technology, promotor
Dr. ir. M. D. Verweij	Delft University of Technology, promotor

Independent members:

Prof. dr. ir. V. Garbin	Delft University of Technology
Prof. dr. ir. N. Ovenden	University College London
Dr. ir. L. Demi	University of Trento
Dr. ir. G. Lajoinie	University of Twente

This research is part of the "Optoacoustic sensor and ultrasonic microbubbles for dosimetry in proton therapy" program (file number: NWA.1160.18.095), which is partly financed by the Dutch Research Council(NWO).

Keywords: medical ultrasound, nonlinear acoustics, contrast-enhanced imaging , microbubbles, multiple scattering, monodisperse, polydisperse, imaging artifacts, proton therapy

Printed by: Gildeprint

Cover illustration: Designed by Agisilaos Matalliotakis. The front cover encapsulates the thesis's context, while the back cover depicts the concept of an individual existing in his own bubble, striving to grasp the fleeting nature of nonlinear time.

ISBN 978-94-6**xxx-xxx-x**

An electronic version of this dissertation is available at https://repository.tudelft.nl/.

Μια αστραπή η ζωή μας... μα προλαβαίνουμε.

Ν. Καζαντζάκης

Contents

Chapter 1

Introduction

This thesis describes the development of a numerical method capable of modeling the nonlinear propagation of ultrasound waves through a population of scatterers, considering various physical phenomena. It builds upon the existing Iterative Nonlinear Contrast Soucre (INCS) method. [1,2] Based on a Neumann iterative scheme, the original INCS method solves the Westervelt equation in a four-dimensional spatiotemporal domain by iteratively updating the acoustic pressure with increasingly accurate field corrections. The current extension of INCS accommodates scattering from large populations of monodisperse contrast agents such as microbubbles (MBs), treating each as an independent point scatterer. The scattering of these agents is obtained by solving the equation governing the oscillation of each MB. Physically, each iteration of INCS adds an extra order of multiple scattering between the MBs. The method is further extended to consider global medium and local nonlinearities, crucial in imaging scenarios involving MBs. Subsequently, INCS is used to demonstrate the effect of different wavefront shapes on the generation of nonlinear imaging artifacts below the MB suspension, by reconstructing B-mode and contrast-enhanced images. Additionally, the efficacy of monodisperse contrast agents is demonstrated in comparison to a population of polydisperse scatterers. Lastly, the primary objective of this thesis is to extend the INCS method by incorporating point emitters simulating proton sources. These advancements combined hold promise for applications in diagnostic contrast-enhanced ultrasound (CEUS) and therapeutic ultrasound. The long-term objective is to devise personalized cancer treatment plans using contrast agents for unconventional approaches like proton therapy.

This introduction discusses the background and context of this thesis. In Section 1.1, we describe the history of medical ultrasound. The fundamentals of nonlinear acoustics are discussed in Section 1.2 with a focus on contrast-enhanced ultrasound imaging. An introduction to MBs, the most conventionally used contrast agents to date, is discussed in Section 1.3. In Section 1.4, the usage of ultrasound for therapeutic applications is introduced. Next, we introduce the fundamental equations that describe the nonlinear acoustic wave propagation and the applied numerical simulation methods in Sec. 1.5 . Finally, an overview of the work presented in this thesis is given in Section 1.6.

1.1 History of medical ultrasound

The history of medical ultrasound reflects a persistent pursuit of knowledge and innovation in healthcare. Originating in the early 20th century, scientists explored sound waves for diagnostic purposes [3]. In the 1920s and 1930s, ultrasound experiments laid the foundation for a crucial diagnostic tool in modern medicine [4]. The breakthrough moment arrived in the late 1940s with the development of conventional A-mode ultrasound machines [5]. This method involves transmitting an acoustic wave inside the human body and receiving backscattered echoes along a line from structures with different mass density and compressibility, such as tissue [6]. As technology advanced, B-mode ultrasound emerged in the 1950s, employing these reflections to reconstruct two-dimensional images of internal organs and revolutionizing noninvasive diagnostics [7].

Echocardiography gained prominence in the second part of the 20th century, enabling detailed real-time visualization and assessment of the heart's structure and function [8]. Ultrasound technology continued to evolve, introducing color Doppler in 1982 and 3D/4D ultrasound in the late 20th century, offering detailed anatomical views and real-time imaging during medical procedures [9].

Today, ultrasound is integral in diverse applications, from prenatal care and cardiac imaging to abdominal examinations and guiding minimally invasive procedures [5]. In obstetrics, it monitors fetal development, assesses fetal health, and aids in identifying potential complications during pregnancy. An example of a conventional echography machine and a typical echography image of a fetus is depicted in Figs. 1.1(a) and (b), respectively. Another application of ultrasound is lung imaging, which provides a non-invasive means to examine pulmonary structures and assess conditions such as pleural effusions, pneumonia, and pneumothorax [10]. The COVID-19 pandemic has underscored ultrasound's utility in monitoring lung health and assessing respiratory conditions. Notably, ongoing advancements include the exploration of nonlinear imaging techniques [11] like harmonic imaging [12] and CEUS [13], enhancing diagnostic capabilities and expanding ultrasound's utility in various medical fields.

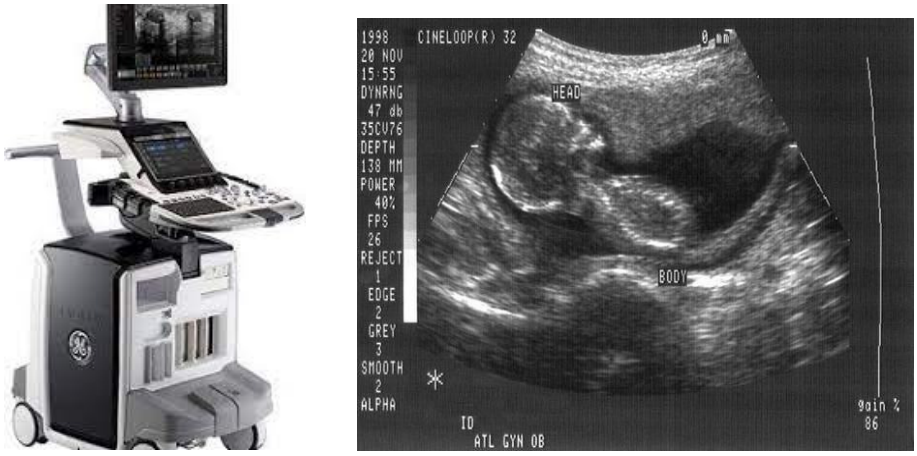

(a) (b)

Figure 1.1: (a) Picture of an echography machine. (b) Echography image of a 4 months old fetus.

1.2 Nonlinear acoustics

Nonlinear acoustic propagation represents a fundamental aspect of ultrasound physics that explores how sound waves propagate at higher amplitudes or in non-ideal conditions [14]. In linear acoustics, sound waves travel through tissues and other media in a predictable, linear fashion, with their behavior primarily governed by factors like wavelength and frequency. However, as acoustic intensity increases, nonlinear effects become prominent. These nonlinearities include phenomena such as the generation of harmonics (multiples of the fundamental frequency) [6]. Figure 1.2 compares the waveform and frequency spectra of an acoustic pressure wave propagating through a lossless homogeneous medium (water) in case of linear (solid line) and nonlinear (dashed line) propagation. In the linear case, the normalized time signal does not experience shape deformation and the energy in the frequency spectra remains concentrated in the fundamental component F0 during propagation, while this is not the case when nonlinear propagation is considered. With nonlinear propagation, the positive high pressures tend to move faster and the negative low pressures tend to slow down, resulting in a distortion of the wave shape. The distortion of this waveform can result in the formation of shocks, heightened attenuation of the acoustic wave, and subsequently increased heating of the medium, posing a challenge in application such as aircraft noise, underwater acoustics, non-destruictive testing and medical ultrasound. In the frequency domain, this distortion manifests itself with the formation of the harmonic components, which are multiples of the trasmitted frequency as shown in Figure 1.2(b).

Harmonic imaging is a sophisticated ultrasound technique that harnesses the non-

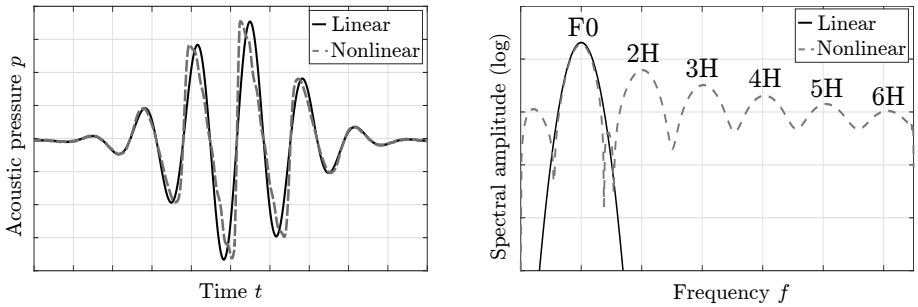

Figure 1.2: Normalized waveforms and frequency spectra for a plane wave propagating through water in case of linear (solid line) and nonlinear (dashed line) propagation (after shockwave).

linear behavior of tissues [12, 15] and contrast agents [13] to create clearer and more detailed images. In harmonic imaging, the ultrasound system transmits a fundamental frequency, typically in the range of 1 to 10 MHz, into the body. As the sound waves propagate and interact with tissues, nonlinear effects distort the waveform, resulting in the production of harmonics that will be reflected by the inclusions of the medium. These harmonic signals are then selectively detected and used to create ultrasound images. Harmonic imaging has proven especially valuable in enhancing image quality, reducing artifacts, and improving the visualization of anatomical structures, making it a valuable tool in various clinical applications [16]. One well known imaging modality is Tissue Harmonic Imaging [17, 18].

Another advanced extension of harmonic imaging is Super Harmonic Imaging that takes advantage of even higher-order harmonics produced during nonlinear acoustic propagation [19–21]. By using ultrasound frequencies that are well above the fundamental frequency, Super Harmonic Imaging can provide exceptionally detailed images with improved resolution and tissue differentiation. This technique is especially beneficial in applications where precise visualization of small structures or lesions is crucial, such as in cardiac imaging and breast ultrasound.

The introduction of contrast agents has revolutionized nonlinear medical ultrasound applications mainly in the field of nonlinear imaging. These contrast agents are administered intravenously, and their behavior during ultrasound imaging in the bloodstream greatly enhances the diagnostic capabilities of ultrasound. When exposed to ultrasound, contrast agents also exhibit nonlinear behavior, leading to the production of strong harmonic and subharmonic signals. This behavior is exploited in applications such as CEUS, where contrast agents are used to enhance the visualization of vascular structures, assess blood perfusion in organs, and detect focal lesions, including tumors and liver lesions. Contrast agents have also found utility in applications like assessing myocardial perfusion and cancer treatment using proton therapy [22]. The most conventionally used contrast agents to date are MBs [23].

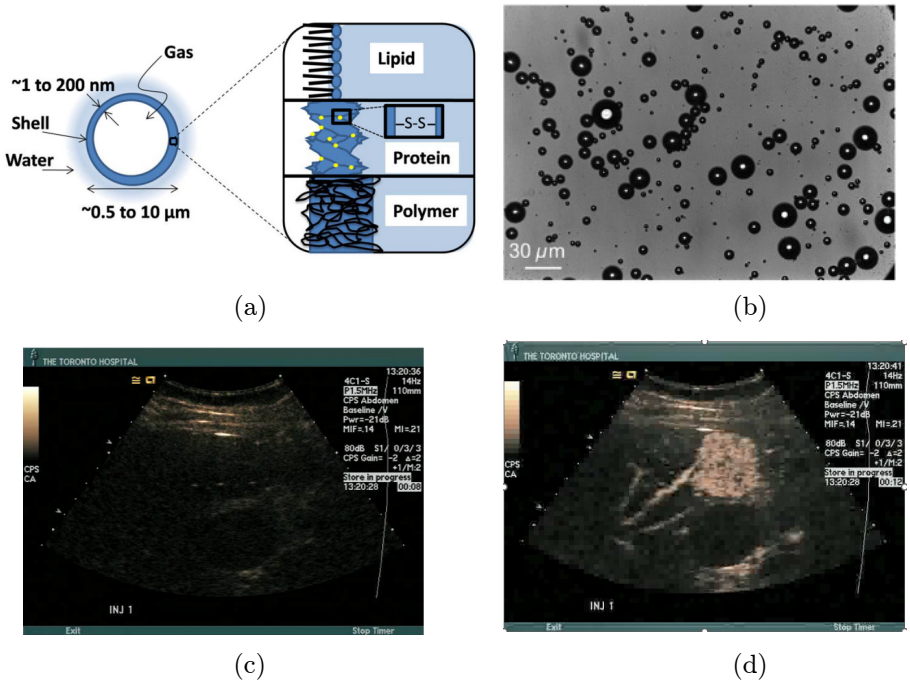

(a) (b)

(c) (d)

Figure 1.3: (a) Schematic of a typical MB [25]. (b) A typical polydisperse concentration of MBs [26]. Contrast-enhanced ultrasound image of the abdomen after injection of MBs at (c) $t = 0$ s and (d) $t = 4$ s. In the first image, the linear reflections from tissue are removed and the MBs have not arrived yet. In the second image, the MBs have filled the abdominal aorta and their branches, which are now visible due to their nonlinear scattering.

1.3 Microbubbles as ultrasound contrast agents

Microbubbles, initially discovered by coincidence during an intravenous saline solution injection [4], have evolved into components of ultrasound contrast agents [24]. Administered through intravenous injection, these spherical MBs have a radius of 1 to 15 µm as illustrated in Fig. 1.3(a), akin in size to red blood cells, enabling them to traverse even the smallest capillaries. Coated with phospholipid, denatured human serum albumin, or polymer shells, these MBs effectively suppress surface tension and impede rapid dissolution in the bloodstream. Their resonance frequency aligns with the optimal imaging frequencies used in medical ultrasound, enhancing contrast by reflecting acoustic waves more efficiently than surrounding tissue due to the large difference in acoustic impedance (see Fig. 1.3(c) & (d)). Moreover, their small size compared to the ultrasound wavelength causes radial oscillations in response to the incident pressure field, generating spherically scattered sound waves [27]. Due to their highly nonlinear resonance behavior, these MBs can produce harmonics, subharmonics and even ultra-harmonics. While the behavior of a single bubble is well

described by detailed physical models [24,28], comprehending the dynamics of a bubble cloud (see Fig. 1.3(b)), particularly in the presence of multiple scattering, remains a challenging task.

Bracco Imaging, GE Healthcare, and Lantheus Medical Imaging [23, 29] lead in MB-based contrast agents, like SonoVue, Optison, and Definity. Typical concentrations of these MB contrast agents injected into the human body vary depending on the specific product and application. However, concentrations are often expressed in terms of the number of MBs per milliliter, with ranges from 10^8 to 10^{10} ml^{-1} [29], when diluted in the human blood volume of 5L upon intravenous injection. The precise dosage and concentration are carefully determined based on the specific medical imaging requirements and the patient's characteristics, ensuring optimal contrast enhancement and safety.

1.4 Proton therapy

Cancer remains a significant public health challenge, claiming 45,000 lives in the Netherlands each year, which constitutes 30% of all deaths nationwide in 2016. Conventional X-ray-based radiation therapy, crucial for half of all cancer patients, comes with the drawback of collateral damage to healthy tissue due to the extensive space of X-ray energy deposition. This collateral irradiation often leads to unwanted side effects and, in the long term, may even induce new cancers. A cutting-edge alternative of cancer treatment, proton therapy, stands out for its precise and targeted approach to irradiating tumors while minimizing damage to surrounding healthy tissues [30].

Proton therapy's efficacy relies on the depositition of the majority of the energy precisely at a defined depth within the tissue, known as the Bragg peak [31]. This property allows tailoring the radiation dose to match the tumor's size and depth while sparing surrounding healthy tissues. Challenges arise in the accurate localization of this peak due to tissue density variations and organ motion. Recent advancements propose the use of nanodroplets [32], as a promising strategy to image the Bragg peak localization and improve proton therapy effectiveness [33].

In this thesis, we consider the innovative concept that involves injecting MBs into the patient's bloodstream before proton therapy, and using ultrasound imaging to visualize their distribution in real-time. By activating MBs within the tumor area with focused ultrasound waves, detectable harmonic signals may be generated, precisely correlating with the Bragg peak's location. This offers real-time feedback for continuous adjustments to proton therapy, ensuring precise alignment with the tumor. Clinical trials are necessary to validate this promising synergy of proton therapy and MB-enhanced ultrasound, transform precision oncology and offer more effective and targeted cancer treatment options. The ultimate goal of ongoing research is to measure the protoacoustic signal using a very sensitive optoacoustic sensor to assist the precise localization of the Bragg peak, as depicted in Fig. 1.4.

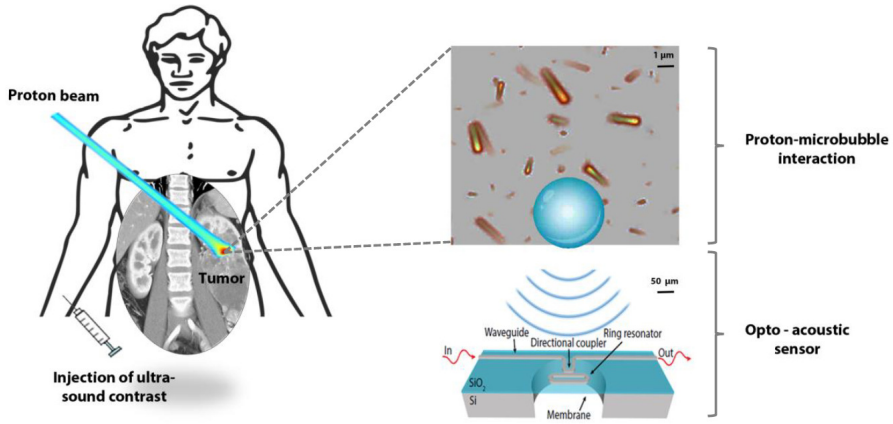

Figure 1.4: Proposed method for proton beam localization and dosimetry using medical ultrasound contrast MBs and optical micromachined ultrasound sensors.

1.5 Modeling of nonlinear medical ultrasound

The fundamental equations governing acoustic wave propagation establish local relationships that adhere to the physics of the acoustic wave field [34]. These equations, when combined with appropriate boundary conditions, formulate a comprehensive system of equations solvable through numerical methods. Assuming a lossless, homogeneous, and source-free medium, the second-order nonlinear differential equation for acoustic pressure is

$$c_0^{-2}\partial_t^2 p - \nabla^2 p = \frac{\beta}{\rho_0 c_0^4}\partial_t^2 p^2 + (\nabla^2 + c_0^{-2}\partial_t^2)\mathcal{L}, \tag{1.1}$$

in which t [s] is the time, and $p(\boldsymbol{x}, t)$ [Pa] is the acoustic pressure. The medium is characterized by the small signal speed of sound $c_0 = 1/\sqrt{\rho_0 \kappa_0}$ [m/s], the mass density ρ_0 [kg/m^3] and the compressibility κ_0 [Pa^{-1}]. The symbol ∂_t is the time derivative and ∇^2 indicates the Laplace operator. β is the coefficient of nonlinearity of the medium, and $\mathcal{L}$ is the Lagrangian density. The last two terms in Eq. (1.1) are related to the generation of global and local medium nonlinearities, respectively. If local nonlinearities are negligible, the Lagrangian density may be omitted, resulting in the lossless Westervelt equation [35]

$$c_0^{-2}\partial_t^2 p - \nabla^2 p = \frac{\beta}{\rho_0 c_0^4}\partial_t^2 p^2. \tag{1.2}$$

This equation forms the basis for simulating nonlinear ultrasound fields, especially in medical applications. Numerical simulation methods for solving these types of equations fall into two main categories: forward wave methods and full wave methods [36, 37]. Forward wave methods initiate simulations with a prescribed pressure distribution within the transducer plane, advancing the acoustic field unidirectionally,

typically following the principal beam orientation [38–43]. This characteristic, seen in methods like the KZK [44] method, results in limited accuracy when dealing with wave fields propagating in various directions. In contrast, full wave methods, utilizing Finite Difference [45–47] or Finite Element [48] methods, aim to solve fundamental acoustic equations without bias toward a specific propagation direction. However, the practical necessity of sampling 10 or more points per wavelength and period makes the computational requirements for realistic domains rapidly prohibitive in terms of grid point numbers. The INCS method effectively models nonlinear ultrasound fields over large computational domains by avoiding a bias toward any specific propagation direction and requiring only two points per wavelength [1, 2].

1.6 This thesis

In this thesis, the principles underlying the INCS method have been retained, and the methodology has been extended to primarily accommodate all the physical phenomena during ultrasound propagation through a large population of scatterers. Here we give an overview of the subjects treated in this thesis.

Chapter 2 contains the extension of INCS with the incorporation of a population of monodisperse point scatterers. These scatterers can be either linear or nonlinear such as MBs. In this chapter it is assumed that the population consisted of only monodisperse scatterers. Here, the significance is set upon multiple scattering phenomena in a population of point scatterers. Finally, results are presented for each case and the significance of the effect of multiple scattering is demonstrated by comparing different concentrations.

In Chapter 3, we expand INCS to take into account the effect of local nonlinearities. To fully describe the nonlinear phenomena when acoustic waves propagate through a population of MBs, we can not neglect the local nonlinear influence in the interacting scattered waves. A simple case of two interacting plane waves is presented. In parallel to the respective numerical results, a mathematically rigorous analysis is presented for this interaction. Furthermore, a case related to a medical application is presented, where the incident field is a focused beam generated by a phased array. The main purpose of this chapter is to showcase the effect of local compared to global nonlinearities.

Chapter 4 contains an example where we use all the aforementioned nonlinear physical phenomena for imaging based on four distinct transmission scenarios. We compare the results for an X-wave or two cross propagating plane waves, for a focused wave, for a plane wave and for a diverging wave. We also incorporate a population of highly nonlinear oscillating monodisperse MBs. Here, we show beamformed images obtained with the numerical results from INCS, and we compare the nonlinear artifacts that emerge downstream the contrast agent inclusion. The primary goal is to illustrate the potentials of INCS and the effectiveness of X-wave to suppress the imaging artifacts due to its heightened specificity and sensitivity.

Chapter 5 entails the extension of INCS with the introduction of polydisperse inclusions of point scatterers. A comparison study is performed for three distinct monodisperse populations: (i) below resonance, (ii) on resonance and (iii) above resonance and a polydisperse suspension, when excited by a 3D propagating finite plane wave. Moreover, we demonstrate the difference between a monodisperse and a polydisperse population of MBs when used as contrast agents, excited by a transmitted plane wave from a conventional medical ultrasound device.

In **Chapter 6**, we construct a model specifically designed for computing the acoustic pressure that is generated by a single proton, covering nanometer and micrometer scales. This model incorporates adiabatic and thermo-acoustic expansion and quantifies the production of secondary electrons.

Chapter 7 expands the knowledge of Chapter 6 to a beam of protons. We use the acoustic incident field emitted by a proton beam to excite a population of MBs. Our goal is to combine protons with MBs to increase the chances for the Bragg peak localization. In this chapter, INCS is extended with the introduction of a point source population as the primary source term. In this way, it is easy to assimilate the inclusion of multiple protons and to illustrate how the effective pressure fields influence a population of MBs. The aim of this study is to find an optimal configuration to achieve coherence between the oscillations of the contrast agents.

Discussions on the overall content of the thesis as well as suggestions for further development together with final conclusions are contained in Chapter 8.

Bibliography

[1] J. Huijssen, "Modeling of nonlinear medical diagnostic ultrasound", PhD Thesis, Delft University of Technology, 35–120 and 171–186 (2008)

[2] L. Demi, "*Modeling nonlinear propagation of ultrasound through inhomogeneous biomedical media*", Ph.D. Thesis, Delft University of Technology (2013)

[3] O'Brien Jr, and W. D., "Ultrasound-biophysics mechanisms", Progress in Bioph. and Mol. Biol., **93** (1-3), 212–255 (2007). DOI:10.1016/j.pbiomolbio.2006.07.010

[4] Gramiak, R., and Shah, P. M., "Echocardiography of the aortic root.", Investigative radiology, **3** (5), 356–366 (1968). DOI:10.1097/00004424-196809000-00011

[5] Carovac, A., Smajlovic, F., and Junuzovic, D., "Application of Ultrasound in Medicine", Acta Inform Med., **19**, (3), 168–171 (2011).DOI:10.5455%2Faim.2011.19.168-171

[6] Szabo, T. L., "Diagnostic ultrasound imaging: Inside out", Academic Press (2004).

[7] P. Newman, and G. Rozycki, "The history of ultrasound", J. Sci. Instrum., **78** (2), 179–195 (1998). DOI: Rozycki

[8] Edler, I., and Hertz, C. H., "The history of echocardiography", Ultrasound Med. Biol., **30** (12), 1565–1644 (1994). DOI: 10.1016/S0301-5629(99)00056-3

[9] R. Chaoui, J. Hoffmann, and K.S. Heling, "Three-dimensional (3D) and 4D color Doppler fetal echocardiography using spatio-temporal image correlation (STIC)", Ultrasound Obstetr. Gynec., **23** (6), 535–545 (2004). DOI: 10.1002/uog.1075

[10] L. Demi, F. Wolfram, C. Klersy, A. De Silvestri, V. V. Ferretti, M. Muller, D. Miller, F. Feletti, M. Wełnicki, N. Buda, A. Skoczylas, A. Pomiecko, D. Damjanovic, R. Olszewski, A. W. Kirkpatrick, R. Breitkreutz, G. Mathis, G. Soldati, A. Smargiassi, R. Inchingolo, and T. Perrone, "New International Guidelines and Consensus on the Use of Lung Ultrasound", J Ultrasound Med. **42** (2), 309–344, (2023).DOI:10.1002/jum.16088

[11] P. J.A. Frinking, A. Bouakaz, J. Kirkhorn, F. J. Ten Cate, and N. de Jong, "Ultrasound contrast imaging: current and new potential methods", Ultrasound Med. Biol., **26** (6), 965–975 (2000).DOI:10.1016/s0301-5629(00)00229-5

[12] M. Averkiou, "Tissue harmonic imaging", in Proc IEEE Ultrason Sympos. 2000, 1530–1541 (2011).DOI:10.1016/S1296-2147(01)01259-8

[13] M. Averkiou, M. Bruce, J. Powers, P. Sheeran, and P. Burns, "Imaging methods for ultrasound contrast agents", Ultrasound Med. Biol. **46**, (3), 498–517 (2020).DOI:10.1016/j.ultrasmedbio.2019.11.004

[14] M.F. Hamilton and C.L. Morfey, "Model equations", in *Nonlinear Acoustics*, edited by M.F. Hamilton and D.T. Blackstock, Academic Press, San Diego, 54–56 (1998).

[15] M.A. Averkiou, D.N. Roundhill, and J.E. Powers, "A new imaging technique based on the nonlinear properties of tissues", Proc. Int. Ultra. Symp. , 1561–1566 (1997).DOI:10.1109/ULTSYM.1997.663294

[16] Hoskins, P. R., "Clinical ultrasound: A comprehensive text - Abdominal and general ultrasound (3rd ed.)", Elsevier (2015).DOI:

[17] B. Ward, A.C. Baker, and V.F. Humphrey, "Nonlinear propagation applied to the improvement of resolution in diagnostic medical ultrasound equipment", J. Acoust. Soc. Am. **101**, (1), 143–154 (1999).DOI:10.1121/1.417977

[18] F. Tranquart, N. Grenier, V. Eder, and L. Pourcelot, "Clinical use of ultrasound tissue harmonic imaging", Ultrasound Med. Biol. **25**, (6), 889–894 (1999).DOI:10.1016/s0301-5629(99)00060-5

[19] A. Bouakaz and N. de Jong, "Native tissue imaging at superharmonic frequencies", IEEE Trans. Ultrason., Ferroelect., Freq. Contr. **50**, (5), 496–506 (2003).DOI:0.1109/TUFFC.2003.1201462

[20] A. Bouakaz, E. Merks, C.T. Lancee, and N. Bom, "Non invasive bladder volume measurements based on nonlinear wave distortion", Ultrasound Med. Biol. **30**, (4), 469–476 (2004).DOI:10.1016/j.ultrasmedbio.2003.11.006

[21] Paul L. M. J. van Neer, Mikhail G. Danilouchkine, Martin D. Verweij, Libertario Demi, Marco M. Voormolen, Anton F. W. van der Steen, and Nico de Jong, "Comparison of fundamental, second harmonic, and superharmonic imaging: A simulation study", J. Acoust. Soc. Am. **130** (5), 3148–3157 (2011).DOI:10.1121/1.3643815

[22] Claudon, M., Cosgrove, D., Albrecht, T., Bolondi, L., Bosio, M., Calliada, F., and Whittingham, T. A., "Guidelines and good clinical practice recommendations for contrast-enhanced ultrasound (CEUS) in the liver?update 2008", Ultraschall in der Medizin-European Journal of Ultrasound **29 (1)**, 28–44(2008).DOI:10.1055/s-2007-963785

[23] Lindner, J. R., "Microbubbles in medical imaging: current applications and future directions", Nat. Rev. Drug Discov. **3** (6), 527–533 (2004).DOI:10.1038/nrd1417

[24] M. Versluis, E. Stride, G. Lajoinie, B. Dollet, and T. Segers, "Ultrasound Contrast Agent Modeling: A review", Ultrasound in Med. & Biol. **46** (9), 2117–2144 (2020).DOI:10.1016/j.ultrasmedbio.2020.04.014

[25] Shashank Sirsi and Mark Borden, "Microbubble Compositions, Properties and Biomedical Applications", Bubble Sci Eng Technol. **1**, 1-2, 3–17 (2009). DOI:10.1179/175889709X446507

[26] Dhiman Das and Manojit Pramanik, "Combined ultrasound and photoacoustic imaging of blood clot during microbubble-assisted sonothrombolysis", Journal of Biomedical Optics **24**, 12, 121902 (2019). DOI:10.1117/1.JBO.24.12.121902

[27] N. de Jong, A. Bouakaz, and P. Frinking, "Basic Acoustic Properties of Microbubbles", Echocardiography **19** (3), 229–240 (2002).DOI:10.1046/j.1540-8175.2002.00229.x

[28] P. Marmottant, S. van der Meer, M. Emmer ,M. Versluis, N. de Jong, S. Hilgenfeldt, and D. Lohse, "A model for large amplitude oscillations of coated bubbles accounting for buckling and rupture", J. Acoust. Soc. Am. **118** (6), 3499–3506 (2005).DOI:10.1121/1.2109427

[29] P. Frinking, T. Segers, Y. Luan, and F. Tranquart, "Three decades of ultrasound contrast agents: A review of the past, present and future improvements", Ultrasound in Med. & Biol. **46**, 4, 892–908 (2020).DOI:10.1016/j.ultrasmedbio.2019.12.008

[30] Durante, M., and Loeffler, J. S., "Charged particles in radiation oncology", Nat. Rev. Clin. Oncol. **7** (1), 37–43 (2010).DOI:10.1038/nrclinonc.2009.183

[31] Paganetti, H., "Range uncertainties in proton therapy and the role of Monte Carlo simulations", Phys. Med. Biol. **57** (11), 99–117 (2012).DOI:10.1088/0031-9155/57/11/R99

[32] G. Collado-Lara, S. V. Heymans, M. Rovituso, B. Carlier, Y. Toumia, M. Verweij, G. Paradossi, E. Sterpin, H. J. Vos, J. D'hooge, N. de Jong, K. Van Den Abeele, and V. Daeichin, "Spatiotemporal Distribution of Nanodroplet Vaporization in a Proton Beam Using Real-Time Ultrasound Imaging for Range Verification", Ultrasound Med. Biol. **48(1)**, 149–156 (2022).DOI:10.1016/j.ultrasmedbio.2021.09.009

[33] J. Lascaud, P. Dash, M. Würl, H.-P. Wieser, B. Wollant, R. Kalunga, W. Assmann, D.-A. Clevert, A. Ferrari, P. Sala, A. S. Savoia, and K. Parodi, "Enhancement of the ionoacoustic effect through ultrasound and photoacoustic contrast agents", Sci. Rep. **11**, 2725 (2021).DOI:10.1038/s41598-021-81964-4

[34] M.D. Verweij, B.E. Treeby, K.W.A. van Dongen, and L. Demi, "Simulation of Ultrasound Fields", Comprehensive Biomedical Physics **2**, 465–500 (2014). DOI:10.1016/B978-0-444-53632-7.00221-5

[35] P. J. Westervelt, "Parametric Acoustic Array", J. Acoust. Soc. Am. **35**, 535–537 (1963). DOI:10.1121/1.1918525

[36] J.H. Ginsberg and M.F. Hamilton, "Computational methods", in Nonlinear acoustics, edited by M. Hamilton and D. Blackstock, 309–341 (1998).

[37] M.D. Verweij and J. Huijssen, "Computational methods for nonlinear acoustic wavefields in homogeneous media", in Computational methods in nonlinear acoustics: Current trends, edited by C. Vanhille and C. Campos-Pozuelo, 1–19 (Research Signpost, Kerala, India)

[38] S. Aanonsen, J. Barkve, J. Naze Tjotta, and S. Tjotta, "Distortion and harmonic generation in the nearfield of a finite amplitude sound beam", J. Acoust. Soc. Am. **74** (3), 749–768 (1984). DOI:10.1121/1.390585

[39] Y.-S. Lee and M.F. Hamilton, "Time-domain modeling of pulsed finite-amplitude sound beams", J. Acoust. Soc. Am. **97** (2), 906–917 (1995).DOI:10.1121/1.412135

[40] P.T. Christopher and K.J. Parker, "New approaches to nonlinear diffractive field propagation", J. Acoust. Soc. Am. **90** (1), 488–499 (1991).DOI:10.1121/1.401274

[41] R. Zemp, J. Tavakkoli, and R. Cobbold, "Modeling of nonlinear ultrasound propagation in tissue from array transducers", J. Acoust. Soc. Am. **113** (1), 139–152 (2003). DOI:/10.1121/1.1528926

[42] J. Tavakkoli, D. Cathignol, R. Souchon, and O.A. Sapozhnikov, "Modeling of pulsed finite amplitude focused sound beams in time domain", J. Acoust. Soc. Am. **104** (4), 2061–2072 (1998). DOI:/10.1121/1.423720

[43] T. Varslot and G. Taraldsen, "Computer simulation of forward wave propagation in tissue", IEEE Trans. Ultrason. Ferroelectr. Freq. Contr. **52** (9), 1473–1482 (2005).DOI:10.1109/TUFFC.2005.1516019

[44] V.A. Khokhlova, A.E. Pomomarev, M.A. Averkiou, and L.A. Crum, "Nonlinear pulsed ultrasound beams radiated by rectangular focused diagnostic transducers", Acoust. Phys. **52**, 481–489 (2006). DOI:10.1134/s1063771006040178

[45] V.W. Sparrow and R. Raspet, "A numerical method for general finite amplitude wave propagation in two dimensions and its application to spark pulses", J. Acoust. Soc. Am. **90** (5), 2683–2691 (1991).DOI:10.1121/1.401863

[46] S. Ginter, M. Liebler, E. Steiger, T. Dreyer, and R.E. Riedlinger, "Full-wave modeling of therapeutic ultrasound: Nonlinear ultrasound propagation in ideal fluids", J. Acoust. Soc. Am. **111** (5), 2049–2059 (2002). DOI:10.1121/1.1468876

[47] I.M. Hallaj and R.O. Cleveland, "FDTD simulation of finite-amplitude pressure and temperature fields for biomedical ultrasound", J. Acoust. Soc. Am. **105** (5), L7–L12 (1999).DOI:10.1121/1.426776

[48] J. Hoffelner, H. Landes, M. Kaltenbacher, and R. Lerch, "Finite element simulation of nonlinear wave propagation in thermoviscous fluids including dissipation", IEEE Trans. Ultrason. Ferroelect. Freq. Contr. **48** (3), 779–786 (2001).DOI:10.1109/58.920712

A. Matalliotakis, and M.D. Verweij, *Computation of ultrasound propagation in a population of nonlinearly oscillating microbubbles including multiple scattering*,
J. Acoust. Soc. Am. **153**, 2209–2222 (2023).

Chapter 2

Computation of ultrasound propagation in a population of nonlinearly oscillating microbubbles including multiple scattering

In contrast-enhanced echography, the simulation of nonlinear propagation of ultrasound through a population of oscillating microbubbles (MBs) imposes a computational challenge. Also, the numerical complexity increases because each scatterer has individual properties. To address these problems, the Iterative Nonlinear Contrast Source (INCS) method has been extended to include a large population of nonlinearly responding MBs. The original INCS method solves the Westervelt equation in a 4D spatiotemporal domain by generating increasingly accurate field corrections to iteratively update the acoustic pressure. The field corrections are computed by the convolution of a nonlinear contrast source with the Green's function of the linear background medium. Because the convolution integral allows a coarse discretization, INCS can efficiently deal with large-scale problems. To include a population of MBs, these are considered as individual contrast point sources with their own nonlinear response. The field corrections are computed as before, but now in each iteration the temporal signature of each contrast point source is computed by solving the bubble's Marmottant equation. Physically, each iteration adds an order of multiple scattering. Here, the performance of the extended INCS method and the significance of multiple scattering is demonstrated through various results from different configurations.

2.1 Introduction

For several decades, encapsulated MBs containing gas have been widely used in medical echography as the primary ultrasound contrast agents (UCA) [1]. These spherical bubbles are injected intravenously and have a size comparable to a red blood cell, which allows them to travel even in the smallest blood vessels. To avoid dissolution in the blood, they are usually coated with a shell made from phospholipid, denatured human serum albumin, or polymer. An important property is that they resonate in the same frequency range as used for ultrasound imaging. Moreover, due to their large difference in acoustic impedance with the surroundings and their highly nonlinear oscillatory behavior [2], MBs scatter sound efficiently in both their fundamental and harmonic modes. Through multiple studies, the dynamics of a single bubble are well understood. However, understanding the behavior of a bubble cloud is much more challenging and is partly still unknown, especially when multiple scattering must be taken into account.

Because of the significance in various marine settings, multiple studies were focused on the acoustic propagation of sound in bubbly liquids [3]. Justified by the small gas volume fraction, an effective medium theory [4–7] was established. This implies that the contribution of the interactions between the scatterers was considered unimportant. Initially, a set of averaged equations was constructed in a heuristic way [8], which later was established by a more mathematically systematic approach [9]. Improvements were made for linear scatterers in small concentrations, retaining the hypothesis of effective medium [10–12].

A study focusing on smaller bubbles in the regime of ultrasound frequencies [13], however, showed that experimental results did not agree with effective medium theory. Therefore, the acoustic response of populations with a high concentration of nonlinear scatterers were investigated analytically [14, 15]. When second-order multiple scattering is taken into account, attenuation at the resonance frequency is increased [16]. The significance of the latter was reinforced computationally by introducing nonlinear monodisperse [17] and polydisperse [18, 19] MBs in a finite difference scheme. These studies assumed a collective behavior of the bubbles, which prohibits them to have an independent response due to having individual properties. Finally, a plethora of groups directed their attention to simplified simulations of multiple bubble interactions inside a 1D or 2D domain [20, 21]. One of the studies was able to successfully model the nonlinear propagation of ultrasound through a uniform distribution of MBs, but was limited to two dimensions due to computational cost [22].

In this article, we will employ the Iterative Nonlinear Contrast Source (INCS) method [23,24] to tackle the challenge of numerically simulating the nonlinear response of a 3D bubble population with significant multiple scattering. This method was originally invented to accurately calculate the cumulative nonlinear effects suffered by an acoustic pressure wave propagating in a fluid with nonlinear medium behavior. The pressure wave originated from a source aperture with a pulsed excitation in a 3D spatial domain. A significant advantage of this algorithm is the coarse discretization of two points per shortest desired wavelength. This is achieved by applying the Filtered Convolution (FC) approach [25], which implies that during the computations, the spatial and temporal spectra are consistently cut off at the predetermined Nyquist

limit of the highest desired frequency. This also makes that INCS can reliably deal with stronger nonlinearities causing relatively strong harmonic components. The directional independence of the nonlinear operation is another benefit that is not common to many other nonlinear computational codes. Furthermore, INCS can be easily expanded to include attenuation and inhomogeneous medium parameters of all kind, provided these can be cast in the form of a so-called contrast source [26–30]. This also offers an opportunity for incorporating bubble inclusions. Added to its ability to address large-scale problems, INCS seems a good basis to simulate the acoustic response of MB populations with high accuracy and relatively low computational cost.

This article will describe the extension of the INCS method to deal with a population of scatterers. The performance of the developed method will also be demonstrated by showing the acoustic response of a population of MBs that oscillate in a nonlinear way, as described by the Marmottant model [31]. The method computes the scattered pressure from the cloud in an iterative way. Numerically, each iteration brings the answer closer to the exact result. Physically, each iteration accounts for an extra order of multiple scattering. To focus on the influence and behavior of the MB cloud, it will be assumed that the embedding fluid is linear.

First, in Section 2.2 the fundamental theory behind the INCS method will be described. In Section 2.3, the INCS method will be extended by the introduction of point contrast sources representing point scatterers. The representation of a linearly scattering sphere by a point scatterer is discussed, followed by the representation of a nonlinear MB, and lastly the representation of an entire population of MBs. In Section 2.4, the details of the numerical implementation of the method are described. Next, in Section 2.5 the results from the numerical simulations for a monodisperse MB population are presented and explained. Concluding remarks are given in Section. 2.6.

2.2 Fundamentals of INCS

2.2.1 Linear field

In a lossless, linear, isotropic and homogeneous acoustic background medium, the pressure field generated by an external or primary source can be described by the wave equation

$$c_0^{-2}\frac{\partial^2 p(\boldsymbol{x},t)}{\partial t^2} - \nabla^2 p(\boldsymbol{x},t) = S_{\mathrm{pr}}(\boldsymbol{x},t), \tag{2.1}$$

where $\boldsymbol{x}$ [m] is the position vector of a point in three-dimensional Cartesian space, t [s] is the time, and $p(\boldsymbol{x},t)$ [Pa] is the acoustic pressure. The medium is characterized by the small signal speed of sound $c_0 = 1/\sqrt{\rho_0\kappa_0}$ [m/s], the mass density ρ_0 [kg/m^3] and the compressibility κ_0 [Pa^{-1}]. The symbol ∇^2 indicates the Laplace operator. The right hand side of Eq. (2.2) is the primary source term

$$S_{\mathrm{pr}}(\boldsymbol{x},t) = \rho_0\frac{\partial q(\boldsymbol{x},t)}{\partial t} - \nabla\cdot\boldsymbol{f}(\boldsymbol{x},t), \tag{2.2}$$

where $q(\boldsymbol{x},t)$ [s^{-1}] is the volume injection rate density and $\boldsymbol{f}(\boldsymbol{x},t)$ [N/m^3] is the volume force density of the external source. Sources with a plane aperture, such as a

phased array transducer, can be represented either by a velocity or a pressure jump condition in the transducer plane $z = 0$.

In INCS, and throughout this paper, the explicit solution for the pressure field due to any source $S(\boldsymbol{x}, t)$ in the background medium is denoted as $p(\boldsymbol{x}, t) = \mathcal{G}[S]$. The symbol $\mathcal{G}$ indicates the linear operation defined by

$$\begin{aligned}\mathcal{G}[S] &= S(\boldsymbol{x}, t) *_{\boldsymbol{x},t} G(\boldsymbol{x}, t) \\ &= \int_{\mathcal{T}} \int_{\mathcal{X}} S(\boldsymbol{x}', t')\, G(\boldsymbol{x} - \boldsymbol{x}', t - t')\, d\boldsymbol{x}' dt'. \end{aligned} \tag{2.3}$$

The symbol $*_{\boldsymbol{x},t}$ denotes a convolution in the spatiotemporal domain, where the integration takes place over the spatial domain $\mathcal{X}$ and over the temporal domain $\mathcal{T}$ of the source S. The three-dimensional Green's function of the lossless, linear, homogeneous and isotropic background medium is denoted as $G(\boldsymbol{x}, t)$ and is given by

$$G(\boldsymbol{x}, t) = \frac{\delta(t - \|\boldsymbol{x}\| / c_0)}{4\pi \|\boldsymbol{x}\|}. \tag{2.4}$$

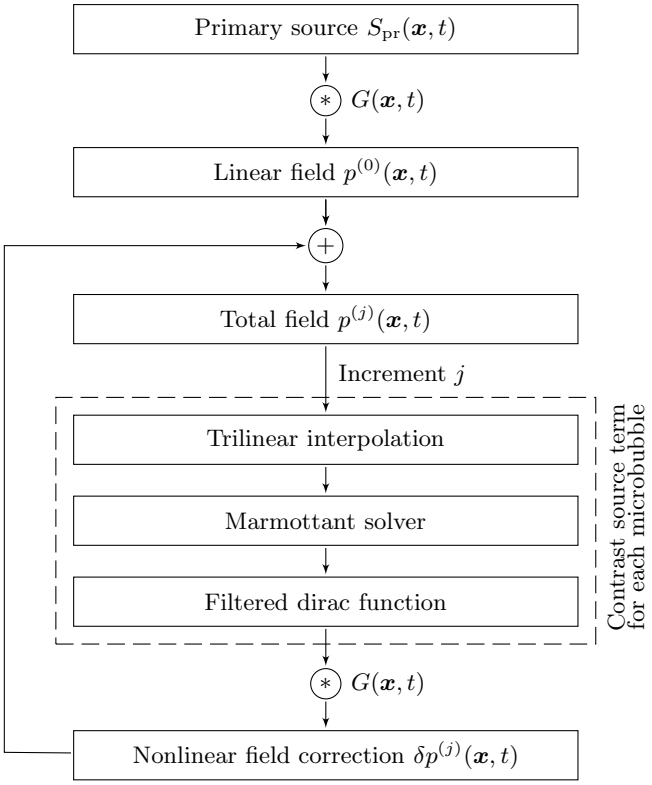

Figure 2.1: Schematic diagram for the INCS method with extension to deal with MBs.

In the numerator, δ is the Dirac delta distribution and $\|\boldsymbol{x}\|$ is the length of $\boldsymbol{x}$. In physical terms, the Green's function is the acoustic pressure at field point $\boldsymbol{x}$ and time t, emitted from a point source of unit impulse located at $(x, y, z) = (0, 0, 0)$, acting at $t = 0$ [32].

The linear acoustic pressure distribution due to the primary source, e.g. an emitting transducer, in the background medium is indicated as $p^{(0)}$. With the notation presented above, it is given by

$$p^{(0)} = \mathcal{G}[S^{(0)}], \tag{2.5}$$

where $S^{(0)} = S_{\mathrm{pr}}$. The field $p^{(0)}$ is the initial field for the Neumann iterative scheme that is used to compute the nonlinear field contribution.

2.2.2 Nonlinear field

In medical diagnostics, the propagation of the pressure wave is dependent on the nonlinear behaviour of the medium. If the so-called local nonlinearities are neglected, the remaining global nonlinearities can be accounted for by extending Eq. (2.1) to the Westervelt equation [33]. In INCS, the lossless form of the Westervelt equation is written as

$$c_0^{-2} \frac{\partial^2 p}{\partial t^2} - \nabla^2 p = S_{\mathrm{pr}} + S_{\mathrm{nl}}, \tag{2.6}$$

where the nonlinear term is given by

$$S_{\mathrm{nl}}(p) = \frac{\beta}{\rho_0 c_0^4} \frac{\partial^2 p^2}{\partial t^2}, \tag{2.7}$$

in which β is the coefficient of nonlinearity. The term in Eq. (2.7) is considered to describe a nonlinear contrast source acting in the linear background medium. As such, it provides the nonlinear contribution to the acoustic pressure field, which can be expressed as $\delta p = \mathcal{G}[S_{\mathrm{nl}}(p)]$ with $\mathcal{G}$ being the same linear operator as in Eq. (2.3) but with integrations running over the entire spatiotemporal support $\mathcal{X}_{\mathrm{nl}} \times \mathcal{T}_{\mathrm{nl}}$ of S_{nl}. Often, this is the entire computational domain. However, combining Eqs. (2.6) and (2.7) yields an implicit solution because the total field p is not yet known. To obtain an explicit solution, an iterative approach is employed in which a nonlinear correction $\delta p^{(j)}$ is obtained from the previous approximation $p^{(j-1)}$ of the total field, according to

$$S_{\mathrm{nl}}^{(j)} = S_{\mathrm{nl}}(p^{(j-1)}), \tag{2.8}$$

$$\begin{aligned} \delta p^{(j)} &= \mathcal{G}[S_{\mathrm{nl}}^{(j)}] \\ &= \int_{\mathcal{T}_{\mathrm{nl}}} \int_{\mathcal{X}_{\mathrm{nl}}} S_{\mathrm{nl}}^{(j)}(\boldsymbol{x}', t)\, G(\boldsymbol{x} - \boldsymbol{x}', t - t')\, d\boldsymbol{x}' dt, \end{aligned} \tag{2.9}$$

$$p^{(j)} = p^{(0)} + \delta p^{(j)}. \tag{2.10}$$

To get a first estimate of the nonlinear correction, the initially computed linear pressure field $p^{(0)}$ is used in the contrast source term. The resulting Neumann iterative

scheme can thus be expressed as

$$p^{(0)} = \mathcal{G}[S_{\text{pr}}], \tag{2.11}$$

$$p^{(j)} = p^{(0)} + \mathcal{G}[S_{\text{nl}}(p^{(j-1)})], \quad \text{if } j \geq 1. \tag{2.12}$$

Using the same methodology, INCS has been extended by the inclusion of other contrast sources, e.g. representing attenuation and inhomonegeous medium properties [26–30].

2.3 Inclusion of microbubbles

2.3.1 Contrast source term representing a point scatterer

In this section we will extend INCS to deal with a medium containing a large population of MBs. Because a MB is much smaller that the spatial grid step, we will represent each bubble by a point scatterer. A point scatterer is an object with an infinitely small volume, which is used to approximate the behavior of a scatterer that is much smaller than the wavelength of the excitation field. The analytical description of a contrast source representing a point scatterer located at point $\boldsymbol{x}_{\text{sc}}$ and with a time signature $A(\boldsymbol{x}_{\text{sc}}, t)$ is

$$S_{\text{sc}}(\boldsymbol{x}, t) = A(\boldsymbol{x}_{\text{sc}}, t)\delta(\boldsymbol{x} - \boldsymbol{x}_{\text{sc}}). \tag{2.13}$$

As explained in a previous publication, [25] the INCS method applies spatial filtering with an ideal low pass filter in all dimensions to avoid aliasing during numerical computation. The spatially filtered version of the Dirac function is

$$\delta_K(\boldsymbol{x}, \boldsymbol{x}_{\text{sc}}) = \prod_{n=1}^{3} \frac{K}{\pi} \text{sinc}\left[K(x_n - x_{n,\text{sc}})\right], \tag{2.14}$$

where $K = \pi/\Delta x$ is the angular spatial cutoff frequency that depends on the spatial stepsize Δx, and $(x_1, x_2, x_3) = (x, y, z)$ are the spatial coordinates.

A point scatterer can represent either a nonoscillating object that reflects the incoming wave because of its contrasting medium properties, or a noncontrasting object that radiates an outward wave because of its radial oscillation induced by the incoming wave [32]. A MB shows contrast with its surroundings but also vibrates, so the question might arise whether both effects should be separately accounted for. To resolve this issue, in Sec. 2.3.2 we will first compare the off-resonance scattering from a linearly responding MB without a shell, as obtained from both representations. Next, we will explain how to describe a nonlinear MB and a distribution of MBs.

2.3.2 Nonoscillating contrasting sphere

As a possible model for a spherical MB, first we will consider the background medium with a spherical inclusion with a fixed radius R_0, a speed of sound c_1, and a density of mass ρ_1. This sphere is insonified by a pressure wave with angular frequency ω.

We assume that the radius of the sphere is much smaller than the wavelength of this wave, i.e. $R_0 \ll 2\pi c_0/\omega$, so it is allowed to consider a plane incident wave as the excitation wave. Let us suppose that in the absence of the sphere, this wave would have a pressure amplitude $p(\boldsymbol{x}_{\text{sc}}, \omega)$ at the location of the center of the sphere. The scattered pressure p_{sc} is most easily obtained in terms of spherical harmonics. To find the dominant behavior of p_{sc} for small spheres and below resonance, we expand this result into a power series of R_0, and keep only the three terms that are of lowest order in R_0. These are the monopole term $p_{\text{sc}}^{\text{mono}}$, the dipole in the intermediate field $p_{\text{sc}}^{\text{dif,if}}$ and the dipole in the far field $p_{\text{sc}}^{\text{dif,ff}}$ as derived from App. 2.A. These are derscribed by the equations

$$p_{\text{sc}}^{\text{mono}} = \frac{\omega^2 p(\boldsymbol{x}_{\text{sc}}, \omega) V_0}{4\pi r} \left(\frac{\rho_0}{\rho_1 c_1^2} - \frac{1}{c_0^2} \right) \exp(-ik_0 r), \tag{2.15}$$

$$p_{\text{sc}}^{\text{dip,if}} = \frac{-i\omega p(\boldsymbol{x}_{\text{sc}}, \omega) V_0}{4\pi r^2} \frac{3(\rho_1 - \rho_0)}{c_0(\rho_0 + 2\rho_1)} \cos(\theta) \exp(-ik_0 r), \tag{2.16}$$

$$p_{\text{sc}}^{\text{dip,ff}} = \frac{\omega^2 p(\boldsymbol{x}_{\text{sc}}, \omega) V_0}{4\pi r} \frac{3(\rho_1 - \rho_0)}{c_0^2(\rho_0 + 2\rho_1)} \cos(\theta) \exp(-ik_0 r). \tag{2.17}$$

where $V_0 = \frac{4}{3}\pi R_0^3$ is the volume of the sphere, $r = \|\boldsymbol{x} - \boldsymbol{x}_{\text{sc}}\|$, θ is the angle of observation relative to the direction of the incident wave, and $k_0 = \omega/c_0$ is the wavenumber in the background medium. Because the term in Eq. (2.15) decays with r^{-1} and is omnidirectional, it describes the field of a physical monopole. The other two terms depend on $\cos(\theta)$ and describe the field of a physical dipole, where Eq. (2.16) represents the intermediate field that decays with r^{-2}, and Eq. (2.17) represents the far field that decays with r^{-1} [34]. In the context of ultrasound contrast agents, it is opportune to consider an incident wave of 1 MHz propagating in a background consisting of water and impinging on a gas-filled sphere with a radius of 1 μm. It turns out that even on the surface of the sphere, the intermediate and far field dipole terms are two and four orders of magnitude smaller, respectively, than the monopole term. From this, we conclude that in this paper we may consider a spherical MB to act solely as a monopole. In that case, the point scatterer that for $r > R_0$ will cause the same pressure as in Eq. (2.15) is

$$S_{\text{sc}}(\boldsymbol{x}, \omega) = \omega^2 p(\omega) V_0 \rho_0 \left(\frac{1}{\rho_1 c_1^2} - \frac{1}{\rho_0 c_0^2} \right) \delta(\boldsymbol{x} - \boldsymbol{x}_{\text{sc}}). \tag{2.18}$$

The time domain equivalent of this equation is

$$S_{\text{sc}}(\boldsymbol{x}, t) = -V_0 \rho_0 \left(\frac{1}{\rho_1 c_1^2} - \frac{1}{\rho_0 c_0^2} \right) \frac{\partial^2 p(\boldsymbol{x}_{\text{sc}}, t)}{\partial t^2} \delta(\boldsymbol{x} - \boldsymbol{x}_{\text{sc}}). \tag{2.19}$$

For a fluid background medium with a gas filled sphere it turns out that $\rho_0 c_0^2 \gg \rho_1 c_1^2$ and Eq. (2.19) may be approximated by

$$S_{\text{sc}}(\boldsymbol{x}, t) = -V_0 \frac{\rho_0}{\rho_1 c_1^2} \frac{\partial^2 p(\boldsymbol{x}_{\text{sc}}, t)}{\partial t^2} \delta(\boldsymbol{x} - \boldsymbol{x}_{\text{sc}}). \tag{2.20}$$

2.3.3 Oscillating noncontrasting sphere

As a second model for a spherical MB, we will consider the background medium with a noncontrasting, oscillating sphere with rest radius R_0. The oscillations are induced by an incident pressure wave. Again we assume that the radius of the sphere is much smaller than the wavelengths present in the incident wave, so the external pressure experienced by the sphere is approximately homogeneous and may be taken equal to the incident pressure $p(\boldsymbol{x}_{\mathrm{sc}}, t)$ at the center of the sphere. As a consequence, we may assume that the sphere will only show radial oscillations, i.e. its instantaneous shape will be fully described by a dynamic radius $R(t)$. The oscillating sphere therefore acts as a monopole source of volume injection, which is consistent with the conclusion in Sec. 2.3.2. The volume injection rate of the monopole source is $Q = dV/dt$, in which $V = \frac{4}{3}\pi R^3(t)$. Integration of Eq. (2.2) over the volume V_0 at rest of the sphere results in a contrast source strength $S_{\mathrm{sc}} = \rho_0 dQ/dt = \rho_0 d^2V/dt^2$. The point scatterer that for $r > R$ will cause the same pressure as the oscillating sphere is

$$S_{\mathrm{sc}}(\boldsymbol{x}, t) = \rho_0 \frac{d^2V}{dt^2}\, \delta(\boldsymbol{x} - \boldsymbol{x}_{\mathrm{sc}}). \tag{2.21}$$

To find the relation between Eqs. (2.19) and (2.21) for linearly responding bubbles below resonance, we consider the linearized equations of motion and continuity. Inside the bubble, these may be written as

$$\nabla p + \rho_0 \frac{\partial \boldsymbol{v}}{\partial t} = (\rho_0 - \rho_1) \frac{\partial \boldsymbol{v}}{\partial t} + \boldsymbol{f}, \tag{2.22}$$

$$\nabla \cdot \boldsymbol{v} + \kappa_0 \frac{\partial p}{\partial t} = (\kappa_0 - \kappa_1) \frac{\partial p}{\partial t} + q. \tag{2.23}$$

The terms at the right hand sides of these equations describe the sources of the scattered field. When these are point sources, or may be considered as such, the right hand sides of Eqs. (2.22) and (2.23) represent the dipole behavior and the monopole behavior of the sphere, respectively [34]. For a nonoscillating contrasting sphere, the density of volume force $\boldsymbol{f}$ and the density of volume injection rate q are zero, and for an oscillating noncontrasting sphere, the mass density contrast $\rho_0 - \rho_1$ and the compressibility contrast $\kappa_0 - \kappa_1$ are zero. To obtain the same monopole scattering from a nonoscillating contrasting sphere and an oscillating noncontrasting sphere, we must therefore have

$$(\kappa_0 - \kappa_1) \frac{\partial p}{\partial t} = q = \frac{1}{V_0} \frac{dV}{dt}, \tag{2.24}$$

where p is the pressure inside the sphere, which in lowest order is equal to the incident pressure $p(\boldsymbol{x}_{\mathrm{sc}}, t)$. Multiplication by $V_0\rho_0$, differentiation with respect to time, and applying the relation $\kappa = 1/(\rho c^2)$ for linear acoustics, yields

$$-V_0\, \rho_0 \left(\frac{1}{\rho_1 c_1^2} - \frac{1}{\rho_0 c_0^2} \right) \frac{\partial^2 p}{\partial t^2} = \rho_0 \frac{d^2 V_{\mathrm{sc}}}{dt^2}. \tag{2.25}$$

The left hand side and right hand side of this equation are exactly the magnitude of the scattering sources in Eqs. (2.19) and (2.21), respectively. From this, we conclude that in the linear case, the oscillating noncontrasting sphere represents the physics

of the bubble equally well as the nonoscillating contrasting sphere. In the following parts of this paper, we extrapolate this to the nonlinear case by assuming that the volume oscillations of a nonlinear bubble fully represent the intricate physics of the interior and shell of that bubble.

2.3.4 Microbubble as a point scatterer

For practical ultrasound contrast bubbles, the above models are not accurate enough because the presence of a shell and the effect of surface tension is missing. Moreover, in medical applications bubbles are often used near resonance, and in the nonlinear regime. To accurately represent a MB by a point scatterer, the applied model should be based on the following assumptions: the surrounding liquid is infinite and behaves in a Newtonian way, there is no mass or heat transfer between the medium and the gas inside the bubble, the buoyancy and gravity effects can be neglected, the wavelength of the exciting pressure field is much larger than the radius, so that the pressure has a uniform distribution over the bubble shell, and the bubble shape remains spherical through time [1]. This implies that the bubble acts as an oscillating noncontrasting monopole source. Usually, the time-dependent bubble radius is obtained by solving some variant of the Rayleigh-Plesset equation. Therefore, it is most logical to represent a MB by a contrast point source

$$S_{\mathrm{sc}}(\boldsymbol{x},t) = \rho_0 \frac{d^2 V_{\mathrm{sc}}}{dt^2}\,\delta(\boldsymbol{x}-\boldsymbol{x}_{\mathrm{sc}}). \tag{2.26}$$

The scatterer's volume depends on the bubble radius as a function of time, which in our case we will calculate by solving the Marmottant equation [31]. This model is most applicable to describe the oscillatory behavior of lipid-encapsulated MBs. We emphasize that our method is not restricted to this specific model, which can be replaced by any other model that suits another type of bubbles.

The Marmottant model relates the radius of a nonlinearly oscillating MB to the acoustic pressure according to

$$\begin{aligned}\rho_0\left(\ddot{R}R+\frac{3}{2}\dot{R}^2\right) &= \left(P_0+\frac{2\sigma(R_0)}{R_0}\right)\left(\frac{R_0}{R}\right)^{3\gamma}\left(1-\frac{3\gamma\dot{R}}{c_0}\right)\\ &\quad - P_0 - p(\boldsymbol{x}_{\mathrm{sc}},t) - 4\mu\frac{\dot{R}}{R} - \frac{2\sigma(R)}{R} - 4\kappa_s\frac{\dot{R}}{R^2},\end{aligned} \tag{2.27}$$

where the quantity P_0 [Pa] is the ambient pressure, γ is the polytropic exponent of the gas encapsulated in the bubble, $p(\boldsymbol{x}_{\mathrm{sc}},t)$ [Pa] is the excitation pressure in the surrounding liquid of the scatterer, μ [Pa. s] is the surrounding liquid dynamic viscosity, κ_s [kg/s] is the shell viscosity and $\sigma(R)$ [N/m] is the effective surface tension. Based on the shell-buckling model of Marmottant, the latter variable is expressed as

$$\sigma(R) = \begin{cases} 0, & \text{if } R \le R_b,\\ \chi\left(\frac{R^2}{R_b^2}-1\right), & \text{if } R_b < R < R_r,\\ \sigma_w, & \text{if } R \ge R_r,\end{cases} \tag{2.28}$$

where χ [N/m] is the shell elasticity, σ_w [N/m] is the surface tension of the gas-water interface, $R_b = R_0/\sqrt{\sigma(R_0)/\chi + 1}$ is the buckling radius, and $R_r = R_b\sqrt{\sigma_w/\chi + 1}$ is the rupture radius.

The solution of the Marmottant equation is the bubble radius as a function of time. Equation (2.27) was solved using the Livermore Solver for Ordinary Differential Equations (LSODE) from the ODEPACK library [35] implemented in Fortran. To enhance performance and efficiency, the Marmottant model is normalized by $\varrho_* = R/R_0 - 1$ and $\tau_* = tf_0$, where f_0 is the center frequency of the incident pressure field. This results in $\dot{R} = R_0 f_0\, d\varrho_*/d\tau_*$ and $\ddot{R} = R_0\ f_0^2\, d^2\varrho_*/d\tau_*^2$. Based on this normalization and to achieve good convergence, the absolute and relative tolerance of the solver is set at 10^{-15}.

2.3.5 Microbubble population as distribution of point scatterers

For a population of N MBs, all corresponding point sources should be added, resulting in the nonlinear contrast source term

$$S_{\mathrm{cs}}(\boldsymbol{x}, t) = \rho_0 \sum_{i=1}^{N} \frac{d^2 V^{(i)}(\boldsymbol{x}_{\mathrm{sc}}^{(i)}, t)}{dt^2}\, \delta(\boldsymbol{x} - \boldsymbol{x}_{\mathrm{sc}}^{(i)}). \tag{2.29}$$

When the MBs are located in an otherwise linear, homogeneous, and lossless fluid medium, the nonlinear wave equation for the acoustic pressure becomes

$$c_0^{-2}\frac{\partial^2 p}{\partial t^2} - \nabla^2 p = S_{\mathrm{pr}} + S_{\mathrm{cs}}. \tag{2.30}$$

The solution of Eq. (2.30) can be obtained by the scheme in Eq. (2.12), provided we replace the nonlinear contrast source S_{nl} by S_{cs} in Eq. (2.29).

The physical interpretation of the iterative process is explained in Fig. 2.2. For $j = 0$, the solution of INCS in an arbitrary point $\boldsymbol{x}$ is the incident field $p^{(0)}$. This is the field that would be generated by the primary source S_{pr} in the backgrond medium in the absence of MBs (Fig. 2.2a). For $j = 1$, the scattering of $p^{(0)}$ by all MBs is computed and summed, resulting in the first-order field correction $\delta p^{(1)}$. This correction is added to $p^{(0)}$ to form the first-order field estimate $p^{(1)}$, which thus consists of the incident field plus the first-order scattering of all MBs (Fig. 2.2b). For $j = 2$, the scattering of $p^{(1)}$ by all MBs is computed and summed, resulting in the second-order field correction $\delta p^{(2)}$. This correction contains both the scattering of $p^{(0)}$ and $\delta p^{(1)}$, i.e. the first and second-order scattering of all MBs. It is added to $p^{(0)}$ to form the second-order field estimate $p^{(2)}$, which consists of the incident field plus the scattering of all MBs up till order two (Fig. 2.2c). Continuing the iterative scheme, each iteration accounts for a next order of multiple scattering (Fig. 2.2d).

After each iteration, we compare the field $p^{(j)}$ with the field $p^{(j-1)}$, using a relative root mean square error (RRMSE). When this error has become negligible after several iterations, we conclude that the highest order of scattering has become insignificant and will no longer influence the final result. At this point, we assume that INCS has sufficiently converged and we terminate the iterative process.

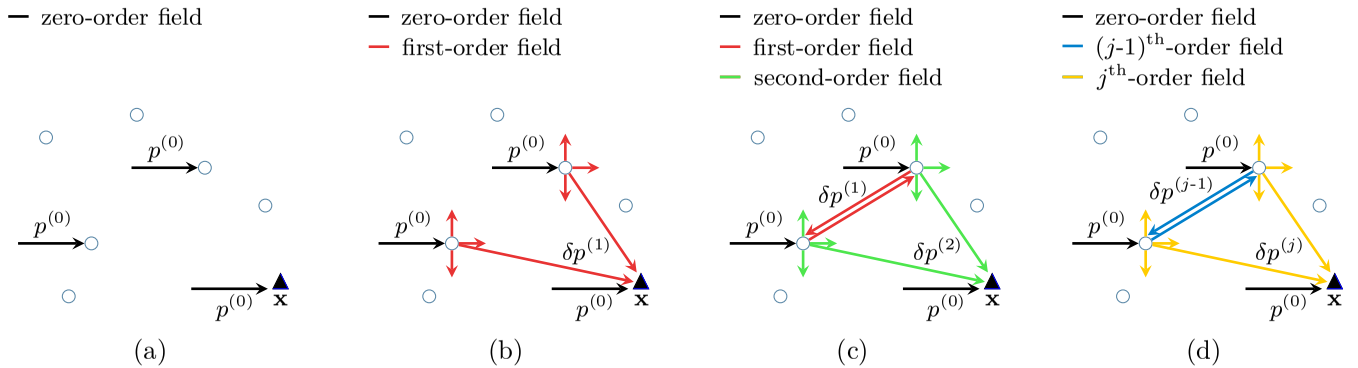

Figure 2.2: (Color online) Physical interpretation of the iterative procedure for a number of scatterers (circles) and an observer $\mathbf{x}$ (triangle), after 0 (a), 1 (b), 2 (c) and n (d) iterations. The black arrows represent the incident field hitting the scattterers. The colored arrows show the field corrections due to multiple scattering orders.

2.4 Numerical implementation

2.4.1 Generation of the random bubble population

Our next step is to generate the positions $\boldsymbol{x}_{\mathrm{sc}}^{(i)}$ in a 3D population of randomly located bubbles. We have implemented two approaches for the positioning of N point scatterers in a rectangular bubble domain. In both cases, a minimum distance between every two point scatterers is assumed to avoid the overlap of the physical bubbles.

The first approach is used to create a discrete uniform distribution of point scatterers over the rectangular bubble domain. This is achieved by dividing the bubble domain in N identical, smaller cubes with a prescribed minimum mutual distance, and randomly positioning one scatterer in each one of these smaller cubes.

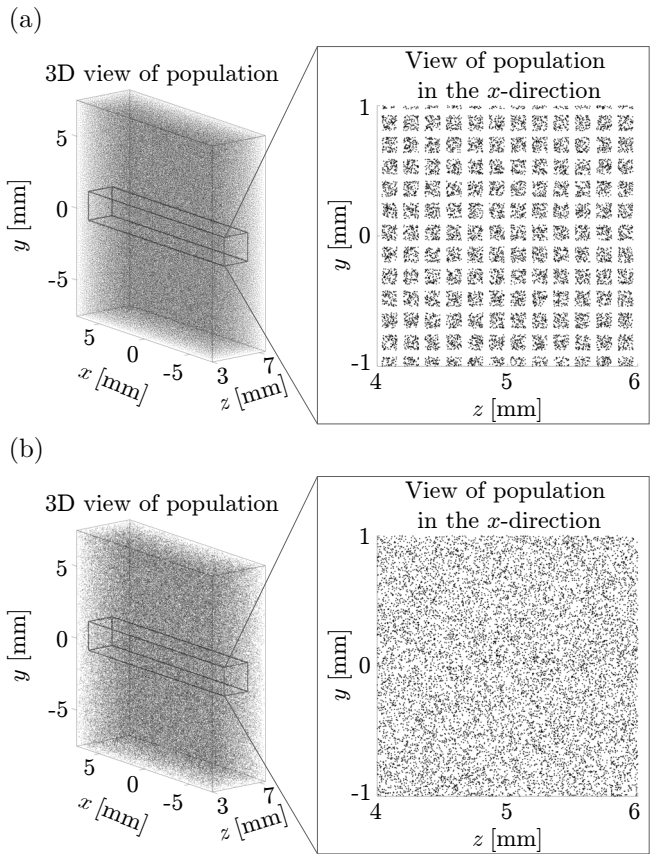

Figure 2.3: Uniform (a) and random (b) distribution of scatterers, shown in 3D view (left) and in the x-direction (inset, right). The populations consist of 2×10^5 scatterers concentrated in volume of 1 ml, having a minimum mutual distance of 50 μm. This distance is taken exceedingly large here to show the difference between (a) and (b).

The second approach is applied to obtain a fully random positioning of the point scatterers, with the minimum mutual distance between scatterers as the only restriction. To accomplish this, point scatterers are randomly positioned in the domain of interest. The separation of each scatterer and its closest neighbors is then determined. Those points who do not fulfill the distancing restriction, are removed from the cloud.

Realizations obtained by these two approaches are presented in Fig. 2.3. The location of the point scatterers in the generated clouds is independent of the location of the computational grid points. In this way, INCS can retain a coarse grid size without 'discretizing' the cloud of particles. This is particularly important for large concentrations of particles.

2.4.2 Off-grid point scatterers

Due to the coarse discretization allowed by the INCS method, some scatterers will unavoidably be placed between the gridpoints. This causes no problem because each point scatterer is represented by its filtered version and by using Eq. (2.14), proper weights are assigned to all grid points. Based on previous research [36], this methodology will provide an accurate solution.

For large bubble concentrations, this process may not be efficient. To improve the computational efficiency and reduce the memory load for large concentrations, during intermediate iterations only a limited number of neighboring grid points is used for the filtered version of each point scatterer. In this way, the scattered pressure is accurately computed in the region where it is strongest, i.e. around each scatterer. In the final iteration, the filtered spatial Dirac function is again using all the grid points. This corrects the errors made in the intermediate iterations. The described approach significantly reduces the computation time, at a cost of a small intermediate error. This reduction is most significant for higher concentrations. For example, we have considered a spatiotemporal computational domain with $N_t \times N_x \times N_y \times N_z = 1299 \times 200 \times 96 \times 600$ gridpoints, with a population of 10^6 point scatterers that are randomly positioned in a volume of 1 ml. The computational job is distributed over 100 Central Processing Units (CPUs). The time required per iteration for computing the contrast source term in all gridpoints and only for a limited number of gridpoints around each scatterer is 91 minutes and 10 minutes, respectively. The RRMSE between these cases is only 0.1%.

2.4.3 Trilinear interpolation and avoiding self scattering

To calculate the pressure field at the off-grid location of a point scatterer, a trilinear interpolation using the eight neighboring gridpoints is implemented. A particular point of attention is to avoid that the pressure experienced by a point scatterer in iteration j contains the pressure that is generated by the same scatterer in iteration $j-1$. To prevent this 'self scattering', in iteration $j-1$ the computed strength of each contrast source is saved in a file. In iteration j, the point sources, represented by the filtered Dirac function, are convoluted with the Green's function to obtain the pressure generated in iteration $j-1$ by each point source at its eight neighboring gridpoints. These pressure values are subtracted from the total computed pressure

before computing the new pressure value at the location of the point source. This correction is particularly significant for strong individual scatterers that don't have strong neighbors nearby.

2.5 Numerical results

For the numerical examples in Sec. 2.5.1 and Sec. 2.5.2, a computational domain of $X \times Y \times Z = 20$ mm $\times$ 20 mm $\times$ 20 mm is used. The incident pressure field is a plane wave being generated at $z = 0$ and propagating in the positive z-direction. A plane wave is used to let all the scatterers experience the same incident pressure.
In Secs. 2.5.1, 2.5.2 and 2.5.3 , the temporal signature of the incident pressure is

$$s(t) = \exp\left[-\left(\frac{t - T_d}{T_w/2}\right)^2\right] \sin[2\pi f_0(t - T_d)], \tag{2.31}$$

where $T_w = 3/f_0$ is the width and $T_d = 6/f_0$ is the delay of a Gaussian envelope with a duration of $12/f_0$, where $f_0 = 1$ MHz is the center frequency. The scatterers will be embedded in water with a density of $\rho = 1060$ kg/m^3 and a speed of sound of $c_0 = 1482$ m/s. In the considered situations, water has negligible losses and nonlinear effects will be hardly noticeable. Therefore, we assume that the embedding medium is lossless and linear. A sampling frequency of 18 MHz was used as the basis for the discretization of the spatiotemporal domain.

2.5.1 Single versus multiple scattering: linear scatterers

In this subsection, we will present the difference between single and multiple scattering in case of linear scatterers. The difference will be more visible for higher concentrations. For this reason, a population of 1.6×10^6 linearly scattering spheres of 1 μm radius is placed in a subdomain -7.50 mm $\leq x \leq 7.50$ mm, -7.50 mm $\leq y \leq 7.50$ mm, 3.00 mm $\leq z \leq 7.44$ mm as indicated in Fig 2.3(b). This yields a concentration of scatterers of 1.6×10^6 ml^{-1}. It is assumed that the gas inside these scatterers is C_4F_{10}, with a density $\rho_1 = 10$ kg/m^3 and a speed of sound $c_1 = 100$ m/s. These spheres have a sharp resonance frequency of 2.68 MHz. The maximum of the incident pressure is $P_0 = 200$ kPa. For first-order scattering, application of Eq. (2.37) with $r = R$ then yields a maximum reflected pressure of 32.4 kPa(0.16218*P_0) on each individual scatterer's surface. In Fig. 2.4(a), the total pressure field after $j = 1$ iterations, i.e. after accounting for one order of scattering, is presented. An increased pressure, compared to the incident wave, is visible in and behind the population of scatterers. This is due to the constructive interference of the scattering in the direction of the propagation of the plane wave, which is a consequence of Huygens's principle. In Fig. 2.4(b), the total pressure field for after $j = 2$ iterations, i.e. including two orders of scattering, is presented. Compared to the first iteration, the total pressure field in and behind the population is reduced and a lower pressure region starts to form behind the population. Virtually no numerical changes occur after $j = 8$ iterations and this result is presented in Fig. 2.4(c). The difference between the three pressure maps is clearly visible. It can be seen that the contribution of the population is strongest in

the first iteration. When more orders of multiple scattering are included, there is a correction in the total pressure field. Furthermore, it can be seen that lower pressure regions form on the sides and behind the population and become more distinct with increasing multiple scattering orders.

A comparison of the time signatures of the total pressure at a point receiver located

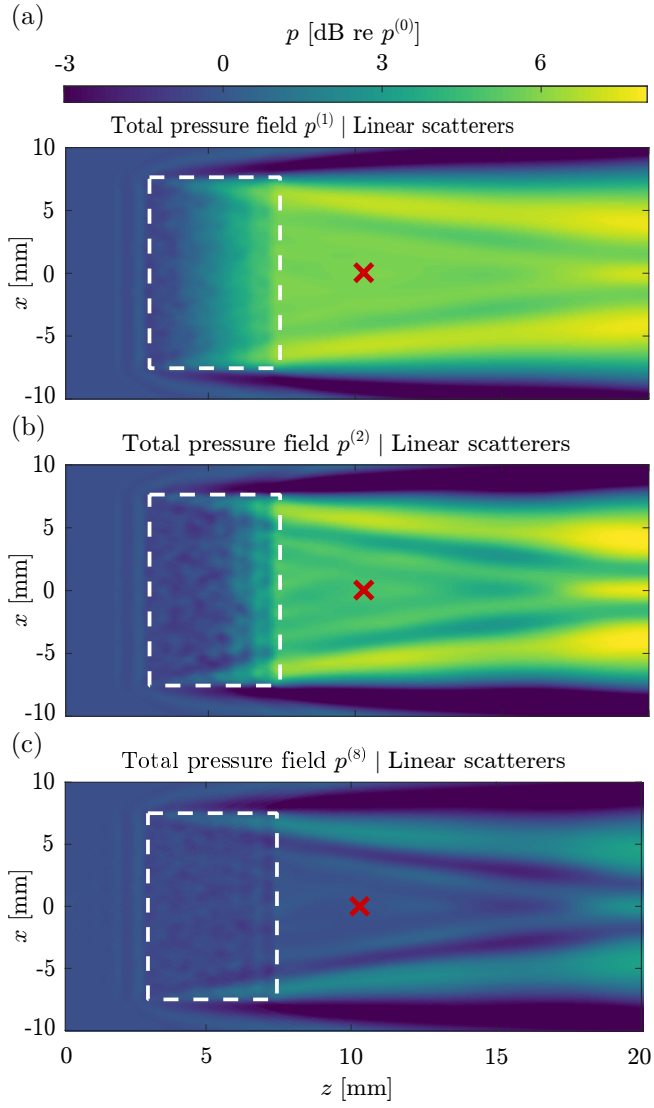

Figure 2.4: (Color online) Maximum of the total pressure field in the plane $y = 0$ mm in case of 1.6×10^6 linear scatterers with 1 μm radius, when taking into account (a) 1, (b) 2 and (c) 8 orders of scattering. The population of scatterers is inside the dotted white square.

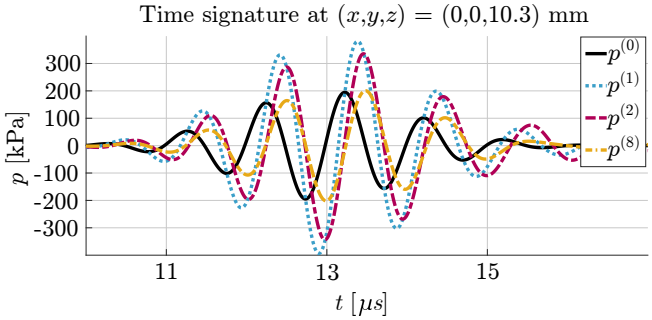

Figure 2.5: (Color online) Comparison between the time signatures of the total pressure pulse that is received by a point receiver located at the red cross in Fig. 2.4, for a number of iterations.

in (0 mm, 0 mm, 10.3 mm) is presented in Fig. 2.5. Subtraction of $p^{(0)}$ from the other signals would result in the scattered pressure for the respective iterations. Besides a correction of the maximum pressure, a change in phase can be seen. It seems like there is a decrease in the effective speed of sound due to the increasing scattering in the population. This figure reinforces the significance of multiple scattering and the need to take into account multiple orders in order to have a more accurate result.

To validate our method, we can also compare the above time signatures results with predictions based on effective medium theory. In the current case, the conditions justify the application of the original theory of Foldy [4]. According to this theory, the effect of a monodisperse population of scatterers is represented by replacing the wave number k_0 in the scattering domain by a corrected wave number

$$k^2 = k_0^2 + 4\pi n g, \tag{2.32}$$

where n is the concentration of the scatterers and g is their individual scattering strength. The shift in wavenumber corresponds to a shift in wave speed, and as a consequence, in a time shift of the wave that has traversed the scattering domain. In the case considered in this subsection, we have $n = 1.6 \times 10^{12}$ m^{-3} and $g = 1.6218 \times 10^{-7}$ m (taking into account the correction for the reflected pressure at the surface of each scatterer, a factor of 1.16218). This yields a wavespeed of 1363.5 m/s in the scattering domain, while the speed in the medium without scatterers is 1482 m/s. Since the scattering domain has a length of 4.4444 mm, the additional time delay caused by the scattering domain, as predicted by the theory of Foldy, is $\Delta t_{\text{Foldy}} = 0.2606$ μs. We have also determined the time delay between the incident wave $p^{(0)}$ and the wave with all significant orders of scattering $p^{(8)}$ in Fig. 2.5, by looking at the shift in the zero crossings around 13 μs. This is found to be $\Delta t_{\text{INCS}} = 0.2595$ μs. Thus,

Table 2.1: Parameters of the Marmottant model of the applied MBs

κ_s [kg/s]	σ_w [N/m]	σ_R [N/m]	γ	χ [N/m]	μ [Pa · s]
3×10^{-8}	0.072	0.036	1.07	0.4	2×10^{-3}

the difference in time delay as predicted by the theory of Foldy and our method is only 0.42%. Moreover, because in our case the wavenumber obtained from Eq. (2.32) does not contain an imaginary part, the theory of Foldy predicts that the wave that traverses the scattering domain does not attenuate. Fig. 2.5 shows that our scheme corrects the larger amplitude of the earlier iterations, and that iteration $p^{(8)}$ indeed has the same amplitude as the incident field $p^{(0)}$. From the above we conclude that both for the time delay and the amplitude of the wave traveling through a scattering domain, there is good agreement between our method and the effective medium theory of Foldy.

2.5.2 Single versus multiple scattering: nonlinear microbubbles

Here, the same configuration as in Sec. 2.5.1 is used, but now we employ the Marmottant model from Section 2.3.4 to demonstrate the difference between populations of linear and nonlinear scatterers. The concentration of the population is $2 \times 10^5 \text{ml}^{-1}$ and the radius of the MBs is 2 μm. The parameters for the Marmottant model are given in Table 2.1. These MBs also have a resonance frequency of 2.68 MHz.

In Fig. 2.6, the difference between $j = 1$ iteration (one order of scattering) and $j = 14$ iterations (14 orders of scattering) is shown. Compared to the population of linear scatterers, the difference between the pressure maps for subsequent iterations is more significant for the population of MBs. This is because the MBs are stronger scatterers than the linear scatterers. Virtually no numerical changes now occur after $j = 14$ iterations. This shows that for the stronger nonlinear scatterers, more iterations should be taken into account. As in Sec. 2.5.1, lower pressure regions also exist in the MB case. Compared to the linear case, these regions are also wider, i.e. relatively more scattering energy is concentrated in the regions behind the horizontal edges of the population.

A comparison between the time signatures at the point receiver is presented in Fig. 2.7(a). A strong negative pressure dip can be seen when only the first order scattering is included. Besides a correction of the maximum pressure, a change in phase is visible in the early part of the pulses. For later times, the signals from subsequent iterations become incoherent due to the nonlinear multiple scattering contributions. The frequency spectrum of the pulses is presented in Fig. 2.7(b). As expected, higher harmonics caused by the nonlinear behavior of the MBs are visible. A significant observation is that for $j = 1$ there is a dip in the fundamental and the higher harmonics are relatively strong, whereas for $j = 14$ orders, the fundamental is partly restored and the higher harmonics have decreased. These results demonstrate that multiple scattering inside a population of nonlinear scatterers plays an important role.

2.5.3 Harmonic imaging

In the previous subsection, we have shown the difference between a population of linear and nonlinear scatterers when excited by a plane wave. In this subsection, we will focus on a medical application and will demonstrate the generation of higher harmonics when a population of bubbles is hit by an ultrasound beam. Here, a

computational domain of $X \times Y \times Z = 22$ mm $\times$ 10 mm $\times$ 60 mm is used. The incident beam is generated by a phased array transducer of 40 elements with $H_{el} \times W_{el} =$ 10 mm $\times$ 0.45 mm, and a kerf with zero width. This corresponds to an aperture with a width of $W_{\text{arr}} = 18$ mm. The origin of the coordinate system is at the center of the transducer aperture. The array has an azimuthal focus at $(x_f, z_f) = (0 \text{ mm}, 35 \text{ mm})$ and an elevation focus at $z_{el} = z_f$. In Fig. 2.8, a sketch of a the geometry of the phased array is presented. The pressure pulse sent from each element of the transducer is again given by Eq. (2.31). The maximum of the emitted pressure is $P_0 = 50$ kPa at the surface, and the pressure is the highest and equal to 191 kPa at the focus. In Fig. 2.9(a) and (b), the incident beam is presented at the elevation plane $x = 0$ mm and the azimuthal plane $y = 0$ mm.

A population of 10^5 monodisperse MBs of 2 μm radius are randomly placed in a subdomain -5.30 mm $\leq x \leq 5.20$ mm, -2.55 mm $\leq y \leq 2.46$ mm, 25.5 mm $\leq z \leq$ 44.5 mm, as indicated in Fig 2.3. This means that the concentration of the MBs is about 10^5 ml^{-1}. The parameters for the Marmottant equation are the same as in Table 2.1.

The results are depicted in Fig. 2.10(a)-(c). The plots are made for $j = 25$

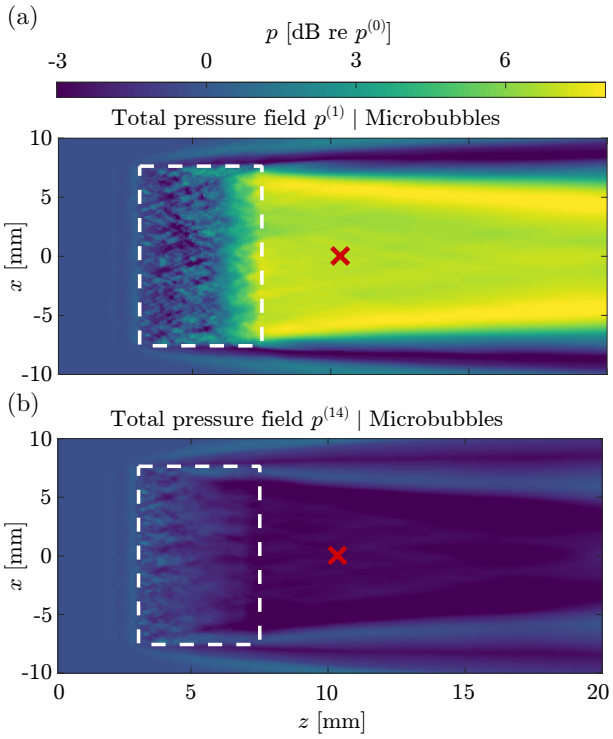

Figure 2.6: (Color online) Maximum of the total pressure field in the plane $y = 0$ mm in case of 2×10^5 nonlinear MBs with 2 μm radius, when taking into account (a) 1, (b) 14 and orders of scattering. The MB population is inside the dotted white rectangle.

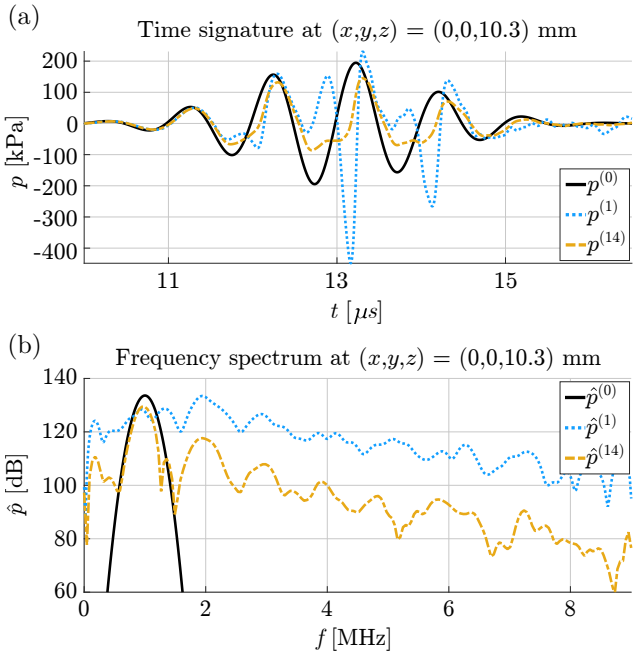

Figure 2.7: (Color online) Comparison between the time signatures (a) and the frequency spectrum (b) of the total pressure pulse that is received by a point receiver located at the red cross, for a number of iterations.

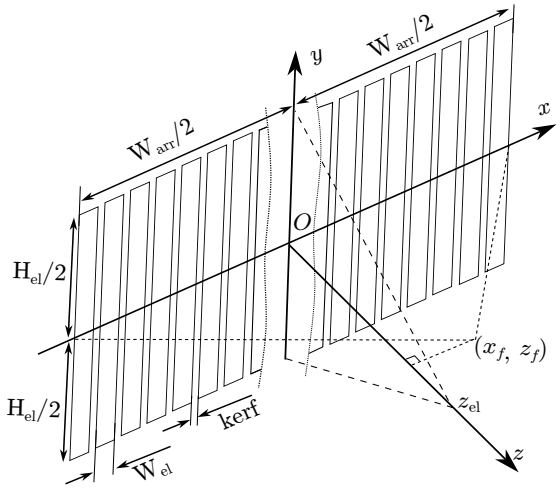

Figure 2.8: (Color online) Sketch of the geometry of the phased array used to generate the incident field.

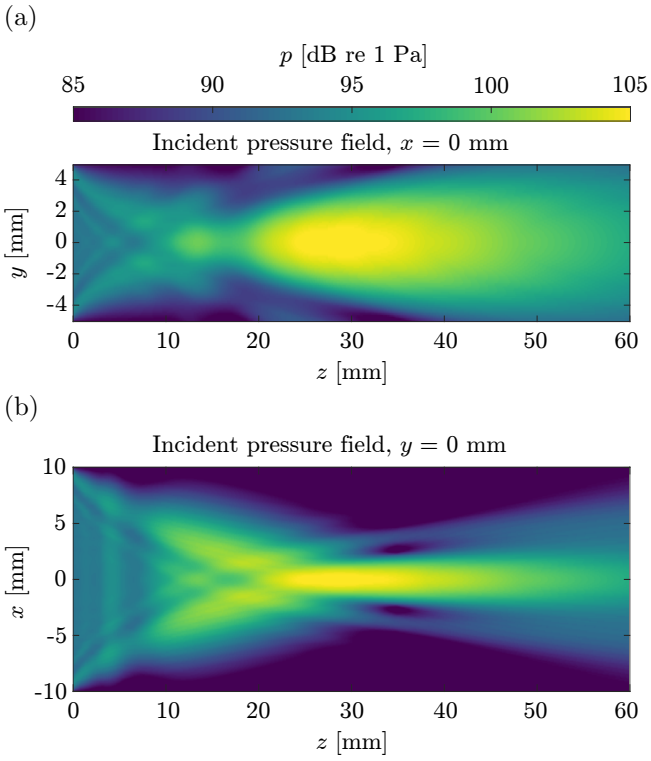

Figure 2.9: (Color online) Maximum pressure of the incident beam generated by a phased array. (a) In the elevation plane $x = 0$ mm, and (b) in the azimuthal plane $y = 0$ mm.

iterations, after which virtually no changes occur. The beam profiles of the harmonics are separated by using a 4th order Butterworth filter with cutoff frequencies indicated in the title of the plots. Because the embedding medium is linear, the higher harmonics are just caused by the MB population. In Fig. 2.10(a)-(c) it is clearly visible that the 2H and 3H beams both come into existence at the point where the incident beam hits the bubble population. In the areas where the incident pressure is high, e.g in the focal area of the incident beam, the MBs oscillate in a more nonlinear way, resulting in higher harmonic pressures. There is 15 dB difference between the maximum pressure in the fundamental and 2H, whereas the difference between 2H and 3H is only about 5 dB. The latter can be explained by the fact that each MB simultaneously generates a number of higher harmonics. Since the MBs have a resonance frequency close to 3 MHz, both 2H and 3H will have about the same strength. These observations demonstrate that the mechanism of generating higher harmonics is quite different from the gradual growth of subsequent harmonics in case of medium nonlinearity. The difference between medium nonlinearity and nonlinearity caused by MBs also becomes manifest in the way the harmonics are generated by the iterative scheme. Loosely speaking, in case of medium nonlinearity, each iteration adds a new harmonic

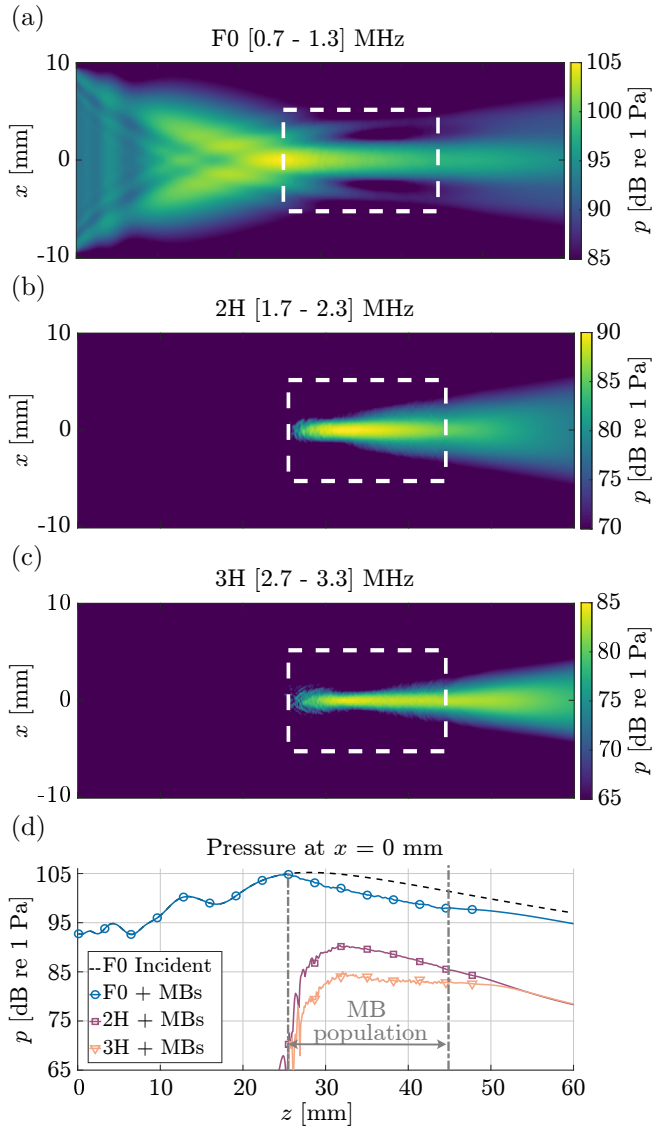

Figure 2.10: (Color online) Spectral profiles at $y = 0$ mm for the beam generated by the phased array. Fundamental (a), second harmonic 2H (b) and third harmonic 3H (c) for $j = 25$ iterations. The MB population is inside the dotted white rectangle. Axial profiles of the harmonic beams (d). The dotted gray lines depict the location of the MB population.

to the previous result [24], and the full spectrum is only obtained after a number of iterations. In case of nonlinear MBs, even the first iteration yields the full scattering spectrum of the bubbles, and each iteration corrects the previous result by adding a new order of scattering. As shown in Fig. 2.10(c), the successive iterations don't cause large changes in the shape of the spectrum, but rather correct the overall amplitude.

Moreover, Fig. 2.10(d) depicts the axial profiles of the harmonic beams. Also, a comparison with the incident pressure field is presented. The pressure of the harmonics amplitude is lower than the pressure of the fundamental, as expected. In the area where the harmonic beams exist, the fundamental beam is lower than the incident beam, i.e. without MBs. This can be explained by the conversion of energy of the fundamental into energy of the higher harmonics.

In Fig. 2.11(a) and (b), a comparison between the fields of the first four orders of scattering are shown for two populations with concentrations of 10^5 ml^{-1} and 10^4 ml^{-1}, respectively. For the higher concentration, the first three orders are of comparable amplitude. The peak amplitude of the fourth order is about 10 dB lower. On the other hand, for the lower concentration, the amplitude of the second scattering order is about 30 dB lower than the first. The third and fourth scattering orders are at least 40 dB lower than the first order. Thus, these scattering orders do not significantly affect the final result. Finally, it is visible that the field of each scattering order is shifted to the left compared to the result of the previous order. This reinforces the fact that multiple scattering should be taken into account, especially for high concentrations.

2.5.4 Convergence

As illustrated in Fig. 2.2, each iteration adds an order of multiple scattering to the computed pressure field. This fact can be used to determine the dependence between the highest significant order of multiple scattering and the concentration of the MB population.

To determine the significance of an order of multiple scattering, we compare the results from the current iteration (j) and the previous iteration $(j-1)$. The difference between these results over the spatial $\mathcal{X}_{\text{cd}}$ and temporal $\mathcal{T}_{\text{cd}}$ computational domain can be expressed by the relative root mean square error (RRMSE), which is defined as

$$\text{RRMSE} = \sqrt{\frac{\int_{\mathcal{X}_{\text{cd}}} \int_{\mathcal{T}_{\text{cd}}} \left[p^{(j)}(\boldsymbol{x},t) - p^{(j-1)}(\boldsymbol{x},t)\right]^2 dt\, d\boldsymbol{x}}{\int_{\mathcal{X}_{\text{cd}}} \int_{\mathcal{T}_{\text{cd}}} \left[p^{(0)}(\boldsymbol{x},t)\right]^2 dt\, d\boldsymbol{x}}}. \tag{2.33}$$

After a number of iterations the error will stabilize at a negligibly small level. In that case, we conclude that the addition of more scattering orders will not further improve the solution and we have reached the insignifcant scattering orders. When this point has been reached, we say that the iterative process has converged.

In Fig. 2.12, the RRMSE as a function of the number of iterations j is depicted for several concentrations of the MB population. We observe that for higher concentrations, the initial iterations have a higher RRMSE. This indicates that the variations between the initial iterations increase with concentration. Moreover, we see that for higher concentrations, more iterations are needed to reach convergence. This can be

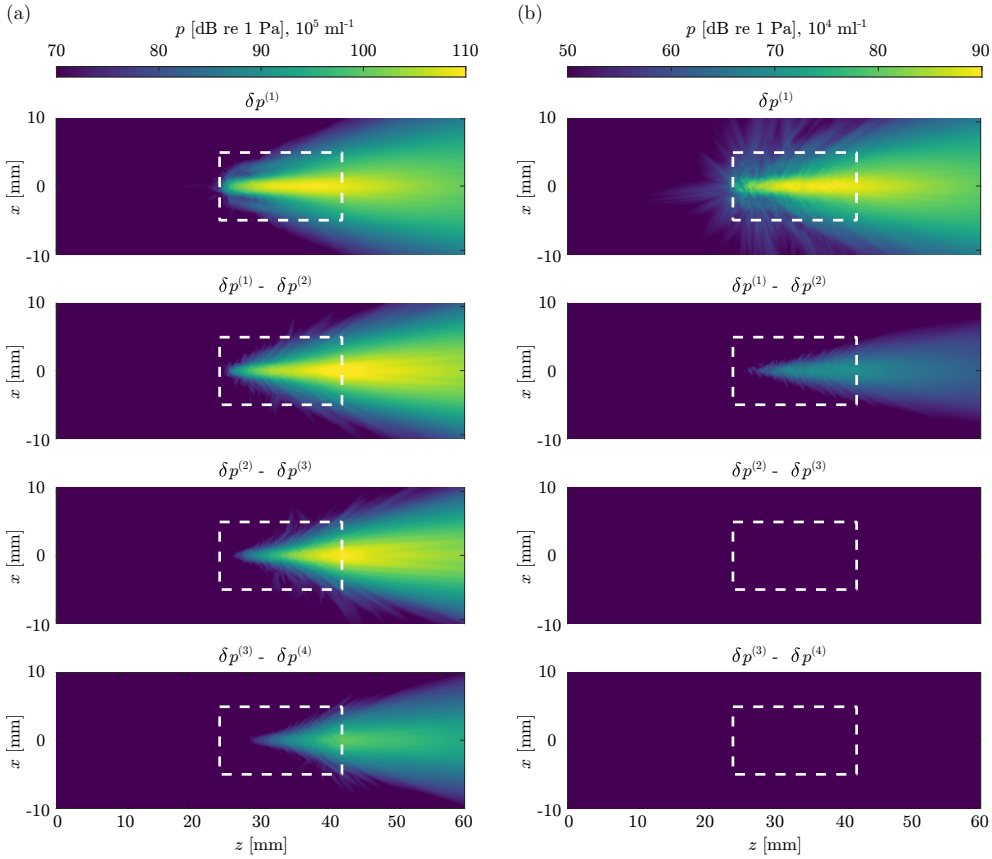

Figure 2.11: (Color online) Beam profiles in the azimuthal plane $y = 0$ mm as generated by the phased array in a MB concentration of 10^5 ml^{-1} (a) and 10^4 ml^{-1} (b). The first, second, third and fourth scattering orders are depicted from top to bottom, respectively. The MB population is inside the dotted white rectangle.

explained by the fact that more close-range interactions occur in higher concentrations, making higher scattering orders more important.

2.6 Conclusions

A novel method of simulating the multiple scattering of a pulsed ultrasound wave by a large 3D population of nonlinearly responding MBs was presented. The approach is based on the Iterative Nonlinear Contrast Source method, which was extended to include a large number of nonlinear contrast point sources. Each of these act as a virtual volume injection source that generates the nonlinear scattering caused by an individual MB. The volume of each MB follows from its radius, which depends in a nonlinear way on the surrounding time dependent pressure, as described by the

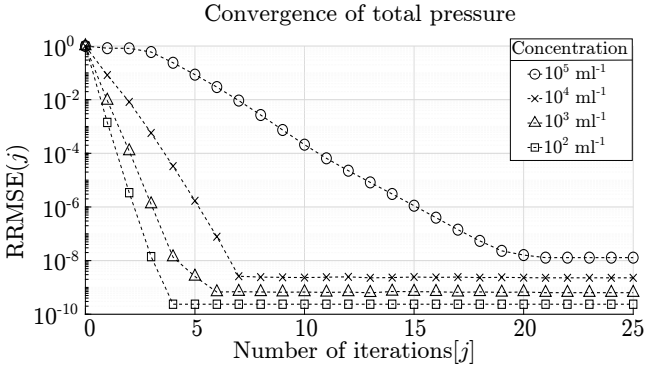

Figure 2.12: RRMSE as a function of iterations for various populations of MBs concentrated in a volume of 1 ml.

Marmottant model. Starting with the incident pressure from the primary transducer, the pressure in the 4D spatiotemporal computational domain is successively updated by using a Neumann iterative scheme.

Physically, each iteration adds an extra order of multiple scattering between the MBs. Numerically, it takes several iterations before the difference between successive iterations stabilizes at a small number. From this, it was deduced that the inclusion of several orders of multiple scattering is necessary to accurately capture the behavior of a population of MBs. It was also observed that higher orders of multiple scattering become more important for increasing concentrations.

The developed method accounts for an accurate representation of the individual nonlinear behavior of each MB, as well as their higher order nonlinear interactions, and may therefore be used for detailed investigations into the behavior of realistic MB populations.

Appendix 2.A Scattering by a small sphere

Here we will show the steps that lead to Eqs. (2.15)-(2.17) in the main text. First, we shortly derive the exact scattering of a plane acoustical wave by a penetrable sphere of arbitrary size; extensive derivations may be found in the literature [32]. The plane wave has an angular frequency ω, and is traveling in the z-direction through a medium with density of mass ρ_0 and speed of sound c_0. The sphere has a radius R, a mass density ρ_1, and a speed of sound c_1. For simplicity, the origin of the coordinate system is positioned at the center of the sphere. Using cartesian coordinates with $\boldsymbol{x} = (x, y, z)$, the plane incident wave is

$$p_{\text{inc}}(\boldsymbol{x}, \omega) = p_0 \exp(-ik_0 z), \tag{2.34}$$

where p_0 is the amplitude of the wave, and $k_0 = \omega/c_0$ is the wavenumber in the surrounding medium. To use the symmetry of the problem, we will turn to spherical coordinates with $\boldsymbol{r} = (r, \theta, \phi)$, where r (radius) is the distance to the origin, θ (elevation) is the angle between the positive z-axis and the position vector, and ϕ (azimuth)

is the angle between the positive x-axis and the projection of the position vector on the xy-plane. In spherical coordinates, the incident wave becomes

$$p_{\text{inc}}(\boldsymbol{r},\omega) = p_0 \sum_{n=0}^{\infty} a_n\, j_n(k_0 r), \tag{2.35}$$

in which

$$a_n = (2n+1)(-i)^n\, P_n[\cos(\theta)]. \tag{2.36}$$

In Eq. (2.35) and Eq. (2.36), P_n is the n-th order Legendre polynomial and j_n is the spherical Bessel function of the first kind and order n. In analogy with Eq. (2.35), the wave p_{sc} that is scattered by the sphere and the wave p_{tr} that is transmitted into the sphere can be written as

$$p_{\text{sc}}(\boldsymbol{r},\omega) = p_0 \sum_{n=0}^{\infty} b_n\, h_n^{(2)}(k_0 r), \tag{2.37}$$

$$p_{\text{tr}}(\boldsymbol{r},\omega) = p_0 \sum_{n=0}^{\infty} c_n\, j_n(k_1 r), \tag{2.38}$$

Here, $h_n^{(2)}$ is the spherical Bessel function of the third kind and order n. The reflection coefficients b_n and the transmission coefficients c_n follow from the continuity of the pressure and the radial particle velocity at the boundary of the sphere, i.e. by requiring for each n that $p(\boldsymbol{r},\omega)$ and $\rho^{-1}\partial p(\boldsymbol{r},\omega)/\partial r$ are continuous at $r = R$. This yields

$$b_n = a_n \frac{\rho_0 c_0\, j_n(k_0 R)\, j_n'(k_1 R) - \rho_1 c_1\, j_n(k_1 R)\, j_n'(k_0 R)}{\rho_1 c_1\, j_n(k_1 R)\, h_n^{(2)\prime}(k_0 R) - \rho_0 c_0\, h_n^{(2)}(k_0 R)\, j_n'(k_1 R)}, \tag{2.39}$$

$$c_n = a_n \frac{\rho_1 c_1\, j_n(k_0 R)\, h_n^{(2)\prime}(k_0 R) - \rho_1 c_1\, h_n^{(2)}(k_0 R)\, j_n'(k_0 R)}{\rho_1 c_1\, j_n(k_1 R)\, h_n^{(2)\prime}(k_0 R) - \rho_0 c_0\, h_n^{(2)}(k_0 R)\, j_n'(k_1 R)}, \tag{2.40}$$

where the prime indicates the derivative of a function. Combination of Eqs. (2.36), (2.37), and (2.39) yields the exact pressure that is scattered by the sphere.

Next, we consider the scattering by a sphere that is much smaller than the wavelength of the incident wave. In that case, it makes sense to represent the scattered pressure by its Taylor series around $R = 0$. If the frequency of the incident wave is much lower than the first resonance frequency of the sphere, it is sufficient to approximate the scattered pressure by the lowest order terms of the Taylor series. These are the terms of order R^3 that are given in Eqs. (2.15)-(2.17), where $p_0 = p(\boldsymbol{x}_{\text{sc}},\omega)$ is the incident pressure at the location of the sphere. The term in Eq. (2.16) decays with r^{-2} and is negligible in the far field, which is dominated by the terms in Eqs. (2.15) and (2.17) with decay r^{-1}. The sum of these terms yields, after normalizing by $p_0 \exp(-ik_0 r)/4\pi r$, the well-known expression for the angle-distribution function of a nonrigid sphere in the long wavelength limit [32].

$$\Phi(\theta) = \frac{k^2 R^3}{3}\left[\frac{\kappa_1 - \kappa_0}{\kappa_0} + \frac{3(\rho_1 - \rho_0)}{2\rho_1 + \rho_0}\cos(\theta)\right]. \tag{2.41}$$

Bibliography

[1] M. Versluis, E. Stride, G. Lajoinie, B. Dollet, and T. Segers, "Ultrasound Contrast Agent Modeling: A review", Ultrasound in Med. & Biol. **46**, 2117–2144 (2020).

[2] N. de Jong, A. Bouakaz, and P. Frinking, "Basic Acoustic Properties of Microbubbles", Echocardiography **19**, 229–240 (2002).

[3] J.W.S. Rayleigh, "The Theory of Sound", (Macmillan, London, UK) (1878).

[4] L.L. Foldy, "The Multiple Scattering of Waves", Phys. Rev. **64**, 107–119 (1945).

[5] E.L. Carstensen, and L.L. Foldy, "Propagation of Sound Through a Liquid Containing Bubbles", J. Acoust. Soc. Am. **19**, 481–501 (1947).

[6] P.C. Waterman, and R. Truell, "Multiple Scattering of Waves", J. Math. Phys. **2**, 512–537 (1961).

[7] A.L. Gower, M.J.A. Smith, W.J. Parnell, and I.D. Abrahams, "Reflection from a multi-species material and its transmitted effective wavenumber", Proc. R. Soc. A. **474**, 1–27 (2018).

[8] L. van Wijngaarden, "On the equations of motion for mixtures of liquid and gas bubbles", J. Fluid Mech. **33**, 465–474 (1968).

[9] R.E. Calfish, M.J. Miksis,G.C. Papanicolaou, and L. Ting, "Effective equations for wave propagation in bubbly liquids", J. Fluid Mech. **153**, 259–273 (1985).

[10] C. Feuillade, "The attenuation and dispersion of sound in water containing multiply interacting air bubbles", J. Acoust. Soc. Am. **99**, 3412–3430 (1996).

[11] F.S. Henyey, "Corrections to Foldy's effective medium theory for propagation in bubble clouds and other collections of very small scatterers", J. Acoust. Soc. Am. **105**, 2149–2154 (1999).

[12] C. Feuillade, "Acoustically coupled gas bubbles in fluids: Time-domain phenomena", J. Acoust. Soc. Am. **109**, 2606–2615 (2001).

[13] K.W. Commander and A. Prosperetti, "Linear pressure waves in bubbly liquids: Comparison between theory and experiments", J. Acoust. Soc. Am. **85**, 732–746 (1989).

[14] L. D'Agostino and C. Brennen, "Linearized dynamics of spherical bubble clouds", J. Fluid Mech. **199**, 155–176 (1989).

[15] S. Kumar and C. Brennen, "Nonlinear effects in the dynamics of clouds of bubbles", J. Acoust. Soc. Am. **89**, 707–714 (1991)

[16] Z. Ye and L. Ding, "Acoustic dispersion and attenuation relations in bubbly mixture", J. Acoust. Soc. Am. **98**, 1629–1636 (1995).

[17] E. Stride and N. Saffari, "Investigating the significance of multiple scattering in ultrasound contrast agent particle populations", IEEE Trans. Ultrason., Ferroelectr. Freq. Control **52**, 2332–2345 (2005).

[18] K. Hibbs, J.-M. Mar, E. Stride, R. Eckersley, A. Noble, and M.-X. Tang, "Nonlinear Propagation of Ultrasound Through Microbubble Clouds: A Novel Numerical Implementation", Proceedings of the 2007 IEEE Ultrasonics Symposium, 1997–2000 (2007).

[19] N.C. Ovenden, J. O'Brienn, and E. Stride, "Ultrasound propagation through dilute polydisperse microbubble suspensions", J. Acoust. Soc. Am. **142**, 1236–1248 (2017).

[20] V. Leroy, A. Strybulevych, M.G. Scanlon, and J.H. Page, "Transmission of ultrasound through a single layer of bubbles", Eur. Phys. J. **29**, 123–130 (2009).

[21] O. Lombard, C. Barrière, and V. Leroy, "Nonlinear multiple scattering of acoustic waves by a layer of bubbles", EPL **112**, 1–6 (2015).

[22] A. Joshi, B.D. Lindsey, P.A. Dayton, G. Pinton, and M. Muller, "An iterative fullwave simulation approach to multiple scattering in media with randomly distributed microbubbles", Phys. Med. & Biol. **62**, 4202–4217 (2017).

[23] J. Huijssen, "Modeling of nonlinear medical diagnostic ultrasound", PhD Thesis, Delft University of Technology, Netherlands (2008), available from http://reposity.tudelft.nl.

[24] J. Huijssen and M.D. Verweij, "An iterative method for the computation of nonlinear, wide-angle, pulsed acoustic fields of medical diagnostic transducers", J. Acoust. Soc. Am. **127**, 33–44 (2010).

[25] M.D. Verweij and J. Huijssen, "A filtered convolution method for the computation of acoustic wave fields in very large spatio-temporal domains", J. Acoust. Soc. Am. **125**, 1868–1878 (2009).

[26] M.D. Verweij, "Modeling space-time domain acoustic wave fields in media with attenuation: The symbolic manipulation approach", J. Acoust. Soc. Am. **97**, 831–43 (1995).

[27] M.D. Verweij, "Transient acoustic wave fields in continuously layered media with depth-dependent attenuation: An analysis based on higher-order asymptotics", J. Acoust. Soc. Am. **101**, 1808–1820 (1997).

[28] L. Demi, M.D. Verweij, J. Huijssen, N. de Jong, and K.W.A. van Dongen, "Attenuation of ultrasound pressure fields described via a contrast source formulation", Proceedings of 2009 IEEE Ultrasonics, 1590–93 (2009).

[29] L. Demi, K.W.A. van Dongen, and M.D. Verweij, "A contrast source method for nonlinear acoustic wave fields in media with spatially inhomogeneous attenuation", J. Acoust. Soc. Am. **129**, 1221–1230 (2011).

[30] J. Huijssen, M.D. Verweij, and N. de Jong, "Modeling nonlinear three-dimensional pulsed acoustic fields in diagnostic ultrasound including tissue-like attenuation", Proceedings of 2008 IEEE Ultrasonics, 375–378 (2008).

[31] P. Marmottant, S. van der Meer, M. Emmer ,M. Versluis, N. de Jong, S. Hilgenfeldt, and D. Lohse, "A model for large amplitude oscillations of coated bubbles accounting for buckling and rupture", J. Acoust. Soc. Am. **118**, 3499–3506 (2005).

[32] P.F. Morse and K.U. Ingard, *Theoretical Acoustics* (McGraw-Hill, New York, USA) (1968).

[33] M.F. Hamilton and D.T. Blackstock, *Nonlinear Acoustics* (Academic Press, San Diego, USA) (1998).

[34] A.T. de Hoop, *Handbook of radiation and scattering of waves* (Academic Press, San Diego, USA), 106–116 (1995).

[35] A.C. Hindmarsh, ""ODEPACK, A Systematized Collection of ODE Solvers", IMACS Trans. on Sc. Comp. **1**, 55–64 (1983).

[36] E.S. Wise, B.T. Cox, J. Jaros, and B.E. Treeby, "Representing arbitrary acoustic source and sensor distributions in Fourier collocation methods", J. Acoust. Soc. Am. **146**, 278–288 (2019).

2

A. Matalliotakis, D. Maresca, and M.D. Verweij, *Nonlinear interaction of two cross-propagating plane waves*, arXiv, 2312.00445 (2023).

Chapter 3

Nonlinear interaction of two cross-propagating plane waves

An ideal contrast-enhanced ultrasound image should display MB-induced nonlinearities while avoiding wave propagation nonlinearities. One of the most successful ultrasound pulse sequences to disentangle these nonlinear effects relies on the transmission of cross-propagating plane waves. However, theory describing the noncollinear nonlinear interaction of two finite plane waves has not been fully developed and a better understanding of these effects would improve contrast-enhanced ultrasound imaging further. Here, local nonlinear interactions at the intersection of two plane-waves are investigated by extending the Westervelt equation with a term including the Lagrangian density. The Iterative Nonlinear Contrast Source (INCS) method is employed to numerically solve this full nonlinear wave equation for two 3D finite cross-propagating pulsed plane waves. In addition, analytical expressions for the cross-propagation of two infinite continuous plane waves are derived. Numerical results obtained with INCS show good agreement with the analytical expressions. Overall, the generated results show that the pressure associated with local nonlinear effects is two orders of magnitude lower than the pressure associated with global nonlinear effects. Local nonlinear effects are therefore expected to be negligible in the context of single-shot ultrasound imaging, but they may influence approaches that subtract pressure fields such as amplitude modulation or pulse inversion.

3.1 Introduction

The combination of ultrasound echography with lipid-shelled MBs administered in the blood stream has enabled quantitative imaging of tissue perfusion [1] and super-resolution imaging of the microvasculature in humans [2]. Pulse sequences exploit the nonlinear response of resonant MBs in an acoustic field to detect their presence in a linearly scattering tissue environment [3]. In practice, pulse sequences are prone to nonlinear wave propagation artifacts and tend to missclassify tissue as MB domain, even at low acoustic pressure. Renaud et al. [4] and Maresca et al. [5] have shown that an amplitude modulation (AM) sequence based on the noncollinear interaction of two ultrasonic wavefronts can significantly reduce such artifacts. A schematic example of the cross-propagation of two finite pulsed plane waves is depicted in Fig. 3.1. To further improve the specificity of contrast-enhanced ultrasound imaging, a full understanding of nonlinear effects occurring in tissue devoid of ultrasound contrast agents is critical.

Previous studies [6–9] have shown that local nonlinear effects emerge from the noncollinear interaction of plane waves. Similar observations were reported for parametric acoustic arrays [10]. To date, simulation tools for solving the Westervelt equation capture global, i.e. cumulative, nonlinear effects but neglect local nonlinear interactions. Local nonlinear effects manifest where the wave field does not resemble a simple progressive plane wave and the potential energy density of the resulting wave is not equal to its kinetic energy density, which happens at the intersection of two cross propagating plane waves. We will therefore extend the INCS [11,12] method to solve the full nonlinear wave equation accounting for both global and local nonlinear effects. In the original INCS method, global nonlinear effects are accounted for by considering the nonlinear term in the Westervelt equation as a contrast source that acts in a linear background medium. Here, we will introduce an additional contrast source term to account for local nonlinear effects, as explained in Fig. 3.2. INCS computes the acoustic pressure due to a source with a pulsed excitation in a 4D spatiotemporal domain. The directional independence of INCS makes it well adapted to the computation of local nonlinearities generated by the noncollinear interaction of cross-propagating plane waves.

In this article, we will explain how INCS is extended to include local nonlinear medium effects. Initially, the velocity potential is computed from the already calculated pressure field. Next, spatial interpolation is used to upsample the pressure and the velocity potential before computing the potential and kinetic energy densities. These terms then are used to calculate the Lagrangian density. Subsequently, the contrast source term representing the local nonlinear effects is obtained by taking the relevant spatial and temporal derivatives. Spatial filtering is then applied to downsample the spatiotemporal contrast source to its initial grid size. After the convolution with the Green's function of the linear background medium, the nonlinear field correction to the incident pressure field is calculated. Iteration of this approach provides an increasingly accurate solution to the nonlinear wave problem.

The manuscript is organized as follows: fundamentals of INCS are described in Section 3.2 and cover the addition of a contrast source term accounting for local nonlinear effects. Section 3.3 derives the analytical expressions for the interaction of

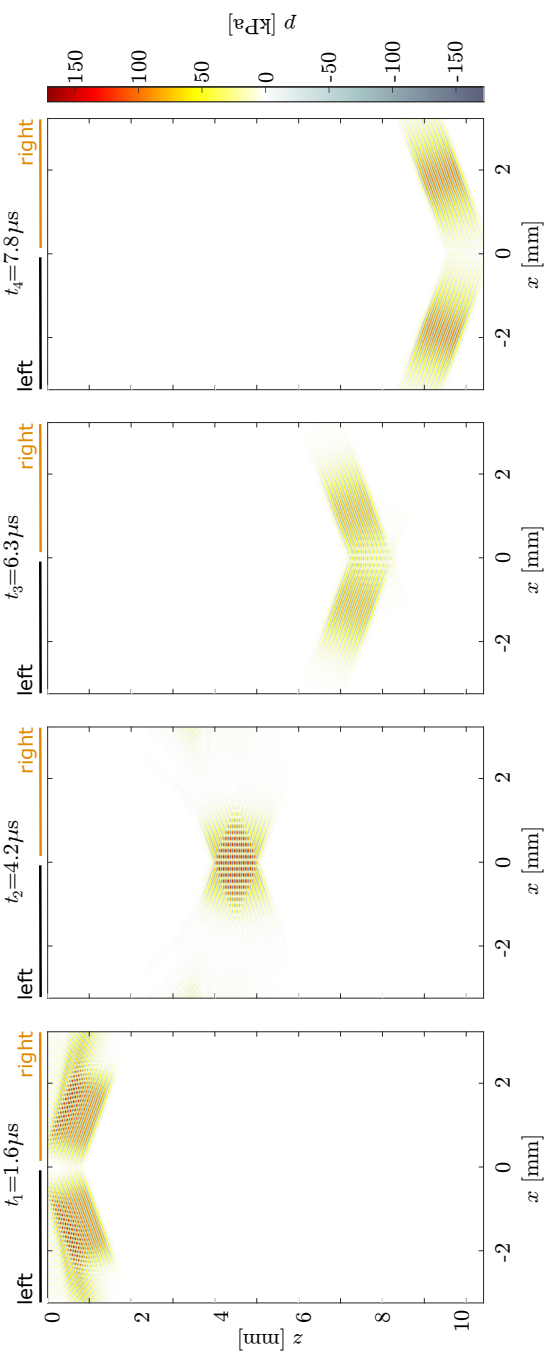

Figure 3.1: (Color online) Interaction of two cross-propagating beams of finite, pulsed plane waves, at four different time instants: t_1 is just before interaction, t_2 is when the area of interaction is at a maximum, t_3 is just before separation, and t_4 is after separation. Transmitting apertures of the ultrasound array are indicated in black and orange at z = 0.

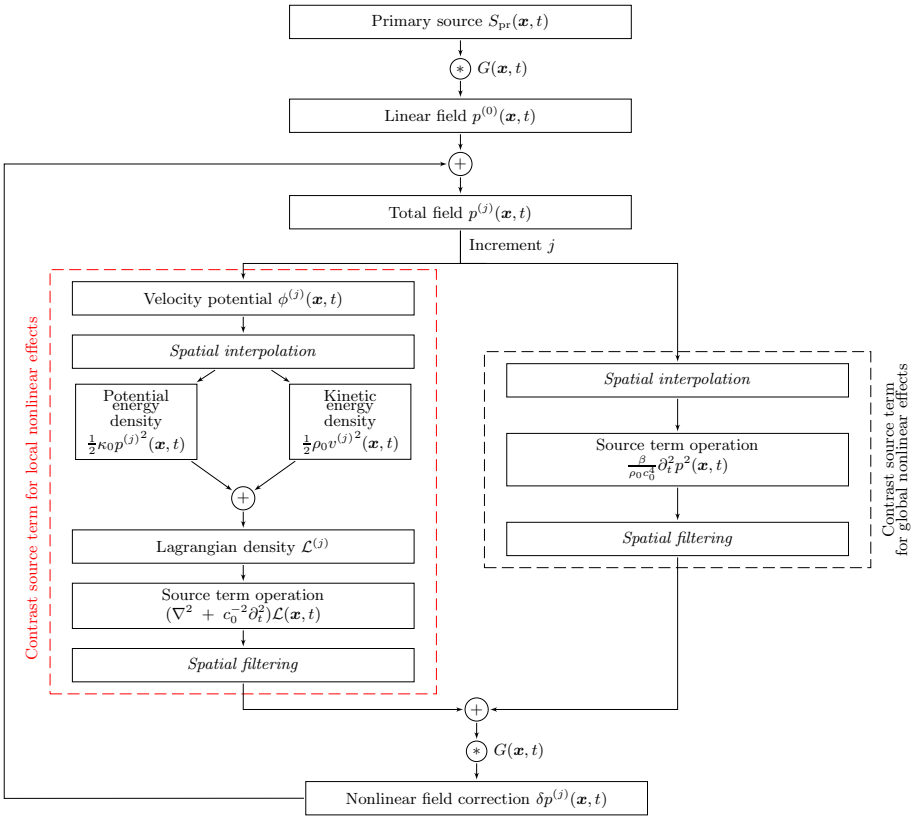

Figure 3.2: (Color online) Schematic diagram for the INCS method with extension to account for local nonlinear effects (red).

two infinite, continuous, cross-propagating plane waves. In Section 3.4, INCS results for two 3D cross-propagating plane waves travelling at a 20° angle are presented and compared with the analytical derivations. Results for the pressure fields generated by a linear array with hyperbolic time delays are also reported. Conclusions are given in Section 3.5.

3.2 Fundamentals of INCS

3.2.1 Linear field

The linear pressure field generated by an external source in a linear, homogeneous acoustic medium is described by the wave equation

$$c_0^{-2}\frac{\partial^2 p(\boldsymbol{x},t)}{\partial t} - \nabla^2 p(\boldsymbol{x},t) = S_{\mathrm{pr}}(\boldsymbol{x},t), \tag{3.1}$$

Here, $\boldsymbol{x}$ [m] is the Cartesian position vector, and t [s] is the time. The symbol $p(\boldsymbol{x}, t)$ [Pa] indicates the acoustic pressure, $c_0 = 1/\sqrt{\rho_0 \kappa_0}$ [m/s] is the small signal sound speed in the background medium, where ρ_0 [kg·m^{-3}] is the mass density and κ_0 [Pa^{-1}] is the compressibility. The Laplacian operator ∇^2 generates the sum of the second order spatial derivatives. The acoustic field is generated by the primary source term

$$S_{\mathrm{pr}}(\boldsymbol{x}, t) = \rho_0 \partial_t q(\boldsymbol{x}, t) - \nabla \cdot \boldsymbol{f}(\boldsymbol{x}, t). \tag{3.2}$$

which contains the volume injection rate density $q(\boldsymbol{x}, t)$ [s^{-1}] and the volume force density $\boldsymbol{f}(\boldsymbol{x}, t)$ [N m^{-3}]. Pressure jump conditions for the velocity or the pressure can be used to represent a source with a plane aperture, e.g. a phased array transducer.

The field p due to a source S can then be obtained as

$$\begin{aligned} p(\boldsymbol{x}, t) &= \mathcal{G}[S] \\ &= \int_{\mathcal{T}} \int_{\mathcal{X}} S(\boldsymbol{x}', t)\, G(\boldsymbol{x} - \boldsymbol{x}', t - t')\, \boldsymbol{x}' dt'. \end{aligned} \tag{3.3}$$

In this equation, the Green's function $G(\boldsymbol{x}, t)$ is the solution of Eq. (3.1) for a spatiotemporal impulsive source, which is known analytically, and the convolution takes place over the spatial domain $\mathcal{X}$ and over the temporal domain $\mathcal{T}$ of the source S. The operator $\mathcal{G}$ denotes the convolution of the Green's function with the source term, providing the solution to the linear wave equation for this given source.

In particular, the acoustic pressure $p^{(0)} = \mathcal{G}[S_{\mathrm{pr}}]$ is the linear field of the primary source. This field will act as the zeroth order iteration for the Neumann iterative scheme that will be used to solve the nonlinear problem.

3.2.2 Nonlinear field due to global nonlinear effects

In medical ultrasound, the nonlinear behaviour of the medium can have a significant impact on the propagation of the acoustic signals. If we account for nonlinear terms up to second order in the acoustic quantities and assume that the cumulative nonlinear behavior dominates the local behavior [6, 7], then it is sufficient to extend Eq. (3.1) to the Westervelt equation

$$c_0^{-2} \frac{\partial^2 p}{\partial t^2} - \nabla^2 p = S_{\mathrm{pr}} + S_{\mathrm{nl}}. \tag{3.4}$$

The additional nonlinear term is given by

$$S_{\mathrm{nl}}(p) = \frac{\beta}{\rho_0 c_0^4} \partial_t^2 p^2, \tag{3.5}$$

in which β is the coefficient of nonlinearity of the medium. In INCS, this term acts as a contrast source term that accounts for the global nonlinear behavior of the medium. A first order nonlinear correction $\delta p^{(1)} = \mathcal{G}[S_{\mathrm{nl}}(p^{(0)})]$ to the acoustic pressure field $p^{(0)}$ can be calculated by following the same approach as in Eq. (3.3), where the integration now takes place over the spatial domain $\mathcal{X}_{\mathrm{nl}}$ and the temporal domain $\mathcal{T}_{\mathrm{nl}}$ of the nonlinear contrast source. The result is the first-order corrected

field $p^{(1)} = p^{(0)} + \delta p^{(1)}$. The correction procedure can be repeated by substituting the corrected field in the nonlinear contrast source $S_{\text{nl}}(p)$ and computing an improved nonlinear correction δp to the acoustic pressure field $p^{(0)}$. This leads to a Neumann iterative scheme that is given by the following set of equations

$$p^{(0)} = \mathcal{G}[S_{\text{pr}}], \tag{3.6}$$

$$p^{(j)} = p^{(0)} + \mathcal{G}[S_{\text{nl}}(p^{(j-1)})], \quad \text{if } j \geq 1. \tag{3.7}$$

Within this scheme, other contrast sources can be accommodated that represent attenuation [13–16], inhomonegeous medium properties [17], or a population of scatterers such as nonlinear oscillating microbbubles [18].

3

3.2.3 Nonlinear field due to local nonlinear effects

We can extend Eq. (3.4) by introducing a contrast source term $S_{\mathcal{L}}(\boldsymbol{x}, t)$ that represents local nonlinear effects. We then get

$$c_0^{-2} \frac{\partial^2 p(\boldsymbol{x}, t)}{\partial t} - \nabla^2 p(\boldsymbol{x}, t) = S_{\text{pr}}(\boldsymbol{x}, t) + S_{\text{nl}}(\boldsymbol{x}, t) + S_{\mathcal{L}}(\boldsymbol{x}, t), \tag{3.8}$$

where $S_{\mathcal{L}}(\boldsymbol{x}, t)$ is described by [6]

$$S_{\mathcal{L}}(\boldsymbol{x}, t) = (\nabla^2 + c_0^{-2} \partial_t^2) \mathcal{L}(\boldsymbol{x}, t). \tag{3.9}$$

Here, $\mathcal{L}(\boldsymbol{x}, t)$ is the Lagrangian density

$$\mathcal{L}(\boldsymbol{x}, t) = \tfrac{1}{2} \rho_0 \left\| \boldsymbol{u}(\boldsymbol{x}, t) \right\|^2 - \tfrac{1}{2} \kappa_0 p^2(\boldsymbol{x}, t), \tag{3.10}$$

where $\boldsymbol{u}(\boldsymbol{x}, t)$ is the particle velocity. The Lagrangian density is the difference between the kinetic energy density and the potential energy density of the acoustic wave. For a plane wave, the Lagrangian density equals zero, but this is not the case for two noncollinear interacting plane waves.

In the current framework, we need an expression that gives the particle velocity as a function of pressure. This is achieved through the velocity potential $\phi(\boldsymbol{x}, t)$, which is defined as

$$\boldsymbol{u}(\boldsymbol{x}, t) = \nabla \phi(\boldsymbol{x}, t). \tag{3.11}$$

In first order, the relation between $p(\boldsymbol{x}, t)$ and $\phi(\boldsymbol{x}, t)$ then becomes

$$p(\boldsymbol{x}, t) = -\rho_0 \frac{\partial \phi(\boldsymbol{x}, t)}{\partial t}. \tag{3.12}$$

In this equation, terms of order two and higher in the acoustic quantities are neglected. This results in neglecting terms of order three and higher in $p^2(\boldsymbol{x}, t)$ and thus in $\mathcal{L}(\boldsymbol{x}, t)$, which is allowed because the wave equation in Eq. (3.8) is only accurate up till order two in the acoustic quantities. With Eqs. (3.11) and (3.12), Eq.(3.10) can be rewritten as

$$\mathcal{L}(\boldsymbol{x}, t) = \frac{\rho_0}{2} \left\{ \left\| \nabla \phi(\boldsymbol{x}, t) \right\|^2 - c_0^{-2} \left[\frac{\partial \phi(\boldsymbol{x}, t)}{\partial t} \right]^2 \right\}. \tag{3.13}$$

Up till second order accuracy, this is identical to [6]

$$\mathcal{L}(\boldsymbol{x},t) = \frac{\rho_0}{4}\left(\nabla^2 - c_0^{-2}\frac{\partial^2}{\partial t^2}\right)\phi^2(\boldsymbol{x},t). \tag{3.14}$$

3.3 Analytical expressions

3.3.1 Pressure and velocity potential

For comparison and benchmarking purposes, here we will derive analytical expressions for the Lagrangian density and the resulting contrast source for cross-propagating plane waves. Specifically, we consider two infinite, steady-state, plane acoustic waves that are propagating in a homogeneous medium. Each wave has an angular frequency ω and propagates under an angle $\pm\theta$ with the z-axis, respectively. The medium has a wave speed c_0, a density of mass ρ_0 and a coefficient of nonlinearity β. Without loss of generality, we consider the plane $y = 0$ and omit the variable y. In this case, the total incident pressure $p(x,z,t)$ may be written as

$$p = P_0[\sin(\omega t - k_x x - k_z z) + \sin(\omega t + k_x x - k_z z)], \tag{3.15}$$

where

$$k_x = \frac{\omega}{c_0}\sin(\theta) = k\sin(\theta), \tag{3.16}$$

$$k_z = \frac{\omega}{c_0}\cos(\theta) = k\cos(\theta). \tag{3.17}$$

Using Eq. (3.12), we find

$$\phi(x,z,t) = \frac{P_0}{\rho_0\omega}[\cos(\omega t - k_x x - k_z z) + \cos(\omega t + k_x x - k_z z)]. \tag{3.18}$$

3.3.2 Lagrangian density

To compute the Lagrangian density, we first need to compute the square of the velocity potential, which is

$$\phi^2 = \frac{P_0^2}{\rho_0^2\omega^2}[I_0 + I_1 + I_2 + I_3 + I_4], \tag{3.19}$$

where

$$I_0 = 1 \tag{3.20}$$

$$I_1 = \tfrac{1}{2}\cos(2\omega t - 2k_x x - 2k_z z), \tag{3.21}$$

$$I_2 = \tfrac{1}{2}\cos(2\omega t + 2k_x x - 2k_z z), \tag{3.22}$$

$$I_3 = \cos(2\omega t - 2k_z z), \tag{3.23}$$

$$I_4 = \cos(2k_x x). \tag{3.24}$$

In order to derive this expression from Eq. (3.18), we have used the trigonometric identity

$$\cos(a+b) + \cos(a-b) = 2\cos(a)\cos(b). \tag{3.25}$$

When computing the Lagrangian density, we can beforehand discard some terms in Eq. (3.19). Because I_0 is a constant, it will not contribute to $\mathcal{L}$. Furthermore, I_1 and I_2 are a representation of plane waves, which also do not contribute to $\mathcal{L}$. Therefore, we can continue the derivation with the remaining terms, giving

$$\begin{aligned}\mathcal{L} &= \frac{P_0^2}{4\rho_0\omega^2}\left(\nabla^2 - \frac{1}{c_0^2}\frac{\partial^2}{\partial t^2}\right)(I_3 + I_4) \\ &= \frac{P_0^2}{4\rho_0\omega^2}\left(\nabla^2 - \frac{1}{c_0^2}\frac{\partial^2}{\partial t^2}\right)[\cos(2\omega t - 2k_z z) + \cos(2k_x x)] \\ &= \frac{P_0^2}{\rho_0 c_0^2}\sin^2(\theta)[\cos(2\omega t - 2k_z z) - \cos(2k_x x)],\end{aligned} \tag{3.26}$$

where we have used

$$\frac{\omega^2}{c_0^2} - k_z^2 = k_x^2. \tag{3.27}$$

3.3.3 Contrast source term for local nonlinear effects

Here, we derive the analytical expression for the contrast source in Eq. (3.9). The first term equals

$$\begin{aligned}\nabla^2\mathcal{L} = -4\frac{P_0^2\omega^2}{\rho_0 c_0^4}\sin^2(\theta)\,[&\cos^2(\theta)\cos(2\omega t - 2k_z z) \\ &- \sin^2(\theta)\cos(2k_x x)],\end{aligned} \tag{3.28}$$

and the second term is

$$c_0^{-2}\frac{\partial^2\mathcal{L}}{\partial t^2} = -4\frac{P_0^2\omega^2}{\rho_0 c_0^4}\sin^2(\theta)\cos(2\omega t - 2k_z z). \tag{3.29}$$

By adding Eqs. (3.28) and (3.29), the source term for the local nonlinear effects is obtained as

$$\begin{aligned}S_{\mathcal{L}} = &-8\frac{P_0^2\omega^2}{\rho_0 c_0^4}\sin^2(\theta)\cos(2\omega t - 2k_z z) \\ &+ 4\frac{P_0^2\omega^2}{\rho_0 c_0^4}\sin^4(\theta)[\cos(2\omega t - 2k_z z) + \cos(2k_x x)],\end{aligned} \tag{3.30}$$

where we have used

$$1 + \cos^2(a) = 2 - \sin^2(a). \tag{3.31}$$

3.3.4 Contrast source term for global nonlinear effects

To find the analytical expression for the contrast source in Eq. (3.5), we first compute the square of the acoustic pressure, which is

$$p^2 = P_0^2[J_0 + J_1 + J_2 + J_3 + J_4], \tag{3.32}$$

where

$$J_0 = 1 \tag{3.33}$$
$$J_1 = -\tfrac{1}{2}\cos(2\omega t - 2k_x x - 2k_z z), \tag{3.34}$$
$$J_2 = -\tfrac{1}{2}\cos(2\omega t + 2k_x x - 2k_z z), \tag{3.35}$$
$$J_3 = -\cos(2\omega t - 2k_z z), \tag{3.36}$$
$$J_4 = \cos(2k_x x), \tag{3.37}$$

in which we have used

$$-\cos(a+b) + \cos(a-b) = 2\sin(a)\sin(b). \tag{3.38}$$

Because J_0 is a constant, and J_4 is independent of time, these terms will have no contribution to S_{nl}. Therefore, we can continue the derivation with the remaining terms, giving

$$\begin{aligned} S_{\text{nl}} =& \frac{\beta P_0^2}{\rho_0 c_0^4}\frac{\partial^2}{\partial t^2}(J_1 + J_2 + J_3) \\ =& 8\frac{\beta P_0^2 \omega^2}{\rho_0 c_0^4}\cos^2(k_x x)\cos(2\omega t - 2k_z z). \end{aligned} \tag{3.39}$$

3.4 Numerical results

3.4.1 Configuration

After the derivation of the analytical expressions, we can continue with the comparison of the numerical outcomes obtained by INCS with the results derived in Sec. 3.3. In the current section, we consider a computational domain of dimensions $X \times Y \times Z = 6.4$ mm $\times$ 5 mm $\times$ 10 mm. The medium considered in the analysis is water, characterized by a density of mass of $\rho = 1060$ kg/m^3, and a speed of sound $c_0 = 1482$ m/s.

The incident beam has a center frequency $f_0 = 15$ MHz and is produced by a phased array transducer comprising of 64 elements, each with dimensions $H_{\text{el}} \times W_{\text{el}} = 5$ mm $\times$ 0.1 mm, and a kerf with zero width. This configuration results in an aperture with a width of $W_{\text{ap}} = 6.4$ mm. The selection of this particular size was done to shift the natural focus of the aperture out of the computational domain, to obtain two cross-propagating pressure fields that closely approximate plane waves. Additionally, the origin of the coordinate system has been positioned at the center of the transducer aperture. A sketch depicting the geometry of the phased array is presented in Fig. 3.3.

The time-varying pressure at the surface of the elements is given by the expression

$$p(t) = P_0 \exp\left[-\left(\frac{t - T_d}{T_w/2}\right)^2\right]\sin[2\pi f_0(t - T_d)], \tag{3.40}$$

where we have chosen $T_w = 10/f_0$, which represents the duration of the Gaussian envelope, and $T_d = 10/f_0 + \Delta_n$, which is the total time delay. The latter consists of

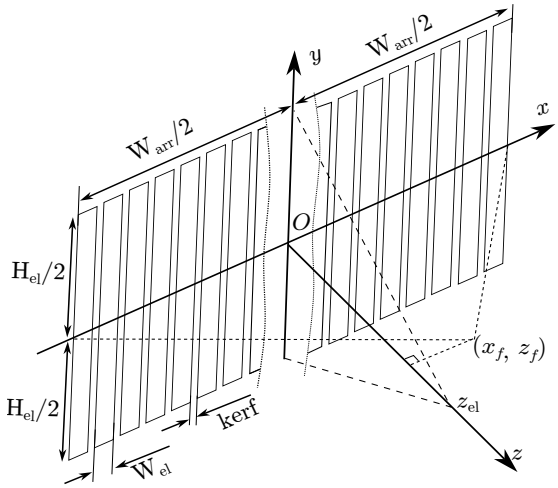

Figure 3.3: Sketch of the geometry of the phased array that generates the incident field.

a fixed delay for keeping $p(t) \approx 0$ at $t = 0$, plus a delay per element for the beam steering Δ_n. The maximum surface pressure of the elements is $P_0 = 100$ kPa.

For accurately solving the full nonlinear wave equation up to the second harmonic, a sampling frequency of 96 MHz has been used to discretize the spatiotemporal domain. To reduce the artifacts arising from the edges of the aperture, a Tukey apodization with a cosine fraction of 0.7 has been applied.

3.4.2 Crossing beams

First we will show results for two cross-propagating beams with finite plane wave fronts. To generate two plane waves that propagate under angles of $-20°$ and $20°$, respectively, a triangular time delay profile is applied as depicted in Fig. 3.4(a). The incident beams in the azimuthal plane $y = 0$ mm and the elevational plane $x = 0$ mm are shown in Figs. 3.4(b) and (c), respectively. In the azimuthal plane, the beams show a constant lateral width. The emitted pulses are long enough to resemble a steady-state wave. In this way, we can compare the results of INCS with the ones from the analytical expressions. Moreover, the maximum pressure in the intersection area is 181 kPa, which corresponds to a mechanical index of 0.047. Although we use a low mechanical index, the values for local and global nonlinear effects will be scaling similarly as they are both a function of the square of the pressure.

In Fig. 3.5(a) and (b), the respective magnitudes of the source terms for global and local nonlinear effects are depicted. The magnitude of the source term for the global nonlinear effects is higher at locations where the incident pressure in Fig. 3.4 is higher. This is because the considered source term depends on the square of the total pressure, which is dominated by the incident pressure. On the other hand, the source term for the local nonlinear effects is stronger at locations where in Fig. 3.4 two waves are crossing under an angle, i.e. at the intersection of the two main beams,

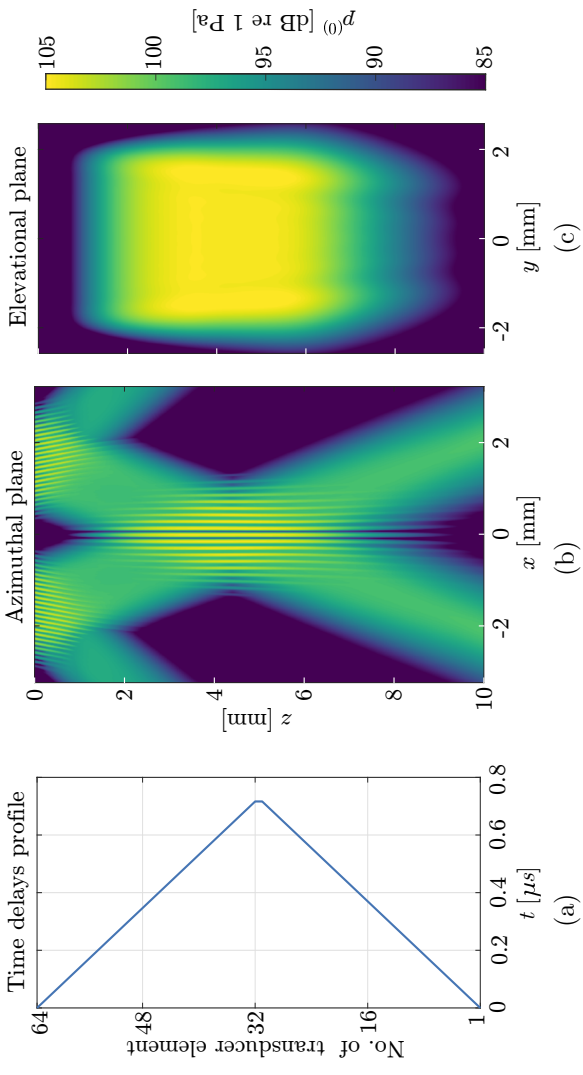

Figure 3.4: (Color online) The incident pressure field for cross-propagating beams generated by the phased array. (a) Delay profile for generating two beams with plane wave fronts that propagate under angles $\theta = \pm 20°$ with respect to the z-axis. (b) Maximum pressure profiles in the azimuthal plane $y = 0$ mm. (c) Maximum pressure profiles in the elevational plane $x = 0$ mm.

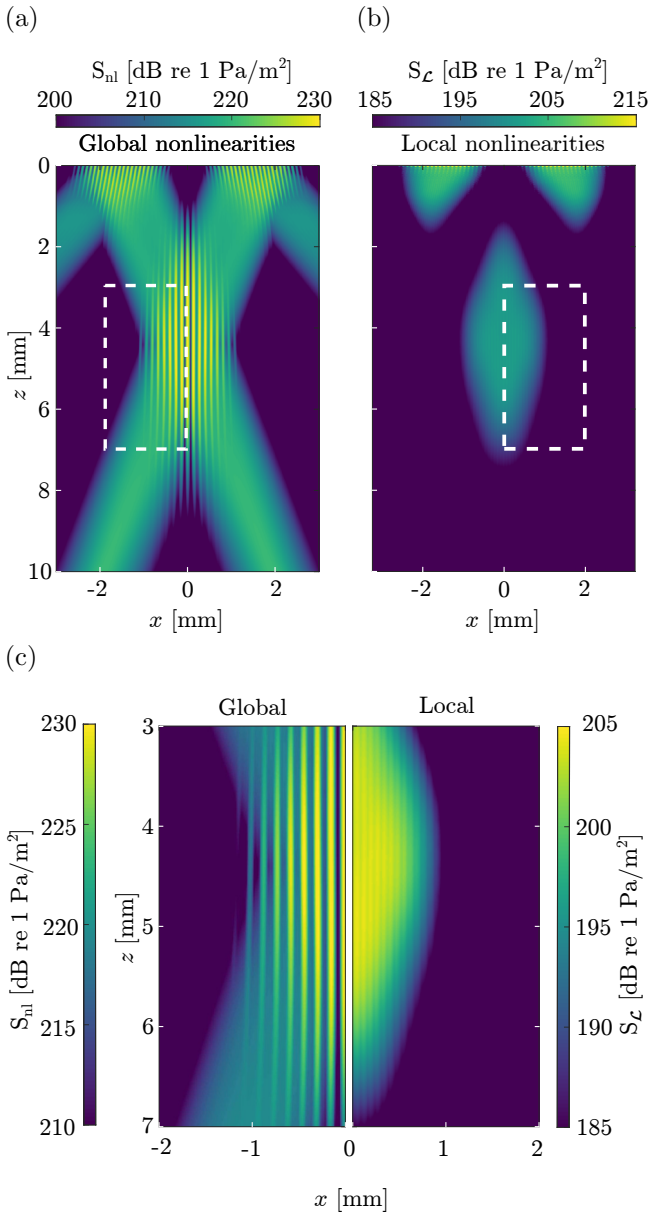

Figure 3.5: (Color online) Maximum values of the nonlinear contrast source terms in the azimuthal plane $y = 0$ mm for the beams generated by the phased array. (a) Source term for global nonlinear effects. (b) Source term for local nonlinear effects. (c) Detailed view of both source terms side by side.

and also at the intersection of a main beam and its grating lobe. This is because at these locations the kinetic energy density is not equal to the potential energy density. In the regions where there is only a single plane wave, the value of the source term is virtually zero. The source term for the local nonlinear effects is in general an order of magnitude smaller than the source term for the global nonlinear effects. This is also predicted by the analytical expressions of Sec. 3.3. Besides the difference in amplitude, the spatial behavior of the source terms also differs, as demonstrated in Fig. 3.5(c). In the left plot, a horizontal modulation of the source term for the global nonlinear effects is depicted. This is due to the interference of the pressure waves of both beams, which results in a horizontal modulation of the p^2 term in the source term, in agreement with Eq. (3.39). In the right plot, the horizontal modulation of the source term for the local nonlinear effects is much weaker. This is because the potential energy density depends on p^2, while the kinetic energy density term depends on v^2. Since both terms spatially alternate in magnitude, the source term will show less horizontal modulation, which agrees with Eq. (3.30). The scaling of the colorbars for both plots are chosen to ease the comparison.

The temporal signatures of the analytical and numerical results for the contrast source that represents the local nonlinear effects are presented in Fig. 3.6(a). The results apply to the point $(x, y, z) = (0\text{ mm}, 0\text{ mm}, 4.3\text{ mm})$, which is the center of intersection of the two plane waves. The depicted time interval spans 9 periods around the center of the incident pressure pulse, to avoid transient effects from the beginning and end of this pulse and to allow comparison with our steady-state analytical results. There is excellent agreement between the analytical results and the numerical results generated by INCS. In Fig. 3.6(b), a comparison between the numerically obtained temporal signatures of the contrast source terms that represent the global and local nonlinear effects is presented. The signatures are 180° out of phase, which agrees with the fact that the first and dominant term in Eq. (3.30) has a minus sign while the expression in Eq. (3.39) has not. The peak amplitude of the source term attributed to local nonlinearities is 11.3×10^9 Pa/m^2 and the peak amplitude of the source term attributed to global nonlinearities is 330×10^9 Pa/m^2. This corresponds to an amplitude rate of approximately 29.2. In the current case with $\theta = 20°$ and $\beta = 3.21$, the same result is obtained upon comparing Eq. (3.39) with Eq. (3.30).

Figure 3.7 shows the pressures that are generated by the source terms in Fig. 3.5. In panel (a), we see that the global nonlinear effects accumulate along each beam because these effects cause progressive pressure waves. In contrast, we observe in panel (b) that the local nonlinear effects emerge only at locations where the source term is present, but these do not cause progressive pressure waves that propagate into other regions. Although the source term for global nonlinear effects is about 30 times larger than that the source term for local nonlinear effects, the cumulative effect makes that the pressure field of the former is about 500 times larger than the latter.

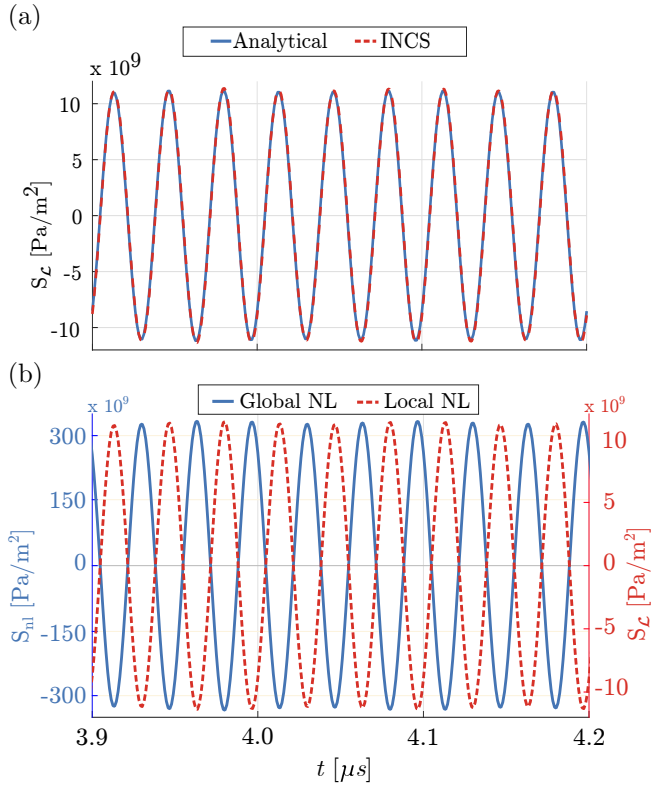

Figure 3.6: (Color online) Time domain signatures of the contrast sources at the center of intersection $(x, y, z) = (0\text{ mm}, 0\text{ mm}, 4.3\text{ mm})$. (a) Analytical results (blue, continuous) and numerical INCS results (red, dashed) for the contrast source for local nonlinear effects. (b) Numerical INCS results for the contrast source terms for global nonlinear effects (blue, continuous) and local nonlinear effects (red, dashed).

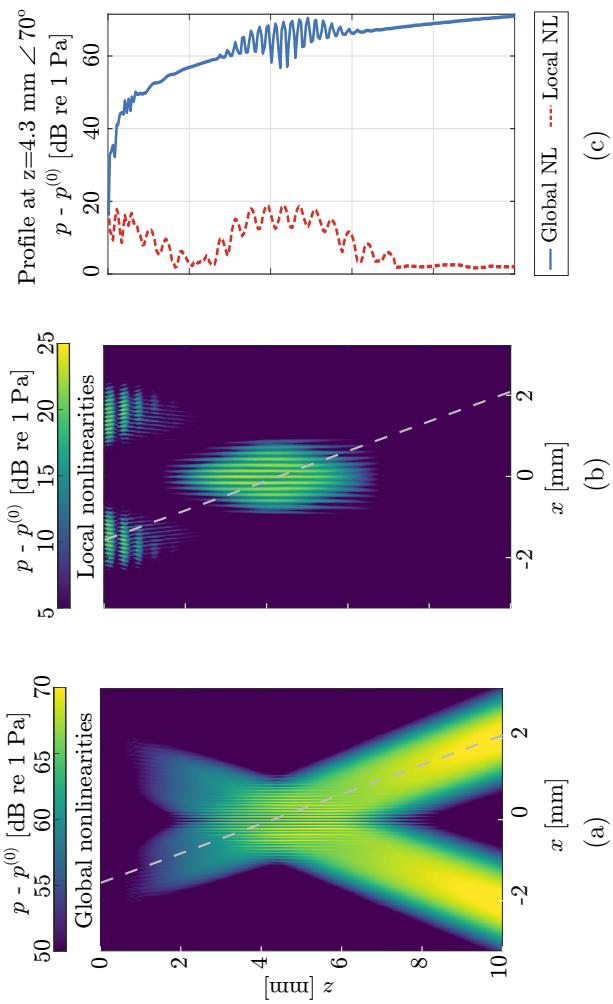

Figure 3.7: (Color online) Maximum pressure profiles in the azimuthal plane $y = 0$ mm for the beams generated by the phased array. (a) Pressure due to global nonlinear effects. (b) Pressure due to local nonlinear effects. (c) Maximum values of the pressures in (a) and (b) at the centerline of the beam emitted by the left part of the phased array.

3.4.3 Focused beam

Next we will show the results for a focused phased array generating a single focused beam, which is commonly utilized on conventional ultrasound machines for multiple medical applications. The computational domain, geometry of the phased array, and the transmitted pulse are identical to those in Sec. 3.4. The only difference is the time delay profile, which is presented in Fig. 3.8(a). The time delays are chosen such that the focus is at the same position as the center of the interaction zone of the crossing beams.

Figure 3.8(b) displays the incident pressure field generated by the focused phased array. Compared to the crossing beams in Fig. 3.4(a), the maximum amplitude is roughly four times larger at the focus while the length of the focal area is considerably smaller than the interaction zone. The pressure field due to global nonlinear effects is presented in Fig. 3.8(c). The cumulative behavior of the global nonlinear effects is evident. Figure 3.8(d) shows the pressure field due to local nonlinear effects. In comparison to the global nonlinear effects, these effects are solely occurring near the focus, i.e. where the waves emitted by the transducer in different directions, interfere constructively. In the current case, the peak amplitude of the global nonlinear effects is about 150 times larger than the peak amplitude of the local nonlinear effects. This is in agreement with the previous findings for focused beams [19].

3.5 Conclusions

The Iterative Nonlinear Contrast Source (INCS) method has been extended with an additional contrast source term to simulate local nonlinear effects that are not included in the commonly employed Westervelt equation for nonlinear wave propagation. For two plane waves propagating under an angle, it has been shown both analytically and numerically that this contrast source is nonzero in the interaction zone of the waves. Numerical results show that the pressure associated with local nonlinear effects does not propagate, and indeed is a local phenomenon. This behavior sets local nonlinear effects apart from global nonlinear effects, which cause harmonic pressure waves that accumulate along the entire propagation path of a single plane wave. Moreover, analytical and numerical results for two beams crossing under 20° in water show that the pressure associated with nonlinear effects is about two orders of magnitude lower than the pressure associated with global nonlinear effects. The same is observed for a highly focused beam with $f_{\#} = 1$. Thus, it is expected that local nonlinear effects will not have a significant influence on ultrasound imaging protocols based on single pulse transmissions, but these may have an influence on protocols in which results from multiple pulse transmissions are subtracted, like pulse inversion and amplitude modulation.

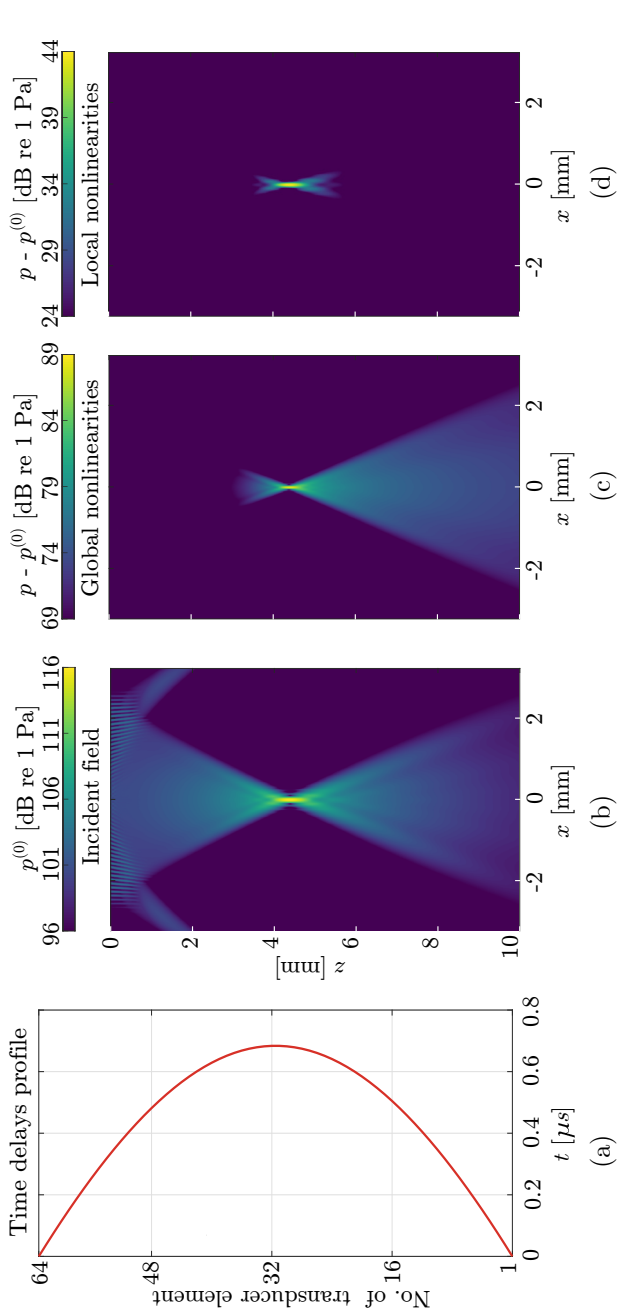

Figure 3.8: (Color online) Results for a focused beam. (a) Delay profile for generating a single beam focused at $(x, y, z) = (0\text{ mm}, 0\text{ mm}, 4.3\text{ mm})$. (b) Maximum incident pressure generated by the phased array. (c) Maximum pressure due to global nonlinear effects. (d) Maximum pressure due to local nonlinear effects.

Bibliography

[1] T. Porter, and F. Xie, "Myocardial Perfusion Imaging With Contrast Ultrasound", J. Am. Coll. Cardiol. Img. **3 (2)**, 176–187 (2010).

[2] C. Demené, J. Robin, A. Dizeux, B. Heiles, M. Pernot, M. Tanter, and F. Perren, "Transcranial ultrafast ultrasound localization microscopy of brain vasculature in patients", Nat. Biomed. Eng. **5 (3)**, 219–228 (2021).

[3] M. Averkiou, M. Bruce, J. Powers, P. Sheeran,and P. Burns, "Imaging methods for ultrasound contrast agents", Ultr. Med. Biol. **46 (3)**, 498–517 (2020).

[4] G. Renaud, J. Bosch, A.F.W. van der Steen, and N. de Jong, "Increasing Specificity of Contrast-Enhanced Ultrasound Imaging Using the Interaction of Quasi Counter-Propagating Wavefronts: A Proof of Concept", Phys. Rev. X **62 (10)**, 1768–1778 (2015).

[5] D. Maresca, D.P. Sawyer, G. Renaud, A.L. Gosselin and M.G. Shapiro, "Nonlinear X-Wave Ultrasound Imaging of Acoustic Biomolecules", Phys. Rev. X **8 (041002)**, 1–12 (2018).

[6] S.I. Aanonsen, T. Barkve, J. Naze Tjotta and S. Tjotta, "Distortion and harmonic generation in the nearfield of a finite amplitude sound beam", J. Acoust. Soc. Am. **75 (3)**, 749–768 (1984).

[7] J. Naze Tjotta and S. Tjotta, "Interaction of sound waves. part I: Basic equations and plane waves", J. Acoust. Soc. Am. **82 (4)**, 1425–1428 (1987).

[8] M.F. Hamilton, and J.A. TenCate, "Sum and difference frequency generation due to non-collinear wave interaction in a rectangular duct", J. Acoust. Soc. Am. **81 (6)**, 1703–1712 (1987).

[9] M.F. Hamilton, and D.T. Blackstock, "On the coefficient of nonlinearity β in nonlinear acoustics", J. Acoust. Soc. Am. **83 (1)**, 74–77 (1988).

[10] M. Cervenka, and M. Bednarik, "An algebraic correction for the Westervelt equation to account for the local nonlinear effects in parametric acoustic array", J. Acoust. Soc. Am. **151 (6)**, 74–77 (2022).

[11] J. Huijssen, "Modeling of nonlinear medical diagnostic ultrasound", PhD Thesis, Delft University of Technology (2008), available from http://reposity.tudelft.nl.

[12] J. Huijssen and M.D. Verweij, "An iterative method for the computation of nonlinear, wide-angle, pulsed acoustic fields of medical diagnostic transducers", J. Acoust. Soc. Am. **127 (1)**, 33–44 (2010).

[13] M.D. Verweij, "Modeling space-time domain acoustic wave fields in media with attenuation: The symbolic manipulation approach", J. Acoust. Soc. Am. **97 (2)**, 831–43 (1995).

[14] M.D. Verweij, "Transient acoustic wave fields in continuously layered media with depth-dependent attenuation: An analysis based on higher-order asymptotics", J. Acoust. Soc. Am. **101 (4)**, 1808–1820 (1997).

[15] J. Huijssen, M.D. Verweij, and N. de Jong, "Modeling nonlinear three-dimensional pulsed acoustic fields in diagnostic ultrasound including tissue-like attenuation", Proceedings of 2008 IEEE Ultrasonics, 375–378 (2008).

[16] L. Demi, M.D. Verweij, J. Huijssen, N. de Jong, and K.W.A. van Dongen, "Attenuation of ultrasound pressure fields described via a contrast source formulation", Proceedings of 2009 IEEE Ultrasonics, 1590–1593 (2009).

[17] L. Demi, K.W.A. van Dongen and M.D. Verweij, "A contrast source method for nonlinear acoustic wave fields in media with spatially inhomogeneous attenuation", J. Acoust. Soc. Am. **129 (3)**, 1221–1230 (2011).

[18] A. Matalliotakis, and M.D. Verweij, "Computation of ultrasound propagation in a population of nonlinearly oscillating microbubbles including multiple scattering", J. Acoust. Soc. Am. **153 (4)**, 2209–2222 (2023).

[19] Y. Jing, D. Shen and G. Clement, "Verification of the westervelt equation for focused transducers", IEEE Trans. Ultrason., Ferroelectr. Freq. Control **58 (5)**, 1097–1101 (2011).

3

A. Matalliotakis, M.D. Verweij, and D. Maresca, *Impact of wavefront shape on nonlinear ultrasound imaging of monodisperse microbubbles*, Phys. Rev. Applied **22** (034062) (2024).

Chapter 4

Impact of transmitted wavefront shape on nonlinear ultrasound imaging of monodisperse microbubbles

The field of contrast-enhanced ultrasound (CEUS) combines nonlinear, resonant microbubbles (MBs) with dedicated pulse sequences to reveal the vascular function of organs. Clinical ultrasound contrast agents consist of polydisperse MB suspensions with diameters ranging from 0.5 to 10 μm and resonance frequencies ranging from 1 to 15 MHz. As a result, just a small fraction of MBs resonates at a given ultrasound frequency. MB suspensions with narrow size distributions can be tuned for a specific imaging frequency, boost CEUS sensitivity and enable deeper vascular imaging. However, their enhanced nonlinear behavior makes imaging susceptible to nonlinear wave propagation artifacts. Here, we numerically investigate the impact of the acoustic wavefront shape on the imaging of nonlinear, monodisperse MBs. Specifically, our approach relies on an extension of the Iterative Nonlinear Contrast Source (INCS) method that accounts for all nonlinear effects in CEUS. We demonstrate that supersonic x-shaped wavefronts referred to as x-waves can be used to generate ultrasound images of monodisperse MBs without nonlinear wave propagation artifacts. On the contrary, imaging based on focused, planar and diverging wavefronts leads to significant nonlinear artifacts. Taken together, our results show that x-waves can harness the full potential of monodisperse MBs by enabling their sensitive and specific detection in a tissue context.

4.1 Introduction

The combination of ultrasound imaging with intravenously administered echogenic MBs has enabled significant advances such as microvascular imaging beyond the diffraction limit [1]. MBs are nonlinear oscillators that scatter ultrasound efficiently thanks to their high contrast in density and compressibility with blood plasma [2] and their resonant behavior in the MHz range [3]. Ultrasound pulse sequences [4] exploit nonlinear MB scattering to detect these vascular agents deep into tissues. A drawback of established pulse sequences such as amplitude modulation (AM) imaging is their susceptibility to cumulative nonlinear effects induced by wave propagation in MB suspensions [5, 6]. Briefly, ultrasound waves propagating in a highly nonlinear effective medium such as a resonant MB suspension experience amplitude-dependent attenuation and amplitude-dependent speed of sound variations [7, 8]. As a result, waves with different amplitudes get distorted differently through a MB suspension. In the end, waves carry that nonlinear distortion deeper into the medium, beyond the MB suspension, where they cause echoes that make AM imaging to misclassify tissue as MBs.

In 2015, Renaud et al. [9] demonstrated that AM imaging based on the intersection of two diverging wavefronts could improve CEUS specificity. Maresca, Sawyer et al. [10] further optimized this approach into a sequence called cross-amplitude modulation (xAM) that relies on cross-propagating plane waves intersecting with a constant angle. xAM presents fundamental advantages over previous AM implementations. First, the constant cross-propagation angle ensures a constant reduction of cumulative nonlinear effects along the line where the wavefronts cross. Second, it generates a non-diffractive beam pattern with a constant beam width [11, 12] that improves the lateral resolution of ultrasound images.

This study numerically investigates the specificity of AM imaging of monodisperse MBs, the most nonlinear ultrasound contrast agent to date [13], for implementations using focused [4], planar [14], diverging [15] and x-shaped [10] ultrasonic wavefronts. We use the Iterative Nonlinear Contrast Source (INCS) method [16, 17] to solve the full nonlinear acoustic wave equation in an acoustic medium containing a suspension of resonant monodisperse MBs. INCS was extended to account for ultrasound attenuation, medium inhomogeneities [18, 19], local medium nonlinearities [20] and nonlinearities arising from the oscillatory behavior of resonant MBs surrounded by tissue-mimicking linear scatterers [21]. Together, these capabilities allow us to simulate CEUS imaging modes such as AM and xAM.

The manuscript is organized as follows. Secs. 4.2.1 and 4.2.2 describe the INCS method and its application to AM imaging. Sec. 4.2.3 describes the media used in the simulations. Sec. 4.2.4 describes the beamforming process that has been implemented to reconstruct ultrasound images. Sec. 4.3.1 presents the incident and residual acoustic pressure fields generated by AM pulses in a homogeneous nonlinear medium free of ultrasound contrast agents. Sec. 4.3.2 presents the total and residual acoustic pressure fields in a medium containing a monodisperse MB suspension. Sec. 4.3.3 describes the origin of nonlinear wave propagation artifacts observed in AM imaging. Furthermore, Sec. 4.3.5 presents numerical AM images of monodisperse MBs generated with x-shaped, focused, planar and diverging wavefronts. Finally, a brief analysis of the

generated results is presented in Sec. 4.4, while concluding remarks of this study are given in Sec. 4.5.

4.2 Methods

4.2.1 Extension of INCS to account for nonlinear effects in CEUS

The linear incident pressure field resulting from an external source in a linear, lossless, homogeneous and isotropic background medium can be mathematically described by the wave equation

$$c_0^{-2}\partial_t^2 p - \nabla^2 p = S_{\mathrm{pr}}, \tag{4.1}$$

where p [Pa] represents the acoustic pressure. The parameter c_0 [m/s] denotes the sound speed in the background medium. The operator ∇^2 denotes the Laplacian and ∂_t^2 represents the second order time derivative. On the right-hand side of the equation, the primary source term S_{pr} is used to describe the action of the transducer. The linear acoustic pressure distribution arising from the primary source in the background medium can be explicitly found as

$$p(\boldsymbol{x}, t) = G(\boldsymbol{x}, t) *_{\boldsymbol{x},t} S_{\mathrm{pr}}(\boldsymbol{x}, t), \tag{4.2}$$

where $G(\boldsymbol{x}, t)$ is the Green's function of the background medium, and the operator $*_{\boldsymbol{x},t}$ denotes convolution over the spatiotemporal domain of S_{pr}. Because the background medium is simple, $G(\boldsymbol{x}, t)$ is known analytically.

Realistic media are modeled by more complex wave equations that also account for inhomogeneities, attenuation, nonlinear behavior, etc. Within the doctrine of the INCS method, all terms in which the more complex wave equation deviates from the simple background wave equation in Eq. (4.1) are shifted to the right hand side and are considered as contrast sources. The result is

$$c_0^{-2}\partial_t^2 p - \nabla^2 p = S_{\mathrm{pr}} + S_{\mathrm{cs}}(p), \tag{4.3}$$

where $S_{\mathrm{cs}}(p)$ is the total of all contrast source terms that account for the inhomogeneity, attenuation, nonlinearity, and the like that are not exhibited by the background medium. The acoustic pressure distribution arising from the primary source in a realistic medium can be implicitly found as

$$p(\boldsymbol{x}, t) = G(\boldsymbol{x}, t) *_{\boldsymbol{x},t} [S_{\mathrm{pr}}(\boldsymbol{x}, t) + S_{\mathrm{cs}}(p)]. \tag{4.4}$$

With the INCS method, an explicit solution is obtained in an iterative way, e.g. by using the Neumann iterative scheme

$$p^{(0)} = G(\boldsymbol{x}, t) *_{\boldsymbol{x},t} S_{\mathrm{pr}}(\boldsymbol{x}, t), \tag{4.5}$$

$$\begin{aligned} p^{(n)} &= G(\boldsymbol{x}, t) *_{\boldsymbol{x},t} [S_{\mathrm{pr}}(\boldsymbol{x}, t) + S_{\mathrm{cs}}(p^{(n-1)})] \\ &= p^{(0)} + G(\boldsymbol{x}, t) *_{\boldsymbol{x},t} S_{\mathrm{cs}}(p^{(n-1)})], \quad (n \geq 1). \end{aligned} \tag{4.6}$$

This general approach is used for the numerical simulations in this paper.

To simulate CEUS imaging, all nonlinear effects occurring during ultrasound wave propagation in a nonlinear medium containing nonlinearly scattering MBs must be taken into account. In addition, simulations should support scattering from tissue-mimicking linear scatterers (LSs) that typically surround a MB suspension in biological tissues. Based on these criteria, INCS was extended using extra contrast source terms resulting in the new nonlinear wave equation

$$c_0^{-2}\frac{\partial^2 p}{\partial t^2} - \nabla^2 p = S_{\text{pr}} + S_{\text{MB}}(p) + S_{\text{LS}}(p) + S_{\text{nl}}(p) + S_{\mathcal{L}}(p), \tag{4.7}$$

where S_{MBs} is the contrast source term describing the scattering of the MBs in the suspension [21], S_{LS} is the contrast source term describing the scattering of the linear scatterers in the LS suspension [21], S_{nl} and $S_{\mathcal{L}}$ are the terms describing global [21] and local [20] medium nonlinearities, respectively. The sum of all the contrast source terms yields the term $S_{\text{cs}}(p)$ in Eq. (4.3), which is then convolved with the 4D spatiotemporal Green's function of the linear background medium to compute a nonlinear field correction. Based on the Neumann iterative scheme described in Eqs. (4.5) and (4.6), INCS successively generates an increasingly accurate solution of Eq. (4.7), taking into account nonlinear effects and multiple scattering.

4

4.2.2 INCS implementation of AM pulse sequences

In this study, we simulate a 64-element ($N_{\text{tr}} = 64$), 15 MHz linear transducer array emulating a L22-14vX probe (Verasonics, Kirkland, WA, USA). Transducer elements have a height $H_{\text{el}} = 1.4$ mm, a width $W_{\text{el}} = 0.08$ mm, a pitch $P_{\text{tr}} = 0.1$ mm and the total focal distance of the array, which includes a lens in elevation is $z_{\text{el}} = 8$ mm. The natural focus of the transducer array is $(N_{\text{tr}}\,P_{\text{tr}})^2/4\lambda = 103$ mm in the azimuthal plane and $H_{\text{el}}^2/4\lambda = 5$ mm in the elevational plane, with λ being the wavelength. All transmitted ultrasound waveforms used in this study are Gaussian-windowed sine bursts defined as follows

$$s(t) = \exp\left[-\left(\frac{t - T_{\text{d}}}{T_{\text{w}}/2}\right)^2\right]\sin[2\pi f_0(t - T_{\text{d}})], \tag{4.8}$$

where $f_0 = 15$ MHz is the center frequency, $T_w = 1.5/f_0 = 0.1$ μs is the width of the Gaussian envelope and $T_d = 3/f_0 = 0.2$ μs is the temporal delay of the window. The simulated medium is water, characterized by a density of mass $\rho_0 = 1060$ kg/m^3 and a speed of sound $c_0 = 1482$ m/s. The first AM sequence implemented in INCS is the sequence with x-shaped wavefronts [10]. xAM pulse transmissions proceed as follows: first, elements 1 to $N/2$ and elements $N/2 + 1$ to N of the array simultaneously transmit two axisymmetric, tilted plane waves with wavefronts that make an angle θ and -θ with respect to the array (see pulse 1, Fig. 4.1(a)). Second, only elements 1 to $N/2$ transmit a single tilted plane wave at an angle -θ with respect to the array (see pulse 2, Fig. 4.1(a)). Third, only elements $N/2 + 1$ to N transmit a single symmetric plane wave at an angle θ with respect to the array (see pulse 3,

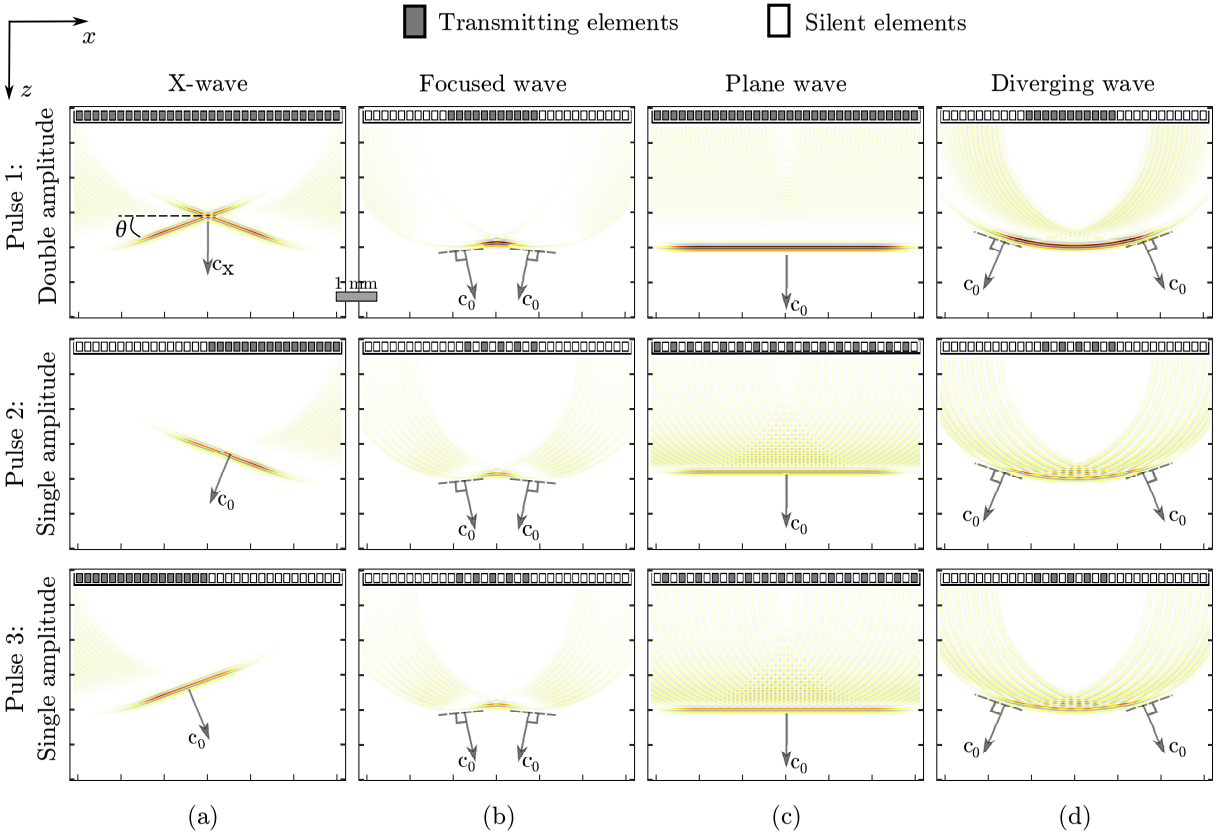

Figure 4.1: Wavefront shapes belonging to the pulse sequences investigated for AM ultrasound imaging of monodisperse MBs. (a) xAM sequence with a wavefront angle $\theta = 20°$, (b) focused AM sequence, (c) plane wave AM sequence and (d) diverging AM sequence. The first row shows the imaging pulses transmitted to elicit a double amplitude response from the medium, while the second and third rows show the pulses transmitted to elicit a single amplitude from the medium. Arrows indicate wavefront velocities.

Fig. 4.1(a)). The two cross-propagating waves depicted as pulse 1 interfere in a small zone around a virtual bisector that separates the two half-apertures. Particles of the insonified medium that are positioned along the bisector experience an identical pressure amplitude from pulses 2 and 3, but a double pressure amplitude from pulse 1 (x-wave transmission). Note that the overpressure at the plane waves' intersection depicted in pulse 1 propagates along the bisector with a supersonic phase velocity

$$c_{\mathrm{X}} = c_0/\cos(\theta). \tag{4.9}$$

The second AM sequence implemented in INCS relies on focused ultrasound wavefronts as depicted in Fig. 4.1(b). Focused AM transmissions proceed as follows: first, all elements of the array are activated following a parabolic delay law to generate a high amplitude transmission (see pulse 1, Fig. 4.1(b)). Second, even transducer elements of the same aperture are activated using the same delay law to generate a half amplitude transmission (see pulse 2, Fig. 4.1(b)). Third, odd transducer elements of the same aperture are activated using the same delay law to generate a second half amplitude transmission (see pulse 3, Fig. 4.1(b)). Here the focal distance is set to $z_{\mathrm{f}} = 5$ mm. Note that in focused AM, acoustic wavefronts propagate at speed of sound c_0.

The third AM sequence implemented in INCS relies on planar ultrasound wavefronts as seen in Fig. 4.1(c). Plane wave transmissions are generated by transmitting the same pulse with all elements of the transducer array. Here as well, the transmitted acoustic pressure amplitude is modulated using either all, even or odd elements of the array aperture (Fig. 4.1(c)). Transmitted plane waves propagate at speed of sound c_0 in the z direction.

The fourth AM sequence implemented in INCS relies on diverging acoustic wavefront transmissions. A virtual point source located at $(x_{\mathrm{f}}, z_{\mathrm{f}}) = (0, -3)$ mm is used to generate the diverging delay law. Here as well, the transmitted acoustic pressure amplitude is modulated using either all, even or odd elements of the array aperture (Fig. 4.1(d)). Transmitted diverging waves also propagate at speed of sound c_0.

4.2.3 Simulation of a monodisperse MB suspension

The dimensions of the computational domain are set to $X \times Y \times Z = 6.4$ mm $\times$ 1.5 mm $\times$ 10 mm as illustrated in Fig. 4.2. To accurately solve the full nonlinear wave equation up to the second harmonic frequency ($h = 2$), we choose a Nyquist frequency F_{nyq} equal to at least $h + 1.5 = 3.5$ times of the center ultrasound frequency. This corresponds to a sampling frequency of $F_s = 2 \cdot F_{nyq} = 2 \cdot 3.5 \cdot 15 = 105$ MHz as a basis for discretizing the spatiotemporal domain. Furthermore, it is known that we need at least $j = h + 1 = 3$ iterations for an accurate prediction of the second harmonic [17]. To achieve a relative root mean square error of 10^{-6} between successive iterations below, we take $j = 5$ iterations. Consequently, our simulations account for MB interactions up to 4th order multiple scattering [21].

We consider a monodisperse MB suspension confined in a cylindrical volume positioned at the center of the simulation domain $(x,\ y,\ z) = (0,\ 0,\ 5)$ mm, with a radius of 1 mm in the xz plane and a length of 1.4 mm in the y dimension, as shown in Fig. 4.2(a). This geometry is chosen to mimic MBs filling the lumen of a blood

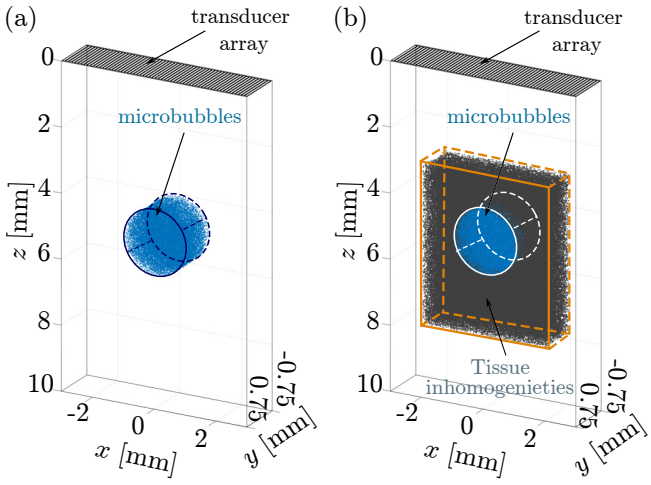

Figure 4.2: Wave propagation media simulated in INCS. (a) Computational domain containing a monodisperse MB concentration equal to 5.7 $\times 10^6$ ml^{-1} (blue) of 0.6 μm radius embedded in a water medium. (b) Second configuration incorporating a tissue-mimicking scatterer concentration of 6.2 $\times 10^6$ ml^{-1} (grey) surrounding the monodisperse MB suspension.

4

vessel. A MB radius $R = 0.6$ μm, corresponding to a resonance frequency of 15 MHz in the elastic oscillation regime, is selected to match the center frequency of the simulated transducer array. We use the Marmottant model [3] to emulate the nonlinear behavior of each MB in the simulation domain. Simulated material properties of MBs are provided in Table 4.1 [22].

A total of 25,000 monodisperse MBs are randomly distributed within the cylindrical volume, resulting in a MB concentration of 5.7×10^6 ml^{-1} and a gas volume concentration of 5.15×10^{-6}, which follows injection protocols reported by MB manufacturers (e.g. Fujifilm VisualSonics, Toronto, ON, Canada).

To reveal AM imaging artifacts due to nonlinear wave propagation, we also consider a second domain with tissue mimicking linear scatterers (Fig. 4.2(b)). These are located in a volume of $L \times W \times H = 4$ mm $\times$ 1.5 mm $\times$ 5 mm surrounding the MB suspension. The linear scatterers have a spherical radius of 0.6 μm to match the speckle pattern generated by monodisperse MBs. Their concentration is 6.2×10^6

Table 4.1: Material properties of a single simulated MB with $R = 0.6$ μm. κ_s [kg/s] is the shell viscosity, σ_{w} [N/m] is the surface tension of water, σ_{R} [N/m] is the effective surface tension, γ is the polytropic exponent of the gas encapsulated in the bubble, χ [N/m] is the shell elasticity, μ [Pa·s] is the surrounding liquid dynamic viscosity increased by a factor of 2 to account for thermal damping.

κ_{s} [kg/s]	σ_{w} [N/m]	σ_{R} [N/m]	γ	χ [N/m]	μ [Pa $\cdot$ s]
2.4×10^{-9}	0.072	0.01	1.07	0.5	2×10^{-3}

ml^{-1}, and their volume concentration is 5.61×10^{-6}, which is approximately similar to the MB suspension. The scattering coefficient of the linear scatterers [21] is set to $g = 6.57 \times 10^{-6}$ m to match the scattering level of monodisperse MBs.

4.2.4 Ultrasound image reconstruction

xAM and focused AM images are reconstructed line-by-line using 42 sliding sub-apertures across the MB suspension. For each sub-aperture position, 3 pulses are transmitted sequentially as illustrated in Figs. 4.1(a) and (b), leading to a total of 126 ultrasound transmissions per AM image. To acquire RF data corresponding to each image line, instead of moving the transducer, we translate the position of the MB suspension laterally with steps $dx = 0.1$ mm, which is the pitch of the imaging array. The reconstructed image width ranges from $x = -2.1$ mm to $x = 2.1$ mm. Plane wave and diverging wave AM images are reconstructed out of 3 pulse transmissions only, as each insonification captures a wide 2D field of view (Fig. 4.1(c) and (d)). B-mode images are reconstructed using the first pulse of each AM sequence.

xAM image reconstruction is performed along the bisector as illustrated in Fig. 4.3. The transmit distance d_{TX} and the transmit time of flight τ_{TX} to a scatterer $\boldsymbol{X}_{\mathrm{s}} = (x_{\mathrm{s}}, z_{\mathrm{s}})$ are given by

$$d_{\mathrm{TX}}(\theta, z_{\mathrm{s}}) = D_{\mathrm{h}} \tan(\theta) + z_{\mathrm{s}}, \tag{4.10}$$

$$\tau_{\mathrm{TX}} = \frac{d_{\mathrm{TX}}}{c_{\mathrm{X}}}, \tag{4.11}$$

with $D_h = N_{\mathrm{tr}} P_{\mathrm{tr}}/2$ being the length of the half aperture. The receive distance d_{RX} and receive time of flight τ_{RX} are given by,

$$d_{\mathrm{RX}}(\boldsymbol{X}_{\mathrm{s}}) = \sqrt{(x_{\mathrm{s}} - x_{\mathrm{i}})^2 + z_{\mathrm{s}}^2}, \tag{4.12}$$

$$\tau_{\mathrm{RX}} = \frac{d_{\mathrm{RX}}}{c_0}, \tag{4.13}$$

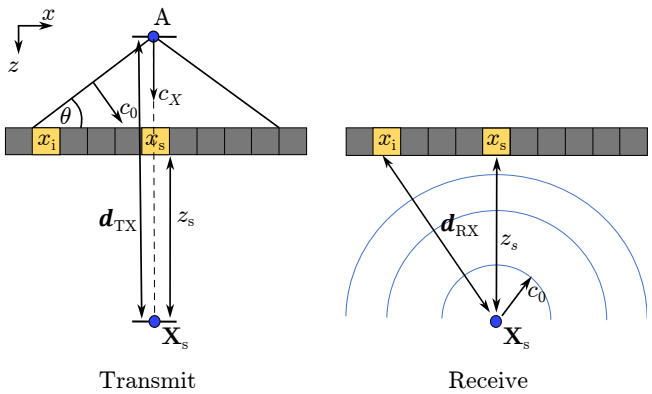

Figure 4.3: Transmit and receive geometry model used for xAM image reconstruction.

with x_i the i-th element position. Knowledge of transmit and receive time of flights enables the reconstruction of one image line using a conventional delay-and-sum (DAS) beamforming algorithm [23]. By repeating the process for each transmitting sub-aperture position, a xAM image of the MB suspension is generated.

Focused AM image reconstruction is performed line-by-line as well using usual transmit and receive time of flights. For plane wave and diverging wave image reconstruction, we use the MUST [24] toolbox and a virtual point source formulation as described by Perrot et al. [23].

4.3 Results

4.3.1 Acoustic pressure fields in the absence of microbubbles

To isolate nonlinear effects due to wave propagation, we first solve the full nonlinear wave equation in a homogeneous nonlinear medium consisting of water that is free of MBs.

Fig. 4.4 presents the simulated incident pressure fields generated by the first pulse of each AM sequence, as well as the time delays and apodization functions used to generate these beam patterns. To ensure a fair comparison of nonlinear effects, we equated the average acoustic pressure delivered by the first pulse of each sequence on the z axis between $z = 4$ mm and $z = 6$ mm (see Appendix 4.A).

We report in Fig. 4.4(a) the x-wave beam pattern simulated for an angle $\theta = 20°$. All 64 elements are used in transmission and a Tukey window apodization, with a parameter $\alpha = 0.3$ representing the ratio of cosine-tapered section length to the entire window length, is applied along the elements of each half aperture of the array to mitigate the side lobe level and diffraction effects. The non-diffractive x-wave beam pattern exhibits a constant beam width along the bisector. Beyond the x-wave intersection zone, a noticeable acoustic pressure drop is observed along the bisector.

Fig. 4.4(b) displays the focused wave beam pattern generated with parabolic time delays applied to a sub-aperture of 22 elements apodized with a Tukey window ($\alpha = 0.3$). The beam focus is equal to $z = 4.75$ mm, corresponding to an f-number of 2.27. Most of the focused beam energy is concentrated between $z = 4$ mm and $z = 6$ mm. The focal length is shorter than the x-wave beam, whereas in the lateral direction, the focused beam is noticeably wider that the x-wave beam.

Fig. 4.4(c) displays the plane wave beam pattern generated with all 64 elements apodized with a Tukey window ($\alpha = 0.3$). The plane wave beam focus is $z = 5.25$ mm and the elevated amplitude around $z = 5$ mm is due to the focusing in elevation.

Fig. 4.4(d) displays the diverging beam pattern generated by inverting the time delays used in Fig. 4.4(b). Here the total beam focus is equal to $z = 4.65$ mm, also due to the focusing in elevation.

The primary objective of CEUS imaging is to suppress nonlinear effects arising from wave propagation in the medium of interest, while retaining nonlinear effects arising from ultrasound contrast agents administered in that medium. To investigate the ability of AM sequences based on x-shaped, focused, planar and diverging wavefronts to suppress nonlinear wave propagation effects, we report the residual acoustic

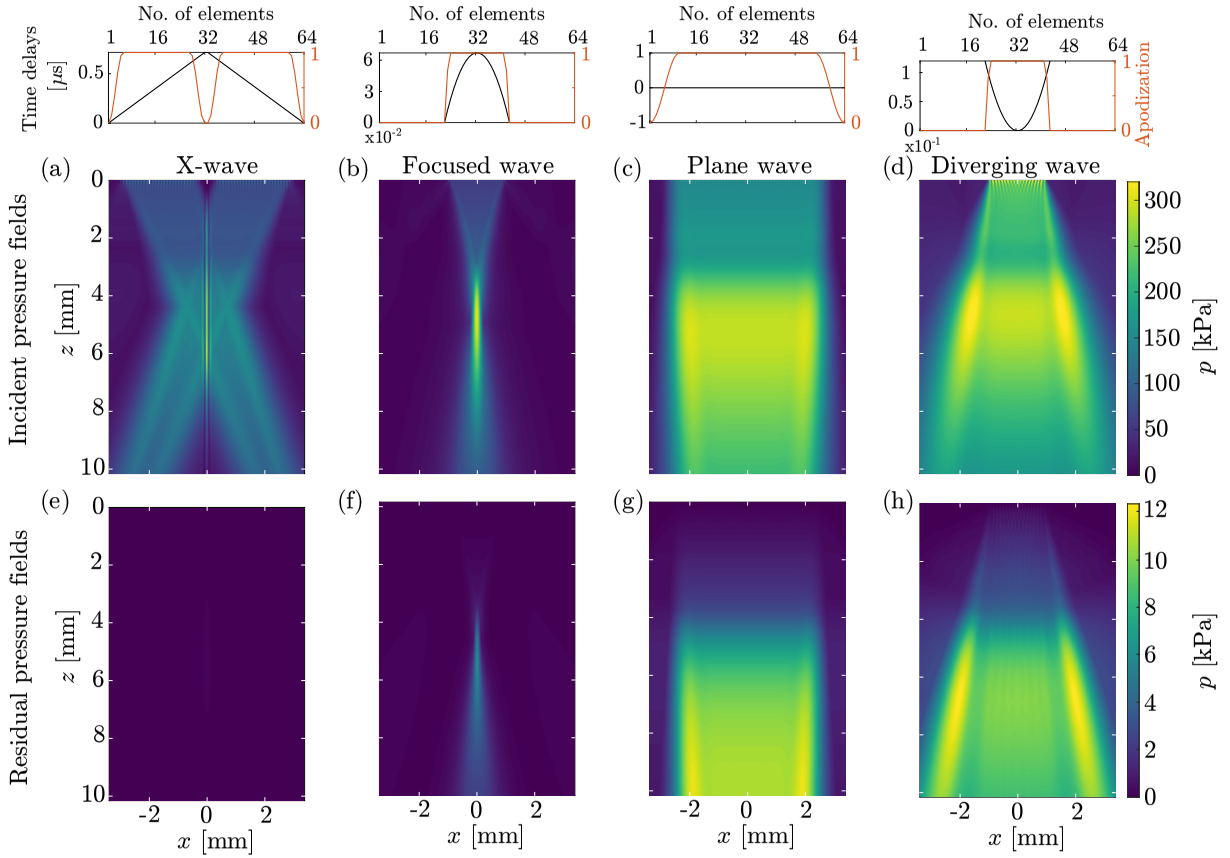

Figure 4.4: Acoustic pressure fields in a homogeneous nonlinear water medium. (Top row) delay laws (black) and apodization (orange) used for the first pulse transmissions. (a)-(d) Incident pressure fields generated by the first pulse transmission of each sequence using x-shaped, focused, planar and diverging wavefronts respectively. (e)-(h) Residual AM pressure fields for the xAM, focused AM, planar AM and diverging AM pulse sequences respectively. xAM transmissions are simulated for $\theta = 20°$.

pressure fields after the AM operation (pulse 1 minus pulse 2 minus pulse 3) and display them on scale in Figs. 4.4(e)-(h).

We observe that AM pulse sequences based on focused, planar and diverging wavefronts suffer from effects arising from nonlinear wave propagation and local non-collinear nonlinear interactions [20], even in the absence of MBs. The xAM residual pressure field on the contrary is nearly free of nonlinear effects. Quantitatively, the residual xAM pressure exhibits the lowest amplitude with a peak of 0.26 kPa (see Appendix 4.B, Fig. 4.10(a)), followed by the residual focused AM pressure field with a peak of 6 kPa, the plane wave residual AM pressure field with a peak of 11.9 kPa, and the residual diverging AM pressure field with a peak of 12.3 kPa.

Qualitatively, for the xAM case (Fig. 4.10(a)), the highest residual pressure values are observed along the bisector. However, we observe that below the plane wave intersection zone the residual xAM pressure level drops significantly.

For the focused AM case (Fig. 4.4(f)), nonlinearities peak at the focus but extend beyond the focus because of cumulative nonlinear wave propagation effects, following the shape of the transmitted beam (Fig. 4.4(b)).

For the plane wave AM case (Fig. 4.4(g)) a gradual onset of nonlinearities is observed as expected for cumulative nonlinear effects due to wave propagation [25]. Additionally, a higher amplitude is observed on the sides of the plane wave beam due to the larger incident pressure in those regions.

For the diverging AM case (Fig. 4.4(h)), the behavior is similar to the plane wave case and nonlinearities reach the highest peak amplitude compared to all the other cases.

4.3.2 Acoustic pressure fields in the presence of monodisperse MBs

Total acoustic pressure fields generated by the first pulse of each AM sequence in the presence of a resonant monodisperse MB suspension are displayed in Figs. 4.5(a)-(d). The x-wave pressure field (Fig. 4.5(a)) is attenuated below the MB suspension and shows a peak acoustic pressure at $(x,\ z) = (0,\ \text{mm},\ 7\ \text{mm})$ of 166 kPa compared to 216 kPa in water without MBs (Fig. 4.4(a)). Compared to the x-wave case, the focused pressure field shows a more substantial level of attenuation below of the MB suspension with peak acoustic pressure at $(x,\ z) = (0,\ \text{mm},\ 7\ \text{mm})$ mm (b) of 140 kPa compared to 205 kPa in water without MBs (Fig. 4.4(b)). Similarly, the planar pressure field shows a peak pressure of 186 kPa compared to 272 kPa in water without MBs (Fig. 4.4(c)) and the diverging pressure field shows a peak pressure of 168 kPa compared to 243 kPa in water without MBs (Fig. 4.4(d)).

Residual AM pressure fields in the presence of a suspension of resonant monodisperse MBs are reported in Figs. 4.5(e)-(h). For the xAM case, a better view of the spatial pattern of Fig. 4.5(e) is illustrated in Fig. 4.10(b) of Appendix 4.B. We observe that nonlinear effects accumulate along the direction of propagation of each plane wave. However, along the bisector and below the MB suspension, nonlinear effects are suppressed. The residual xAM pressure field reaches a maximum of 15.2 kPA within the MB suspension, as desired for a CEUS pulse sequence, and immediately drops beyond the MB suspension. A 1.7 kPa peak pressure is measured at $z = 6.3$

mm.

For the focused AM case (Fig. 4.5(f)), the amplitude of the residual pressure field builds up inside the MB suspension along the z-axis and reaches a maximum of 51 kPa at z=5.7 mm, which is deeper than the transducer focus of 5.25 mm. Below the MB suspension, the amplitude of the residual AM pressure field remains high and reaches 47.7 kPa at $z = 6.3$ mm, which is 28 times higher than for the xAM case.

For the planar AM case (Fig. 4.5(g)), the amplitude of the residual pressure field builds up along the z-axis and expands across the width of the plane wave beam profile. We observe an increase of nonlinear effects within and below the MB suspension, which is as wide as the MB cloud. Cumulative nonlinear effects are also observed besides of the MB suspension, and are caused by nonlinear wave propagation alone. The planar AM pressure field reaches a peak of 52 kPa within the MB suspension and 53.4 kPa at $z = 6.3$ mm, which is 31 times higher than for the xAM case.

For the diverging AM case (Fig. 4.5(h)), we observe an increase of nonlinear effects below the MB suspension that spans the full width of the MB suspension as well. The AM pressure field peaks at 58.6 kPa within the MB suspension and 59.4 kPa at $z = 6.3$ mm, which is 35 times higher than for the xAM case.

4

4.3.3 Reason of reduction of nonlinear wave propagation artifacts by an x-shaped wavefront

To elucidate why cumulative nonlinear effects do not build up along the bisector in the xAM case, in Fig. 4.6 we present the transmitted waveforms with a planar wavefront and an x-shaped wavefront at a depth $z = 7$ mm, which is below the MB suspension.

Fig. 4.6(a) displays the three pulses of the planar AM sequence at a depth of 7 mm. Pulses reach $z = 7$ mm in 4.73 μs (including 0.1 μs delay), corresponding to a wave velocity of 1482 m·s^{-1}. The residual waveform derived from the AM operation exhibits a non-zero pressure amplitude with a residual AM peak pressure of 50.6 kPa compared to 162.2 kPa for the first pulse of the sequence. We observe that the sum of the second and third pulses of the sequence (Fig. 4.6(a), dashed magenta line) does not match the waveform of the double amplitude pulse 1 (Fig. 4.6a, continuous black line).

In comparison, Fig. 4.6(b) shows that the three pulses of the xAM sequence propagate to a depth of 7 mm in 4.45 μs (including 0.1 μs delay), corresponding to a supersonic wave velocity of $c_{\mathrm{X}} = 1577$ m·s^{-1}. The sum of the second and third pulses of the xAM sequence overlaps nearly perfectly with the first pulse. The residual waveform derived from the xAM operation exhibits a quasi-zero residual pressure amplitude of 1.7 kPa after the xAM operation compared to 152.1 kPa for the first pulse.

4.3.4 Effect of the cross-propagation angle θ on the reduction of the nonlinear artifact

Figs. 4.7(a) and (b) display the peak of the AM residual pressure as a function of depth along the bisector, in the absence and presence of monodisperse MBs, respectively.

Figure 4.5: Acoustic pressure fields in the presence of resonant monodisperse MBs. (a)-(d) Total acoustic pressure fields generated by the x-shaped, focused, planar and diverging wavefront transmissions respectively. (e)-(h) Residual acoustic pressure fields generated by the xAM, focused AM, planar AM and diverging AM pulse sequences respectively.

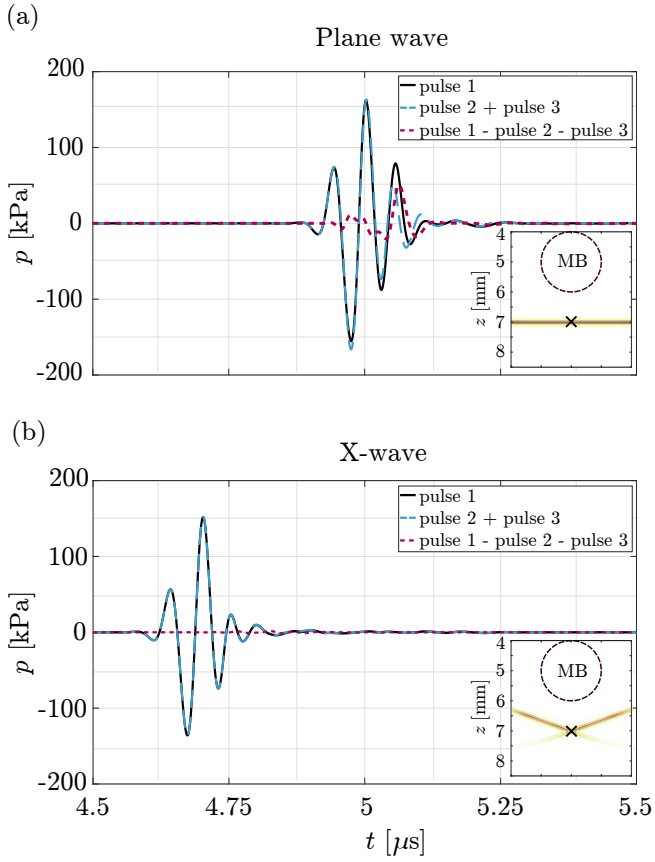

Figure 4.6: Propagation of AM and xAM pulses to a depth of 7 mm. (a) Waveforms retrieved with the AM pulse sequence. (b) Waveforms retrieved with the xAM pulse sequence.

Figure 4.7(a) shows that higher angles θ are more effective at suppressing effects arising from nonlinear wave propagation in the medium.

Figs. 4.7(a) and (b) display the peak of the AM residual pressure as a function of depth along the bisector, in the absence and presence of monodisperse MBs, respectively. Figure 4.7(a) shows that higher angles θ are more effective at suppressing effects arising from nonlinear wave propagation in the medium.

Figure 4.7(b) shows that the presence of monodisperse MBs leads to a substantial increase in the residual xAM peak pressure level within the boundaries of the MB suspension, as desired for a CEUS imaging mode. However, we observe that angles of $\theta = 0°$ and $\theta = 10°$ do not strongly suppress nonlinear effects below the MB suspension. In contrast, an angle of $\theta = 20°$ strongly reduces the xAM pressure amplitude beyond the boundary of the MB suspension.

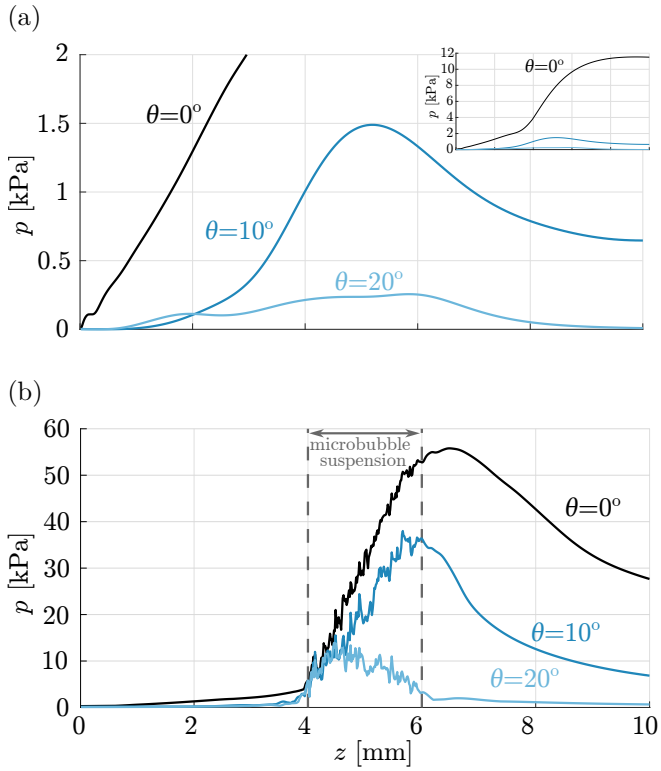

Figure 4.7: xAM peak residual pressure as a function of depth for increasing angles θ. (a) Residual pressure profiles in the absence of MBs. (b) Residual pressure profiles in the presence of monodisperse MBs. The boundaries of the MB suspension are indicated with dashed vertical lines. Results are simulated for θ angles of 0°, 10°, and 20°.

4.3.5 Impact of wavefront shape on AM imaging of monodisperse MBs

In this section, we use INCS to simulate ultrasound imaging of a monodisperse MB suspension applying AM pulse sequences with four different wavefront shapes (Fig. 4.1). The computational domain is shown in Fig. 4.2(b). Conventional single-shot ultrasound images, also referred to as B-mode images, are reported in Figs. 4.8(a)-(d). The backscattered amplitude arising from tissue-mimicking linear scatters and resonant monodisperse MBs generates a similar echogenicity level, independent of the acoustic wavefront shape. As such, B-mode images do not allow to disentangle monodisperse MBs and tissue mimicking scatterers.

AM images generated with each wavefront shape are reported in Figs. 4.8(e)-(h). The xAM sequence (Fig. 4.8(e)) generates a highly specific image of monodisperse MBs. On the contrary, AM sequences based on focused, planar and diverging wavefronts (Figs. 4.8(f)-(h)) generate images of MBs that suffer from significant nonlinear

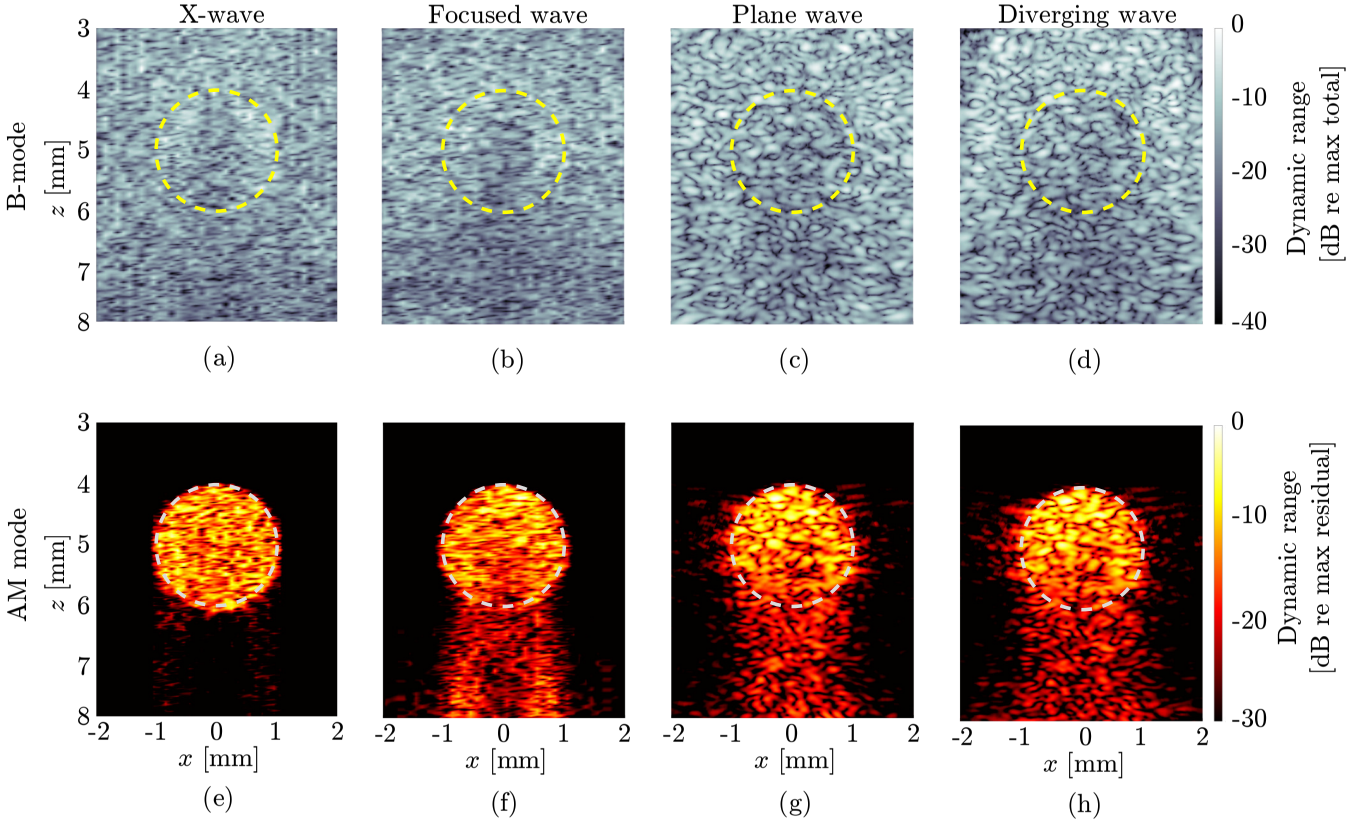

Figure 4.8: B-mode and AM numerical ultrasound images of monodisperse MBs. (a)-(d) Single-shot ultrasound images acquired with x-shaped, focused, planar and diverging wavefronts respectively. (e)-(h) AM ultrasound images acquired with x-shaped, focused, planar and diverging wavefronts respectively. The position of the MB suspension is outlined by a dashed circle. The rest of the simulation domain is filled with tissue-mimicking linear scatterers.

wave propagation artifacts below the MB suspension. The level of nonlinear artifacts is -30 dB for the xAM image, -9 dB for the focused AM image, -12 dB for the plane wave AM image and -12 dB for the diverging AM image.

4.4 Discussion

We report a numerical investigation of CEUS imaging and demonstrate that AM imaging based on x-shaped wavefronts enables specific and sensitive imaging of monodisperse MBs at a high ultrasound frequency. Our results reveal that the shape of transmitted ultrasonic wavefronts plays a critical role in the specificity of AM ultrasound imaging of monodisperse MBs. Widely used AM pulse sequence implementations based on focused, planar and diverging wavefronts (Figs. 4.1(b)-(d)) are all subject to significant nonlinear wave propagation artifacts appearing below monodisperse MB suspensions (Figs. 4.8(f)-(h)).

The INCS method enables to disentangle different nonlinear effects involved in CEUS. In the absence of MBs, a first observation is that AM pulse sequences for all four wavefront shapes capture cumulative nonlinear effects caused by ultrasound wave propagation, despite the low acoustic pressure transmitted in the medium, which corresponds to a mechanical index of 0.074 in our study (Figs. 4.4(f)-(h)). A second observation is that a resonant monodisperse MB suspension amplifies cumulative nonlinear wave propagation effects in the direction of wave propagation for all wavefront shapes investigated (Figs. 4.5(e)-(h)). As a result, for the focused, planar and diverging wavefronts, the AM operation is compromised below the monodisperse MB suspension as the involved pulses do not cancel each other anymore (Fig. 4.6(a)). This amplitude-dependent nonlinear scattering effect leads to nonlinear wave propagation artifacts in AM images of monodisperse MBs (Figs. 4.8(f)-(h)).

X-shaped wavefronts provide a solution to this problem. In the absence of MBs, residual xAM pressure fields prevent cumulative nonlinear wave propagation effects along the bisector, i.e. the imaging line, as seen in Fig. 4.4(e). In the presence of monodisperse MBs, cumulative nonlinear effects are visible in the direction of propagation of each cross-propagating plane wave (see Fig. 4.10(b) of Appendix 4.B), however nonlinear effects do not build up along the bisector. In xAM imaging, the segments of each wavefront that contribute to the double amplitude can only co-propagate for short periods of time. As a consequence, amplitude-dependent cumulative nonlinear effects are minimized and higher angles θ lead to a higher suppression of these effects (Fig. 4.7).

A limitation of our study is that we investigate AM ultrasound imaging of a perfectly monodisperse ultrasound contrast agent rather than an ultrasound contrast agent with a narrow size distribution. However, nonlinear artifacts observed in our study are therefore maximized and our study represents the worst-case test scenario for xAM imaging. Another limitation is that we only investigate perfectly symmetric geometries. In the future, it would be interesting to evaluate the effect of a scattering structure located in the path of one of the two cross-propagating plane waves. Nevertheless, in vivo experiments prove that xAM imaging is also performing well in non-symmetric soft biological tissue [26]. Another interesting pulse sequence to inves-

tigate would be pulse inversion. It is acknowledged that pulse inversion sequences are prone to artifacts [5] since they were initially developed to isolate second harmonic generated by nonlinear wave propagation [27, 28].

Our study also has implications for the field of ultrasound localization microscopy [29]. Approaches that rely on AM sequences with focused, planar or diverging wavefronts [15] are likely to be subject to artifacts, especially when mapping the coronary vasculature of the inferior myocardial wall which sits below the left ventricle chamber filled with MBs.

4.5 Conclusions

We numerically investigated AM ultrasound imaging of monodisperse MBs for implementations relying of x-shaped, focused, planar and diverging acoustic wavefronts. We show that xAM ultrasound imaging can detect monodisperse MBs, the most nonlinear ultrasound contrast agent to date, with high sensitivity and specificity. All other AM sequence implementations were prone to nonlinear wave propagation artifacts. This study paves the way for numerical investigations and optimization of CEUS imaging.

Appendix 4.A Equalization of incident acoustic pressure levels

In this paper we compare AM sequences for four different wavefront shapes. These are obtained with varying numbers of active elements, different time delays and apodization, which may result in substantial differences in the generated incident pressure

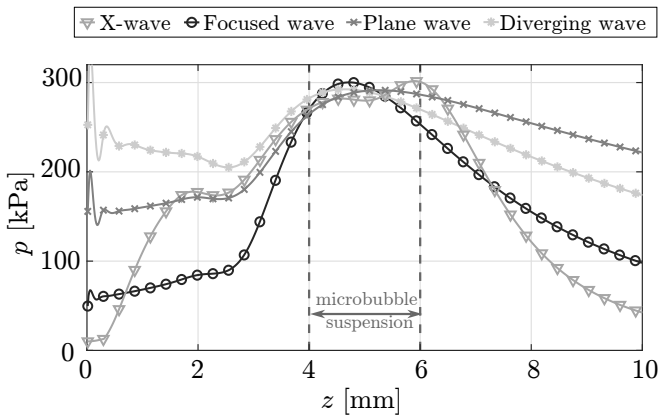

Figure 4.9: Equalization of the average acoustic pressure transmitted by the first pulse of each sequence. Transmission for (a) x-wave (triangles), (b) focused wave (circles), (c) plane wave (xs) and (d) diverging wave (asterisks). The position of the MB suspension is indicated by the dashed vertical lines.

fields. To ensure a fair comparison of CEUS imaging results, it is necessary to deliver the same average peak pressure within the MB suspension for all cases. Furthermore, since image reconstruction for the x-wave and focused wave methods is performed in a line-by-line format, it is critical to equalize the average peak pressure along the bisector at the location of the MB suspension ($x = 0,\ 4\text{mm} < z < 6\text{mm}$). We have chosen to deliver an average peak acoustic pressure of 285.5 kPa over this interval for the first pulse of each AM pulse sequence. This corresponds to a mechanical index of 0.074. The resulting peak pressure as a function of depth along the bisector is given in (Fig. 4.9) for each AM pulse sequence.

Appendix 4.B Residual xAM pressure in the absence and presence of MBs

To better visualize the residual xAM pressure fields reported in Figs. 4.4(e) and 4.5(e), in Fig. 4.10 we show the same results using a smaller pressure range.

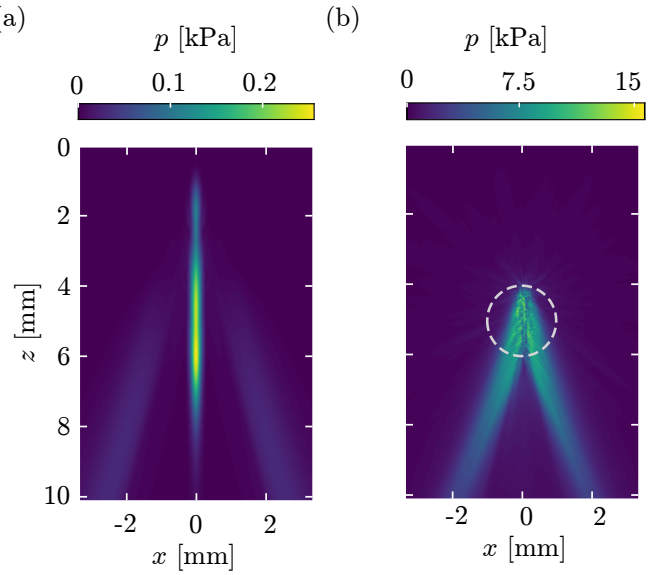

Figure 4.10: Residual xAM pressure fields in (a) a homogeneous nonlinear water medium without MBs and (b) a medium containing nonlinear monodisperse MBs. Dashed white lines indicate the position of the MB suspension.

Bibliography

[1] C. Errico, J. Pierre, S. Pezet, Y. Desailly, Z. Lenkei, O. Couture and M. Tanter, "*Ultrafast ultrasound localization microscopy for deep super-resolution vascular imaging*", Nat. **527**, 499–502 (2015).

[2] B. Heiles, D. Terwiel, and D. Maresca, "*The Advent of Biomolecular Ultrasound Imaging*", Neurosc. **474**, 122–133 (2021).

[3] P. Marmottant, S. van der Meer, M. Emmer, M. Versluis, N. de Jong, S. Hilgenfeldt, and D. Lohse, "*A model for large amplitude oscillations of coated bubbles accounting for buckling and rupture*", J. Acoust. Soc. Am. **118**, 6, 3499–3506 (2005).

[4] M. Averkiou, M. Bruce, J. Powers, P. Sheeran, and P. Burns, "*Imaging methods for ultrasound contrast agents*", Ultrasound Med. Biol. **46**, 3, 498–517 (2020).

[5] M.-X. Tang, and R. Eckersley, "*Nonlinear propagation of ultrasound through microbubble contrast agents and implications for imaging*", IEEE Trans. Ultrason. Ferroelectr. Freq. Control **53**, 12, 2406–2415 (2006).

[6] G. ten Kate, G. Renaud, A. Akkus, S. van den Oord, F. ten Cate, V. Shamdasani, R. Entrekin, E. Sijbrands, N. de Jong, J. Bosch, A. Schinkel, and A.F. van der Steen, "*Far-wall pseudoenhancement during contrast-enhanced ultrasound of the carotid arteries: clinical description and in vitro reproduction*", Ultrasound Med. Biol. **38**, 4, 593-600 (2012).

[7] M. Emmer, H.J. Vos, D.E. Goertz, A. van Wamel, M. Versluis, and N. de Jong, "*Pressure-Dependent Attenuationand Scattering of Phospholipid-Coated Microbubbles at Low Acoustic Pressures*", Ultrasound Med. Biol. **35**, 1, 102–111 (2009).

[8] A. J. Sojahrood, Q. Li, H. Haghi, R. Karshafian, T.M. Porter, and M.C.Kolios, "*Probing the pressure dependence of sound speed and attenuation in bubbly media: Experimental observations, a theoretical model and numerical calculations*", Ultrason. Sonoch. **95**, 106319, (2023).

[9] G. Renaud, J. Bosch, A.F. van der Steen, and N. de Jong, "*Increasing Specificity of Contrast-Enhanced Ultrasound Imaging Using the Interaction of Quasi Counter-Propagating Wavefronts: A Proof of Concept*", IEEE Trans. Ultrason. Ferroelectr. Freq. Control **62**, 10, 1768–1778 (2015).

[10] D. Maresca, D.P. Sawyer, G. Renaud, A. Lee-Gosselin, and M.G. Shapiro, "*Nonlinear X-Wave Ultrasound Imaging of Acoustic Biomolecules*", Phys. Rev. X **8**, 041002 (2018).

[11] S. Nagai, and K. Iizuka, "*A practical ultrasound axicon for non-destructive testing*", Ultrasonics **20**, 6, 265–270 (1982).

[12] T. L. Szabo, "*Diagnostic ultrasound imaging: Inside out*", Academic Press (2014).

[13] T. Segers, P. Kruizinga, M. Kok, G. Lajoinie, N. de jong, and M. Versluis, "*Monodisperse Versus Polydisperse Ultrasound Contrast Agents: Non-Linear Response, Sensitivity, and Deep Tissue Imaging Potential*", Ultrasound Med. Biol. **44**, 7, 1482–1492 (2018).

[14] C. Tremblay-Darveau, R. Williams, L. Milot, M. Bruce, and P. Burns, "*Visualizing the Tumor Microvasculature With a Nonlinear Plane-Wave Doppler Imaging Scheme Based on Amplitude Modulation*", IEEE Trans. Ultrason. Ferroelectr. Freq. Control **35**, 2, 699–709 (2015).

[15] J. Yan, B. Huang, J. Tonko, M. Toulemonde, J. Hansen-Shearer, Q. Tan, K. Riemer, K. Ntagiantas, R. Chowdhury, P. Lambiase, R. Senior, and M.-X. Tang, "*Transthoracic super-resolution ultrasound localisation microscopy of myocardial vasculature in patients*", arXiv (2023).

[16] J. Huijssen, "*Modeling of nonlinear medical diagnostic ultrasound*",Ph.D. Thesis, Delft University of Technology (2008)

[17] J. Huijssen, and M.D. Verweij, "*An iterative method for the computation of nonlinear, wide-angle, pulsed acoustic fields of medical diagnostic transducers*", J. Acoust. Soc. Am. **127**, 1, 33–44 (2010).

[18] L. Demi, "*Modeling nonlinear propagation of ultrasound through inhomogeneous biomedical media*", Ph.D. Thesis, Delft University of Technology (2013)

[19] L. Demi, K.W.A. van Dongen, and M.D. Verweij, "*A contrast source method for nonlinear acoustic wave fields in media with spatially inhomogeneous attenuation*", J. Acoust. Soc. Am. **129**, 3, 1221–1230 (2011).

[20] A. Matalliotakis, D. Maresca, and M.D. Verweij, "*Nonlinear interaction of two cross-propagating plane waves*", arXiv (2023).

[21] A. Matalliotakis, and M.D. Verweij, "*Computation of ultrasound propagation in a population of nonlinearly oscillating microbubbles including multiple scattering*", J. Acoust. Soc. Am. **153**, 4, 2209–2222 (2023).

[22] T. Segers, E. Gaud, M. Versluis, and P. Frinking, "*High-precision acoustic measurements of the nonlinear dilatational elasticity of phospholipid coated monodisperse microbubbles*", Soft Matter **14**, 9550–9561 (2018).

[23] V. Perrot, M. Polichetti, F. Varray, and D.Garcia, "*So you think you can DAS? A viewpoint on delay-and-sum beamforming*", Ultrasonics **111** , 106309, (2021).

[24] D.Garcia, "*Make the most of MUST, an open-source MATLAB UltraSound Toolbox*", IEEE Int. Ultrason. Symp., (2021).

[25] T. Lai, M. Bruce, and M. Averkiou, "*Modeling of the Acoustic Field Produced by Diagnostic Ultrasound Arrays in Plane and Diverging Wave Modes*", IEEE Trans. Ultrason. Ferroelectr. Freq. Control **66**, 7, 1158–1169 (2019).

[26] R. Hurt, M. Buss, M. Duan, K. Wong, M. You, D. Sawyer, M. Swift, P. Dutka, P. Barturen-Larrea, D. Mittelstein, Z. Jin, M. Abedi, A. Farhadi, R. Deshpande, and M.G. Shapiro, "*Genomically mined acoustic reporter genes for real-time in vivo monitoring of tumors and tumor-homing bacteria*", Nat. Biotech. **41**, 919–931 (2023).

[27] M. Averkiou, "*Tissue harmonic imaging*", IEEE Int. Ultrason. Symp., 1563–1572 (2000).

[28] C.-C. Shen, Y.-H. Chou, P.-C. Li, "*Pulse inversion techniques in ultrasonic nonlinear imaging*", J. Med. Ultrasound **13**, 1, 3–17 (2005).

[29] B. Heiles, A. Chavignon, A. Bergel, V. Hingot, H. Serroune, D. Maresca, S. Pezet, M. Pernot, M. Tanter, and O. Couture, "*Volumetric Ultrasound Localization Microscopy of the Whole Rat Brain Microvasculature*", IEEE Open Trans. Ultrason. Ferroelectr. Freq. Control **2**, 261–282 (2022).

4

Chapter 5

Polydisperse versus monodisperse microbubbles: A simulation study

Contrast-enhanced ultrasound (CEUS) presents distinct advantages in diagnostic echography. Utilizing microbubbles (MBs) as conventional contrast agents enhances vascular visualization and organ perfusion, facilitating real-time, non-invasive procedures. There is a shift towards replacing traditional polydisperse MBs with novel monodisperse formulations to optimize contrast enhancement and guarantee consistent behavior and reliable imaging outcomes. This study investigates contrast enhancement by monodisperse MBs of different sizes, and their influence on nonlinear imaging artifacts observed in traditional CEUS. To compare monodisperse and polydisperse populations without excessive experimentation, numerical simulations are employed for delivering precise, objective and expeditious results. The Iterative Nonlinear Contrast Source (INCS) method has previously demonstrated its efficacy in simulating ultrasound propagation in large populations in which each bubble has individual properties and several orders of multiple scattering are significant. Therefore, this method can realistically simulate both monodisperse and polydisperse MBs. Our findings in CEUS imaging indicate that scattering from resonant monodisperse MBs is 11.8 dB stronger than scattering from the polydisperse population. Furthermore, the amplitude of nonlinear imaging artifacts downstream of the monodisperse population is 19.4 dB stronger compared to polydisperse suspension. Investigating the impact of multiple scattering on various populations, reveals that monodisperse MBs are more effective contrast agents than polydisperse, especially when at resonance. Despite the strong signal to noise ratio of monodisperse populations, the imaging artifacts due to nonlinear wave propagation are also enhanced, resulting in more missclassification of tissue as MBs.

5.1 Introduction

Achieving superior deep tissue imaging of blood vessels with ultrasound remains a challenge in medical diagnostics. Contrast-enhanced imaging, particularly using MBs, has emerged as a promising solution [1, 2]. These gas-filled microspheres, stabilized with a lipid or protein shell, enhance blood contrast for improved organ and lesion visualization. MBs, characterized by small size, biocompatibility, and vascular navigability, resonate in the ultrasound frequency range (1-10 MHz). Their efficient sound scattering in both fundamental and harmonic modes, driven by substantial acoustic impedance difference with surroundings and highly nonlinear oscillatory behavior [3, 4], enhances image quality. As ultrasound waves propagate through a resonant MB suspension, they undergo nonlinear distortion due to nonlinear MB scattering influenced by size, shell characteristics, ultrasound pressure and frequency [5–7]. Because of these properties, MBs are also efficient contrast agents in various applications besides CEUS, such as ultrasound localization microscopy [8].

As a drawback, wave distortion extends beyond a MB suspension and this leads to the misidentification of tissues as MBs, diminishing the specificity of CEUS imaging [9]. Narrowing of the size distribution of the MB population might be a way to provide improved acoustic scattering, reduce imaging artifacts and enhance scattering homogeneity. Historically, polydisperse MBs with varying size distributions (typical radii 0.5 to 15 μm) have been standard in ultrasound contrast imaging [10, 11]. Recent technological breakthroughs have introduced the possibility of using monodisperse, i.e. uniformly sized, MBs [12]. Studies highlight the superiority of monodisperse MBs [13], offering enhanced predictability, improved acoustic performance, and clearer imaging signals [14, 15]. Nevertheless, we think that it is important to shed more light on the effect of monodisperse MBs as contrast agents for deep vessel imaging, especially on the generation of clearer echoes and reducing imaging artifacts.

The use of computational tools is an efficient way to perform comprehensive investigations without performing extensive measurements. Initially, studies focused on the collective behavior of bubbly media for marine applications [16, 17]. Effective medium theory facilitated 1D computational studies for both monodisperse [18, 19] and polydisperse [20, 21] MB suspensions in medical ultrasound, including high intensity focused ultrasound (HIFU) [22]. Previous models successfully captured nonlinear ultrasound propagation through uniform MB distributions in two dimensions using iterative schemes [23, 24]. Challenges arise when coupling the nonlinear dynamics of multiple MBs in 3D realistic simulations, due to the complexity of the coupled Rayleigh-Plesset equation [25]. Another difficulty shows up when the number of polydisperse MBs is small and the use of averaged quantities becomes questionable. Various computational methods have been explored to understand the dynamics between polydisperse and monodisperse MB populations. Among these, the Iterative Nonlinear Contrast Source (INCS) method has demonstrated efficacy in simulating bubble cloud behavior in a three-dimensional domain when excited either by a plane wave or a focused beam. The method enables the generation and comparison of echoes produced by dense monodisperse MB populations, considering multiple scattering [26]. This is crucial for optimizing contrast-enhanced ultrasound (CEUS) applications and reducing the need for excessive experimentation.

The aim of this numerical study is to investigate the efficacy of monodisperse and polydisperse populations when used as contrast agents for deep tissue imaging. More precisely, this article discusses the extension of INCS method to simulate the behaviour of a population of polydisperse scatterers. Furthermore, the effectiveness of the extended INCS method is illustrated through simulating the multiple scattering occurring inside a population of polydisperse MBs, each with individual properties represented by its own Marmottant model [4]. INCS is based on an iterative scheme for computing the scattered acoustic signals [27,28]. Numerically, the accuracy of the final result is improved after each iteration. In a physical sense, each iteration adds an extra order of multiple scattering corresponding to an additional path of wave propagation.

First, in Section 5.2, the fundamental theory behind the INCS method is explained, followed by its extension with the introduction of polydisperse point scatterers. In Section 5.3, the configurations for the numerical experiments are discussed. Next, in Section 5.4 the results from the numerical simulations for each different test case are presented. Concluding remarks are given in Section. 5.5.

5.2 Inclusion of a polydisperse MB population

5.2.1 Linear Field

The linear pressure field generated by an external source in a linear, lossless, homogeneous acoustic background medium is described by the wave equation

$$c_0^{-2}\frac{\partial^2 p(\boldsymbol{x},t)}{\partial t^2} - \nabla^2 p(\boldsymbol{x},t) = S_{\mathrm{pr}}(\boldsymbol{x},t). \tag{5.1}$$

Here, $\boldsymbol{x}$ [m] is the Cartesian position vector, and t [s] is the time. Furthermore, $p(\boldsymbol{x},t)$ [Pa] is the acoustic pressure, $c_0 = 1/\sqrt{\rho_0\kappa_0}$ [m/s] is the small signal sound speed in the background medium, where ρ_0 [kg·m^{-3}] is the mass density and κ_0 [Pa^{-1}] is the compressibility. The symbol ∇^2 indicates the Laplacian operator. The acoustic field is generated by the primary source term S_{pr}

$$S_{\mathrm{pr}}(\boldsymbol{x},t) = \rho_0\frac{\partial q(\boldsymbol{x},t)}{\partial t} - \nabla\cdot\boldsymbol{f}(\boldsymbol{x},t), \tag{5.2}$$

where $q(\boldsymbol{x},t)$ [s^{-1}] is the volume density of volume injection rate and $\boldsymbol{f}(\boldsymbol{x},t)$ [N/m^3] is the volume density volume force of the external source. A source with a plane aperture, e.g. a phased array transducer, can be represented by a pressure jump in the particle velocity or the pressure. This can formally be described by a primary source term with a Dirac delta function, [27] but in our numerical implementation of INCS the source is modeled as a boundary condition at the location of the source aperture.

5.2.2 Nonlinear field due to contrast agents

In medical ultrasound, nonlinearities arising from contrast media can have a significant impact on the propagation of the acoustic signals. To incorporate any phenomena

that affect the pressure field, it is possible to extend Eq. (5.1) with a contrast source term S_{cs}

$$c_0^{-2}\frac{\partial^2 p}{\partial t^2} - \nabla^2 p = S_{\text{pr}} + S_{\text{cs}}(p). \tag{5.3}$$

With this approach, multiple contrast sources can be accommodated that represent global nonlinear effects [27, 28], attenuation [29, 30], inhomogeneous medium properties [31], or local nonlinear effects [32]. In contrast-enhanced imaging, the nonlinear oscillatory behavior of the MBs influences the pressure field. To include the contribution of a population of N MBs, each will be described as a point scatterer and the source term will be written as [26]

$$\begin{aligned} S_{\text{cs}}(\boldsymbol{x}, t) &= \sum_{i=1}^{N} S_{\text{MB}_i} \\ &= \rho_0 \sum_{i=1}^{N} \frac{d^2 V^{(i)}(\boldsymbol{x}_{\text{sc}}^{(i)}, t)}{dt^2}\, \delta(\boldsymbol{x} - \boldsymbol{x}_{\text{sc}}^{(i)}), \end{aligned} \tag{5.4}$$

where $V^{(i)}$ [m^3] is the volume of the ith MB, $\boldsymbol{x}_{\text{sc}}^{(i)}$ is the position vector of its center and $\delta(\boldsymbol{x} - \boldsymbol{x}_{\text{sc}}^{(i)}) = \delta(x - x_{\text{sc}}^{(i)})\,\delta(y - y_{\text{sc}}^{(i)})\,\delta(z - z_{\text{sc}}^{(i)})$ [m^{-3}] is the three-dimensional Dirac delta distribution. Each scatterer's volume depends on the bubble radius R as a function of time, which in our case will be calculated by solving the Marmottant equation [4, 26].

In the case of a population of monodisperse MBs, the equilibrium radius R_0 is the same for all the scatterers, whereas for a polydisperse distribution, each scatterer has its own equilibrium radius $R_0^{(i)}$.

5.3 Configurations used in the simulations

5.3.1 Simulation of pressure fields

Incident field and contrast domain

To study the influence of different populations of MBs on a propagating plane wave, we will consider the computational domain and the domain for the contrast media as depicted in Fig. 5.1(a). This configuration is used in Secs. 5.4.1 and 5.4.2 for the INCS validation and the comparison between different populations, respectively. The computational domain has dimensions $X \times Y \times Z = 20$ mm $\times$ 20 mm $\times$ 30 mm is used. The scatterers are placed in a domain with dimensions $X \times Y \times Z = 15$ mm $\times$ 15 mm $\times$ 4.444 mm, resulting in a 1 ml volume. These configuration choices are made to simplify the comparison between polydisperse and monodisperse populations.

The incident pressure field is a plane wave being generated at $z = 0$ and propagating in the positive z-direction. A plane wave is used to initially excite all the scatterers by an incident wave that everywhere has the same pressure amplitude. The temporal

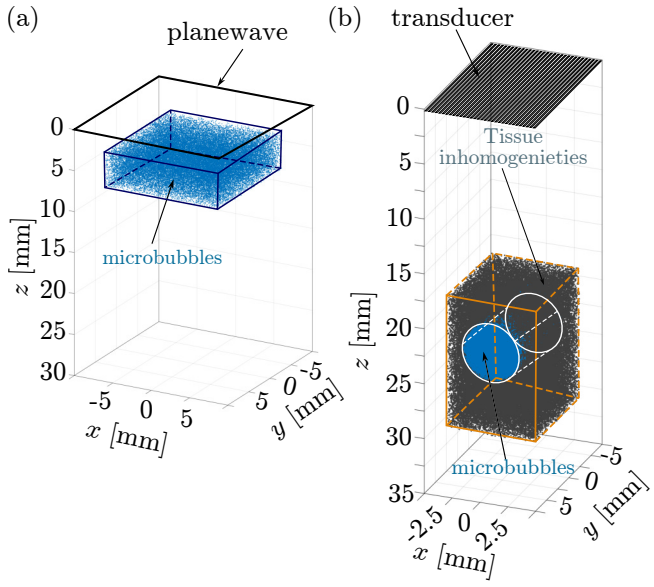

Figure 5.1: Configurations used in the INCS simulations. (a) Computational domain containing a suspension of 3.5 $\times 10^4$ ml^{-1} (blue) monodisperse MB with 3.2 μm equilibrium radius, embedded in water. (b) Computational domain incorporating 7×10^5 ml^{-1} tissue-mimicking linear scatterers (grey) surrounding a suspension of 5×10^5 ml^{-1} monodisperse MBs with 1.4 μm equilibrium radius (blue).

signature of the incident pressure is

$$p(t) = P_0 \exp\left[-\left(\frac{t - T_d}{T_w/2}\right)^2\right] \sin[2\pi f_0 (t - T_d)], \tag{5.5}$$

where $T_w = 3/f_0$ is the width and $T_d = 6/f_0$ is the delay of a Gaussian envelope with a duration of $12/f_0$, where $f_0 = 1$ MHz is the center frequency. Therefore, this is a narrowband pulse. The peak pressure is $P_0 = 200$ kPa. The scatterers will be embedded in water with a density of $\rho_0 = 1060$ kg/m^3 and a speed of sound of $c_0 = 1482$ m/s. In the considered situations, water has negligible losses and nonlinear effects will be hardly noticeable. Therefore, we assume that the embedding medium is lossless and linear. A sampling frequency of 18 MHz was used as the basis for the discretization of the spatiotemporal domain [26].

Configuration for validation

To validate INCS we compare our results by those following from effective medium theory. The analytical expressions that describe the effective behavior of a population of isotropic linear scatterers (LSs) are derived from Foldy [16, 17]. A similar validation has been used in a previous publication for a monodisperse population of scatterers [26], but here we will consider a polydisperse population. For the INCS

implementation, we assume that the contrast source term for each LS is given by

$$S_{\mathrm{sc}}(\boldsymbol{x},t) = -f(R_0)\,V_0\,\frac{\rho_0}{\rho_1 c_1^2}\,\frac{\partial^2 p(\boldsymbol{x}_{\mathrm{sc}},t)}{\partial t^2}\,\delta(\boldsymbol{x}-\boldsymbol{x}_{\mathrm{sc}}), \tag{5.6}$$

where R_0 is equilibrium radius, V_0 is its initial volume, ρ_1 is the density of mass of the gas inside the LS, c_1 is the speed of sound inside the LS and $f(R_0)$ is the polydispersity coefficient given by

$$f(R_0) = \frac{A_0}{(R_0/R_{0,\mathrm{ref}})^{\gamma}}. \tag{5.7}$$

The constant A_0 is used to adjust the scattering strength if necessary and γ is the polydispersity scale parameter to control the scattering distribution of the population.

In the case of a plane wave excitation as in Eq. (5.5), the scattered pressure is given by [26]

$$\begin{aligned} p_{\mathrm{sc}}(\boldsymbol{x},\omega) &= f(R_0)\,V_0\,\frac{\rho_0}{\rho_1 c_1^2}\,\omega^2\,\frac{p(\omega)}{4\pi r}e^{-ikr} \\ &= g(R_0,\omega)\,\frac{p(\omega)e^{-ikr}}{r}, \end{aligned} \tag{5.8}$$

where $k = \omega/c_0$ is the wavenumber, $g(R_0,\omega)$ is the scattering strength of an individual LS, and r is the distance from the scatterer. We follow this approach in order to match the variables as defined previously in Foldy [16].

For the considered linear isotropic scatterers, we chose the scattering strength to be a linear function of the (fictitious) radius of a scatterer, instead of its (fictitious) volume. In this way we avoid the extreme dominance of the larger bubbles in the polydisperse population. This is achieved by setting $\gamma = 2$ in Eq. (5.7). To assure that INCS yields convergent results under the considered circumstances, we assume $A_0 = 0.6$ and $R_{0,ref} = 1\ \mu$m.

For the polydisperse populations considered in this paper, the density of the MBs varies with the equilibrium radius R_0 according to the gamma distribution

$$n(R_0) = \frac{N}{V}\,\frac{1}{b^{\alpha}\Gamma(\alpha)}\,R_0^{\alpha-1}e^{-R_0/b}, \tag{5.9}$$

where N is the total number of scatterers, and V is the volume in which the homogeneous population resides. Furthermore, α and b are the scale and shape parameters, and Γ is the gamma function [33]. In this paper, we choose $\alpha = 2.24$ and $b = 1.23\,\mu$m to mimic the size distribution of Optison [13]. By employing this wide distribution, we can compare the INCS results for a polydisperse population with those obtained from the effective medium theory of isotropic scatterers [16]. Moreover, this distribution has a mean of $\hat{\mu} = \alpha b = 2.76\ \mu$m, which is close to the radius of the bubbles that will resonate at the excitation frequency. In this way, the polydisperse population will contain considerable amounts of bubbles that are below resonance, close to resonance, and above resonance.

In practice, the range of the equilibrium radius in a polydisperse population is limited [11, 13]. In this paper, we consider bubbles with equilibrium radii between

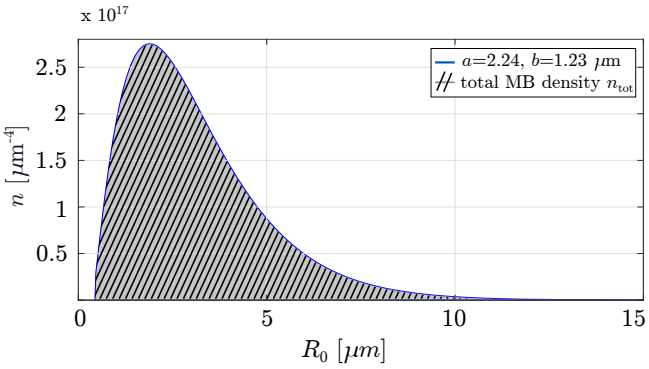

Figure 5.2: Graph depicting the continuous gamma distribution with $\alpha = 2.24$ and $b = 1.23$ μm (blue). For $R_{0,\min} = 0.5$ μm and $R_{0,\max} = 15$ μm, the area below the curve yields a concentration of approximately $n_{\text{tot}} = 10^6$ ml^{-1}.

$R_{0,\min} = 0.5$ μm and $R_{0,\max} = 15$ μm, as depicted in Fig. 5.2. The total density of the MBs considered is

$$n_{\text{tot}} = \int_{R_{0,\min}}^{R_{0,\max}} n(R_0)\, dR_0. \tag{5.10}$$

The discarded MBs account for 4% of the concentration and 0.9% of the gas volume of the untruncated population.

Types of monodisperse and polydisperse suspensions

To make a comparison between the efficiency of a population of monodisperse and polydisperse MBs, we take into account four distinct populations:

1. A monodisperse population of MBs with a equilibrium radius $R_0 = 4$ μm and a resonance frequency $f_{\text{res}} = 0.8$ MHz (below the center excitation frequency);
2. A monodisperse population of MBs with a equilibrium radius $R_0 = 3.2$ μm and a resonance frequency $f_{\text{res}} = 1$ MHz (at the center excitation frequency);
3. A monodisperse population of MBs with a equilibrium radius $R_0 = 1$ μm and a resonance frequency $f_{\text{res}} = 3.9$ MHz (above the center excitation frequency);
4. A polydisperse population of MBs with a equilibrium radius between $R_{0,\min} = 0.5$ μm to $R_{0,\max} = 15$ μm, distributed as described in Section 5.3.1, corresponding to a resonance frequency between $f_{\text{res}} = 0.3$ MHz and 10 MHz (a number of MBs will be near the resonance frequency, others will be above of below resonance)

In our simulations, we use high driving pressures to activate the nonlinear oscillatory behaviour of the MBs and therefore the contribution of the shell stiffness becomes unimportant. As a result, the resonance frequency of the MBs shifts towards the resonance frequency of an uncoated bubble [2], which is different from the

resonance frequency of a linearly oscillating MB with a shell. As explained in detail in [34], we may therefore approximate the resonance frequency by the eigenfrequency

$$f_{\text{res}} = \frac{1}{2\pi R_0}\sqrt{\frac{1}{\rho_0}\left[3\gamma P_{\text{amb}} + (3\gamma - 1)\frac{2\sigma_w}{R_0}\right]}, \tag{5.11}$$

where R_0 is the equilibrium radius of the MB, $\gamma = 1.07$ is the polytropic exponent of the gas encapsulated in the bubble, $P_{\text{amb}} = 101.3$ kPa is the static ambient pressure, and $\sigma_w = 0.072$ N/m is the surface tension of the gas-water interface. The center excitation frequency $f_0 = 1$ MHz corresponds to a resonance frequency of an uncoated MB of equilibrium radius $R_0 = 3.2$ μm.

For solving the Marmottant equation [4], we further use the surrounding liquid dynamic viscosity increased by a factor of 2 to account for thermal damping $\mu = 2 \times 10^{-3}$ Pa $\cdot$ s, the effective surface tension $\sigma(R) = 0.036$ N/m, the shell elasticity

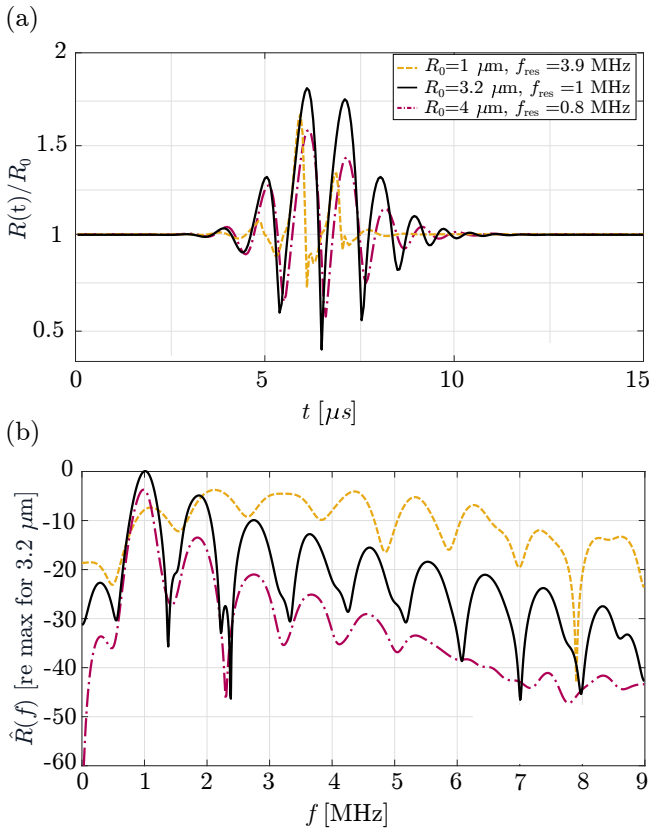

Figure 5.3: (a) Temporal radial responses $R(t)$ of MBs with rest radii of 1 μm (dashed orange), 3.2 μm (black continuous), and 4 μm (dotted purple), when excited by a 3 cycle pulse with 200 kPa peak pressure and 1 MHz center frequency. (b) The frequency spectra $\hat{R}(f)$ corresponding to the signals in (a).

$\chi = 0.4$ N/m [13, 14]. The surface dilatational viscosity of the shell is given by $\kappa_s = 1.5 \times 10^{-9} \exp(8 \times 10^5 R_0)$ kg/s, which is an approximation to the data in Fig. 6(B) in [35]. Combined with the aforementioned, the oscillatory behavior and the frequency spectrum of a single MB when excited with a driving pressure $P_0 = 200$ kPa and a center frequency $f_0 = 1$ MHz is depicted in Fig. 5.3.

5.3.2 Simulation of CEUS imaging

To actually see the difference between monodisperse and polydisperse populations for contrast-enhanced imaging, it is necessary to visualize the reconstructed beamformed images from the scattered radio frequency (RF) data generated by a realistic configuration. To mimic tissue with an enclosed vessel, we distribute LSs surrounding a cylindrical population of MB, as depicted in Fig. 5.1(b). We need to take into account all the relevant phenomena that occur during the propagation of ultrasound through the populations of scatterers inside the water background medium. Based on this, the new nonlinear wave equation is given by

$$c_0^{-2}\partial_t^2 p - \nabla^2 p = S_{\text{pr}} + S_{\text{MBs}}(p) + S_{\text{LSs}}(p) + S_{\text{nl}}(p) + S_{\mathcal{L}}(p), \tag{5.12}$$

where S_{MBs} is the contrast source term for the MB population [26], S_{LSs} is the contrast source term for the LS population [26], S_{nl} and $S_{\mathcal{L}}$ are the terms for global [26] and local medium nonlinearities [32], respectively. The description of each source term is given in Appendix 5.A. Equation (5.12) is solved iteratively using a Neumann scheme, as described in previous publications [26, 36].

The incident pressure field is computed for a P4-1 probe (Verasonics, Washington, USA). Transducer elements have a height of $H_{\text{el}} = 16$ mm, a width of $W_{\text{el}} = 0.245$ mm, a pitch of $D_{\text{tr}} = 0.295$ mm. The emitted pressure field is approximately a plane wave with a time signature as given by Eq. (5.5). The center frequency is $f_0 = 2.5$ MHz and the peak pressure at the transducer surface is $P_0 = 200$ kPa, to activate the nonlinear behavior of the monodisperse MBs. Next, the domain of the MB population is a cylinder with center $(x,\ y,\ z) = (0,\ 0,\ 22.5)$ mm, diameter of 5 mm and length of 10 mm, as illustrated in Fig. 5.1(b). This corresponds to a total volume of 0.2 ml. The domain of LSs surrounding the MBs is a cube of $X \times Y \times Z = 8$ mm $\times$ 10 mm $\times$ 12 mm, corresponding to a volume of 0.76 ml centered at $(x,\ y,\ z) = (0,\ 0,\ 24)$ mm, as depicted in Fig. 5.1(b). Furthermore, the background medium is water with a coefficient of nonlinearity of $\beta = 3.21$ (see Eq. 5.18)).

To accurately solve the full nonlinear wave equation up to the second harmonic frequency ($h = 2$) of the incident pressure pulse, we need to have a Nyquist frequency of at least $F_{\text{nyq}} = (h + 1.5)f_0 = 3.5 f_0$. To also safely capture the higher harmonics of the MB scattering, we used $F_{\text{nyq}} = 5 f_0 = 12.5$ MHz. Thus, the sampling frequency, used for discretizing the spatiotemporal domain, is $F_{\text{s}} = 2F_{\text{nyq}} = 25$ MHz. Furthermore, we need at least $j = h + 1 = 3$ iterations for an accurate prediction of the second harmonic [28]. We take $j = 10$ iterations to ensure that the relative root mean square error between successive iterations is below 10^{-6}. This also implies that our simulations account for MB interactions up to ninth order multiple scattering [26].

We compare CEUS imaging with two different MB populations:

5. A resonant monodisperse population of MBs with a equilibrium radius $R_0 = 1.4$ μm and a resonance frequency $f_{\text{res}} = 2.5$ MHz (at the center excitation frequency);

6. A polydisperse population of MBs with a equilibrium radius between $R_0 = 0.5$ μm and 15 μm, distributed as described in Section 5.3.1, and a resonance frequency between $f_{\text{res}} = 0.3$ MHz and 10 MHz.

Each LS has a scattering strength which can be computed through Eq. (5.17), for a polydispersity coefficient $f = 1$.

For the beamforming process, we use the MUST [37] toolbox after employing the amplitude modulation (AM) technique and a virtual point source formulation as described by Garcia et. al. [38].

5.4 Numerical results

5.4.1 Comparison of INCS and effective medium theory

In this section, we assume that there are $N = 10^6$ MBs located in the $V = 1$ ml volume indicated in Fig. 5.1(a). The suspension has a type 4 polydisperse distribution, as described in Section 5.3.1. The total gas volume corresponds to 2.38×10^{-4} ml. It is assumed that the gas inside the bubbles is C_4F_{10}, with a density $\rho_1 = 10$ kg/m^3 and a speed of sound $c_1 = 100$ m/s. As we want to perform a simplified comparison with effective medium theory, we do not take into account the resonance frequency and the nonlinear behavior of the MBs. Instead, we assume that each bubble can be described by its scattering behavior as describe in Eqs. (5.17) to (5.8). In other words, we are only interested on the scattered signal of each point scatterer. The maximum of the incident pressure $P_0 = 200$ kPa will not affect the final result because we operate in the linear regime.

According to Foldy's theory [16, 17], the effect of a polydisperse population of scatterers is represented by replacing the wave number k_0 in the scattering domain by a corrected wave number k according to

$$k^2 = k_0^2 + 4\pi \int_{R_{0,\min}}^{R_{0,\max}} g(R_0, \omega)\, n(R_0)\, dR_0, \tag{5.13}$$

where $g(R_0, \omega)$ [m] is derived from Eq. (5.8), and $n(R_0)$ is computed through Eq. (5.9). The shift in wavenumber corresponds to a shift in wave speed, and as a consequence, in a time shift of the wave that has traversed the scattering domain. In the case considered in this subsection, the integral amounts to 2.3×10^5 m^{-2}. This yields a wavespeed of 1375.5 m/s in the scattering domain, while the speed in the medium without scatterers is 1482 m/s. Since the scattering domain has a length of 4.4444 mm, the additional time delay caused by the scattering domain, as predicted by the theory of Foldy, is $\Delta t_{\text{Foldy}} = 0.228$ μs. We have also determined the time delay between the incident wave $p^{(0)}$ and the wave with all significant orders of scattering $p^{(8)}$ from

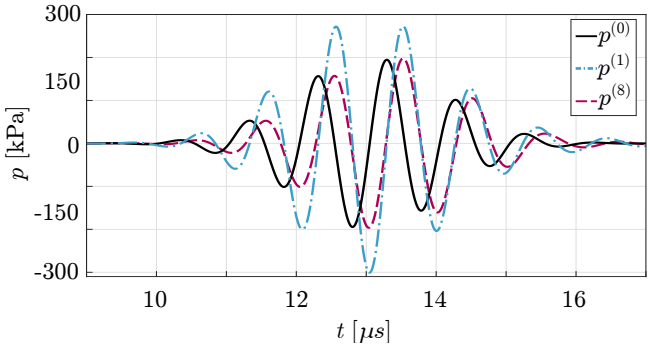

Figure 5.4: Comparison between the time signatures of the incident pressure pulse ($p^{(0)}$, black continuous line), and the total pressure pulse after $j = 1$ ($p^{(1)}$, blue dotted line) and $j = 8$ ($p^{(8)}$, magenta dashed line) iterations that is received by a point receiver located on the z axis at $z = 10.3$ mm.

Fig. 5.4, by looking at the shift in the zero crossings around 13 μs. This is found to be $\Delta t_{\text{INCS}} = 0.232$ μs. Thus, the difference in time delay as predicted by the theory of Foldy and our method is only 1.75%.

Furthermore, since the wavenumber derived from Eq. (5.13) lacks an imaginary component in our specific case, according to Foldy's theory [16,17], the wave traversing the scattering domain is not subject to attenuation. As illustrated in Fig. 5.4, in our approach the later iterations correct the larger amplitudes observed in earlier iterations, and iteration $p^{(8)}$ has the same amplitude as the incident field $p^{(0)}$. This consistency in both time delay and wave amplitude across a scattering domain indicates a good quantitative agreement between our method and Foldy's effective medium theory in case of a polydisperse distribution of scatterers.

5

5.4.2 Plane wave: monodisperse vs polydisperse populations

We continue with a comparison between four different populations of MBs, as mentioned in Sec. 5.3.1. To start, our reference is the type 2 monodisperse resonant population, for which we use 35,000 MBs, resulting on a total gas volume of 4.8×10^{-6} ml. To achieve a fair comparison, the total gas volume concentration of the MB suspension should be the same in all the cases [26]. Therefore, the type 1 monodisperse population will contain 17,920 MBs, the type 3 monodisperse population will consist of about 10^6 MBs (1146880) and the type 4 polydisperse population will count 20,000 MBs. The bubble populations are placed in the volume $V = 1$ ml as indicated in Fig. 5.1(a).

Scattered pressure field: Full spectrum

The scattered pressure field in each case is depicted in Fig. 5.5. At first sight, the scattered pressure generated from the resonant MBs (type 2, $R_0 = 3.2$ μm) is the strongest between all the cases with a peak pressure of +1.1 dB relative to the peak

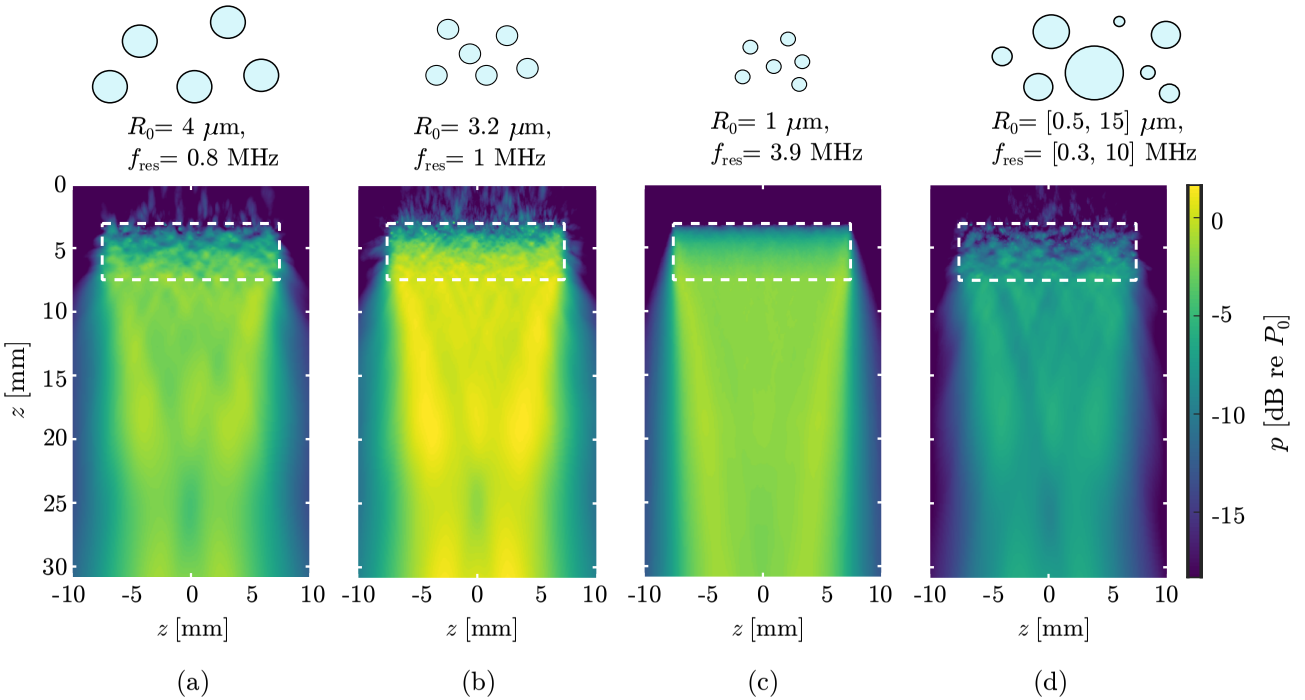

Figure 5.5: Peak of the total scattered pressure at $y = 0$ mm for (a) a type 1 monodisperse distribution of MBs, (b) a type 2 monodisperse distribution of MBs, (c) a type 3 monodisperse distribution of MBs, and (d) a type 4 polydisperse distribution of MBs. In all four cases, the population is located inside the dashed white rectangle.

incident pressure P_0. Next, the case below resonance (type 1, $R_0 = 4$ μm) follows with a relative peak amplitude of -1.13 dB. Although these MBs have a pressure dependent resonance frequency that is still close to the excitation frequency, their peak amplitude is significantly smaller than the resonant MBs. The third case with a relative peak amplitude of -1.45 dB is the one above resonance (type 3, $R_0 = 1$ μm) and the last one is the polydisperse distribution (type 4) with a peak pressure of -5.47 dB. These results demonstrate that when the pressure dependent resonance frequency is closer to the excitation frequency then the scattered pressure field is stronger, with the scattering of the resonant contrast agents being the highest. Another observation is that the beam profile is smoother if the bubbles are smaller. This is because more MBs are necessary to achieve the same gas volume concentration, and the higher the number of scatterers gives a smoother beam profile of the scattered field. Finally, as the incident wave propagates through every MB population, it undergoes attenuation and speed of sound variations, which are interrelated to a pressure dependent shift of the resonance frequency of the MBs [7].

Scattered pressure field: Harmonics

In this section we look at the different harmonics of the excitation pulse that are present in the scattered pressure field. These are obtained by decomposing the scattered signal into specific frequency bands using an 4th order Butterworth filter. These frequency bands are (i) the fundamental F0 $[0.7, 1.3]$ MHz, (ii) the second harmonic 2H $[1.7, 2.3]$ MHz and (iii) the third harmonic 3H $[2.7, 3.3]$ MHz, where the intervals define the cutoff frequencies of the applied filter.

Figure 5.6 shows the harmonic contributions of the scattered pressure field for each of the considered populations. In the fundamental (F0) frequency band (top row of Fig. 5.6), we observe that the strongest scattered field is generated by the type 2 resonant MB suspension with a peak amplitude of -1.23 dB. The type 1 population with the below-resonance oscillating MBs has the second highest peak pressure of -2.61 dB as the resonance frequency is closer to the excitation frequency, in comparison to the other two remaining cases. A significant observation is that the scattered field from the type 4 polydisperse population has a peak amplitude of -7.1 dB and is stronger than the case of type 3 above-resonance MBs, which have a peak pressure of -8.74 dB. This can be explained due to the presence of MBs with a resonance frequency around 1 MHz in the polydisperse suspension.

In the second harmonic (2H) frequency band (middle row of Fig. 5.6), we observe that the scattered field of the type 2 resonant MBs is still the highest of all the four distinct cases. The peak amplitude in this case is -10.3 dB. The peak pressure of the type 3 above-resonance oscillating MBs is -12.09 dB, which is larger than the respective value of -15.82 dB of the type 1 population with the below-resonance oscillating MBs. This is explained due to the fact that the resonance frequency of the system of the former is closer to the 2H frequency band around 2 MHz. The type 4 polydisperse distribution shows the weakest peak pressure amplitude of -18.89 dB. Compared to the monodisperse populations, hardly any constructive interferences are observed below the polydisperse suspension, due to the varying phases of the oscillations that result from the different sizes of the contrast bubbles.

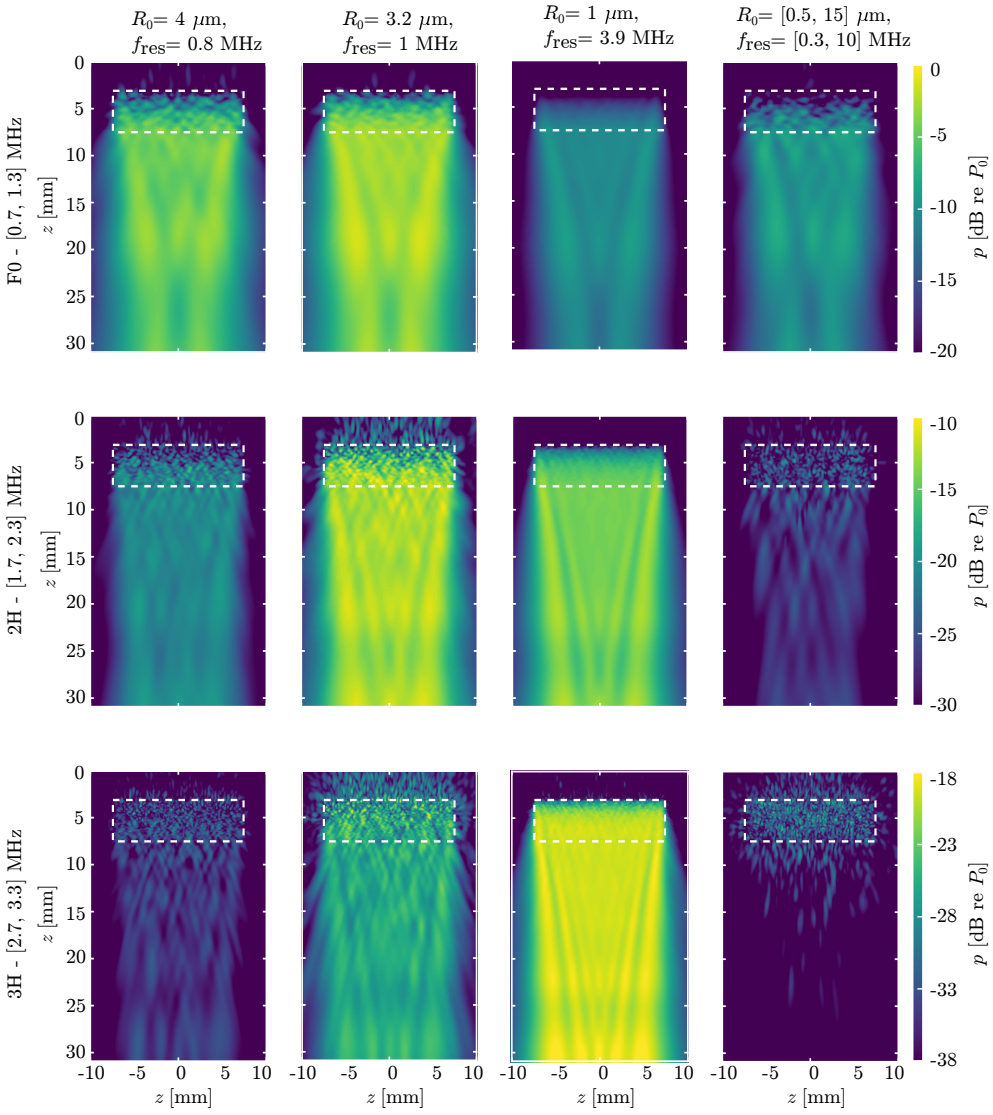

Figure 5.6: Peak of the scattered pressure at $y = 0$ mm for: (first column) a type 1 monodisperse distribution of MBs, (second column) a type 2 monodisperse distribution of MBs, (third column) a type 3 monodisperse distribution of MBs, and (fourth column) a type 4 polydisperse distribution of MB. Each row corresponds to a specific frequency band: (first row) fundamental F0 [0.7, 1.3] MHz, (second row) second harmonic 2H [1.7, 2.3] MHz, and (third row) third harmonic 3H [2.7, 3.3] MHz. In all four cases, the population is located inside the dashed white rectangle.

Finally for the third harmonic (3H) frequency band (bottom row of Fig. 5.6), the type 3 below resonance MBs exhibit the strongest scattered pressure field with a peak amplitude of −17.49 dB, as their resonance frequency of 3.9 MHz is closer to the 3H frequency band. Still, the type 2 resonant MBs scatter the second highest pressure field with a peak amplitude of −18.49 dB. Inside the MB suspension, the type 4 polydisperse MBs give a peak pressure of −22.66 dB. This is stronger than the peak of the pressure field of the type 1 below-resonance oscillating MBs (−25.91 dB), because the smaller MBs with a resonance frequency close to 3 MHz add to the strong scattering of the larger MBs. Similar to 2H, the type 4 polydisperse MBs hardly yield constructive interference below the suspension, as is the case for the type 1, 2 and 3 monodisperse MBs. This observation predicts that the uniformity of the size distribution of a population might have an impact on the nonlinear imaging artifacts downstream the population. The cumulative scattered pressure field is the addition of the signals emitted from all the MBs in the population taken into account their individual position and therefore all the phase delays. A simplified expression is to linearly project the behavior of a single MB to the behavior of a whole population of MBs. Thus, the simulated pressure fields of the populations show similar behavior with the projected response of the single MB in Fig. 5.3.

Total pressure field: Attenuation and speed of sound variations

To show the influence of the nonlinear MB behavior on a propagating pressure wave, in Fig. 5.7 we show the temporal signatures and the respective frequency spectra after traversing each type of MB population. From Fig. 5.7(a) it is clear that the type 2 monodisperse resonant population (black line) causes the most nonlinear distortion. The distortion takes place mainly after the second cycle as the MBs need to get a large oscillation amplitude before they demonstrate significant nonlinear behavior. The influence of the nonlinear bubble oscillation on the propagation through each one of the other three populations is much less visible in the time domain. By observing the frequency spectra in Fig. 5.7(b), we can better see the effect of the nonlinear bubble behavior. Similar as in Sec. 5.4.2, the type 2 population of monodisperse oscillating MBs, shows a shift of energy from the fundamental to the second and higher harmonics. Furthermore, the maximum spectral amplitude of the fundamental is about equal for the other types of populations. The type 3 population of monodisperse below resonance MBs shows a strong second harmonic, and the highest third harmonic of all the populations, even higher than for the type 2 population.

To quantify attenuation and speed of sound changes in the fundamental frequency band, we have subjected the temporal signatures in Fig. 5.7(a) to a Butterworth filter of 8th order and a frequency pass band of $[0.75, 1.25]$ MHz. The results are plotted in Fig. 5.8. For the type 1 population of bubbles that are below resonance, there is a decrease in peak pressure of 92.2 kPa relative to the incident field, and the speed of sound has been increased to 1517 m/s. For the type 2 population with resonant bubbles, the peak pressure undergoes a drop of 126.9 kPa, and the speed of sound has been maintained at 1482 m/s. For the type 3 population of bubbles that are above resonance, the peak pressure experiences a drop of 19.9 kPa, and the speed of sound has decreased to 1458 m/s. Finally, for the type 4 polydisperse population,

the decay in peak pressure is 44.8 kPa, and the speed of sound has been increased to 1497 m/s. We observe that the differences for the type 3 MBs are the smallest from all the populations, because they present the strongest effect mainly on the second harmonic. As in previous studies [7], the INCS simulations demonstrate that for MBs with a resonance frequency below the excitation frequency there is an increase of the wave speed, whereas for a resonance higher than the excitation frequency there is a decrease of the wave speed. Finally, for the MBs with a resonance frequency equal to the excitation frequency, the wave speed is equal to the speed of sound of the background medium.

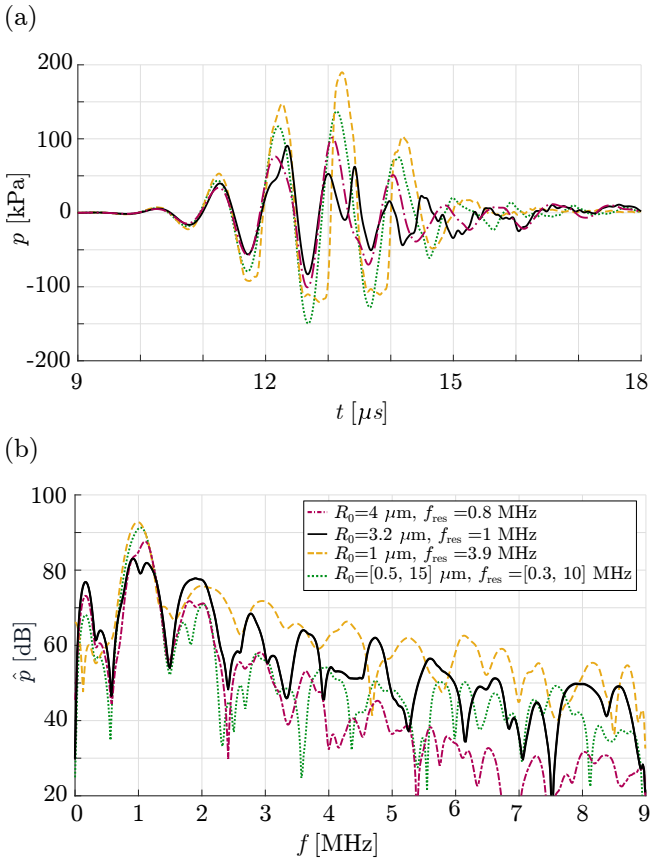

Figure 5.7: (a) Temporal signature and (b) frequency spectrum of the total pressure field, after propagation through each of the four distinct MB populations. The pressure is obtained for a point receiver located on the z-axis at a depth of $z = 10.3$ mm.

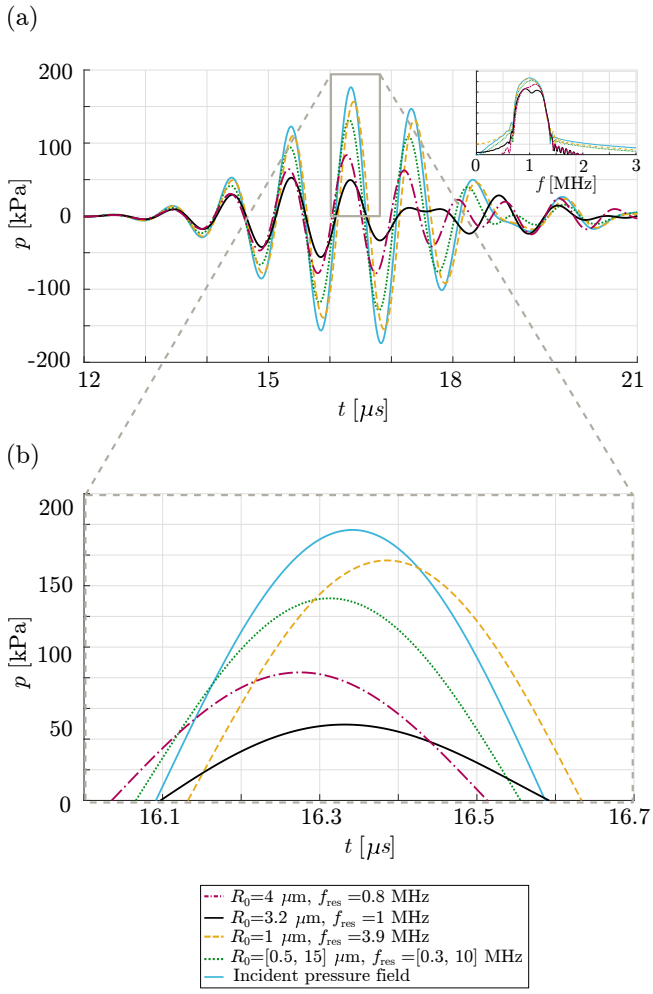

Figure 5.8: (a) Temporal signature of the total pressure field in the fundamental frequency band, after propagation through each of the four distinct MB populations. (b) Zoomed-in version of (a) to demonstrate the attenuation and speed of sound changes of the transmitted wave. The pressure is obtained for a point receiver located on the z-axis at a depth of $z = 10.3$ mm.

Total pressure field: Convergence behavior

To quantify the numerical performance of our scheme, we analyzed the difference between the successive iterations using the Relative Root Mean Square Error (RRMSE)

$$\mathrm{RRMSE} = \sqrt{\frac{\int_{\mathcal{X}_{\mathrm{cd}}} \int_{\mathcal{T}_{\mathrm{cd}}} \left[p^{(j)}(\boldsymbol{x},t) - p^{(j-1)}(\boldsymbol{x},t)\right]^2 dt\, d\boldsymbol{x}}{\int_{\mathcal{X}_{\mathrm{cd}}} \int_{\mathcal{T}_{\mathrm{cd}}} \left[p^{(0)}(\boldsymbol{x},t)\right]^2 dt\, d\boldsymbol{x}}}, \tag{5.14}$$

where $\mathcal{X}_{\mathrm{cd}}$ is the spatial computational domain, $\mathcal{T}_{\mathrm{cd}}$ is the temporal computational domain, j is the iteration number and $p^{(j)}$ is the total pressure obtained in the jth iteration. The decay of the RRMSE is illustrated in Fig. 5.9 as a function of the number of iterations. A first observation is that after a certain number of successive iterations, the error tends to stabilize at a level of 10^{-5} or below. At this juncture, it can be inferred that incorporating additional multiple scattering orders will not yield further enhancements to the solution, indicating the attainment of insignificant scattering orders. Upon reaching this stage, it is assumed that the iterative process has converged to the lowest achievable error.

For the type 2 monodisperse resonant MBs, it turns out that the initial iterations even show an RRMSE above 1. This indicates that the first multiple scattering orders are highly significant. Moreover, for these MBs more iterations are needed to reach convergence, and therefore more multiple-scattering orders should be included to achieve an accurate result. A general observation is that the closer the resonance frequency of the population is to the excitation frequency, the more iterations need to be taken into account. This can be explained by the fact that stronger close-range interactions occur in populations with resonant MBs due to the stronger scattering strength, making higher scattering orders more important. By observing the case of type 3 above-resonance monodisperse MBs, the RRMSE of the initial iterations is also above 1. This is due to the larger number of scatterers that are used to achieve the same gas volume concentration. This corresponds to higher number of bubble-bubble

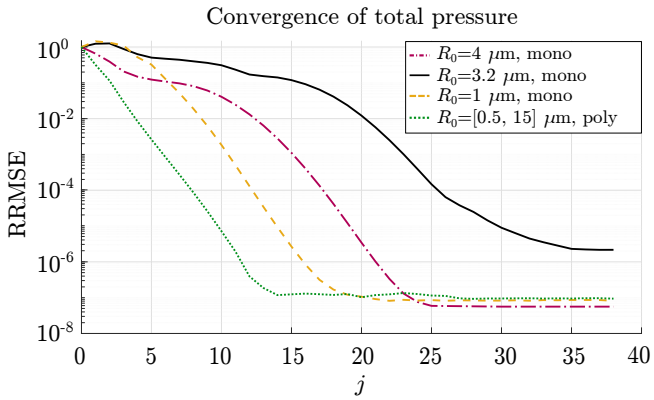

Figure 5.9: RRMSE as a function of the number of iterations j, for the considered types of MB populations.

interactions at short distances. Finally, the type 4 polydisperse MBs yield a faster convergence (in the 13th iteration) than every other type of monodisperse suspension, demonstrating the relative significance of multiple scattering for the monodisperse populations.

5.4.3 CEUS imaging

Scattered pressure fields

In this section we compare the nonlinear scattering coming from suspensions of type 5 resonant monodisperse MBs and type 6 polydisperse MBs when these are surrounded by linear scatterers, as illustrated in Fig. 5.1(b). To resemble an in vivo setting and match the gas volume concentration, for the type 5 suspension, we use a concentration of 5×10^5 ml^{-1} MBs with 1.4 μm equilibrium radius, corresponding to a total gas volume of 5.8×10^{-6} ml. Furthermore, for the type 6, we use 3.1×10^4 ml^{-1} MBs, corresponding to the same total gas volume. First, the total pressure fields in these configurations are computed for three different excitations: field p_1 is due to a double amplitude excitation (full aperture), and the fields p_2 and p_3 result from two single amplitude excitations (odd elements and even elements), respectively. After employing the AM procedure, the peak residual AM pressures are as shown in Fig. 5.10. For the monodisperse case in Fig. 5.10(a), nonlinear effects accumulate in the suspension and propagate in the area below the population. The peak AM residual pressure is -3.7 dB relative to the pressure at the source surface P_0. On the other hand, for the polydisperse case in Fig. 5.10(b), the residual pressure field shows a relative peak amplitude of -19.9 dB, which is 6.5 times smaller than the respective of the monodisperse suspension. Most MBs in the polydisperse suspension are less efficient scatterers than the MBs in the resonant monodisperse population. More importantly, bubbles with different sizes will cause nonlinear scattering with different phases, which makes that the nonlinearities due to scattering do not propagate outside the MB domain. These results indicate that in CEUS the nonlinear wave propagation artifacts will be stronger for a resonant monodisperse population than a polydisperse population.

To demonstrate what this means for the AM imaging process, in Fig. 5.11 we compare the time signatures of the double amplitude pulse p_1, the sum $p_2 + p_3$ of the two single amplitude pulses, and the AM residual $p_1 - (p_2 + p_3)$, for both the type 5 monodisperse and the type 6 polydisperse case. We depict the temporal signatures for the center of the aperture of the linear array. In Fig. 5.11(a), the AM residual of the monodisperse population is a strong signal with a peak pressure of 1.5 kPa, compared to 2.11 kPa for the incident double excitation field. The sum of the two single amplitude signals matches the waveform of the double amplitude signal only for smaller time instants, which corresponds to the scattering of the LSs that are present above the MB suspension. The AM residual signal is stronger for larger time instants, which indicates the propagation of the nonlinear scattering of the MBs to the LSs that are located below the MB suspension.

In contrast, Fig. 5.11(b) shows that for the polydisperse case, the peak pressure of the AM residual corresponds to 0.35 kPa, which is 4.3 times smaller than the respective value of the type 5 monodisperse population. Moreover, the sum of the

single amplitude signals overlaps with the double amplitude signal, both for smaller time instants (scattering from the LSs above the MB suspension) and for larger time instants (scattering from the LSs below the MB suspension). This indicates that the nonlinear scattering that propagates below the polydisperse MB suspension is relatively small.

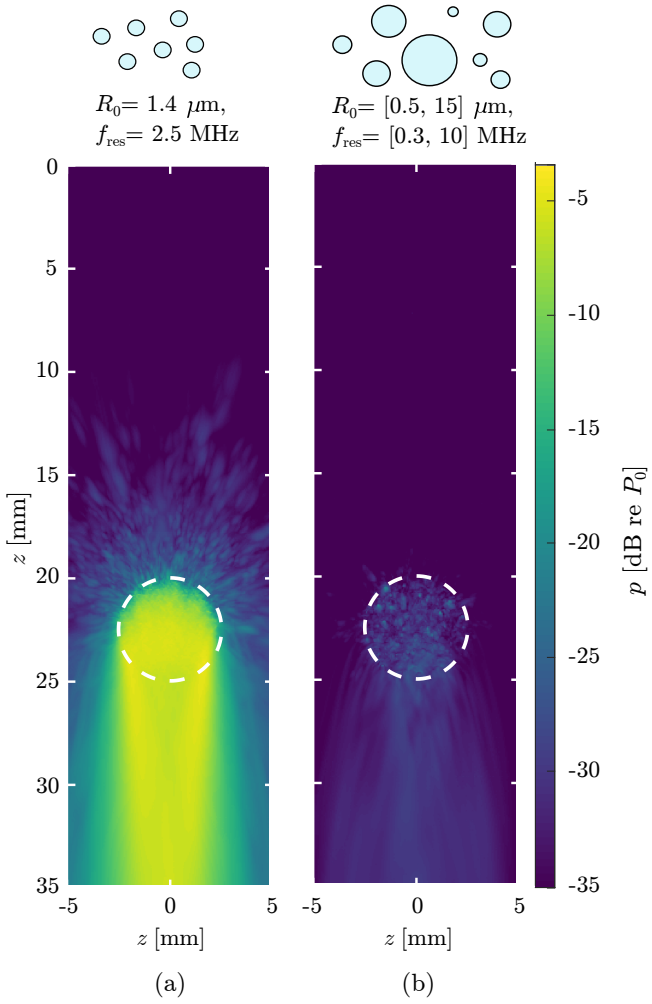

Figure 5.10: Residual acoustic pressure fields after the AM operation in the presence of (a) a type 5 resonant monodisperse population and (b) a type 6 polydisperse population. The MBs are located inside the dashed white circle.

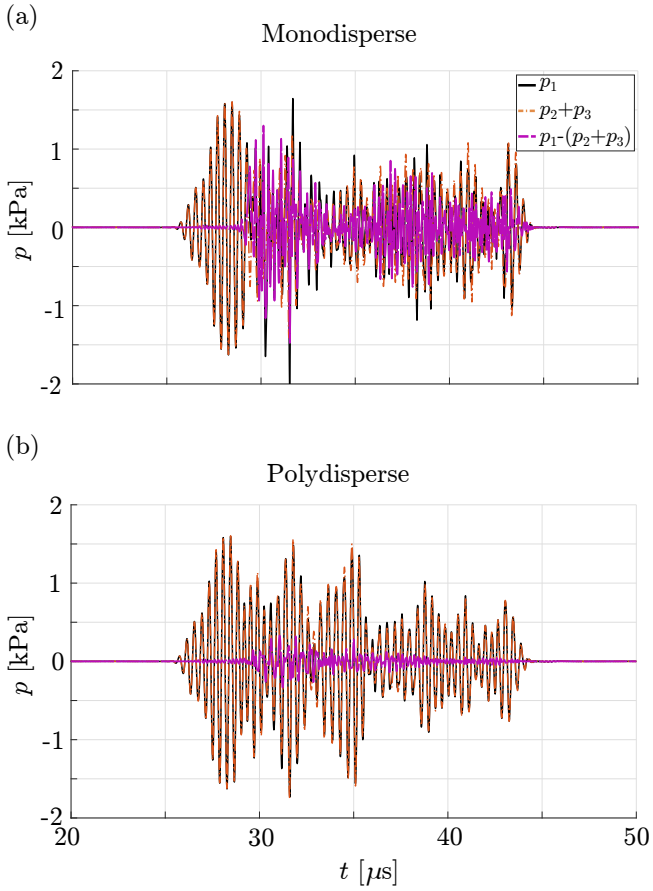

Figure 5.11: Temporal signatures used in the AM procedure for (a) a type 5 monodisperse resonant population and (b) a type 6 polydisperse population, both surrounded by tissue-mimicking LSs and measured at the center of the aperture of the linear array. Each of these graphs encompasses three plots, representing the double amplitude signal p_1, the sum of the two respective single amplitude signals $p_2 + p_3$, and the AM residual signal $p_1 - (p_2 + p_3)$.

Effect of size distribution on imaging artifacts

To assess the imaging effects of the nonlinear fields below each MB population, it is necessary to generate the reconstructed B-mode (single-shot) images and the images that are obtained after employing the AM procedure. The results are depicted in Fig. 5.12. To achieve this, we placed 7×10^5 ml^{-1} tissue-mimicking linear scatterers (grey) surrounding the MB suspension.

Figures 5.12(a) and (b) depict the B-mode images for the configuration with a resonant monodisperse MB population and a polydisperse population, respectively. In both cases the backscattering from tissue-mimicking LSs and the MBs is indistinguishable because the areas with LSs and MBs have a similar echogenicity, independent

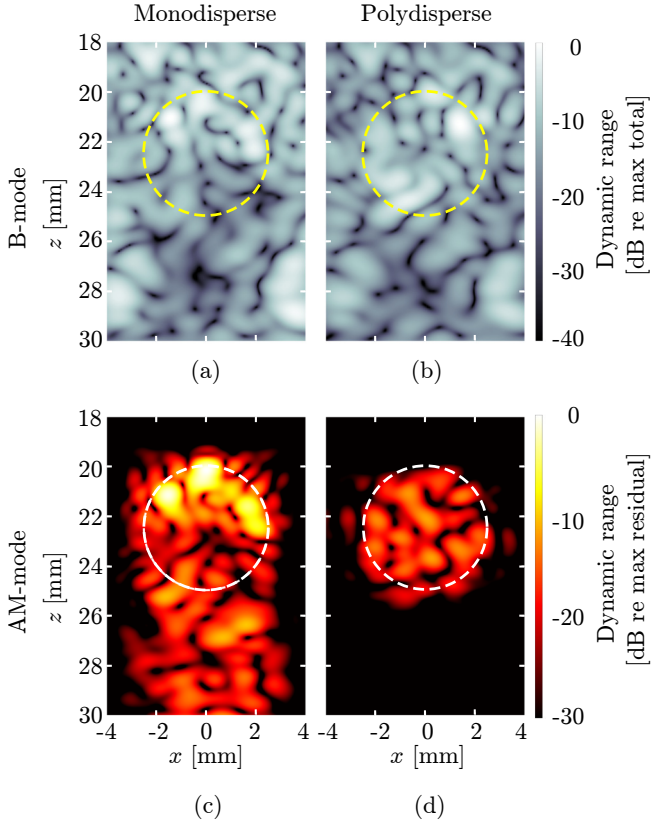

Figure 5.12: B-mode and AM-mode images of the population of monodisperse MBs and its surrounding region. B-mode (single-shot) ultrasound images acquired for a region with (a) type 5 monodisperse resonant population and (b) type 6 polydisperse MB population. AM ultrasound images acquired for the same regions of (c) monodisperse and (d) polydisperse MB populations. The position of the MB populations is outlined by a dashed circle. The rest of the simulation domain is filled with tissue-mimicking LSs.

of the size distribution. This demonstrates that B-mode imaging does not allow to disentangle nonlinear MB scattering from tissue mimicking scattering.

Figures 5.12(c) and (d), show the AM images for the configuration with a resonant monodisperse MB population and a polydisperse population, respectively. Employing the AM sequence for imaging a monodisperse MB population generates an image with significant nonlinear artifacts below of the MB area, meaning that tissue scatterers get misclassified as MBs. On the contrary, applying the AM sequence for imaging the polydisperse population delivers an image with much higher specificity. The peak amplitude in the image of the monodisperse area (0 dB) is stronger than in the image of the polydisperse area (−11.8 dB). The peak value of the nonlinear artifact level is −10.04 dB for the monodisperse population and −29.4 dB for the polydisperse population. This is an indication that monodisperse MBs are more efficient scatterers than polydisperse populations, especially in applications that require to enhance deep tissue imaging. A drawback of CEUS with monodisperse MBs is that the generated artifacts due to propagation of nonlinear scattering in the area below the MBs, is of comparable magnitude and can lead to missclassification of tissue as contrast agents.

5.5 Conclusions

We simulated AM ultrasound imaging of both monodisperse and polydisperse MBs using the INCS method, taking into account all the relevant physical phenomena occurring during ultrasound propagation through a MB population. We highlighted the significance of multiple scattering in monodisperse populations. Resonant monodisperse MBs are shown to be the most efficient scatterers, which corresponds to high sensitivity for CEUS. This property is crucial for optimizing contrast enhancement, guaranteeing consistent behavior and reliable imaging outcomes, especially compared to using polydisperse contrast agents. The drawback of resonant monodisperse MBs is the generation of imaging artifacts, which reduce the specificity of CEUS. This research approach is useful for optimizing CEUS imaging by designing the size distribution and parameters of a MB population through simulations.

Appendix 5.A Description of the source terms in Eq. (5.12)

Primary source that generates the incident field

$$S_{\mathrm{pr}}(\boldsymbol{x},t) = \rho_0 \frac{\partial q(\boldsymbol{x},t)}{\partial t} - \nabla \cdot \boldsymbol{f}(\boldsymbol{x},t), \tag{5.15}$$

Contrast source representing the scattering of a population of nonlinear MBs

$$S_{\mathrm{MBs}}(\boldsymbol{x},t) = \rho_0 \sum_{i=1}^{N} \frac{d^2 V^{(i)}(\boldsymbol{x}_{\mathrm{sc}}^{(i)},t)}{dt^2}\, \delta(\boldsymbol{x} - \boldsymbol{x}_{\mathrm{sc}}^{(i)}), \tag{5.16}$$

Contrast source representing the scattering of a population of linear scatterers

$$S_{\mathrm{LSs}}(\boldsymbol{x},t) = -\frac{\rho_0}{\rho_1 c_1^2}\sum_{m=1}^{M} V_0^{(m)}\,\frac{\partial^2 p(\boldsymbol{x}_{\mathrm{sc}}^{(m)},t)}{\partial t^2}\,\delta(\boldsymbol{x}-\boldsymbol{x}_{\mathrm{sc}}^{(m)}), \tag{5.17}$$

Contrast source representing the nonlinear global effects of the embedding medium

$$S_{\mathrm{nl}}(\boldsymbol{x},t) = \frac{\beta}{\rho_0 c_0^4}\frac{\partial^2 p(\boldsymbol{x},t)^2}{\partial t^2}, \tag{5.18}$$

Contrast source representing the local nonlinear effects of the embedding medium

$$S_{\mathcal{L}}(\boldsymbol{x},t) = (\nabla^2 + c_0^{-2}\partial_t^2)\mathcal{L}(\boldsymbol{x},t), \tag{5.19}$$

in which

$$\mathcal{L}(\boldsymbol{x},t) = \tfrac{1}{2}\rho_0 v^2(\boldsymbol{x},t) - \tfrac{1}{2}\kappa_0 p^2(\boldsymbol{x},t), \tag{5.20}$$

is the so-called Lagrangian density, with $p(\boldsymbol{x},t)$ indicating the acoustic pressure and $v(\boldsymbol{x},t)$ indicating the particle velocity.

Bibliography

[1] M. Averkiou, M. Bruce, J. Powers, P. Sheeran,and P. Burns, "Imaging methods for ultrasound contrast agents", Ultr. Med. Biol. **46 (3)**, 498–517, (2020).

[2] M. Versluis, E. Stride, G. Lajoinie, B. Dollet, and T. Segers, "Ultrasound Contrast Agent Modeling: A review", Ultrasound in Med. & Biol. **46**, 2117–2144, (2020).

[3] N. de Jong, A. Bouakaz, and P. Frinking, "Basic Acoustic Properties of Microbubbles", Echocardiography **19**, 229–240, (2002).

[4] P. Marmottant, S. van der Meer, M. Emmer ,M. Versluis, N. de Jong, S. Hilgenfeldt, and D. Lohse, "A model for large amplitude oscillations of coated bubbles accounting for buckling and rupture", J. Acoust. Soc. Am. **118**,3499–3506, (2005).

[5] M. Emmer, H.J. Vos, D.E. Goertz, A. van Wamel, M. Versluis, and N. de Jong, "Pressure-Dependent Attenuationand Scattering of Phospholipid-Coated Microbubbles at Low Acoustic Pressures", Ultr. Med. Biol. **35 (1)**, 102–111, (2009).

[6] A. Sojahrood, O. Falou, R. Earl, R. Karshafian, & M. Kolios, "Influence of the pressure-dependent resonance frequency on the bifurcation structure and backscattered pressure of ultrasound contrast agents: a numerical investigation", Nonlinear Dynamics **80**, 889-904, (2015).

[7] A. J. Sojahrood, Q. Li, H. Haghi, R. Karshafian, T.M. Porter, and M.C.Kolios, "Probing the pressure dependence of sound speed and attenuation in bubbly media: Experimental observations, a theoretical model and numerical calculations", Ultrason. Sonoch. **95 (106319)**, (2023).

[8] C. Errico, J. Pierre, S. Pezet, Y. Desailly, Z. Lenkei, O. Couture, & M. Tanter, "Ultrafast ultrasound localization microscopy for deep super-resolution vascular imaging", Nat. **527**, 499-502, (2015).

[9] M. Tang, and R. Eckersley, "Nonlinear propagation of ultrasound through microbubble contrast agents and implications for imaging", IEEE Trans. Ultrason., Ferroelectr. Freq. Control **53 (12)**, 2406–2415, (2006).

[10] J.R.Lindner, "Microbubbles in medical imaging: current applications and future directions", Nat. Rev. Drug Discov. **3 (6)**,527-532, (2004).

[11] P. Frinking, T. Segers, Y. Luan, and G. Tranquart, "Three Decades of Ultrasound Contrast Agents: A Review of the Past, Present and Future Improvements", Ultrasound in Med. & Biol. **46(4)**, 892–908, (2020).

[12] T. Segers, N. Jong, & M. Versluis, "Uniform scattering and attenuation of acoustically sorted ultrasound contrast agents: Modeling and experiments", J. Acoust. Soc. Am.**140**, 2506-2517, (2016).

[13] A. Helbert, E. Gaud, T. Segers, C. Botteron, P. Frinking, and V. Jeannot, "Monodisperse versus Polydisperse Ultrasound Contrast Agents: In Vivo Sensitivity and safety in Rat and Pig", Ultrasound in Med. & Biol. **46(12)**, 3339–3352, (2020).

[14] T. Segers, P. Kruizinga, M. Kok, G. Lajoinie, N. de Jong, and M. Versluis, "Monodisperse Versus Polydisperse Ultrasound Contrast Agents: Non-Linear Response, Sensitivity, and Deep Tissue Imaging Potential", Ultr. Med. & Biol. **44(7)**, 1482–1492, (2018).

[15] B. van Elburg, J. Deprez, M. van den Broek, S. De Smedt, M. Versluis, G. Lajoinie,I. Lentacker, and T. Segers, "Dependence of sonoporation efficiency on microbubble size: An in vitro monodisperse microbubble study",J. Contr. Rel. **363**, 747–755, (2023).

[16] L.L. Foldy, "The Multiple Scattering of Waves", Phys. Rev. **64**, 107–119, (1945).

[17] E.L. Carstensen, and L.L. Foldy, "Propagation of Sound Through a Liquid Containing Bubbles", J. Acoust. Soc. Am. **19**, 481–501, (1947).

[18] E. Stride, & N. Saffari, "Investigating the significance of multiple scattering in ultrasound contrast agent particle populations", IEEE Trans. Ultrason., Ferroelectr. Freq. Control **52**, 2332-2345, (2005).

[19] K. Hibbs, J. Mari, E. Stride, R. Eckersley, A. Noble, & M. Tang, "Nonlinear Propagation of Ultrasound Through Microbubble Clouds: A Novel Numerical Implementation", 2007 IEEE Ultr. Symp. Proc. (2007).

[20] K. Ando, T. Colonius, and C. Brennen, "Numerical simulation of shock propagation in a polydisperse bubbly liquid", J. Acoust. Soc. Am. **142**, 596-608, (2011).

[21] N. Ovenden, J. O'Brien, & E. Stride, "Ultrasound propagation through dilute polydisperse microbubble suspensions", J. Acoust. Soc. Am. **142**, 1236-1248, (2017).

[22] Vanhille, & H. Hynynen, "Numerical Simulations of the Nonlinear Interaction of a Bubble Cloud and a High Intensity Focused Ultrasound Field", Acoustics **1**, 825-836, (2019).

[23] G. Pinton, J. Dahl, S. Rosenzweig, & G. Trahey, "A heterogeneous nonlinear attenuating full-wave model of ultrasound", IEEE Trans. Ultrason., Ferroelectr. Freq. Control. **56**, 474-488, (2009).

[24] A. Joshi, B. Lindsey, P. Dayton, G. Pinton, & M. Muller, "An iterative fullwave simulation approach to multiple scattering in media with randomly distributed microbubbles", Phys. Med. & Biol. **62**, 4202-4217, (2017).

[25] H. Haghi, A. J. Sojahrood, and M.C.Kolios, "Collective nonlinear behavior of interacting polydisperse microbubble clusters", Ultrason. Sonoch. **58 (104708)**, (2019).

[26] A. Matalliotakis, and M.D. Verweij, "Computation of ultrasound propagation in a population of nonlinearly oscillating microbubbles including multiple scattering", J. Acoust. Soc. Am. **153**, 2209–2222, (2023).

[27] J. Huijssen, "Modeling of nonlinear medical diagnostic ultrasound", PhD Thesis, Delft University of Technology (2008), available from http://repository.tudelft.nl.

[28] J. Huijssen and M.D. Verweij, "An iterative method for the computation of nonlinear, wide-angle, pulsed acoustic fields of medical diagnostic transducers", J. Acoust. Soc. Am. **127 (1)**, 33–44, (2010).

[29] L. Demi, "Modeling nonlinear propagation of ultrasound through inhomogeneous biomedical media", PhD Thesis, Delft University of Technology (2013), available from http://reposity.tudelft.nl).

[30] L. Demi, M.D. Verweij, J. Huijssen, N. de Jong, and K.W.A. van Dongen, "Attenuation of ultrasound pressure fields described via a contrast source formulation", Proceedings of 2009 IEEE Ultrasonics, 1590–1593, (2009).

[31] L. Demi, K.W.A. van Dongen and M.D. Verweij, "A contrast source method for nonlinear acoustic wave fields in media with spatially inhomogeneous attenuation", J. Acoust. Soc. Am. **129**, 1221–1230, (2011).

[32] A. Matalliotakis, D. Maresca, and M.D. Verweij, "Nonlinear interaction of two cross-propagating plane waves", arXiv, (2023).

[33] M. Abramowitz , and I. Stegun , "Handbook of Mathematical Functions: With Formulas, Graphs, and Mathematical Tables.", print.; [Nachdr. der Ausg. von 1972]. Dover Books on Mathematics (2013).

[34] M. Overvelde, V. Garbin,J. Sijl,B. Dollet, N. de Jong, M. Lohse, and P. Versluis, "Nonlinear Shell Behavior of Phospholipid-Coated Microbubbles", Ultrasound in Med. & Biol. **36(12)**, 2080–2092, (2010).

[35] T. Segers, E. Gaud, M. Versluis, and P. Frinking, "High-precision acoustic measurements of the nonlinear dilatational elasticity of phospholipid coated monodisperse microbubbles", Soft Matter **14**, 9550–9561, (2018).

[36] A. Matalliotakis, R. Waasdorp, M.D. Verweij, and D. Maresca, "Impact of wavefront shape on nonlinear ultrasound imaging of monodisperse microbubbles", Phys. Rev. Applied **22** (034062), (2023).

[37] D.Garcia, "Make the most of MUST, an open-source MATLAB UltraSound Toolbox", IEEE Int. Ultr. Symp., (2021).

[38] V. Perrot, M. Polichetti, F. Varray, and D.Garcia, "So you think you can DAS? A viewpoint on delay-and-sum beamforming", Ultrasonics **111** (106309), (2021).

F.R. Deurvorst, G. Collado Lara, A. Matalliotakis, H. Vos, N. de Jong, V. Daeichin, and M.D. Verweij, *A spatial and temporal characterisation of single proton acoustic waves in proton beam cancer therapy*, J. Acoust. Soc. Am. **151**, 1200–1210 (2022).

Chapter 6

A spatial and temporal characterisation of single proton acoustic waves in proton beam cancer therapy

An in vivo range verification technology for proton beam cancer therapy, preferably in real-time with submillimeter resolution, is desired to reduce the present uncertainty in dose localization. Acoustical imaging technologies exploiting possible local interactions between protons and MBs or nanodroplets might be an interesting option. Unfortunately, a theoretical model characterizing the acoustical field generated by an individual proton on nanometer and micrometer scales is still missing. In this work, such a model is presented. The proton acoustic field is generated by the adiabatic expansion of a region that is locally heated by a passing proton. To model the proton heat deposition, secondary electron production due to protons has been quantified using a semi-empirical model based on Rutherford's scattering theory, reproducing experimentally obtained electronic stopping power values for protons in water within 10% over the full energy range. The electrons transfer energy into heat via electron-phonon coupling to atoms along the proton track. The resulting temperature increase is calculated using an inelastic thermal spike model. Heat deposition is regarded as instantaneous, stress confinement is ensured, and acoustical initial conditions are set. The resulting thermoacoustic field in the nanometer and micrometer range from the single proton track is computed by solving the thermoacoustic wave equation using k-space Green's functions, yielding the characteristic amplitudes and frequencies present in the acoustic signal generated by a single proton in an aqueous medium. Wavefield expansion and asymptotic approximations are used to extend the spatial and temporal ranges of the proton acoustic field.

6.1 Introduction

Proton therapy is an alternative for conventional photon therapy in radiation oncology. Proton beams have a theoretical advantage over photon beams by having a more localised dose distribution characterised by a peak at the end of their range, the Bragg peak, behind which no dose is present. Therefore, a more conformal therapeutic dose can be applied to the tumour while sparing the surrounding healthy tissue. Realising this advantage in the clinic relies on an accurate positioning of the Bragg peak within the tumour volume, which is a challenging demand. In particular, range uncertainties are characteristic of proton therapy. These are considered to be the greatest issue in current clinical practice and have induced an urgent need for accurate *in vivo* range verification techniques. [1, 2].

An envisaged way of improving dose deposition accuracy in proton therapy is to measure the location of proton dose deposition within the anatomy of the patient, preferably in real-time and with a sub-millimeter resolution. Monitoring the actual delivered dose during or after the treatment provides the opportunity to either modify the treatment or compensate in later stages in case of deviations from the original treatment plan. Several methods for dosimetry in proton therapy are currently under investigation at the clinical or experimental level [3, 4], including prompt gamma imaging [5, 6], positron emission tomography [7, 8] and ionoacoustic imaging [9]. In positron emission tomography and prompt gamma imaging, the correlation between the emerging nuclear induced secondary radiation and the Coulomb-induced dose deposition is not straightforward, so that a Bragg peak positioning accuracy better than a few millimeters cannot be expected in clinical situations.

Ionoacoustic imaging employs acoustic pressure signals generated by thermoelastic expansion of the area where protons rapidly deposit the majority of their energy as heat [9]. The dimensions of the heated area determine the frequency content of the emitted acoustic pressure wave. As such, the ionoacoustic signal is a result of combined heat deposition of all protons delivered by the beam. Stopping of protons is a stochastic process which makes that not all protons have the same range. While the stopping range of an individual proton is several micrometers, the effective stopping range for the proton beam, consisting of roughly a billion protons, is several millimeters. Consequently, ionoacoustic signals have frequencies in the order of kilohertz, hampering desired submillimeter localisation resolution.

To approach the problem from another perspective, one may consider the heat deposition of an individual proton. As this heat is deposited over a range of several micrometers, an impacting proton generates a broadband acoustic pressure wave. We will refer to this wave as the proton acoustic signal, in order to distinguish it from the previously mentioned ionoacoustic signal. The higher frequency of this proton acoustic signal will allow a higher localisation resolution than the ionoacoustic signal. However, the proton acoustic pulses cannot be detected at the surface of the body because their high frequency will give rise to high acoustic attenuation, and the pulses that are simultaneously generated by all protons will largely cancel each other. In the absence of these effects, the ionoacoustic signal would contain much higher frequencies than mentioned above.

Clinical ionoacoustic signals typically have a peak pressure on the order of tens

of mPa in the kHz band [10]. Averaging is necessary to detect these, as the state-of-the-art medical transducers have a noise-equivalent pressure on the order of hundreds of mPa [11, 12] . Thus, it is now clear that there is a challenge of measuring proton-induced pressure pulses at the surface of the human body in a higher frequency band, where the pressure content is even lower. To tackle this challenge, we assume that ultrasound contrast agents (UCAs) consisting of micron-sized bubbles may be useful [13]. These MBs can be injected in the blood flow of patients and act as acoustic scatterers. If a single proton impacts in the vicinity of a MB, the proton acoustic wave might drive the MB into oscillation at its resonance frequency, which is typically on the order of a few megahertz. Moreover, monodisperse bubbles that are excited simultaneously might oscillate synchronously at the same resonance frequency. In this way, MBs might convert the broadband proton acoustic pulses into acoustic waves with amplitudes and frequencies detectable outside the body and with frequencies allowing submillimeter resolution. This idea was substantiated by experiments using broadband photoacoustic pulses with center frequency in the hundreds of MHz band, which drove MBs into oscillation at their natural frequency in the much lower MHz range [14, 15]. A similar concept could be based on the vaporization of nanodroplets by a proton beam, which has been recently observed in experiments [16].

Since MB oscillations are driven by the pressure difference in the gas-liquid interface, the acoustic fields of single protons play a key role in the interaction with MBs and nanodroplets. The temporal evolution of the signal is relevant in the nanometer and micrometer distances, as this is the distance expected between the proton stopping position and the closest MB. To numerically simulate these interactions, models for the proton acoustic wave generation and the MB response to these waves are necessary but have not yet been developed. Until now, the pressure generation in proton beams has been described as a bulk phenomenon where in a certain region of interest the thermoacoustic effect of all protons in the beam was considered, resulting in the ionoacoustic signal. [17] has reviewed theoretical and experimental work on the generation of acoustic waves through the interaction between ionizing radiation, such as protons, and materials. It was proven that the ionoacoustic signal generated by a proton beam fits with a theory based on the thermoacoustics of heating along the tracks of the particles. However, the properties of the acoustic waves generated by the individual protons are still obscured. To bridge this theoretical gap, we have developed a framework that combines a single proton heat deposition model with numerical wave simulation algorithms, such that acoustic waves generated by single protons could be computed. Importantly, our model does not account for the possibility of a proton stopping within the gas core of a MB, as this is considered a highly unlikely event. An envisaged next step in this simulation study is to compute the MB response to the computed single proton acoustic waves, but the modelling of this physical process is out of the scope of this paper.

Localized heat deposition in a medium that is irradiated with swift ions has been studied for a variety of applications including proton beam cancer therapy [18]. In previous work, the inelastic thermal spike model has been used to study the temporal temperature distribution along the track of an individual proton stopping in water. The model that we will use inherently treats the proton heating process as a two step process, firstly the absorption of proton energy by electrons, creating secondary elec-

trons or delta rays, and secondly the heating of the molecules through electron-phonon coupling. In an earlier study temperature spikes and pressure spikes in irradiated water have been discussed [19], but here all the energy lost by the ions was assumed to be immediately transferred to the molecules, thus neglecting the electronic component, resulting in the prediction of much higher temperatures and consequently pressure spikes.

We will use methods originating from the field of photoacoustics to predict the acoustic field generated due to thermoelastic expansion following localised radiation heating. The thermoacoustic wave equation will be solved in k-space using a wavenumber integration algorithm, yielding the proton acoustic wave [20]. In addition, spatial and temporal wave extrapolation algorithms will be used to stretch the computational limits on simulation ranges. In this way, the characteristic amplitudes and frequency content of the proton acoustic wave were obtained, providing a theoretical basis for continuing research on the behaviour of ultrasound contrast agents and nanodroplets in a proton beam.

6.2 Numerical methods

As described above, in interactions between protons and the medium they are traversing, kinetic energy is converted to heat. As a result of this, a temperature distribution is induced along the proton track, which generates an acoustic wave through local thermoelastic expansion of the medium. Models for the heating process and acoustic wave generation are described in Sec. 6.2.1 and 6.2.2, respectively. All presented calculations have been performed for a proton in water, but the framework can straightforwardly be extended to other media or ion species [18, 21].

6.2.1 Proton heat deposition model

A proton traversing a medium mainly slows down by transferring kinetic energy to electrons, creating a cascade of secondary electrons. These energetic secondary electrons heat the medium when becoming thermalized and bound. This radiation heating process can be modelled phenomenologically as a two-step process: (1) the absorption of proton energy by electrons and (2) the heating of the atoms through electron-phonon coupling [22]. Previously, for a proton in water this process was mathematically described by an inelastic thermal spike model consisting of two coupled equations of energy transfer [18], given by

$$\begin{aligned} C_e \frac{\partial T_e}{\partial t} &= \nabla \cdot [K_e \nabla T_e] - g[T_e - T] + D \\ \rho C(T) \frac{\partial T}{\partial t} &= \nabla \cdot [K(T) \nabla T] + g[T_e - T] \end{aligned} \tag{6.1}$$

where $T_e(\vec{r}, t)$ and $T(\vec{r}, t)$ denote temperature increases of the electronic and molecular subsystems resulting from proton impact. The symbols C_e, $C(T)$, K_e, and $K(T)$ denote the specific heats and thermal conductivities of the electronic and molecular subsystems [18, 23, 24]. The electron-phonon coupling constant g is linked to the

electron-phonon mean free path λ by the relation $g = K_e/\lambda^2$ [18,24–26]. The symbol $D(\vec{r},t)$ denotes the energy density, or dose, supplied by the incident proton to the electronic subsystem and carried via the electron cascade over a distance $r = |\vec{r}|$ from the proton track [21, 24, 27], where $\vec{r}$ is the position vector in a three-dimensional cylindrical domain with the longitudinal axis aligned with the proton track. Cylindrical symmetry is imposed such that the quantities are independent of the azimuthal coordinate. Equation 6.1 was solved numerically for the temperature distribution $T(\vec{r},t)$ resulting from proton impact. An overview of the parameters in the inelastic thermal spike model is displayed in Table 6.1.

6.2.2 Proton acoustic wave model

When a region of a fluid is heated, a sound wave will be generated through thermoelastic expansion. The relation between the proton-induced temperature distribution $T(\vec{r},t)$ and the resulting proton acoustic wave $p(\vec{r},t)$ is described by the thermoacoustic wave equation.

We consider a homogeneous, linear and lossless acoustic medium. In general, the acoustic pressure $p(\vec{r},t)$ generated through thermoelastic expansion obeys the following wave equation

$$\nabla^2 p(\vec{r},t) - \frac{1}{v_s^2}\frac{\partial^2 p(\vec{r},t)}{\partial t^2} = -\frac{\beta_V}{\kappa v_s^2}\frac{\partial^2 T(\vec{r},t)}{\partial t^2} \tag{6.2}$$

with

$$p(\vec{r},t=0) = 0 \qquad \text{and} \qquad \left.\frac{\partial p(\vec{r},t)}{\partial t}\right|_{t=0} = 0 \tag{6.3}$$

The symbol t denotes the time coordinate, and ∇^2 indicates the Laplace operator. $T(\vec{r},t)$ denotes the temperature, v_s is the ambient speed of sound, β_V is the volume thermal expansivity and κ is the isothermal compressibility. Implicitly, it is assumed that thermal conductivity during heat deposition can be neglected, which condition holds for sufficiently short heating pulses and is known as thermal confinement [28].

Proton heat deposition occurs on a timescale much shorter than the characteristic acoustic travel time of the resulting wave, thus may be regarded as instantaneous. Therefore, it may be assumed that all heat energy has been deposited before the

Table 6.1: Parameters for the inelastic thermal spike model in water.

Symbol	Condition	Value	Unit
C	273 - 373 K	4.2	J g^{-1} K^{-1}
	> 373 K	2.0	J g^{-1} K^{-1}
C_e		1	J cm^{-3} K^{-1}
K		$6 \cdot 10^{-3}$	J s^{-1} cm^{-1} K^{-1}
K_e		2	J s^{-1} cm^{-1} K^{-1}
λ		$2 \cdot 10^{-7}$	cm
ρ		1.0	g cm^{-3}

medium has expanded and its equilibrium mass density ρ has changed. This condition is known as stress confinement and holds if the heating pulse duration t_0 satisfies $t_0 < d_c/v_s$ with d_c being the characteristic length of the temperature distribution. The concept of stress confinement originates from the field of photoacoustics, where short laser pulses are used as a heating source. In Sec. 6.3, it is proved that the condition for stress confinement is satisfied for single proton acoustics. Under isochoric conditions, the change in density $\Delta\rho(\vec{r}, t_0)$, just after the proton heating pulse, is related to the change in temperature $T(\vec{r}, t_0)$ and change in pressure $p(\vec{r}, t_0)$ via the thermodynamic equation $\Delta\rho(\vec{r}, t_0) = \rho\kappa p(\vec{r}, t_0) - \rho\beta_V T(\vec{r}, t_0)$. Setting $\Delta\rho(\vec{r}, t_0)$ to zero, which is dictated by stress confinement, yields a relation for the acoustic pressure at time t_0

$$p_0(\vec{r}) = \frac{\beta_V}{\kappa} T(\vec{r}, t_0) \tag{6.4}$$

Equation 6.4 should be in agreement with the solution $p(\vec{r}, t)$ of Eq. 6.2 at the time instance $t = t_0$. Intuitively it can be deduced that, whereas Eq. 6.2 included a source term, in the case of instantaneous proton heating, the problem can be recast as an initial value problem with no explicit source term but with a given pressure distribution at the instant of the proton heating pulse $p(\vec{r}, t_0)$. This makes the two initial conditions required for a unique solution explicit. Mathematically, the initial value problem for the specific case of proton acoustics is then defined as

$$\nabla^2 p(\vec{r}, t) - \frac{1}{v_s^2} \frac{\partial^2 p(\vec{r}, t)}{\partial t^2} = 0 \tag{6.5}$$

with

$$p(\vec{r}, t = t_0) = p_0(\vec{r}) \qquad \text{and} \qquad \left.\frac{\partial p(\vec{r}, t)}{\partial t}\right|_{t=t_0} = 0 \tag{6.6}$$

The first condition in Eq. 6.6 defines the acoustic pressure distribution at a time t_0 after proton impact, when the temperature increase has reached its maximum value. The second initial condition is equivalent to zero particle velocity $\vec{v}_p(\vec{r})$ everywhere at t_0, which can be safely assumed. Solving Eq. 6.5, using these initial conditions and the acoustic parameters from table 6.2, yields the proton acoustic wave $p(\vec{r}, t)$ in water. Three algorithms were used for full spatiotemporal characterisation of the proton acoustic field, which will be introduced in the following subsections. The algorithm in subsec. 6.2.2 calculates the proton acoustic field in a three dimensional Cartesian domain for a single time instant. As such, spatial characteristics of the field can be visualised efficiently but studying dynamic behavior requires successive evaluation of the algorithm for a series of time instants and therefore is, particularly for large domains, computationally involving. With the applied algorithm the maximum distance to the proton track $|\vec{r}|$ and time t at which $p(\vec{r}, t)$ can be evaluated is limited by the amount of available computational memory. To tackle this, wave extrapolation algorithm were used as a complement to the propagation algorithm. The algorithm in subsec. 6.2.2 was used to efficiently calculate the proton acoustic wave for large radial distances. The long time behaviour was approximated by using the temporal wave extrapolation algorithm from subsec. 6.2.2.

Wave propagation: field for single time instant

This scheme relies on the Green's function in k-space for computing a pressure field $p(\vec{r},t)$ from an arbitrary initial pressure distribution [20]. For the acoustic wave following the proton-induced pressure distribution $p_0(\vec{r}')$, it provides an exact solution that is given by

$$p(\vec{r},t) = \frac{1}{(2\pi)^3}\int\int p_0(\vec{r}')\cos(v_s k(t-t_0))e^{i\vec{k}\cdot(\vec{r}-\vec{r}')}d\vec{k}d\vec{r}' \tag{6.7}$$

with $\vec{r}'$ a position vector given in Cartesian coordinates. Using the definition of the Fourier transformation, Eq. 6.7 may be written as

$$p(\vec{r},t) = \mathcal{F}^{-1}_{x,y,z}\left\{\cos(v_s k(t-t_0))\mathcal{F}_{x,y,z}\left\{p_0(\vec{r})\right\}\right\} \tag{6.8}$$

where $\mathcal{F}_{x,y,z}$ and $\mathcal{F}^{-1}_{x,y,z}$ denote the three-dimensional spatial Fourier and inverse Fourier transformation, respectively. Numerical computation of the acoustic field at any time t requires only two three-dimensional Fast Fourier Transformations and a multiplication with the exact time propagator $\cos(v_s k(t-t_0))$. Because the changes of $p(\vec{r},t)$ over time are calculated using an exact propagator, it is not necessary to calculate the field at intermediate times, as would be required with, for example, finite difference methods. Since the pressure is calculated on a grid of points, the grid spacing must meet the usual Nyquist criterion to avoid aliasing in the spatial domain.

Spatial Wavefield Extrapolation

A scheme is introduced that may be used to extrapolate the pressure field $p(r_p,z,t)$ recorded along a line parallel to the proton track at an arbitrary radial distance r_p, to larger radial distances $r > r_p$. It exploits the cylindrical symmetry of the proton acoustic problem, thereby reducing the number of spatial dimensions from three to two. This makes the extrapolation algorithm suitable for swift computation of the pressure field for micrometer radial distances. The algorithm is based on the Eq. [29]

$$p(r,z,t) = \mathcal{F}^{-1}_{t,z}\left\{\frac{H_0^{(1)}(\mu r)}{H_0^{(1)}(\mu r_p)}\mathcal{F}_{z,t}\left\{p(r_p,z,t)\right\}\right\} \tag{6.9}$$

with $H_0^{(1)}$ denoting the zeroth order Hankel function of the first kind and μ defined as

$$\mu = \begin{cases} (\frac{\omega^2}{v_s^2} - k_z^2)^{\frac{1}{2}}, & |\frac{\omega}{v_s}| > k_z \\ i(k_z^2 - \frac{\omega^2}{v_s^2})^{\frac{1}{2}}, & |\frac{\omega}{v_s}| < k_z \end{cases} \tag{6.10}$$

Table 6.2: Acoustic properties of water [33,34]

Symbol	Value	Unit
v_s	1481	m s^{-1}
β_V	$2 \cdot 10^{-4}$	K^{-1}
κ	$5 \cdot 10^{-11}$	cm s^2 g^{-1}
ρ	1	g cm^{-3}

For μr greater than about 2, using an asymptotic expansion of the Hankel function is justified to accelerate numerical computations. The asymptotic expansion of Hankel functions of the first kind is [30]

$$H_\nu^{(1)}(\mu r_p) = \sqrt{\frac{2}{\pi \mu r_p}} e^{i(\mu r_p - \frac{\nu\pi}{2} - \frac{\pi}{4})} \tag{6.11}$$

Combining equations 6.9 and 6.11 yields the following Eq. for accelerated wavefield extrapolation

$$p(r,z,t) \approx \mathcal{F}_{t,z}^{-1} \left\{ \sqrt{\frac{r_p}{r}} e^{i\mu(r-r_p)} \mathcal{F}_{z,t} \left\{ p(r_p,z,t) \right\} \right\} \tag{6.12}$$

For the scheme to yield accurate results, the grid spacing in the axial direction should be sufficiently small compared to the typical wavelength λ of the acoustic signal recorded at r_p. Typically, Δz should be less than $\lambda/2$, and much smaller than $\lambda/2$ for increased accuracy. A smart interpolation method can be used to adjust the sampling frequency of $p(r_p,z,t)$ [31].

Temporal Wavefield Extrapolation

A scheme is presented that may be used to extrapolate the solution $p(r,z,t_p)$ at a sufficiently large time instant t_p to later times $t > t_p$. In doing so, the cylindrical symmetry of the proton heat deposition and the temporal characteristics of the heat deposition will be exploited. The algorithm enables obtaining of the low frequency content of the proton acoustic wave, which is desirable given the typical megahertz resonance frequency of ultrasound contrast agents. Given the symmetry of the proton acoustic problem, the thermoacoustic equation from Eq. 6.2 may be written in cylindrical coordinates as

$$\nabla^2 p(r,z,t) - \frac{1}{v_s^2} \frac{\partial^2 p(r,z,t)}{\partial t^2} = -\frac{\beta_V}{\kappa v_s^2} \frac{\partial^2 T(r,z,t)}{\partial t^2} \tag{6.13}$$

The temporal characteristics of the heat deposition shown in Fig. 6.1 confirm the statement made in Sec. 6.2.2 that the temperature rise is some orders of magnitudes faster than typical acoustic time scales. Therefore, it is justifiable to approximate the temporal behaviour of the temperature distribution by a step function, such that

$$T(r,z,t) \approx T(r,z,t_0) H(t-t_0) \tag{6.14}$$

with $H(t-t_0)$ representing the Heaviside step function. Next, combining equations 6.13 and 6.14 yields

$$\nabla^2 p(r,z,t) - \frac{1}{v_s^2} \frac{\partial^2 p(r,z,t)}{\partial t^2} = -\frac{\beta_V T(r,z,t_0)}{\kappa v_s^2} \frac{\partial \delta(t-t_0)}{\partial t} \tag{6.15}$$

Now, suppose we assume that the pressure at an arbitrary location behaves as if it were generated by a uniform line source. In that case, the solution for the acoustic

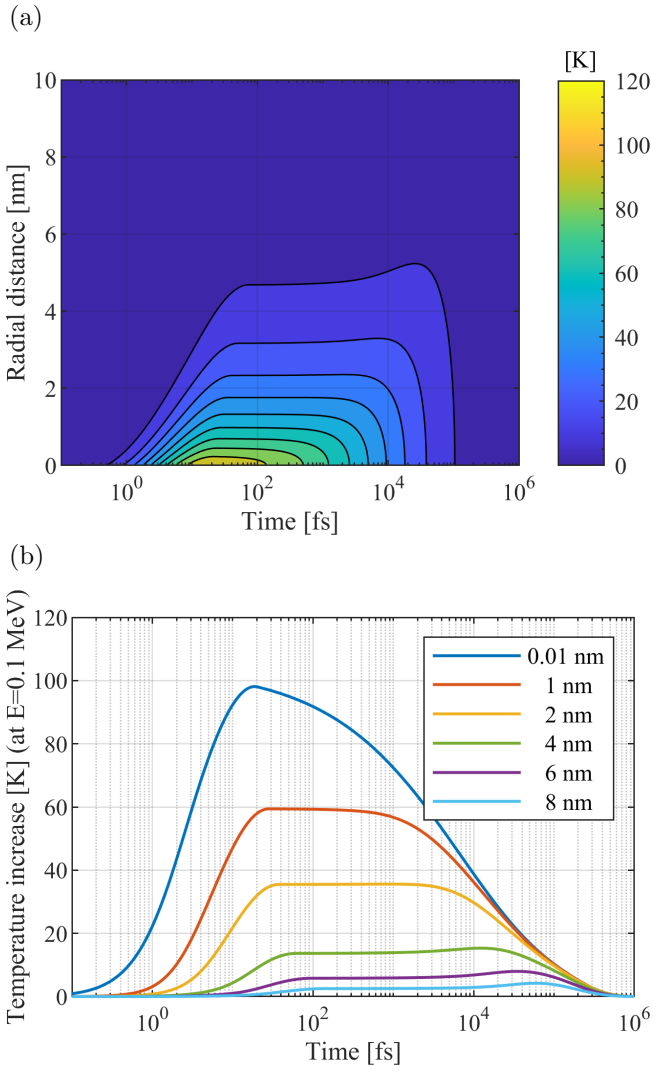

Figure 6.1: (Color online) Temperature increase as a function of time and radial distance, in the axial plane of the Bragg peak ($z = \text{xx}\ \mu\text{m}$). The temperature peaks in around 70 fs after proton impact, due to the swift energy deposition into the electronic subsystem and subsequent electron-phonon interactions. Since heat diffusion in the atomic subsystem occurs on considerably longer time scales, the temperature remains approximately constant over a picosecond until finally relaxing to the ambient value again.

pressure field in Eq. 6.15 will behave as the time derivative of the cylindrical Green's function. The cylindrical Green's function is given by

$$G(r,t) = \frac{1}{2\pi\sqrt{t^2 - r^2/c^2}} H(t - r/c) \tag{6.16}$$

Taking the time derivative yields

$$\frac{\partial G(r,t)}{\partial t} = \frac{\delta(t - r/c)}{2\pi\sqrt{t^2 - r^2/c^2}} - \frac{tH(t - r/c)}{2\pi[t^2 - r^2/c^2]^{3/2}} \tag{6.17}$$

The asymptotic behaviour of the acoustic pressure field for long times is thus

$$p(r,z,t) \sim -\frac{1}{t^2}, \quad \text{for} \quad t \to \infty \tag{6.18}$$

The corresponding asymptotic frequency behaviour can be found by obtaining the frequency domain counterpart of the time derivative of the Green's function, and performing a low frequency approximation. The Fourier transform of Eq. 6.17 is

$$\begin{aligned} j\omega\hat{G}(r,\omega) &= \frac{\omega}{4} H_0^{(1)}(\omega r/c) \\ &= \frac{\omega}{4}\left[J_0(\omega r/c) + jY_0(\omega r/c)\right] \end{aligned} \tag{6.19}$$

where J_0 and Y_0 represent the zeroth order Bessel functions of the first and second kind, respectively. As the frequency approaches zero the Bessel functions can be approximated as [32]

$$J_0\left(\frac{\omega r}{c}\right) \approx 1 - \left(\frac{\omega r}{2c}\right)^2, \quad \text{for} \quad \left(\frac{\omega r}{c}\right) \ll 1 \tag{6.20}$$

$$Y_0\left(\frac{\omega r}{c}\right) \approx \frac{2}{\pi}\left[\log\left(\frac{\omega r}{2c}\right) + \gamma\right], \quad \text{for} \quad \left(\frac{\omega r}{c}\right) \ll 1 \tag{6.21}$$

By plugging equations 6.20 and 6.21 into Eq. 6.19 and taking the modulus, it is found that the low frequency behaviour of the pressure signal is characterised by

$$p(r,z,\omega) \sim \frac{\omega}{4}\left[\left[1 - \left(\frac{\omega r}{2c}\right)^2\right]^2 + \frac{4}{\pi^2}\left[\log\left(\frac{\omega r}{2c}\right) + \gamma\right]^2\right]^{\frac{1}{2}}, \quad \text{for} \quad \omega \to 0 \tag{6.22}$$

In deriving equations 6.18 and 6.22, the dependence of the initial temperature distribution $T(r,z,t_0)$ on z has been implicitly neglected. In reality this is not the case, as is illustrated in Fig. 6.2. It can be seen that the temperature distribution has a dependency on the axial position, with a characteristic length scale in the order of a micrometer. Positions close to the proton track, say for radial distances in the order of a nanometer, thus see the distribution as if it were a uniform line source. The validity of the assumption weakens for larger radial distances, however, it may be expected that the derived asymptotic behaviour at least yields information about the order of magnitude of the low frequency energy content of the proton acoustic wave.

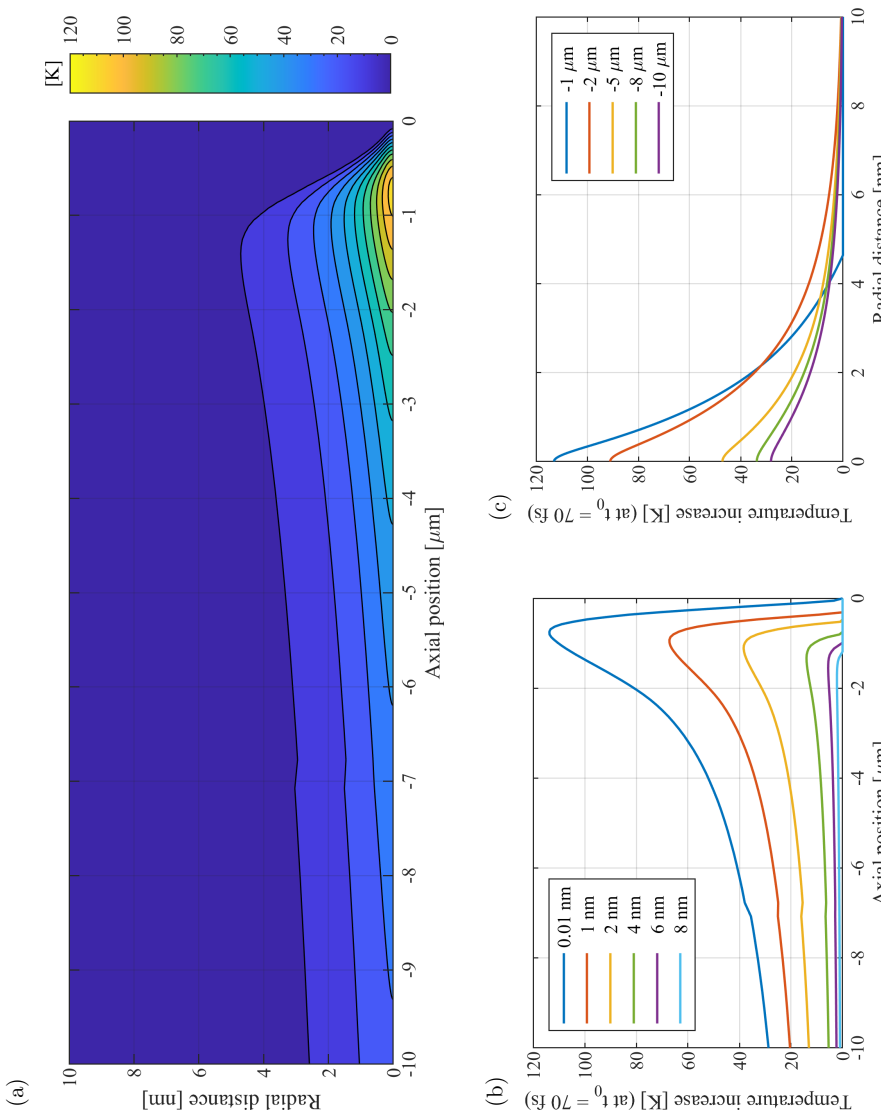

Figure 6.2: (Color online) Temperature distribution at $t_0 = 70$ fs after proton impact. The Bragg peak spans a region of approximately 3 μm axially and 5 nm radially. Highly localised temperature increases approaching 120 K are observed.

6.3 Results and discussion

6.3.1 Proton heat deposition

Solving the inelastic thermal spike model from Eq. 6.1 yields the temperature increase distribution $T(\vec{r}, t)$. In our case this distribution is cylindrically symmetric. First, the transient characteristics of $T(\vec{r}, t)$ are computed to determine the duration t_0 of the proton heating pulse. Figure 6.1 shows the temperature increase as functions of time and radial distance to the proton track for a location in the axial plane of the Bragg peak (z = -1.6 μm). It is found that proton heat deposition occurs within a time $t_0 = 70$ fs. From an acoustical perspective, the spatial temperature distribution $T(\vec{r}, t_0)$ is of interest as it sets the acoustical initial conditions. A snapshot of the spatial temperature distribution at $t_0 = 70$ fs after proton impact is displayed in Fig. 6.2.

6.3.2 Proton acoustic wave simulation

It can be derived from the temperature distribution in Fig. 6.2 that the characteristic radial dimension of the heat heterogeneity d_c is less than 10 nm. Considering the derived heating pulse duration of $t_0 = 70$ fs and a speed of sound in water $v_s = 1483$ m/s, the condition $t_0 < \frac{d_c}{v_s}$ for acoustic confinement is well-satisfied for the case of single proton heating. Thus, Eq. 6.4 may be used to obtain the proton-induced acoustic pressure distribution. Since the pressure field in this equation sets the acoustical initial conditions, it will be referred to as the initial pressure distribution, see Fig. 6.3.

Wave propagation: field for single time instant

In Fig. 6.4, snapshots of the acoustic field are shown for three time instants. These are computed with a scheme based on Eq. 6.8. Note that the axial dimension is three orders of magnitude larger than the lateral dimensions, such that relative axial wave propagation is marginal over the simulated time scale.

The temporal behavior of the proton acoustic signal, recorded on a line at a radial distance of 30 nm from the proton track, is shown in Fig. 6.5. The proton acoustic signal in the axial plane of the Bragg peak consists of a bipolar spike with a center frequency of 86.7 GHz. At 30 nm radial distance, the pressure in the Bragg peak has dropped from 45.2 MPa to 3.1 MPa. The dropping of the peak pressure is attributed to the geometrical spreading of the acoustic field, considering that attenuation was not incorporated. The shape of the proton acoustic signal is similar to the signature of the source term in Eq. 6.2. This signature is the double time derivative of the almost stepwise increase of the temperature in Fig. 6.1, yielding the bipolar behavior of the pressure pulse. Considering the absence of dispersion in the numerical scheme, the shape of the simulated signal necessarily remains unchanged during propagation. The red crosses in Fig. 6.5c indicate the center frequency of the signal recorded at the corresponding axial position. Lower frequencies are observed for positions before the Bragg peak. This can be explained by the more widespread initial pressure distribution at these locations, see Fig. 6.3a.

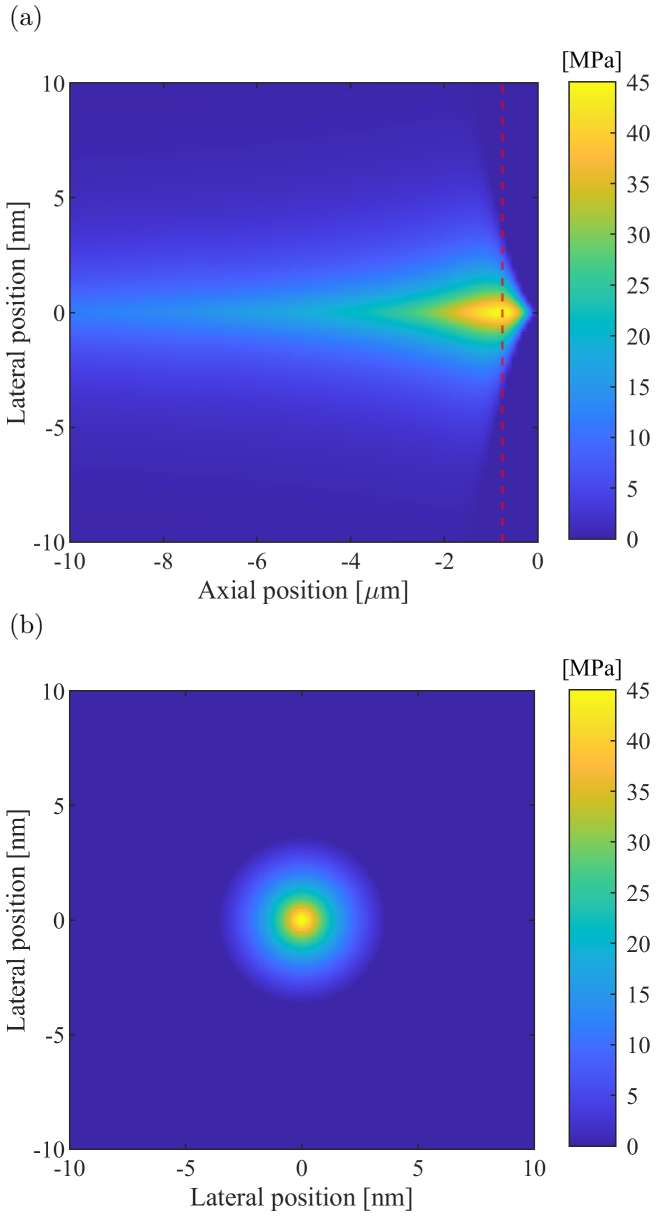

Figure 6.3: (Color online) Initial pressure distribution induced by proton impact. Due to the applicability of acoustic confinement, this pressure distribution is essentially a scaled version of the temperature distribution at 70 fs after proton impact. A peak pressure of 45.2 MPa was found in the Bragg peak, of which the axial location is denoted by the red dashed line.

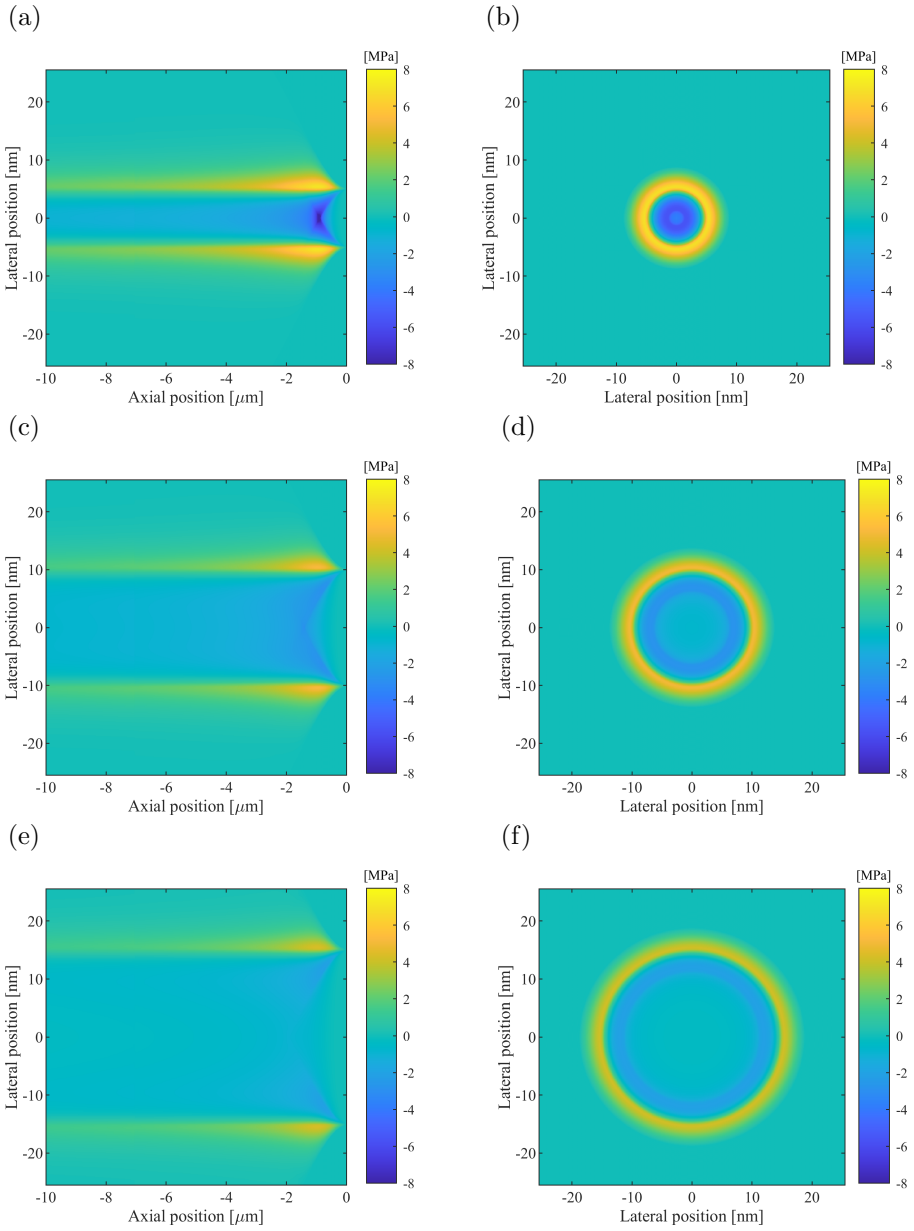

Figure 6.4: (Color online) Snapshots of the propagating proton acoustic wave. The images are made with 3.4 ps time intervals, equivalent to a snapshot for every 5 nm of propagation distance. Note the cylindrical symmetry of the propagating wave and the dropping of the peak pressure due to geometric spreading.

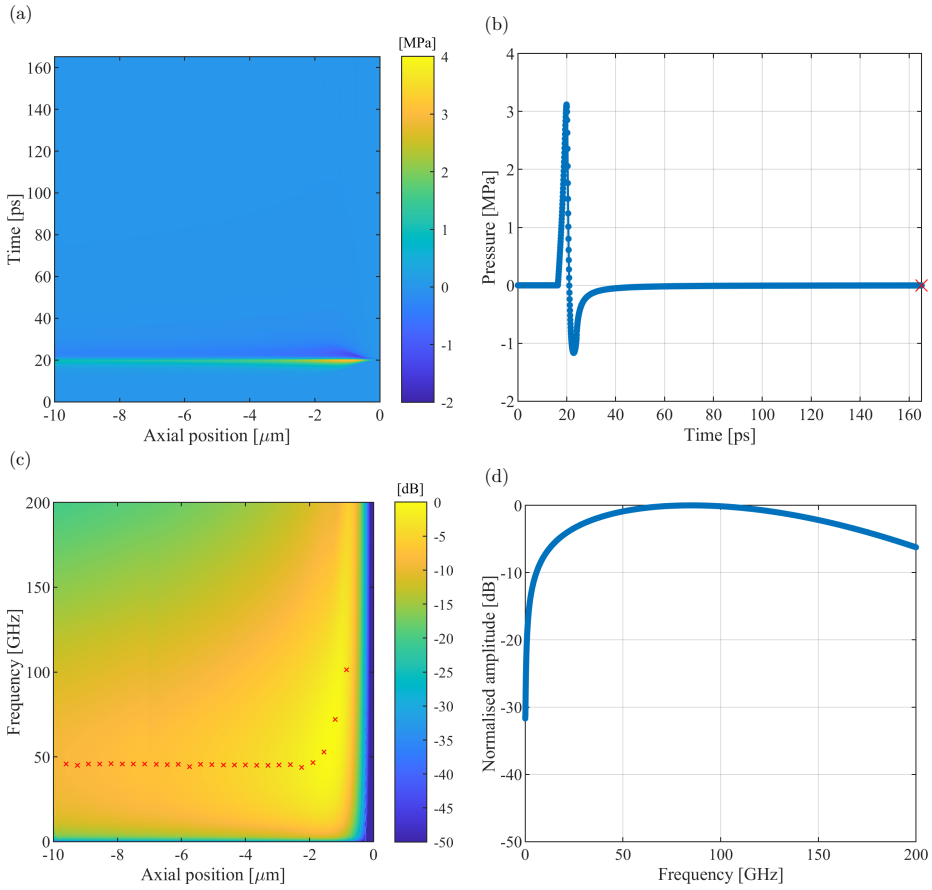

Figure 6.5: (Color online) Temporal and spectral behaviour of the proton acoustic signal, at a radial distance of 30 nm from the proton track. (a) Time signal. (b) Time signal in the axial plane of the Bragg peak. Although hardly visible, at the position of the red cross a negative pressure of approximately 25 kPa is present. (c) Frequency spectrum of the time recording, normalised against the maximum of the spectrum. The red crosses indicate the center frequency of the signal recorded at the corresponding axial detector position. (d) Frequency spectrum in the axial plane of the Bragg peak. Note that the low frequency part of the spectrum is highly influenced by the truncation of the time domain signal, and therefore is not reliable.

To study possible interactions with ultrasound contrast agents, in particular the acoustic energy in the megahertz frequency bands is of interest. As such, it is desirable to simulate the signal for time scales in the order of nanoseconds. Due to memory limitations this was not possible with the current scheme using Eq. 6.8.

Spatial wavefield extrapolation

Figure 6.6 shows the local positive peak pressure for the last five micrometers of the proton track. Peak values up to approximately 5 nm radial distance are set by the initial pressure distribution. Hereafter, the values show a pressure fall-off according to an inverse square root relationship with radial distance. For locations close to the proton track, the energy spreading is essentially cylindrical. For cylindrical waves, acoustic energy spreads inversely proportional with radial distance. Since acoustic energy scales with the square of pressure, an inverse square root proportionality for pressure could intuitively be expected.

The spatial wave extrapolation scheme using Eq. 6.12 was used to simulate the proton acoustic wave for radial distances from 150 nm to 5 μm. Figure 6.7 shows the local positive peak pressures for these radial distances, for the last five micrometers of the proton track. The positive peak pressure decreases further, according to the inverse square root relationship in Eq. 6.12, from 1.41 MPa to 0.24 MPa between 150 nm and 5 μm radial distance. Note that in Fig. 6.7 at a radial distance of 5 μm a discrepancy, though small, arises with the inverse square root relationship. This is presumably because of the nonuniform initial pressure distribution in the axial direction, which makes that for very large radial distances the proton may be seen as a point source rather than a cylindrical source.

Temporal wave extrapolation

The temporal wave extrapolation scheme was used to approximate the proton acoustic wave for long times and to approximate its frequency spectrum in the low frequency regime. In Fig. 6.8 the asymptotic behaviour from equations 6.18 and 6.22 has been plotted and compared to the simulated data from Fig. 6.5. These analytical expressions were plotted by fitting the relation to a single simulation data point. The agreement is good for short times and high frequencies, and therefore the analytical expressions may be used to estimate the pressure for long times and for low frequencies. In Fig. 6.8a it is shown that the time signal runs until 160 ps and is cut-off afterwards. In creating the simulated frequency spectrum in Fig. 6.8b, this signal was windowed before Fourier transformation, which unavoidably affects the low frequency regime. The analytical approach taken to derive the asymptotic behaviour in Fig. 6.8b does not suffer from such a procedure and is therefore considered to be a better reflection of reality. The discrepancy between the simulation results and the asymptotic behaviour in 6.8b is therefore a result of the sensitivity of the simulation to windowing. According to the inverse quadratic behaviour with time, it is found that the simulated negative pressure of -2.6 kPa after 160 picoseconds at a radial distance of 30 nanometers from the Bragg peak will decay to -68 Pa after 1 nanosecond.

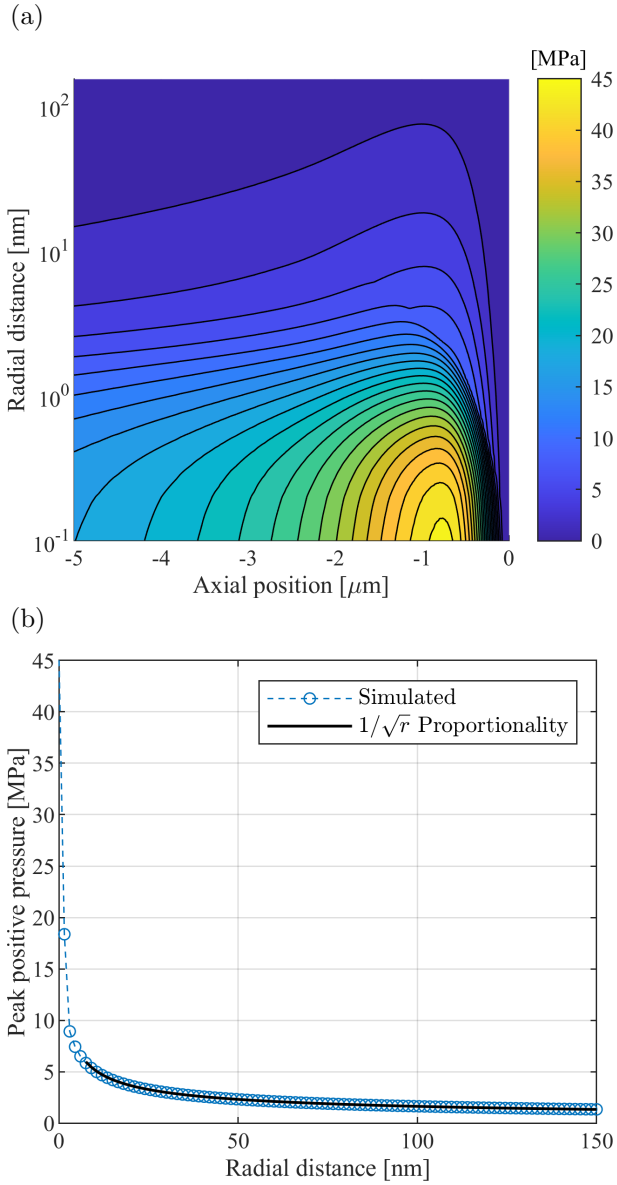

Figure 6.6: (Color online) Local positive peak pressures for radial distances up to 150 nm. Peak values up to approximately 5 nm radial distance are set by the initial pressure distribution. Hereafter, the values show a pressure fall-off according to an inverse square root relationship with radial distance.

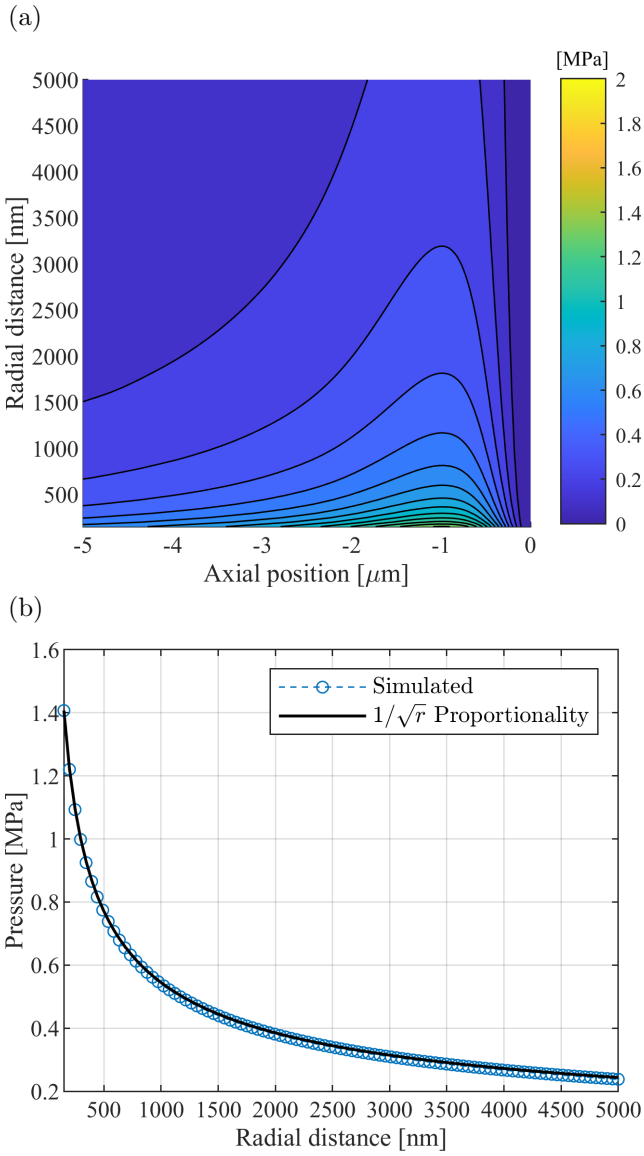

Figure 6.7: (Color online) Local positive peak pressures for radial distances up to 5 μm. This figure is complementary to Fig. 6.6.

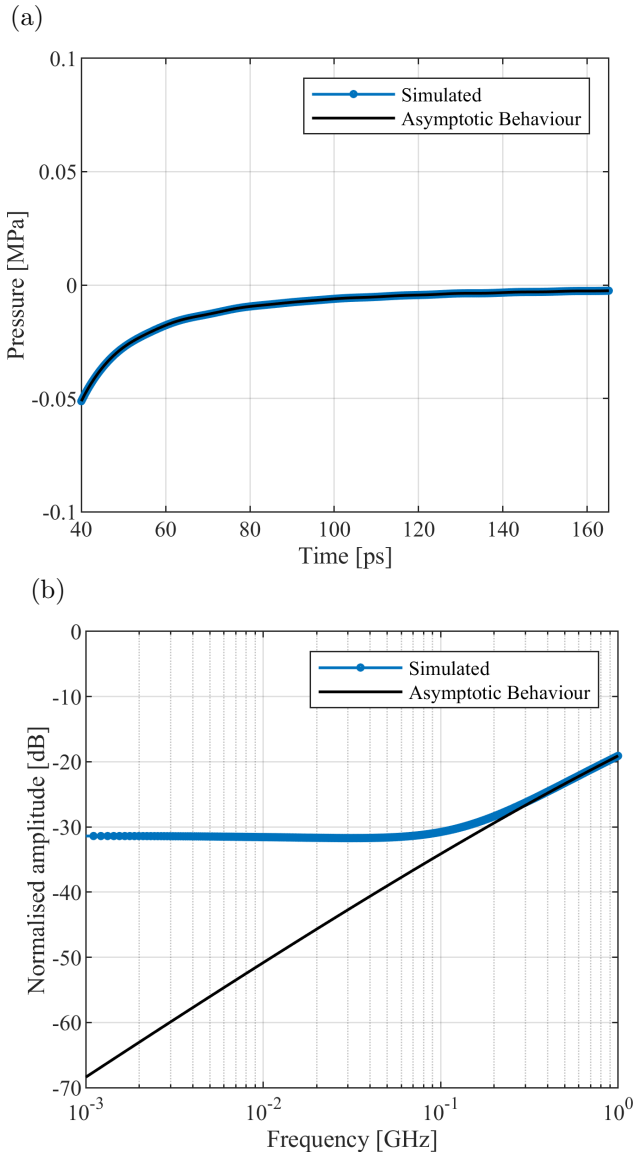

Figure 6.8: (Color online) Asymptotic temporal and spectral behaviour of the proton acoustic signal. The normalisation basis in (b) is the maximum of the spectrum. Note that the discrepancy between the simulation results and the asymptotic behaviour in (b) is a result of the sensitivity of the simulation result to windowing of the time domain signal in (a), while the asymptotic behaviour does not suffer from this effect.

6.4 Conclusions

A theoretical model for describing the acoustic field caused by a single proton has been developed, laying a foundation for characterisation of possible acoustic interactions between protons and ultrasound contrast agents or nanodroplets. The model consists of a set of equations describing the heat deposition of a proton and schemes to solve the thermoacoustic wave equation. The numerical simulations yielded the shape, frequency content and amplitude of the proton acoustic wave on nanometer and micrometer scales. It was found that the proton acoustic wave consists of a bipolar spike with a center frequency of around 86.7 GHz. Positive peak pressures of 45.2 MPa were found in the single proton Bragg peak, falling off according to an inverse square root relationship with radial distance to 0.24 MPa at 5 μm radial distance from the Bragg peak. The temporal behaviour was simulated up to 160 ps and showed that at 30 nm from the Bragg peak a negative pressure of -2.6 kPa was present at that time. An analytical approximation illustrated that the the pressure falls off according to an inverse square relationship with time.

All in all, this work has provided a full spatiotemporal characterisation of the acoustic field of a single proton. As next steps, it would be interesting to use this model for predicting how ultrasound contrast agents and nanodroplets would respond to the combined acoustical field generated in a proton beam, where one has an abundant amount of protons, each generating an acoustical field. Comparing these results to recent observations of ultrasound contrast agents in a proton beam could yield valuable insight in the physical processes happening at nanometer and micrometer scales [13]. However, a theoretical gap currently still exists in describing the MB response to submicrometer length acoustic pulses, which should first be filled to enable further characterisation of the interaction between protons and ultrasound contrast agents or nanodroplets.

Bibliography

[1] Paganetti, H., ed. (**2018**). *Proton Therapy Physics* (CRC Press).

[2] Parodi, K., and Polf, J. C. (**2018**). "In vivo range verification in particle therapy" Medical Physics **45**(11).

[3] Knopf, A., and Lomax, A. (**2013**). "In-vivo proton range verification: a review" Physics in Medicine and Biology **58**(15), R131–R160.

[4] Parodi, K. (**2020**). "Latest developments in in-vivo imaging for proton therapy" The British Journal of Radiology **93**.

[5] Hueso-González, F., Enghardt, W., Fiedler, F., Golnik, C., Janssens, G., Petzoldt, J., Prieels, D., Priegnitz, M., Römer, K., Smeets, J., Vander Stappen, F., Wagner, A., and Pausch, G. (**2015**). "First test of the prompt gamma ray timing method with heterogeneous targets at a clinical proton therapy facility" Physics in Medicine and Biology **60**(16), 6247–6272.

[6] Min, C., Kim, C., Youn, M., and Kim, J. (**2006**). "Prompt gamma measurements for locating the dose falloff region in the proton therapy" Applied Physics Letters **89**(18), 183517.

[7] Parodi, K. (**2015**). "Vision 20/20: Positron emission tomography in radiation therapy planning, delivery, and monitoring" Medical Physics **42**(12), 7153–7168.

[8] Parodi, K., Paganetti, H., Shih, H., Michaud, S., Loeffler, J., DeLaney, T., Liebsch, N., Munzenrider, J., Fischman, A., Knopf, A., and Bortfeld, T. (**2007**). "Patient study of in vivo verification of beam delivery and range, using positron emission tomography and computed tomography imaging after proton therapy" International Journal of Radiation Oncology, Biology, Physics **68**.

[9] Hickling, S., Xiang, L., Jones, K., Parodi, K., Assmann, W., Avery, S., Hobson, M., and El Naqa, I. (**2018**). "Ionizing radiation-induced acoustics for radiotherapy and diagnostic radiology applications" Medical Physics **45**(7), e707–e721.

[10] Jones, K. C., Stappen, F. V., Bawiec, C. R., Janssens, G., Lewin, P. A., Prieels, D., Solberg, T. D., Sehgal, C. M., and Avery, S. (**2015**). "Experimental observation of acoustic emissions generated by a pulsed proton beam from a hospital-based clinical cyclotron" Medical Physics **42**(12), 7090–7097.

[11] Matte, G. M., Neer, P. L. M. J. V., Danilouchkine, M. G., Huijssen, J., Verweij, M. D., and Jong, N. D. (**2011**). "Optimization of a phased-array transducer for multiple harmonic imaging in medical applications: frequency and topology" IEEE Transactions on Ultrasonics, Ferroelectrics and Frequency Control **58**(3), 533–546.

[12] Van Neer, P. L. M. J., Matte, G., Danilouchkine, M. G., Prins, C., Adel, F. V. D., and Jong, N. D. (**2010**). "Super-harmonic imaging: development of an interleaved phased-array transducer" IEEE Transactions on Ultrasonics, Ferroelectrics, and Frequency Control **57**(2), 455–468.

[13] Lascaud, J., Dash, P., Würl, M., Wieser, H.-P., Wollant, B., Kalunga, R., Assmann, W., Clevert, D.-A., Ferrari, A., Sala, P., Savoia, A. S., and Parodi, K. (**2021**). "Enhancement of the ionoacoustic effect through ultrasound and photoacoustic contrast agents" Scientific Reports **11**(2725).

[14] Daeichin, V., Lum, J., Borden, M., and Murray, T. (**2020**). "A new photoacoustic based technique for single microbubble characterization" in *The 25th European Symposium on Ultrasound Contrast Imaging*, pp. 42–44.

[15] Lum, J., Stobbe, D., and Murray, T. (**2018**). "Photoacoustic technique to measure temperature effects on microbubble viscoelastic properties" Applied Physics Letters **112**(11).

[16] Carlier, B., Heymans, S., Nooijens, S., Toumia, Y., Ingram, M., Paradossi, G., D'Agostino, E., Himmelreich, U., D'hooge, J., Van Den Abeele, K., and Sterpin, E. (**2020**). "Proton range verification with ultrasound imaging using injectable radiation sensitive nanodroplets: a feasibility study" Physics in Medicine & Biology **65**.

[17] Baily, N. (**1992**). "A review of the processes by which ultrasound is generated through the interaction of ionizing radiation and irradiated materials: Some possible applications" Medical Physics **19**(3), 525–532.

[18] Toulemonde, M., Surdutovich, E., and Solov'yov, A. (**2009**). "Temperature and pressure spikes in ion-beam cancer therapy" Physical review E **80**, 031913.

[19] Sun, Y. Y., and Nath, R. (**1993**). "Pressure wave generated by the passage of a heavy charged particle in water" Medical Physics **20**(3), 633–638.

[20] Cox, B. T., and Beard, P. C. (**2005**). "Fast calculation of pulsed photoacoustic fields in fluids using k-space methods" The Journal of the Acoustical Society of America **117**(6), 3616–3627.

[21] Waligórski, M., Hamm, R., and Katz, R. (**1986**). "The radial distribution of dose around the path of a heavy ion in liquid water" International Journal of Radiation Applications and Instrumentation. Part D. Nuclear Tracks and Radiation Measurements **11**(6), 309–319.

[22] Qiu, T., and Tien, C. (**1992**). "Short-pulse laser heating on metals" International Journal of Heat and Mass Transfer **35**(3), 719 – 726.

[23] Dufour, C., Audouard, A., Beuneu, F., Dural, J., Girard, J., Hairie, A., Levalois, M., Paumier, E., and Toulemonde, M. (**1993**). "A high-resistivity phase induced by swift heavy-ion irradiation of Bi: a probe for thermal spike damage?" Journal of Physics: Condensed Matter **5**(26), 4573–4584.

[24] Toulemonde, M., Costantini, J., Dufour, C., Meftah, A., Paumier, E., and Studer, F. (**1996**). "Track creation in SiO_2 and $BaFe_{12}O_{19}$ by swift heavy ions: a thermal spike description" Nuclear Instruments and Methods in Physics Research Section B: Beam Interactions with Materials and Atoms **116**(1), 37–42.

[25] Toulemonde, M., Dufour, C., Meftah, A., and Paumier, E. (**2000**). "Transient thermal processes in heavy ion irradiation of crystalline inorganic insulators" Nuclear Instruments and Methods in Physics Research Section B: Beam Interactions with Materials and Atoms **166-167**, 903 – 912.

[26] Meftah, A., Costantini, J., Khalfaoui, N., Boudjadar, S., Stoquert, J., Studer, F., and Toulemonde, M. (**2005**). "Experimental determination of track cross-section in $Gd_3Ga_5O_{12}$ and comparison to the inelastic thermal spike model applied to several materials" Nuclear Instruments and Methods in Physics Research Section B: Beam Interactions with Materials and Atoms **237**(3), 563–574.

[27] Gervais, B., and Bouffard, S. (**1994**). "Simulation of the primary stage of the interaction of swift heavy ions with condensed matter" Nuclear Instruments and Methods in Physics Research Section B: Beam Interactions with Materials and Atoms **88**(4), 355–364.

[28] Wang, L. (**2009**). "Modeling photoacoustic propagation in tissue using k-space techniques" in *Photoacoustic Imaging and Spectroscopy*, CRC Press, pp. 25–34.

[29] Candel, S. M., and Chassaignon, C. (**1984**). "Radial extrapolation of wave fields by spectral methods" The Journal of the Acoustical Society of America **76**(6), 1823–1828.

[30] Arfken, G., Weber, H., and Harris, F. (**2013**). "Chapter 7 - Ordinary Differential Equations" in *Mathematical Methods for Physicists*, edited by G. Arfken, H. Weber, and F. Harris, seventh edition ed. (Academic Press, Boston), pp. 329–380.

[31] Verweij, M., and Huijssen, K. (**2009**). "A filtered convolution method for the computation of acoustic wave fields in very large spatiotemporal domains" The Journal of the Acoustical Society of America **125**, 1868–1878.

[32] Abramowitz, M. (**1974**). *Handbook of Mathematical Functions, With Formulas, Graphs, and Mathematical Tables* (Dover Publications, Inc., USA).

[33] Fine, R. A., and Millero, F. J. (**1973**). "Compressibility of water as a function of temperature and pressure" The Journal of Chemical Physics **59**(10), 5529–5536.

[34] Huang, C., Wikfeldt, K. T., Tokushima, T., Nordlund, D., Harada, Y., Bergmann, U., Niebuhr, M., Weiss, T. M., Horikawa, Y., Leetmaa, M., Ljungberg, M. P., Takahashi, O., Lenz, A., Ojamäe, L., Lyubartsev, A. P., Shin, S., Pettersson, L. G. M., and Nilsson, A. (**2009**). "The inhomogeneous structure of water at ambient conditions" Proceedings of the National Academy of Sciences **106**(36), 15214–15218.

Chapter 7

Impact of a proton beam on a microbubble population

An in vivo range verification technology for proton beam cancer therapy, preferably in real-time with submillimeter resolution, is desired to reduce the present uncertainty in dose localization. Acoustical imaging technologies exploiting possible local interactions between protons and MBs might be an interesting option. Although there has been research for the pressure field emission from a single proton, a theoretical model characterizing the scattering of a MB population when excited by the acoustical field generated from a beam of protons is still uknown. To deal with this challenge, we extend the Iterative Nonlinear Contrast Source (INCS) method with the incorporation of a cloud of protons as the primary source term that responsible for the incident pressure field. We study the influence of the pressure field from a proton beam on the scattering from a MB population by incorporating an extra contrast source term in the wave equation. Multiple parameters and all the necessary assumptions that affect the behavior of the total system are described. Overall, this work sheds light on the simulation of the interactions between a proton beam and a population of MBs, and can give insightful information to expand the horizons of therapeutic ultrasound, mainly for the unconventional proton therapy.

7.1 Introduction

Proton therapy offers an alternative to conventional photon therapy in radiation oncology. Proton beams provide a theoretical advantage over photon beams due to their more localized dose distribution characterized by a peak at the end of their range, known as the Bragg peak, beyond which no dose is present. This feature allows for a more conformal therapeutic dose to be applied to the tumor while sparing surrounding healthy tissue. However, realizing this advantage in clinical practice relies on accurately positioning the Bragg peak within the tumor volume, which poses a significant challenge. Range uncertainties, inherent to proton therapy, are considered the primary issue in current clinical practice, necessitating accurate *in vivo* range verification techniques [1, 2].

Improving dose deposition accuracy in proton therapy entails measuring the location of proton dose deposition within the patient's anatomy, preferably in real-time and with sub-millimeter resolution. Monitoring the actual delivered dose during or after treatment offers the opportunity to modify the treatment or compensate for deviations from the original plan. Various methods for dosimetry in proton therapy are under investigation [3, 4], including prompt gamma imaging [5, 6], positron emission tomography [7, 8], and ionoacoustic imaging [9]. However, achieving Bragg peak positioning accuracy better than a few millimeters in clinical situations remains challenging due to the complex correlation between emerging secondary radiation and Coulomb-induced dose deposition.

Clinical ionoacoustic signals typically exhibit a peak pressure in the range of tens of mPa in the kHz band [10]. Averaging is necessary to detect these signals, as state-of-the-art medical transducers have a noise-equivalent pressure on the order of hundreds of mPa [11, 12]. Consequently, improving resolution by directly measuring proton-induced pressure pulses at the body's surface in a higher frequency band, where pressure content is even lower, presents a significant challenge. One proposed solution involves utilizing ultrasound contrast agents (UCAs) consisting of micron-sized bubbles [13]. These MBs, injected into the patient's bloodstream, act as acoustic scatterers. When a proton impacts near a MB, the resulting proton acoustic wave may drive the MB into oscillation at its resonance frequency, typically in the megahertz range. This concept has been substantiated by experiments using broadband photoacoustic pulses, which drove MBs into oscillation at their natural frequency in the lower MHz range [14, 15]. A similar concept could be based on the vaporization of nanodroplets by a proton beam, which has been recently observed in experiments [16, 17].

Microbubble oscillations, driven by pressure differences at the gas-liquid interface, are influenced by the acoustic fields of proton beams. Previous research has developed numerical models describing the spatiotemporal profiles of acoustic pressure waves emitted from a single proton in submillimeter ranges [18]. However, understanding how a beam of individual protons deposits energy into the medium remains unknown. Until now, the pressure generation in proton beams has been described as a bulk phenomenon where in a certain region of interest the thermoacoustic effect of all protons in the beam was considered, resulting in the ionoacoustic signal. To simulate interactions between protons and MBs, models for acoustic wave generation by a cloud of protons and the response of the MB population are necessary but currently

undeveloped.

This numerical study aims to explore the sychronous oscillations of a MB population, stimulated by the acoustic pressure fields from a cloud of individual protons. To achieve this, we employ the extended Iterative Nonlinear Contrast Source (INCS) [19, 20] method that already accounts for the interactions within a MB population [21]. The behavior of each MB, characterized by its individual properties, is modeled by solving its own Marmottant equation [22]. In this chapter, the INCS method is extended to incorporate the proton cloud as the primary source term in the full wave equation, causing the incident protoacoustic field. Each proton is assumed to behave as a point emitter. Based on a Neumann iterative scheme, the INCS method calculates the scattered acoustic signals, progressively enhancing accuracy with each iteration until convergence is achieved. Each iteration introduces an additional order of multiple scattering, corresponding to an extra path of wave propagation.

First, in Section 7.2, the fundamental theory behind the INCS method is explained followed by its extension with the cloud of point sources. In Section 7.3, the configuration for the numerical experiments is discussed, which is used for the validation of INCS and the comparison between polydisperse and monodisperse populations when excited by a plane wave. Next, in Section 7.4 the results from the numerical simulations for each different test case are presented. Concluding remarks are given in Section. 7.5.

7.2 Extension of INCS with a cloud of protons

7.2.1 Linear Field

The linear pressure field generated by an external source in a linear, homogeneous acoustic medium is described by the wave equation

$$c_0^{-2}\frac{\partial^2 p(\boldsymbol{x},t)}{\partial t^2} - \nabla^2 p(\boldsymbol{x},t) = S_{\mathrm{pr}}(\boldsymbol{x},t), \tag{7.1}$$

Here, $\boldsymbol{x}$ [m] is the Cartesian position vector, and t [s] is the time. The symbol $p(\boldsymbol{x},t)$ [Pa] indicates the acoustic pressure, $c_0 = 1/\sqrt{\rho_0\kappa_0}$ [m/s] is the small signal sound speed in the background medium, where ρ_0 [kg·m^{-3}] is the mass density and κ_0 [Pa^{-1}] is the compressibility. The Laplacian operator ∇^2 generates the sum of the second order spatial derivatives. The acoustic field is generated by the primary source term S_{pr}, which can also be described by a pressure jump condition for either the velocity or the pressure. These jump conditions can be used to represent a source with a plane aperture, e.g. a phased array transducer, via boundary conditions.

Here, we assume that each proton can be represented by a point emitter. Therefore, to account for a cloud of point sources, the primary source term is given by

$$S_{\mathrm{pr}}(\boldsymbol{x},t) = \sum_{i=1}^{M} A^{(i)} s^{(i)}(t)\, \delta(\boldsymbol{x} - \boldsymbol{x}_{\mathrm{p}}^{(i)}), \tag{7.2}$$

where i is the integer index of the point source in the population, M is the number of point sources, $\boldsymbol{x}_{\mathrm{p}}^{(i)}$ is the position vector, $A^{(i)}$ is the pressure amplitude and $s^{(i)}(t)$ is the temporal signature of the i^{th} point source. The symbol δ indicates the Dirac delta distribution. As every proton has the same properties, they all have the same peak amplitude A and temporal signature $s(t)$. In other words, all point sources act at the same time and synchronously emit the same pulse.

7.2.2 Nonlinear field due to contrast agents

In medical ultrasound, nonlinearities arising from contrast media can have a significant impact on the propagation of the acoustic signals. To incorporate any propagation phenomena that affect the incident field, it is sufficient to extend Eq. (7.1) with a contrast source term S_{cs}, thus

$$c_0^{-2}\frac{\partial^2 p}{\partial t^2} - \nabla^2 p = S_{\mathrm{pr}} + S_{\mathrm{cs}}(p) \tag{7.3}$$

Within this scheme, multiple contrast sources can be accommodated that represent attenuation [20, 24], inhomonegeous medium properties [25], or the effect of local nonlinearities. [26] In contrast-enhanced imaging, the nonlinear oscillatory behavior of the MBs distorts the incident field. To include the contribution of a population of MBs, each described as a point scatterer, the source term should be rewritten as [21]

$$S_{\mathrm{cs}}(\boldsymbol{x}, t) = \rho_0 \sum_{i=1}^{N} \frac{d^2 V^{(i)}(\boldsymbol{x}_{\mathrm{sc}}^{(i)}, t)}{dt^2}\, \delta(\boldsymbol{x} - \boldsymbol{x}_{\mathrm{sc}}^{(i)}), \tag{7.4}$$

where V is the volume of each MB, $\boldsymbol{x}_{\mathrm{sc}}$ is the position vector of each point scatterer, i is the integer index of the scatterer in the population, and N is the number of MBs. Each scatterer's volume depends on the bubble radius R as a function of time, which in our case will be calculated by solving the Marmottant equation [22].

7.3 Configurations of the simulations

To construct the configurations, first we need to understand our research question.

How can we efficiently localize the Bragg peak with submillimeter resolution in real-time with the introduction of contrast agents, such as MBs?

To answer this, we need to achieve :

- Uniform distribution of the generated pressure fields. To localize the Bragg peak, it is necessary to detect the protoacoustic signal through multiple sensors at different locations. To correlate these signals, they should have similar temporal signatures and therefore a uniform distribution.

- Coherent signal assisted by the synchronous oscillations of the MBs

- Enlongated temporal profile due to the oscillatory behavior of the MBs
- Energy concentration in the band around resonance frequency of the MBs
- Bandlimited and sensitive optoacoustic sensors

Next, we need to describe the parameters of the simulation that will make the detection of the broadband protoacoustic signal feasible.

7.3.1 Incident field

First, we describe the parameters for the generation of the incident field, as it primarily excites of the MB population.

Statement 1: *High frequencies, from hundreds of MHz to GHz, undergo significant attenuation as the wave propagates further from the protons' location, rendering them insignificant for bubble excitation and signal detection by the optoacoustic sensor.*
Assumption 1: *Therefore, it is assumed that the effect due to high frequencies is negligible, and the bubbles are, on average, excited by a pulse in the lower MHz range.*

As can be deduced from Deurvorst et al. [18], the temporal signature of a single proton is a short broadband pulse of the form

$$s(t) = \exp\left[-\left(\frac{t - 2.41T_d}{T_w/2}\right)^2\right] \sin[2\pi f_0(t - T_d)], \tag{7.5}$$

where $f_0 = 1.5$ MHz is the center frequency, $T_w = 0.5/f_0$ is the width and $T_d = 5/f_0$ is the delay of a Gaussian envelope. The scatterers will be embedded in water with a density of $\rho = 1060$ kg/m^3 and a speed of sound of $c_0 = 1482$ m/s. In the considered situations, water has negligible losses and nonlinear effects will be hardly noticeable. Therefore, we assume that the embedding medium is lossless and linear. A sampling frequency of 15 MHz was used as the basis for the discretization of the spatiotemporal domain. We run our simulations for j=10 iterations to ensure accurate results. [21] These conditions are ideal and are used due to the restrictions for the generation of the computational domain.

The configuration provides an idealized situation with a uniform distribution of primary point sources, which will cause the incident field that it experienced by the MB cloud. At least three different cubical primary source will be used, with sides: (i) shorter than, (ii) equal to, (iii) longer than the wavelength of the excitation frequency. The configurations for this scenario are depicted in Fig. 7.1.

To avoid resonance effects due to the size of the computational domain, Tukey tapering is applied at the edges of the point source distribution, resulting in a smoother incident pressure field. Increasing the size of the computational domain for the point sources leads to greater distances between the points located at the edges of the cube, resulting in a longer cumulative temporal signature. Conversely, stronger tapering reduces these distances, shortening the cumulative temporal profile.

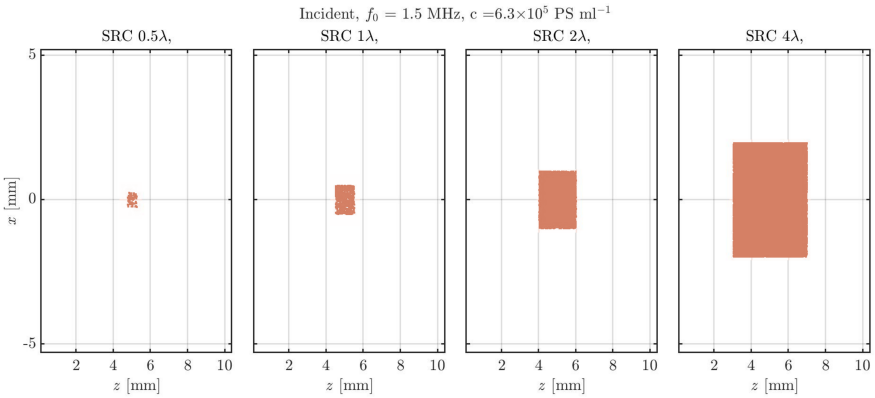

Figure 7.1: Configurations used in the INCS simulations for the primary source. Primary source domain containing a homogeneous suspension of 6.3 $\times 10^5$ ml^{-1} point sources, embedded in water for a cubical domain with a side of 0.5λ, 1λ, 2λ and 4λ.

7.3.2 Microbubble population

Computational domain

To choose the configuration for the contrast sources, we need to make some assumptions about the MBs:

Assumption 2: *In the remaining frequency range, each MB can be considered as a point scatterer.*

Assumption 3: *The oscillatory behavior of each MB is descibed through the Marmottant model.*

Assumption 4: *The MBs are oscillating in the linear regime; hence, the results can be scaled linearly.*

Additionally, for a broadband excitation pulse, a portion of the energy aligns with the resonance frequency of the MBs. An added advantage of a broadband pulse is the ease with which the effects of MB scattering can be identified in the frequency spectrum.

The next step is to describe the contrast domain with the MB population. The size and shape of the scattered field generated by the MB population are expected to be influenced by the size and shape of both the primary source domain and the contrast domain. To understand the mehcanisms behind the MB-proton interaction, we will use three different test cases of cubical contrast domains with sides: (i) smaller than, (ii) equal to, and (iii) larger than the wavelength of the excitation frequency. These configurations will allow us to test the importance of the contrast source domain size relative to the primary source domain size. These contrast domains are depicted in Fig. 7.2

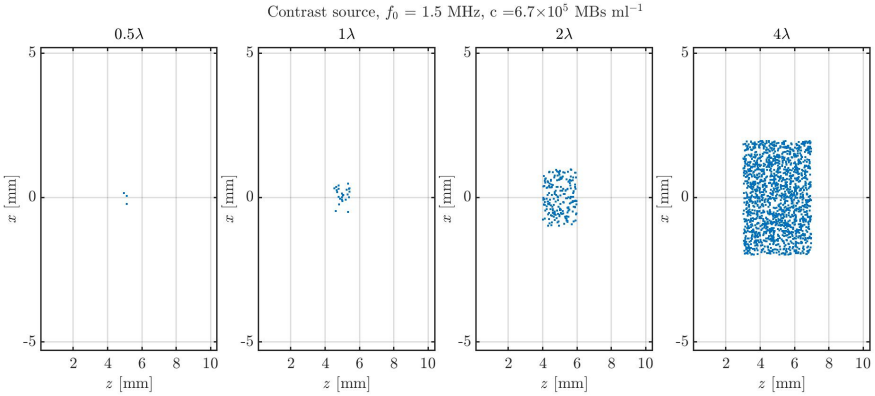

Figure 7.2: Configurations used in the INCS simulations for the contrast source. Contrast domain containing a suspension of 6.3 $\times 10^5$ ml^{-1} MBs, embedded in water for a cubical domain with a side of 0.5λ, 1λ, 2λ and 4λ.

Due to Huygens principle, it is expected that the scattered pressure field will favor a specific direction of propagation, based on the relative location of the primary and contrast source domain. To avoid this and achieve a uniform scattered field, we assume:

Assumption 5: *The domains of the contrast and primary sources should be concentric to avoid any preference in a specific direction of propagation.*

Additionally, another significant parameter in this problem is the concentration of the MB population. As the concentration increases, there are more point sources within the same volume, which can generate smoother pressure patterns and yield more realistic results. Moreover, increasing the concentration renders multiple scattering more significant, which can substantially alter the total pressure field. Additionally, since INCS relies on a Neumann iterative scheme, utilizing a highly concentrated MB population may lead to numerical divergence issues. To solve these problems, we have to limit the concentration so convergence is guaranteed. This limitation is specific to our simulations, whereas in reality, we are not constrained by these numerical boundaries. The reason for this is that in our simulations, the total pressure field is incrementally corrected with each iteration, whereas in reality, the entire pressure field is generated instantaneously.

Another restriction of our computational tool is the way the contrast agents experience the incident field. We assume :

Assumption 6: *The number of protons that stop close to a MB is small compared to the total population and it will on average not significantly affect the incident field experienced by the MBs.*

Table 7.1: Parameters of the Marmottant model of the applied MBs

κ_s [kg/s]	σ_w [N/m]	σ_R [N/m]	γ	χ [N/m]	μ [Pa · s]
1×10^{-8}	0.072	0.03	1.07	0.5	2×10^{-3}

Microbubble size and shell properties

Determining the optimal MB size is crucial as it significantly influences the generation of the scattered pressure field. We can categorize MB sizes based on their resonance frequency relative to the center frequency of the incident pulxe: (i) below, (ii) equal to, and (iii) above the center frequency. This corresponds to phase differences between the scattered and incident fields of (i) 0°, (ii) 90°, and (iii) 180°, respectively. The response of the MB system is a function of the excitation frequency and the resonance frequency of the MBs. Thus, these parameters will also have an effect on the frequency spectrum of the total pressure field, leading to a peak or a dip close to the resonance frequency of the MBs. To ensure synchronous oscillations of the MBs and coherence between the incident and scattered fields, we assume:

Assumption 7: *Coherence can be achieved if the resonance frequency of the MBs is lower than the excitation frequency.*

Concentrating the scattered energy at lower frequencies can also be advantageous for designing sensitive optoacoustic sensors.

The resonance frequency of a single MB increases as its size decreases. [27, 28] Therefore, to achieve a system with a low resonance frequency, it is more logical to use larger MBs. However, the scattered pressure field is a function of the volume, and using larger MBs can lead to numerical divergence at lower concentrations. To address this computational challenge, we can artificially reduce the scattering strength of each point scatterer by some factor, thereby reducing the cumulative scattered field by the same factor.

Now that we have described the effect of MB size, the final parameters to study are the shell properties. To achieve a longer temporal signature, it is crucial for the MB oscillations to last longer. The parameter responsible for this phenomenon is shell viscosity. Additionally, multiple scattering can extend the temporal signature of the system. The stronger the multiple scattering, the more significant its impact on the total pressure field.

Assumption 8: *A low-viscosity shell of a MB will enlongate the temporal signature of the pressure field.*

Assumption 9: *Increasing concentration and thereby enhancing the significance of multiple scattering can generate a longer signal, assisting in the localization of the Bragg peak.*

Based on these assumptions the properties of the MBs that we used for solving the Marmottant equation [22] for an equilibrium radius $R_0 = 6$ μm are given in Table 7.1 [23]. These values correspond to a resonance frequency equal to 0.66 MHz.

7.4 Numerical results

7.4.1 Incident Pressure Fields

In this section, we present the results from the numerical simulations using INCS. Figure 7.3 illustrates the incident pressure fields generated by proton sources for four different primary source domains. As expected, increasing the volume while maintaining the same concentration results in a higher amplitude. This occurs because larger volumes incorporate more point sources, that contributes to the incident field. Moreover, larger volumes and more point sources lead to less uniform pressure fields due to phase differences between various point sources. Moreover, although it is a cubical domain, we observe a smooth pattern of the pressure fields due to the tukey tappering that is applied.

Furthermore, we present the temporal profiles of the generated incident pressure field in Fig. 7.4(a), with sensors placed along the (x, 0 mm, 2 mm) line. As the volume increases, the amplitude and the temporal length of the cumulative pulse also increase, mainly due to the larger number of point sources and larger distances, respectively. To highlight the effect of the MBs on the incident field, we need to isolate the frequency components around the resonance frequency of the MBs, which equals to 0.66 MHz. [29] To achieve this, we apply a Butterworth filter of 4th order with cutoff frequencies between 0.56 and 0.76 MHz. The resulting temporal signatures within this frequency band are shown in Fig. 7.4(b). The length of the generated signals is more distinct in these results.

7.4.2 Scattered Pressure Fields

In Fig. 7.5, we present the pressure fields generated by the MBs. As the volume of the contrast source domain increases, the peak amplitude also increases, mirroring the behavior observed for the incident pressure field. Generally, increasing both the primary and contrast source domains results in higher peak amplitudes. This occurs because larger primary source domains generate higher excitation pressures for the MBs, leading to stronger oscillations and, consequently, stronger scattering. When combined with more point scatterers, this results in a more robust scattered pressure field.

A key observation from these results is that when the MB domain is smaller than or equal to the primary source domain, the distribution is more uniform, and the peak amplitude is higher. A notable example illustrating this observation is the case with sides 2λ for both the primary and the contrast source domains (3,3). This can be explained by the fact that for contrast source domains smaller or equal than the primary source domain, all the MBs are excited at the same time, minimizing the phase differences. On the other hand, if we observe the case with sides of 2λ for the primary source domain and 4λ for the contrast source domain (2,4), the pressure field favors some directions while there are also locations where we have destructive interferences, rendering localization more difficult. This can be explained by the fact that part of the MB population is excited simultaneously, while the rest is excited later resulting in directional behavior. Additionally, as the waves propagate through

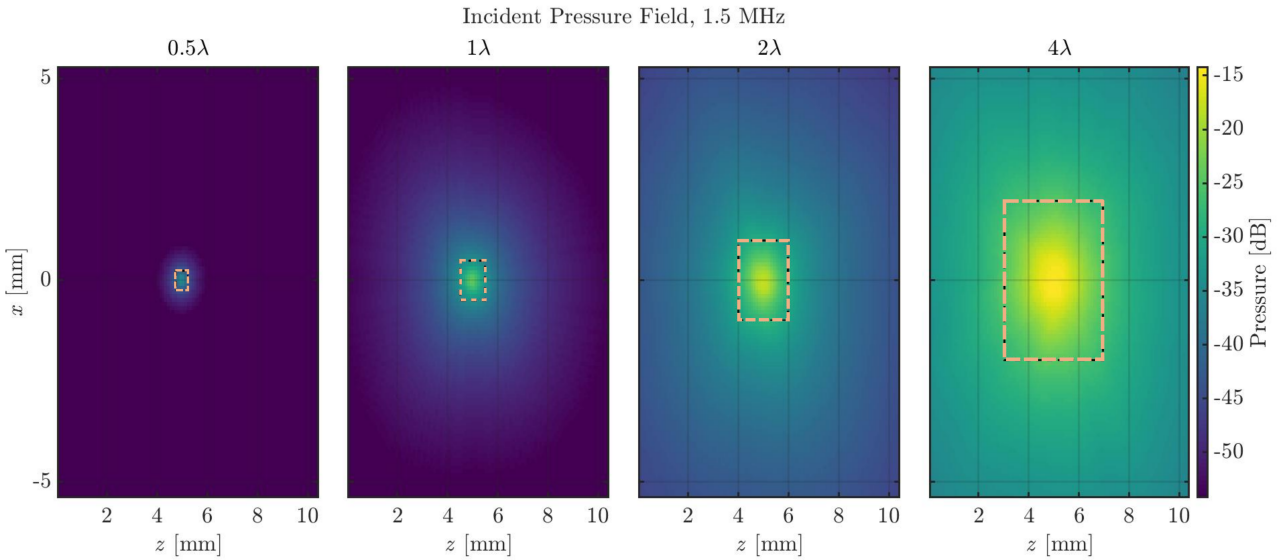

Figure 7.3: Beam profiles of the incident pressure field for a domain with sides of 0.5λ, 1λ, 2λ and 4λ. The proton sources are located inside the orange dashed square.

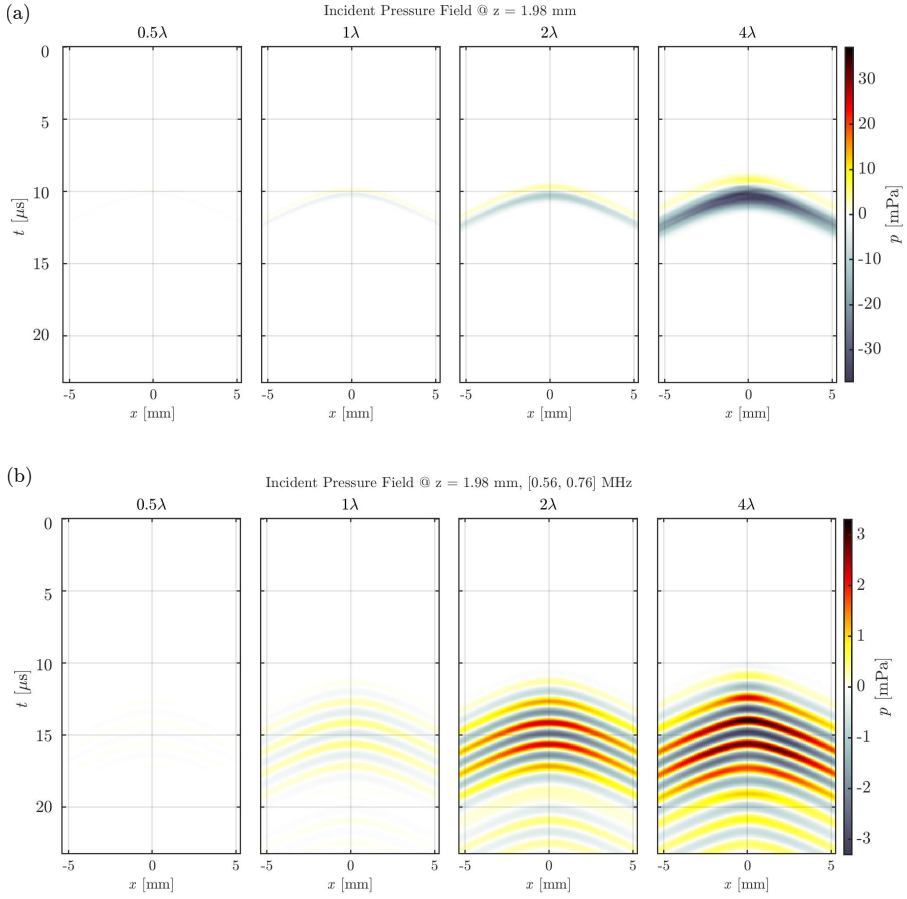

Figure 7.4: Temporal profiles of the generated incident pressure field along the x axis for $z = 2$ mm in for the same four computational domains. The presented results contain (a) all the simulated frequency components and (b) frequencies between [0.56, 0.76] MHz after applying a Butterworth filter of 4th order around the resonance frequency of the MBs (0.66 MHz).

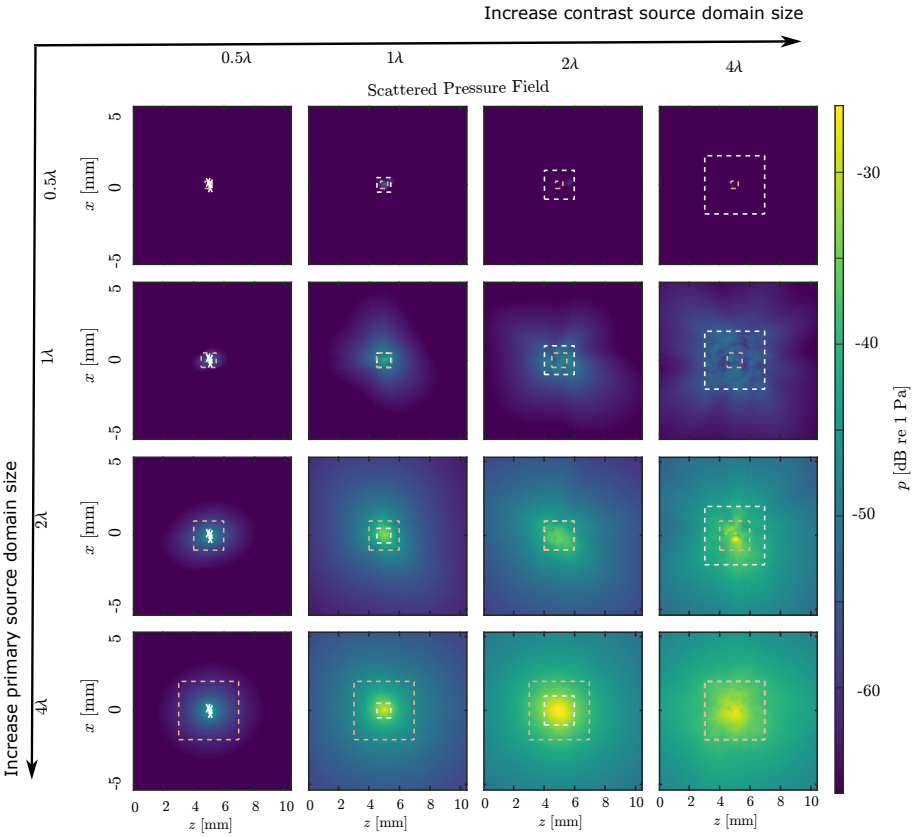

Figure 7.5: Beam profiles of the scattered pressure field for a combination of source and scattering domain with sides of 0.5λ, 1λ, 2λ and 4λ. The proton sources are located inside the orange dashed square and the MBs in the white dashed square.

the MB population, they attenuate and distort, resulting in different excitation fields for MBs located outside the primary source domain boundaries.

In Fig. 7.6, we present the temporal profiles of the scattered pressure fields after applying a Butterworth filter of 4th order with cutoff frequencies 0.56 and 0.76 MHz. Similar patterns emerge as observed with the incident field: as the contrast source domain size increases, mainly the peak amplitude rises, and secondary the pulse duration extends with higher peaks. Similarly, if the both the primary and the contrast source domain become larger (diagonal), there is a faster increase of the peak amplitude and the pulse length due to higher number of point sources and scatterers, and due to the extended boundaries of the volume.

7.4.3 Discussion

Comparing the results in Fig. 7.6 with the total pressure field depicted in Fig. 7.7 highlights the MBs' impact. Unlike the scattered pressure fields, increasing the con-

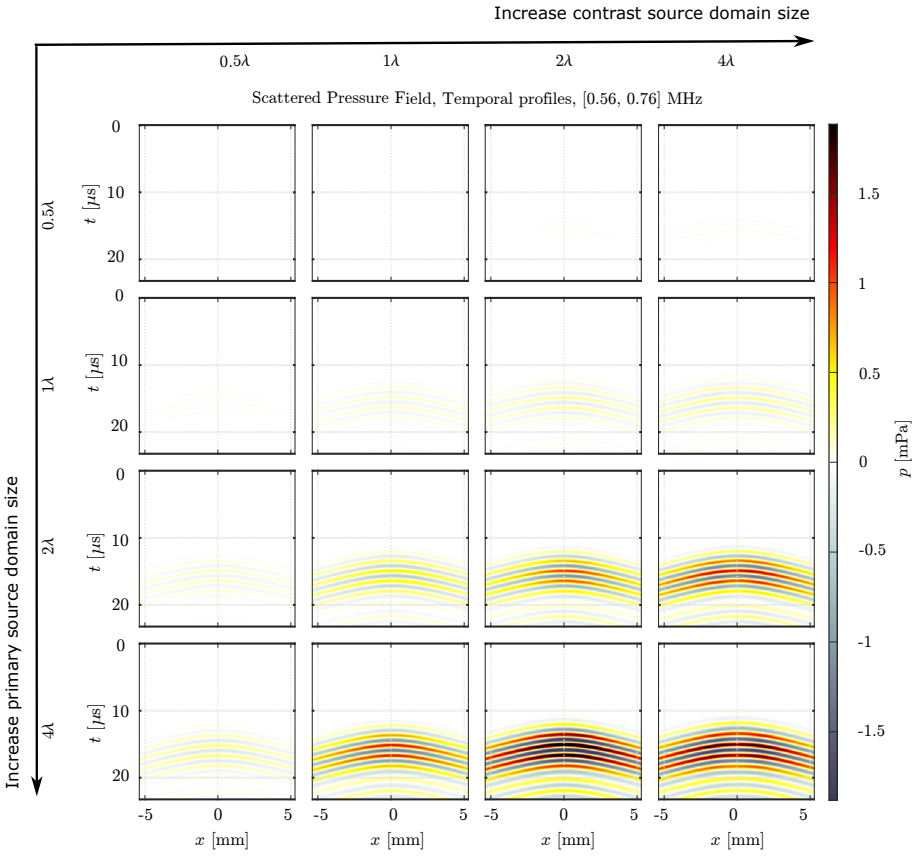

Figure 7.6: Temporal profiles of the generated scattered pressure field along the line (x, 0, 2 mm) for the same four distinct test computational domains as in Fig. 7.5. The presented results contain all the frequencies between [0.56, 0.76] MHz after applying a Butterworth filter of 4th order around the resonance frequency of the MBs (0.66 MHz).

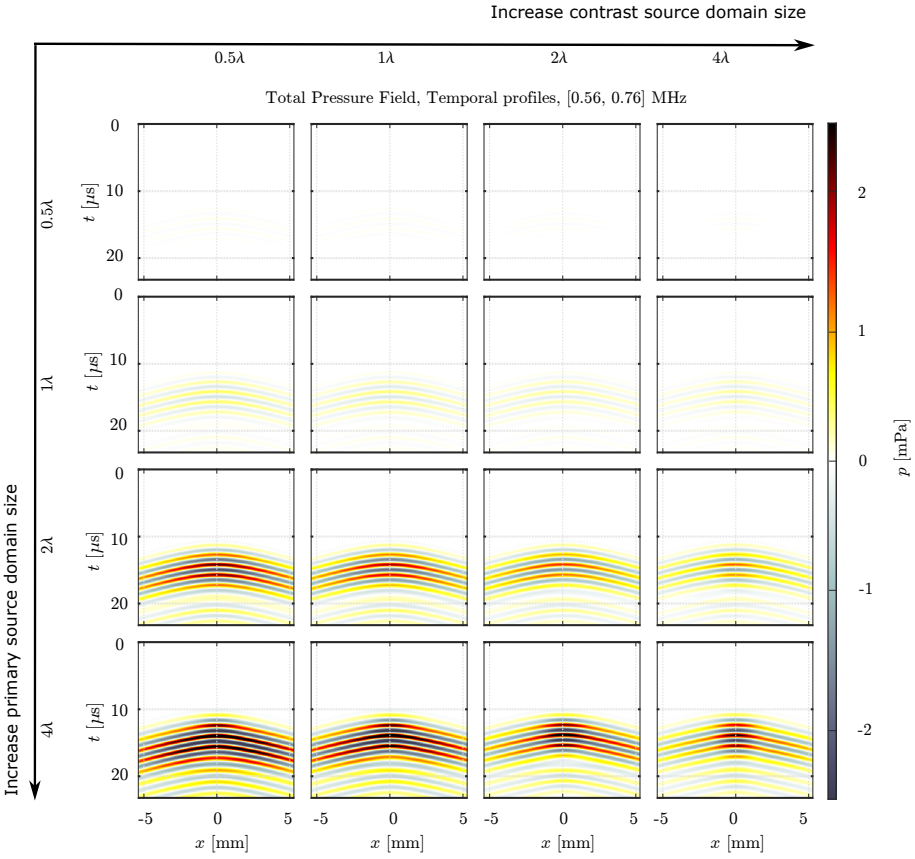

Figure 7.7: Temporal profiles of the generated total pressure field along the line (x, 0, 2 mm) for the same four distinct test computaitional domains as in Fig. 7.5. The presented results contain all the frequencies between [0.56, 0.76] MHz after applying a Butterworth filter of 4th order around the resonance frequency of the MBs (0.66 MHz).

trast source domain size results in a smaller peak amplitude and shorter pulse in the total pressure field. This is due to the destructive interference between the primary and scattered field. Additionally, the distance from the edges of the contrast source domain to the location at $z = 2$ mm varies in each case.

Finally, comparing the incident and total pressure fields reveals differences in frequencies and pulse peaks, as illustrated in Figs. 7.8 and 7.9. These preliminary results showcase the MBs' ability to alter the transmitted field and potentially modify the pulse to enhance Bragg peak localization. We also present the temporal signatures and their respective frequency spectra for each configuration, recorded with a sensor placed at $(x,\ y,\ z) = (0\text{ mm},\ 0\text{ mm},\ 2\text{ mm})$. In this test case, the scattered pressure field is out of phase with the incident field due to the oscillatory behavior of the MBs at the recording location, corresponding to a dip in the frequency spectrum at the resonance frequency of the MBs. This effect becomes more pronounced as both the primary and contrast source domain sizes increase.

Moreover, we observe that increasing the primary or contrast source domain size, and consequently the number of point sources or scatterers, results in a longer total signal. The frequency spectrum shifts from a smooth curve of a broadband pulse to one resembling a narrowband pulse. Additionally, more peaks are observed, reflecting the constructive and destructive interferences of the incident and scattered pressure fields.

7.5 Conclusions

In this chapter, we have detailed the process of extending the INCS method by introducing a point source cloud representing impacting protons alongside a population of MBs. These preliminary results demonstrate the temporal signatures of recorded signals, both with and without MB contrast agents. We show how the length and amplitude of the pulses are influenced and examine the effect on the frequency spectra. Combined with interference between the incident and scattered signals, this can significantly impact the recorded signals, enhancing the submillimeter localization of the Bragg peak.

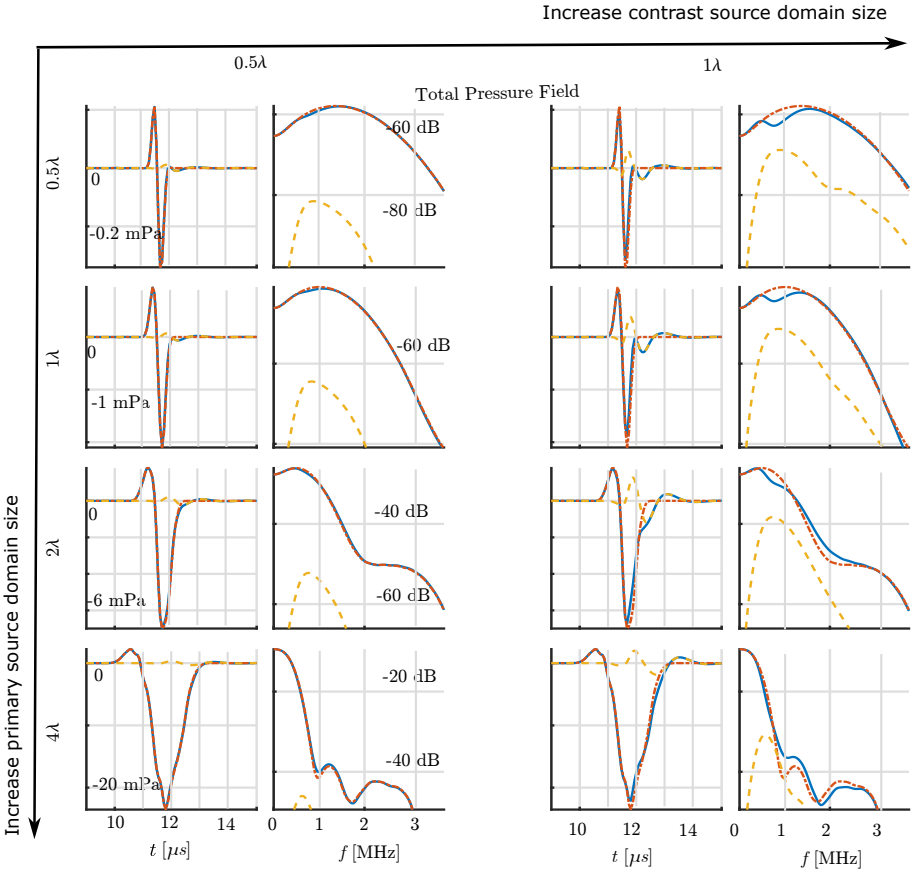

Figure 7.8: Qualitative results of the temporal signatures of the incident (dotted red), scattered(dashed orange) and total (continuous blue) pressure fields at (0 mm, 0 mm, 2 mm). Part (a) : Combinations of source domains with sides equal to 0.5λ and 1λ.

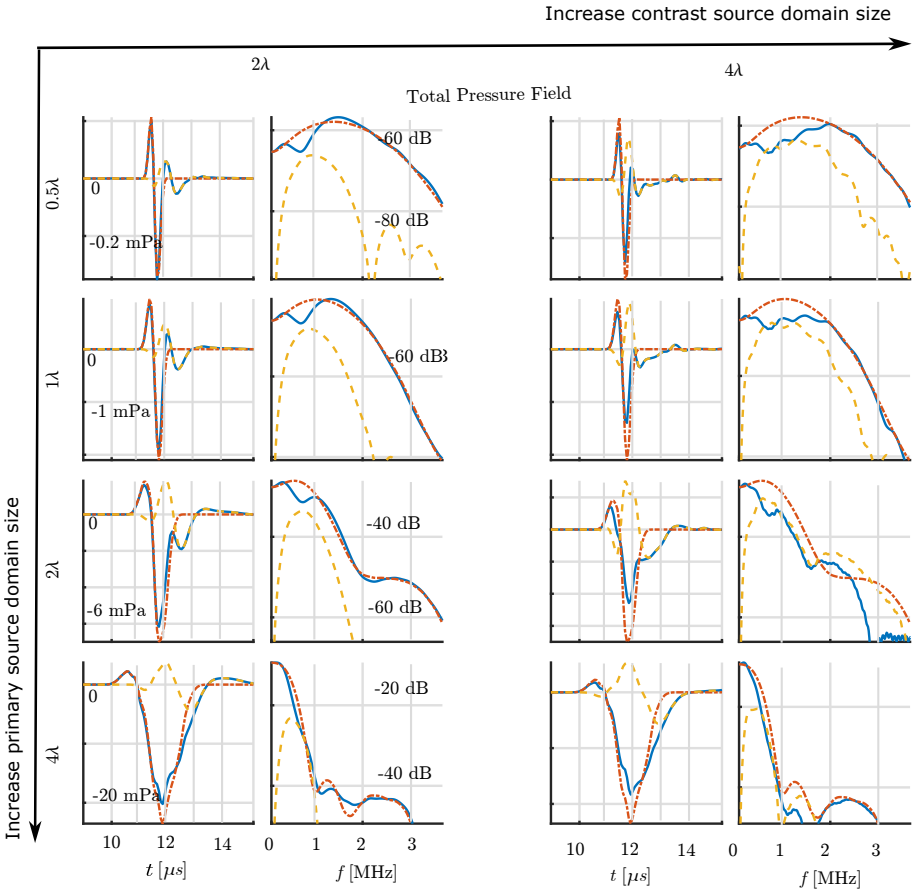

Figure 7.9: Qualitative results of the temporal signatures of the incident (dotted red), scattered(dashed orange) and total (continuous blue) pressure fields at (0 mm, 0 mm, 2 mm). Part (b) : Combinations of source domains with sides equal to 2λ and 4λ.

Bibliography

[1] Paganetti, H., ed. (**2018**). *Proton Therapy Physics* (CRC Press).

[2] Parodi, K., and Polf, J. C. (**2018**). "In vivo range verification in particle therapy" Medical Physics **45**(11).

[3] Knopf, A., and Lomax, A. (**2013**). "In-vivo proton range verification: a review" Physics in Medicine and Biology **58**(15), R131–R160.

[4] Parodi, K. (**2020**). "Latest developments in in-vivo imaging for proton therapy" The British Journal of Radiology **93**.

[5] Hueso-González, F., Enghardt, W., Fiedler, F., Golnik, C., Janssens, G., Petzoldt, J., Prieels, D., Priegnitz, M., Römer, K., Smeets, J., Vander Stappen, F., Wagner, A., and Pausch, G. (**2015**). "First test of the prompt gamma ray timing method with heterogeneous targets at a clinical proton therapy facility" Physics in Medicine and Biology **60**(16), 6247–6272.

[6] Min, C., Kim, C., Youn, M., and Kim, J. (**2006**). "Prompt gamma measurements for locating the dose falloff region in the proton therapy" Applied Physics Letters **89**(18), 183517.

[7] Parodi, K. (**2015**). "Vision 20/20: Positron emission tomography in radiation therapy planning, delivery, and monitoring" Medical Physics **42**(12), 7153–7168.

[8] Parodi, K., Paganetti, H., Shih, H., Michaud, S., Loeffler, J., DeLaney, T., Liebsch, N., Munzenrider, J., Fischman, A., Knopf, A., and Bortfeld, T. (**2007**). "Patient study of in vivo verification of beam delivery and range, using positron emission tomography and computed tomography imaging after proton therapy" International Journal of Radiation Oncology, Biology, Physics **68**.

[9] Hickling, S., Xiang, L., Jones, K., Parodi, K., Assmann, W., Avery, S., Hobson, M., and El Naqa, I. (**2018**). "Ionizing radiation-induced acoustics for radiotherapy and diagnostic radiology applications" Medical Physics **45**(7), e707–e721.

[10] Jones, K. C., Stappen, F. V., Bawiec, C. R., Janssens, G., Lewin, P. A., Prieels, D., Solberg, T. D., Sehgal, C. M., and Avery, S. (**2015**). "Experimental observation of acoustic emissions generated by a pulsed proton beam from a hospital-based clinical cyclotron" Medical Physics **42**(12), 7090–7097.

[11] Matte, G. M., Neer, P. L. M. J. V., Danilouchkine, M. G., Huijssen, J., Verweij, M. D., and Jong, N. D. (**2011**). "Optimization of a phased-array transducer for multiple harmonic imaging in medical applications: frequency and topology" IEEE Transactions on Ultrasonics, Ferroelectrics and Frequency Control **58**(3), 533–546.

[12] Van Neer, P. L. M. J., Matte, G., Danilouchkine, M. G., Prins, C., Adel, F. V. D., and Jong, N. D. (**2010**). "Super-harmonic imaging: development of an interleaved phased-array transducer" IEEE Transactions on Ultrasonics, Ferroelectrics, and Frequency Control **57**(2), 455–468.

[13] Lascaud, J., Dash, P., Würl, M., Wieser, H.-P., Wollant, B., Kalunga, R., Assmann, W., Clevert, D.-A., Ferrari, A., Sala, P., Savoia, A. S., and Parodi, K. (**2021**). "Enhancement of the ionoacoustic effect through ultrasound and photoacoustic contrast agents" Scientific Reports **11**(2725).

[14] Daeichin, V., Lum, J., Borden, M., and Murray, T. (**2020**). "A new photoacoustic based technique for single microbubble characterization" in *The 25th European Symposium on Ultrasound Contrast Imaging*, pp. 42–44.

[15] Lum, J., Stobbe, D., and Murray, T. (**2018**). "Photoacoustic technique to measure temperature effects on microbubble viscoelastic properties" Applied Physics Letters **112**(11).

[16] Carlier, B., Heymans, S., Nooijens, S., Toumia, Y., Ingram, M., Paradossi, G., D'Agostino, E., Himmelreich, U., D'hooge, J., Van Den Abeele, K., and Sterpin, E. (**2020**). "Proton range verification with ultrasound imaging using injectable radiation sensitive nanodroplets: a feasibility study" Physics in Medicine & Biology **65**.

[17] G. Collado-Lara, S. V. Heymans, M. Rovituso, B. Carlier, Y. Toumia, M. Verweij, G. Paradossi, E. Sterpin, H. J. Vos, J. D'hooge, N. de Jong, K. Van Den Abeele, and V. Daeichin, "Spatiotemporal distribution of nanodroplet vaporization in a proton beam using real-time ultrasound imaging for range verification", Ultrasound Med. Biol. **48**, 1, 149–156 (2022).

[18] F. R. Deurvorst, G. Collado Lara, A. Matalliotakis, H. J. Vos, N. de Jong, V. Daeichin, and M. D. Verweij, "A spatial and temporal characterisation of single proton acoustic waves in proton beam cancer therapy", J. Acoust. Soc. Am. **151**, 2, 1200 (2022). https://doi.org/10.1121/10.0009567.

[19] J. Huijssen, "Modeling of nonlinear medical diagnostic ultrasound", PhD Thesis, Delft University of Technology(2008), available from http://reposity.tudelft.nl).

[20] L. Demi, "Modeling nonlinear propagation of ultrasound through inhomogeneous biomedical media",PhD Thesis, Delft University of Technology(2013), available from http://reposity.tudelft.nl).

[21] A. Matalliotakis, and M.D. Verweij, "Computation of ultrasound propagation in a population of nonlinearly oscillating microbubbles including multiple scattering", J. Acoust. Soc. Am. **153**, 2209–2222 (2023).

[22] P. Marmottant, S. van der Meer, M. Emmer ,M. Versluis, N. de Jong, S. Hilgenfeldt, and D. Lohse, "A model for large amplitude oscillations of coated bubbles accounting for buckling and rupture", J. Acoust. Soc. Am. **118**,3499–3506(2005).

[23] T. Segers, P. Kruizinga, M. Kok, G. Lajoinie, N. de Jong, and M. Versluis, "Monodisperse Versus Polydisperse Ultrasound Contrast Agents: Non-Linear Response, Sensitivity, and Deep Tissue Imaging Potential", Ultr. Med. & Biol. **44(7)**, 1482–1492, (2018).

[24] L. Demi, M.D. Verweij, J. Huijssen, N. de Jong, and K.W.A. van Dongen, "Attenuation of ultrasound pressure fields described via a contrast source formulation", Proceedings of 2009 IEEE Ultrasonics, 1590–93 (2009).

[25] L. Demi, K.W.A. van Dongen and M.D. Verweij, "A contrast source method for nonlinear acoustic wave fields in media with spatially inhomogeneous attenuation", J. Acoust. Soc. Am. **129**, 1221–1230 (2011).

[26] A. Matalliotakis, D. Maresca, and M.D. Verweij, "Nonlinear interaction of two cross-propagating plane waves", arXiv, (2023).

[27] S. M. van der Meer, B. Dollet, M. M. Voormolen, C. T. Chin, A. Bouakaz, N. de Jong, M. Versluis, & D. Lohse, "Microbubble spectroscopy of ultrasound contrast agents", J. Acoust. Soc. Am. **121**(1), 648–656 (2007).

[28] A. A. Doinikov, J. F. Haac, and P. A. Dayton, "Resonance frequencies of lipid-shelled microbubbles in the regime of nonlinear oscillations", Ultrasonics **49**(2), 263–268 (2009).

[29] A. Matalliotakis, M.D. Verweij, and D. Maresca, "Polydisperse versus monodisperse microbubbles: A simulation study for contrast-enhanced ultrasound", arXiv, (2023).

Chapter 8

Conclusions and Discussion

8.1 Conclusions

We have presented a comprehensive numerical method to fully describe both the linear and nonlinear physical phenomena encountered during ultrasound propagation through a population of oscillating MBs. This method is an extension of the existing Iterative Nonlinear Contrast Source (INCS) method, originally devised to solve the four-dimensional spatiotemporal Westervelt equation. Initially developed to compute pulsed acoustic pressure fields in nonlinear, homogeneous, and lossless media, INCS has been later expanded to incorporate spatially varying frequency power law attenuation, nonlinearity coefficients, and speed of sound. With its coarse discretization, omnidirectionality and scalability, INCS emerges as an ideal framework for simulating the collective dynamics of MB populations under an external ultrasonic pressure field in large-scale configurations. By extending INCS, we have provided the field of medical ultrasound with an efficient and accurate computational tool that advance diagnostic and therapeutic applications.

From the research presented in this thesis, the following conclusions may be drawn:

- We have shown that INCS can be extended by introducing a pressure-dependent contrast source term for linear scatterers and nonlinear MBs. Each MB is represented as a point source. The strength of the point source is a function of the volume acceleration of the MB, thus dependent on the time-varying radius, which is computed by solving the extended Rayleigh Plesset equation for each MB. This approach treats each MB independently, refraining from treating the problem as an effective medium but rather as a many-body system. Furthermore, this methodology accounts for multiple scattering effects. Being based on the Neumann iterative scheme, physically each iteration in INCS represents an additional order of multiple scattering. Convergence of the method is ontained when the inclusion of an extra order of multiple scattering yields a negligible impact on the solution. Consequently, INCS is capable of disentangling scattering orders and offering valuable insights into interactions within a MB population. Notably, our findings highlight the critical role of multiple scattering, particularly at higher concentrations.

- Our research demonstrates the extension of INCS through the inclusion of a contrast source term that represents local nonlinearities. Our results show the local behavior of these nonlinearities in case of non-collinear wave interactions, in contrast to global medium nonlinearities, which accumulate throughout depth. Moreover, analytical descriptions allow for the prediction of the amplitude of local nonlinearities, which in line with the generated computational results, indicate their weak strength compared to global medium nonlinearities.

- We conducted a comprehensive comparative analysis, contrasting conventional pulsing schemes with a novel imaging approach employing cross-propagating plane waves, known as X-waves. To assess their impact on contrast-enhanced ultrasound, we propagated each wave through a population of nonlinear oscillating monodisperse MB and compared the accumulation of the nonlinearities due to wave propagation below this suspension. By employing amplitude modulation techniques, our investigation highlights the superior sensitivity and specificity of the supersonic X-shaped wavefronts over imaging techniques based on focused, planar and diverging wavefronts. To visualize these findings, we reconstructed beamformed images from our computational results. Distinguishing MBs from tissue-mimicking scatterers proves challenging in B-mode images, while nonlinear imaging artifacts are notably pronounced in focused, planar, and diverging wave scenarios in the contrast-enhanced images. Conversely, X-waves exploit the full potential of nonlinear scattering from monodisperse MBs without generating significant imaging artifacts. The outcomes of our study establish a robust link between simulations and clinical applications in diagnostic medical ultrasound, paving the way for further advancements in the field.

- We have shown the ability of INCS to incorporate populations of polydisperse MBs. Through a comparative analysis employing plane wave excitation, our findings reveal that resonant monodisperse MBs exhibit the highest degree of nonlinear scattering. Conversely, polydisperse suspensions exhibit less constructive interference and weaker scattering compared to monodisperse populations. we successfully disentangled the harmonics that are present in the scattering from each population, providing valuable insights into the collective dynamics of MB populations. Additionally, we simulated an incident acoustic pressure field generated by a phased array, conventionaly used in contrast-enhanced imaging. While resonant monodisperse MBs prove to be robust and efficient scatterers, they are susceptible to generating nonlinear imaging artifacts. In contrast, polydisperse MBs, characterized by their non- constructive scattering, produce less imaging artifacts. However, their weaker scattering may pose challenges in detection, particularly in applications such as deep tissue imaging.

- Finally, INCS was validated as a robust tool for simulating the acoustic pressure generated by a therapeutic proton beam. We successfully modeled the incident acoustic pressure fields produced by a cloud of point emitters representing impacting protons, along with a population of monodisperse microbubbles (MBs). To investigate the interaction between protons and MBs, simulations were conducted for cubic domains with side lengths of 0.5λ, 1λ, 2λ, and 4λ. These

preliminary results reveal the temporal characteristics of the recorded signals, both with and without MB contrast agents. We demonstrate how the pulse length and amplitude are affected, and we analyze the resulting impact on the frequency spectra. Additionally, interference between incident and scattered signals is shown to significantly influence the recorded signals, improving the submillimeter localization of the Bragg peak. This framework serves as a foundational study, aiming to advance the understanding of Bragg peak localization using the most conventionally used ultrasound contrast agents.

8.2 Discussion

The work presented in this thesis can be used as a basis to further investigate limitations, extensions and applications of the described numerical method.

Limitations :

- As described in Chapter 2, a limitation of our method is the restricted convergence of the extended INCS method that deals with large populations of scatterers. The convergence of the iterative scheme hinges on factors such as gas volume concentration, scattering strength, and excitation frequency. Moreover, the accuracy of the acoustic pressure field improves incrementally with each iteration through increasingly precise field corrections. Thus, for achieving a highly accurate implicit solution, all field corrections are necessary. If the Neumann scheme diverges, alternative iterative schemes can be explored, particularly those employing preconditioners to restrict large differences between in the initial iterations. For instance, more advanced Conjugate Gradient schemes may prove effective in handling strong contrasts while significantly enhancing convergence rates.

- The memory usage poses a challenge when computations in large domains are performed through CPU parallelization. In that case, a bottleneck arises in the MPI_Alltoall command within the current INCS implementation, used to transpose the matrix that stores the spatiotemporal pressure field and used to transition distribution from space=frequency $(x - \omega)$ space to wavenumber-frequency $(k - \omega)$ space. With multiple nodes employment, communication inefficiencies emerge, leading to increased total simulation time. This poses a problem especially in the applications in which we want to receive the scattered echoes at the transducer surface.

Extensions :

- Numerous enhancements can elevate the simulations, rendering them more comprehensive and applicable in clinical settings. One such improvement involves integrating experimentally measured incident pressure fields as input for the simulations. Furthermore, refining domain geometries to mirror complex human organ physiology can enhance realism and applicability. While we succeeded in incorporating multiple populations of scatterers, expansion to more intricate

combinations is feasible. Moreover, elevating the assumption of non-moving MBs (due to the short temporal framework) by implementing a two-way coupling method can provide a solution. This approach involves feeding the total acoustic pressure field into a solver for the 4D spatiotemporal Navier-Stokes equation, which in turn offers fluid motion as output. Additionally, employing more intricate equations to model MB oscillations, considering phenomena like heat transfer or nonspherical oscillations, can enhance accuracy. Finally, using point populations can accurately describe an abstract primary source or an abstract contrast scatterer.

- At a computational level, GPU parallelization becomes imperative to enhance INCS capabilities for larger MB populations. Achieving convergence is pivotal, where a significant bottleneck arises in dense populations due to the multiplication of the temporal with the spatial signatures of each MB, implemented via the library DGEMM of CBLAS, used for matrix multiplication.

Applications :

- An essential and intriguing aspect of advancing this research and fortifying the connection between simulations and clinical practice involves comparing the generated acoustic pressure fields of MB populations with corresponding experimental data. These experiments could encompass measurements of scattering amplitude, frequency content, variations in speed of sound, and pressure-dependent attenuation within populations of both monodisperse and polydisperse MBs. Initially, the results obtained from in vitro experiments serve as a crucial validation step for the extended INCS method, implemented in this research framework, illustrating the differences between simulations and experimental outcomes. Second, such experiments can highlight the importance of multiple scattering and provide valuable insights into the collective dynamics of scatterer populations.

- It would be interesting to implement a large-scale parametric study that aims to obtain a nonlinearity parameter β for the Westervelt equation from the MB parameters.

The full potential of the developed methods has not been exhaustively explored in this thesis, as the primary focus of the research presented here was on extending the original INCS method to model nonlinear propagation in MB populations. However, the findings of this research underscore INCS as a valuable simulation tool for various diagnostic and therapeutic scenarios. Indeed, INCS demonstrates efficacy in diagnostic applications like contrast-enhanced imaging, as well as in therapeutic settings such as optimizing patient-specific treatment plans for proton therapy. Additionally, its versatility extends to other medical ultrasound applications, including drug delivery with targeted MBs and ultrasound localization microscopy. In conclusion, INCS emerges as a key facilitator in bridging the gap between simulation capabilities and clinical applications, thus paving the way for advancements in medical ultrasound technologies.

Summary

For over 50 years, medical ultrasound has been a pioneering force in healthcare, seamlessly blending diagnostic and therapeutic applications. In diagnostics, ultrasound reveals intricate internal structures based on the generation of acoustic pressure waves in the human body and capturing reflections from tissue and body structures, enabling precise anomaly identification. Simultaneously, in therapy, ultrasound utilizes its acoustic prowess for targeted interventions and submillimeter localization in unconventional cancer treatments like proton therapy. The field has shifted significantly with the advent of nonlinear acoustics, exploring wave propagation phenomena. Contrast agents marked a revolutionary leap, enhancing the specificity, sensitivity, and efficiency of diagnostic and therapeutic ultrasound. Microbubbles, as the most conventionally used agents, exhibit strong nonlinear scattering under ultrasonic excitation, making them suitable for CEUS applications.

While the three-dimensional oscillatory dynamics of a single MB are well-explored, the collective behavior of a MB population remains unknown. To establish the complete physical understanding of the nonlinear phenomena that occur during ultrasound propagation through a cloud of MBs, a comprehensive multiparametric experimental study is imperative. However, exploring every conceivable property combination for a single MB and project it to a cloud of MBs in such detail would entail a highly expensive, time-consuming, and facility-restrictive procedure. This becomes especially pronounced in cancer treatment applications, where time is of the essence.

To overcome these challenges, we employ an already-developed and dedicated numerical algorithm called the Iterative Nonlinear Contrast Source (INCS) method. Due to its coarse discretization of two points per wavelength or period, it proves to be the most suitable among existing methods for handling large-scale simulations. Methods based on Finite Differences (FD) or Finite Elements (FE) involve finer discretization, resulting in memory-intensive simulations. An additional advantage of INCS, crucial for simulating the scattering of three-dimensional spherical waves emitted from each MB, is its omnidirectionality. In contrast, forward-wave methods that favor a specific direction of propagation are unsuitable for these types of numerical experiments. A final benefit of INCS is its easy expandability to include phenomena such as attenuation, inhomogeneities, and more. The objective of this study is to extend INCS to simulate the occurring nonlinear phenomena during ultrasound propagation through a MB population for diagnostic and therapeutic applications.

Originally, INCS was developed to solve the four-dimensional spatiotemporal West-

ervelt equation. Based on the Neumann iterative scheme, the acoustic pressure is updated by generating increasingly accurate field corrections. These field corrections are computed through the four-dimensional spatiotemporal convolution of the Green's function of the linear, homogeneous, lossless background medium with each contrast source term added to the simple wave equation. This process can be implemented as long as the contrast source term can be expressed directly or indirectly as a function of the acoustic pressure.

In **Chapter 2**, INCS is extended to incorporate the scattering of a population of monodisperse scatterers. Initially, we explain how to introduce linear and nonlinear scatterers, with the contrast source term being a direct function of acoustic pressure. Later, each MB is included as a contrast point scatterer with independent properties. In this case, the temporal signature of the source term is a function of the volume acceleration and therefore the radius of the MB. Assuming spherical oscillations, we can acquire the radius as a function of time by solving the Marmottant equation (indirectly related to acoustic pressure) of each MB in each iteration. Physically, each iteration accounts for an order of multiple scattering. Numerical results demonstrate that multiple scattering should be taken into account, especially for populations of high concentration.

With the initial step towards our goal established, we conduct a rigorous analytical and numerical study to compare the impact of local and global medium nonlinearities in **Chapter 3**. Local nonlinearities are observed during noncollinear wave interaction and therefore they might manifest themselves due to scattering inside a MB population. INCS is extended with the source term due to local nonlinearities, which is a function of the Lagrangian density, the difference between kinetic energy density and potential energy density. A simple test case is studied where two finite pulsed plane waves cross-propagate under an angle of 20° generating an x-shaped wavefront. Numerical results reveal that local nonlinearities are a localized and instantaneous phenomenon, weaker in amplitude than gradually accumulating global medium nonlinearities. Consequently, the nonlinear contrast source term due to local nonlinearities can be neglected, whereas the effect should be studied in the presence of nonlinear oscillating MBs.

In **Chapter 4**, we showcase the inaugural application of CEUS imaging using INCS for a monodisperse MB suspension. Our investigation delves into the impact of four distinct wavefront shapes, including two cross-propagating plane waves (x-waves), a focused beam, a diverging wave, and a finite pulsed plane wave, as they propagate through monodisperse MBs. INCS is expanded to incorporate local and global medium nonlinearities, MB scattering, and reflections from tissue-mimicking linear scatterers surrounding the suspension, facilitating the reconstruction of CEUS images. Focusing on monodisperse resonant MBs, recognized as the most nonlinear conventionally used contrast agents, this study marks the first instance of employing multiple populations and generating beamformed images using INCS, establishing a direct link between simulations and future clinical studies. Our numerical findings highlight that imaging with focused, planar, and diverging wavefronts induces nonlinear artifacts, potentially leading to the misclassification of tissue as ultrasound contrast agents. Notably, x-waves enhance the sensitivity and specificity of ultrasound imaging for monodisperse MBs surrounded by tissue, without generating distal

imaging artifacts due to nonlinear propagation.

After successful B-mode and CEUS image generation, **Chapter 5** focuses on a numerical comparison between monodisperse and polydisperse MB populations. Extending INCS to incorporate polydisperse MB clouds, where each scatterer varies in size, we showcase its ability to disentangle harmonics of scattered waves when excited by a finite pulsed plane wave, providing insights into collective MB behavior. Results indicate resonant monodisperse populations exhibit the strongest scattering in the fundamental frequency, while off-resonance monodisperse populations display the highest amplitude around their resonance frequency. Despite simulations offering valuable insights, connecting them with clinical applications like CEUS for deep tissue imaging is crucial. Consequently, we present a comparative study between polydisperse and monodisperse populations when excited by a field from a conventional ultrasound machine. While monodisperse populations enhance ultrasound sensitivity, nonlinear imaging artifacts accumulate downstream of the MBs. In contrast, polydisperse suspensions, despite weaker scattering, exhibit a more favorable response without significant artifact accumulation.

In **Chapter 6**, we address the need for real-time *in vivo* range verification in proton beam cancer therapy with submillimeter precision. Acoustic imaging technologies, potentially leveraging local interactions between protons and MBs, offer an intriguing avenue. Employing INCS for this purpose requires a missing theoretical model characterizing the acoustic field from an individual proton. In this research framework, we develop an acoustic imaging model for a single proton on nanometer and micrometer scales, incorporating adiabatic expansion and quantifying secondary electron production. Numerical simulations unveil spatiotemporal characteristics, revealing a bipolar spike with a center frequency around 86.7 GHz. Positive peak pressures decrease radially, reaching 0.24 MPa at 5 μm, with a -2.6 kPa negative pressure at 30 nm from the Bragg peak. Utilizing wavefield expansion and asymptotic approximations extends the spatial and temporal ranges of the proton acoustic field. Overall, this work provides a comprehensive spatiotemporal characterization of the acoustic field from a single proton.

After developing an acoustic model predicting pressure waves from a single proton's heat deposition, a theoretical model for MB population scattering when excited by a proton-generated acoustic field becomes crucial. In this way, we employ INCS not only for diagnostic but also for therapeutic ultrasound. In **Chapter 7**, we demonstrate the novel extension of INCS also to the primary source term which is responsible for the generation of the incident pressure field. In this study, we examine the influence of the proton beam's pressure field on MB population scattering by introducing an extra contrast source term in the wave equation. The domain size and location impact the overall system behavior, providing insights into the interaction between a proton beam and a MB population.

This research highlights the effectiveness of INCS in addressing clinically significant applications of medical ultrasound for both diagnostic and therapeutic purposes. INCS proves adept at thoroughly elucidating the physics behind the nonlinear propagation of medical ultrasound through populations of either monodisperse or polydisperse contrast agents, fostering an understanding of the mechanisms underlying occurring acoustic phenomena. Additionally, INCS enables the exploration of differ-

ences between conventionally used pulsing schemes in CEUS imaging, enhancing vascular visualization through real-time and non-invasive procedures. Moreover, INCS facilitates multiparametric studies for therapeutic ultrasound, providing a means to streamline the cost and time associated with patient-specific treatment plans in cancer therapy. Ultimately, this study paves the way for advancing numerical tools to establish a connection between simulations and clinical studies in medical ultrasound applications.

Samenvatting

Voor meer dan 50 jaar is medische echografie een baanbrekende kracht geweest in de gezondheidszorg, naadloos integrerend met diagnostische en therapeutische toepassingen. In de diagnostiek onthult echografie ingewikkelde interne structuren op basis van de generatie van akoestische drukgolven in het menselijk lichaam en het vastleggen van reflecties van weefsels en lichaamsstructuren, waardoor nauwkeurige identificatie van afwijkingen mogelijk is. Tegelijkertijd gebruikt echografie in therapie zijn akoestische kracht voor gerichte interventies en submillimeterlokalisatie bij onconventionele kankerbehandelingen zoals protontherapie. Het vakgebied heeft aanzienlijke verschuivingen ondergaan met de opkomst van niet-lineaire akoestiek, waarbij fenomenen in golfvoortplanting worden verkend. Contrastmiddelen markeerden een revolutionaire sprong, waardoor de specificiteit, gevoeligheid en efficiëntie van diagnostische en therapeutische echografie werden verbeterd. Microbellen, als de meest conventioneel gebruikte middelen, vertonen sterke niet-lineaire verstrooiing onder ultrasone excitatie, waardoor ze geschikt zijn voor CEUS-toepassingen.

Hoewel de driedimensionale oscillerende dynamiek van een enkele microbel goed is onderzocht, blijft het collectieve gedrag van een populatie microbellen onbekend. Om het volledige fysieke begrip van de niet-lineaire verschijnselen die optreden tijdens de echografische voortplanting door een wolk van microbellen vast te stellen, is een uitgebreide multiparametrische experimentele studie noodzakelijk. Het verkennen van elke denkbare combinatie van eigenschappen voor een enkele microbel en dit tot in detail projecteren op een wolk van microbellen zou echter een zeer kostbare, tijdrovende en faciliteitsbeperkende procedure vereisen. Dit wordt vooral duidelijk bij toepassingen in de behandeling van kanker, waar tijd van essentieel belang is.

Om deze uitdagingen te overwinnen, maken we gebruik van een reeds ontwikkeld en toegewijd numeriek algoritme genaamd de Iterative Nonlinear Contrast Source (INCS) methode. Vanwege de grove discretisatie van twee punten per golflengte of periode blijkt dit de meest geschikte methode onder bestaande methoden voor het behandelen van grootschalige simulaties. Methoden gebaseerd op Finite Differences (FD) of Finite Element (FE) omvatten fijnere discretisatie, resulterend in geheugenintensieve simulaties. Een extra voordeel van INCS, cruciaal voor het simuleren van de verstrooiing van driedimensionale bolvormige golven uitgezonden door elke microbel, is de omni-richtingsgevoeligheid ervan. In tegenstelling tot voorwaartse golfmethoden die een specifieke voortplantingsrichting begunstigen, zijn ongeschikt voor dit soort numerieke experimenten. Een laatste voordeel van INCS is de eenvoudige uitbrei-

dbaarheid om fenomenen zoals demping, onhomogeniteiten en meer op te nemen. Het doel van deze studie is om INCS uit te breiden om de optredende niet-lineaire verschijnselen tijdens echografische voortplanting door een microbellenpopulatie voor diagnostische en therapeutische toepassingen te simuleren.

Oorspronkelijk werd INCS ontwikkeld om de vierdimensionale spatiotemporale Westervelt-vergelijking op te lossen. Gebaseerd op het Neumann-iteratie schema wordt de akoestische druk bijgewerkt door steeds nauwkeurigere veldcorrecties te genereren. Deze veldcorrecties worden berekend via de vierdimensionale spatiotemporale convolutie van de Green's-functie van het lineaire, homogene, verliesloze achtergrondmedium met elk contrastbronterm die aan de eenvoudige golfvergelijking is toegevoegd. Dit proces kan worden geïmplementeerd zolang de contrastbronterm direct of indirect als een functie van de akoestische druk kan worden uitgedrukt.

In **Hoofdstuk 2** wordt INCS uitgebreid om de verstrooiing van een populatie monodisperse verstrooiers op te nemen. Eerst leggen we uit hoe lineaire en niet-lineaire verstrooiers kunnen worden geïntroduceerd, waarbij de contrastbronterm een directe functie is van de akoestische druk. Later wordt elke microbel opgenomen als een contrastpuntverstrooier met onafhankelijke eigenschappen. In dit geval is de tijdsignatuur van de bronterm een functie van de volumebeweging en dus de straal van de microbel. Door uit te gaan van sferische oscillaties kunnen we de straal als functie van de tijd verkrijgen door de Marmottant-vergelijking (indirect gerelateerd aan de akoestische druk) van elke microbel in elke iteratie op te lossen. Fysisch gezien houdt elke iteratie rekening met een orde van meervoudige verstrooiing. Numerieke resultaten tonen aan dat meervoudige verstrooiing in aanmerking moet worden genomen, vooral voor populaties van hoge concentratie.

Met de initiele stap naar ons doel gevestigd, voeren we een grondige analytische en numerieke studie uit om het verschil te vergelijken tussen lokale en globale mediumniet-lineariteiten in **Hoofdstuk 3**. Lokale niet-lineariteiten worden waargenomen tijdens niet-collineaire golfinteractie en kunnen zich dus manifesteren door verstrooiing binnen een microbellenpopulatie. INCS wordt uitgebreid met de bronterm als gevolg van lokale niet-lineariteiten, die een functie is van de Lagrangiaanse dichtheid, het verschil tussen de dichtheid van kinetische energie en potentiele energie. Er wordt een eenvoudig testgeval bestudeerd waarbij twee eindige gepulseerde vlakke golven dwars gepropageerd worden onder een hoek van 20°, wat resulteert in een X-vormige golffront. Numerieke resultaten tonen aan dat lokale niet-lineariteiten een gelokaliseerd en onmiddellijk fenomeen zijn, zwakker in amplitude dan geleidelijk opbouwende globale mediumniet-lineariteiten. Bijgevolg kan de niet-lineaire contrastbronterm als gevolg van lokale niet-lineariteiten verwaarloosd worden, terwijl het effect bestudeerd moet worden in aanwezigheid van niet-lineair oscillerende microbellen.

In **Hoofdstuk 4** laten we de inaugurale toepassing van CEUS-beeldvorming met INCS zien voor een monodisperse microbellenoplossing. Onze studie onderzoekt de impact van vier verschillende golfvormen, waaronder twee kruislings voortplantende vlakke golven (X-golven), een gefocuste bundel, een divergerende golf en een eindige gepulseerde vlakke golf, terwijl ze zich voortplanten door monodisperse microbellen. INCS wordt uitgebreid om lokale en globale mediumniet-lineariteiten, microbellenverstrooiing en reflecties van weefselmimiciserende lineaire verstrooiers rondom de

oplossing op te nemen, waardoor de reconstructie van CEUS-beelden mogelijk is. Met de nadruk op resonante monodisperse microbellen, erkend als de meest niet-lineaire conventioneel gebruikte contrastmiddelen, markeert deze studie het eerste geval van het genereren van beeldgevormde beelden met INCS, waarbij een directe link wordt gelegd tussen simulaties en toekomstige klinische studies. Onze numerieke bevindingen benadrukken dat beeldvorming met gefocuste, vlakke en divergerende golfvormen niet-lineaire artefacten veroorzaakt, wat mogelijk leidt tot de misclassificatie van weefsel als contrastmiddelen voor echografie. Opmerkelijk verbeteren X-golven de gevoeligheid en specificiteit van echografie voor monodisperse microbellen omgeven door weefsel, zonder distale artefacten te genereren door niet-lineaire voortplanting.

Na succesvolle B-mode en CEUS-beeldgeneratie richt **Hoofdstuk 5** zich op een numerieke vergelijking tussen monodisperse en polydisperse microbellenpopulaties. Door INCS uit te breiden naar polydisperse microbellenwolken, waarbij elke verstrooier in grootte varieert, laten we zien dat het in staat is om harmonischen van verstrooide golven te ontwarren wanneer ze worden opgewekt door een eindige gepulseerde vlakke golf, waardoor inzicht wordt verkregen in het collectieve gedrag van microbellen. Resultaten geven aan dat resonante monodisperse populaties de sterkste verstrooiing vertonen in de fundamentele frequentie, terwijl monodisperse populaties buiten resonantie de hoogste amplitude vertonen rond hun resonantiefrequentie. Ondanks dat simulaties waardevolle inzichten bieden, is het cruciaal om ze te verbinden met klinische toepassingen zoals CEUS voor diepe weefselbeeldvorming. Bijgevolg presenteren we een vergelijkende studie tussen polydisperse en monodisperse populaties wanneer ze worden opgewekt door een veld van een conventionele echografiemachine. Terwijl monodisperse populaties de gevoeligheid van echografie verbeteren, stapelen niet-lineaire beeldvormingsartefacten zich op stroomafwaarts van de microbellen. In tegenstelling hiermee vertonen polydisperse suspensies, ondanks zwakkere verstrooiing, een gunstiger respons zonder significante ophoping van artefacten.

In **Hoofdstuk 6** gaan we in op de behoefte aan real-time *in vivo* bereiksverificatie bij protonenbundelkankertherapie met submillimeternauwkeurigheid. Akoestische beeldvormingstechnologieen, die mogelijk gebruikmaken van lokale interacties tussen protonen en microbellen, bieden een intrigerende mogelijkheid. Het gebruik van INCS hiervoor vereist een ontbrekend theoretisch model dat de akoestische veldkarakteristieken van een individuele proton karakteriseert. In dit onderzoekskader ontwikkelen we een akoestisch beeldvormingsmodel voor een enkele proton op nanometer- en micrometerschalen, waarbij adiabatische expansie wordt meegenomen en secundaire elektronenproductie wordt gekwantificeerd. Numerieke simulaties onthullen spatiotemporale kenmerken en tonen een bipolaire piek met een middenfrequentie rond 86,7 GHz. Positieve piekdrukken nemen radiaal af en bereiken 0,24 MPa op 5 μm, met een negatieve druk van -2,6 kPa op 30 nm van de Bragg-piek. Het gebruik van golfveldexpansie en asymptotische benaderingen breidt de ruimtelijke en temporele bereiken van het protonakoestische veld uit. Over het algemeen biedt dit werk een uitgebreide spatiotemporele karakterisering van het akoestische veld van een enkele proton.

Na het ontwikkelen van een akoestisch model dat drukgolven voorspelt uit de warmteafgifte van een enkele proton, wordt een theoretisch model voor de verstrooiing van een populatie microbellen wanneer deze wordt opgewekt door een protongenererend akoestisch veld cruciaal. Op deze manier gebruiken we INCS niet alleen

voor diagnostische, maar ook voor therapeutische echografie. In **Hoofdstuk 7** demonstreren we de nieuwe uitbreiding van INCS ook naar de primaire bronterm, die verantwoordelijk is voor de generatie van het incidentele drukveld. Deze studie omvat bijdragen van een wolk van puntzenders die een bundel protonen simuleren, waarbij een lineair verband tussen het drukveld en de protonenconcentratie wordt onthuld tot een specifieke drempel. De grootte en locatie van het domein beïnvloeden het algehele systeemgedrag, wat inzichten biedt in de interactie tussen een protonenbundel en een microbellenpopulatie.

Dit onderzoek benadrukt de effectiviteit van INCS bij het aanpakken van klinisch relevante toepassingen van medische echografie voor zowel diagnostische als therapeutische doeleinden. INCS blijkt bekwaam te zijn in het grondig verduidelijken van de natuurkunde achter de niet-lineaire voortplanting van medische echografie door populaties van zowel monodisperse als polydisperse contrastmiddelen, waardoor begrip ontstaat van de mechanismen die ten grondslag liggen aan optredende akoestische verschijnselen. Bovendien maakt INCS de verkenning van verschillen tussen conventioneel gebruikte pulsing-schema's in CEUS-beeldvorming mogelijk, waardoor vasculaire visualisatie wordt verbeterd door middel van realtime en niet-invasieve procedures. Bovendien vergemakkelijkt INCS multiparametrische studies voor therapeutische echografie, waardoor de kosten en tijd verbonden aan patiëntspecifieke behandelplannen in kankertherapie kunnen worden gestroomlijnd. Uiteindelijk effent deze studie de weg voor de ontwikkeling van numerieke tools om een verbinding te leggen tussen simulaties en klinische studies in toepassingen van medische echografie.

List of Publications

Papers in international journals

1. F.R. Deurvorst, G. Collado Lara, A. Matalliotakis, H. Vos, N. de Jong, V. Daeichin, and M.D. Verweij, *A spatial and temporal characterisation of single proton acoustic waves in proton beam cancer therapy*, J. Acoust. Soc. Am. **151**, 1200–1210 (2022).

2. A. Matalliotakis, and M.D. Verweij, *Computation of ultrasound propagation in a population of nonlinearly oscillating microbubbles including multiple scattering*, J. Acoust. Soc. Am. **153**, 2209–2222 (2023).

3. A. Matalliotakis, D. Maresca, and M.D. Verweij, *Nonlinear interaction of two cross-propagating plane waves*, arXiv, (2023).

4. A. Matalliotakis, M.D. Verweij, and D. Maresca, *Impact of wavefront shape on nonlinear ultrasound imaging of monodisperse microbubbles*, Phys. Rev. Applied **22** (034062) (2024).

5. A. Matalliotakis, and M.D. Verweij, *Polydisperse versus monodisperse microbubbles: A simulation study for contrast-enhanced ultrasound imaging*, Ultr. Med. & Biol., (2024).

6. B. Heiles, F. Nelissen, D. Terwiel, B.M. Park, E. Munoz Ibarra, A. Matalliotakis, R. Waasdorp, T. Ara, P. Barturen-Larrea, M. Duan, M.G. Shapiro, V. Gazzola, and D. Maresca, *Nonlinear sound-sheet microscopy: imaging opaque organs at the capillary and cellular scale*, Submitted to Science, September 2024.

Conference contributions

1. A. Matalliotakis, G. Collado Lara, F.R. Deurvorst, V. Daeichin, H. Vos , N. de Jong, and M.D. Verweij, *Nonlinear propagation of medical ultrasound through a microbubble cluster in view of multiple scattering effects*, The 26th European Symposium on Ultrasound Contrast Imaging, Rotterdam (NL), 14-15 Jan. (2021).

2. A. Matalliotakis, N. de Jong, and M.D. Verweij, *Modeling of ultrasound propagation through a microbubble population*, Dutch Society of Medical Ultrasound, Virtual, (2021).

3. A. Matalliotakis, and M.D. Verweij, *The iterative nonlinear contrast source method for simulating ultrasound propagation through a polydisperse microbubble population*, 179th Meeting of the Acoustical Society of America Acoustics Virtually Everywhere (AVE) – Virtual, 7–11 Dec., (2020).

4. A. Matalliotakis, X. Li, M.S. van der Heiden, P.L.M.J. van Neer, N. de Jong, and M.D. Verweij, *Multiple scattering inside a population of nonlinear oscillating microbubbles excited by a cloud of acoustic point sources*, The 27th European Symposium on Ultrasound Contrast Imaging, Rotterdam (NL), 20-21 Jan. (2022).

5. A. Matalliotakis, D. Maresca, and M.D. Verweij, *Analysis of the nonlinear local interaction between two noncolinear plane waves*, The 22nd International Symposium on Nonlinear Acoustics, Oxford (UK), 4-8 July (2022).

6. A. Matalliotakis, M.D. Verweij, and D. Maresca, *On the importance of local nonlinear interaction between two cross-propagating plane-waves*, IEEE Int. Ultrason. Symp., Venice (IT), 10-13 Oct. (2022).

7. A. Matalliotakis, and M.D. Verweij, *Simulating multiple scattering inside a population of nonlinearly oscillating microbubbles using the Iterative Nonlinear Contrast Source method*, 183rd Meeting of the Acoustical Society of America, Nashville, TN (USA), 5-9 Dec. (2022).

8. M.D. Verweij, and A. Matalliotakis, *Extending the Iterative Nonlinear Contrast Source method to simulate mutual interaction in large populations of microbubbles*, 183rd Meeting of the Acoustical Society of America, Nashville, TN (USA), 5-9 Dec. (2022).

9. A. Matalliotakis, M.D. Verweij, and D. Maresca, *Comparison of amplitude modulation and cross amplitude modulation pressure fields through a monodisperse microbubble cloud*, The 28th European Symposium on Ultrasound Contrast Imaging, Rotterdam (NL), 19-20 Jan. (2022).

10. A. Matalliotakis, D. Maresca, and M.D. Verweij, *Simulating the response of a population of nonlinear oscillating microbubbles*, The Artimino Conference on Medical Ultrasound Technology, Artimino (IT), 11-14 June (2023).

11. A. Matalliotakis, M.D. Verweij, and D. Maresca, *Cross amplitude modulation imaging of monodisperse microbubbles: a simulation study*, IEEE Int. Ultrason. Symp., Montreal (CA), 3-8 Sep. (2023).

Acknowledgements

The previous text was enhanced with the help of AI but this part is written with the mistakes of my character. The most significant chapter of this thesis is the people that were part of my life during this long journey and contributed with their physical or mental support. My nonlinear PhD journey can be likened to the pages of a book and I would like to thank everyone that made it more dense, richer and more meaningful than this thesis itself.

Πάνω απ'όλα, θέλω να ευχαριστήσω την υπέροχη οικογένεια μου, τον πατέρα μου **Γιώργο**, τη μητέρα μου **Μαρία** και τον αδερφό μου **Μιχάλη**. Σας ευχαριστώ πολύ που με στηρίξατε ακόμα και με το εμπόδιο των φυσικών συνόρων. Υπήρξατε πάντα παρόντες σε κάθε δύσκολη στιγμή με την αγάπη σας. Αδερφέ μου, αυτό το ταξίδι ηταν πολύ πιο γεμάτο εξαιτίας σου και με την βοήθεια σου κατάφερα να σταθώ στα πόδια μου και να το ολοκληρώσω. Δεν μπορώ να παραλείψω να ευχαριστήσω και όλα τα μέλη της ευρύτερης οικογένειας μου , θείους, θείες και ξαδέρφια στην Κρητη που με υποστήριζαν με κάθε μέσο εστω και χωρίς την φυσική παρουσία τους.

A huge thanks goes also to my Greek friends who gave me so much motivation to complete my PhD, and filled my life with beautiful memories outside the academic grind. **Vassia** you have been the cornerstone of my life for many years and you share an essential role for shaping the person I am today. Thank you for all the special and emotional moments we have lived together. Many pages of this journey were written alongside with **Ntatsis** and **Tasos**. You were my support during the toughest phase -the beginning of the PhD in a foreign country- bringing joy to the everyday through countless stories, cookings, gatherings, travels, and unforgettable moments. **Apostoli** you significantly enhanced the spicyness of this group, partying everywhere and in concerts, and organizing very successful BBQs often together with **Tzo**. **Achillea**, I can't thank you enough for the laughs, the drinks, and our skiing adventures. **Napo, Chris**, even in such a short time, we managed to create so many memories —devouring ice creams, hosting and enjoying parties, cooking together before and after the chaos of a burning house, and living some truly special cycling tours. **Stelan** and **Pavlidi**, your humor made things easier even in tough times. Special thanks to all of you for being there when I fractured my tibia; your presence made all the difference. I also want to express my gratitude to my friends beyond the Netherlands: **Tsony, Markos, Mitsos, Markodi, Dimitris, Eva, Katerina**, and **Despoina**. Next to my family, you've been an invaluable part of my life, and I

look forward to writing many more chapters with you in the years to come. Finally, a big thank you to everyone I met in the Netherlands, who became such an important part of these past years. I deeply appreciate the time we spent together and all the intense, unforgettable memories we created.

Next, I want to express my gratitude to everyone I've met in my academic environment. First and foremost, I would like to acknowledge my promotor **Martin**, for his invaluable guidance throughout these past years. From the beginning of this journey, we had our share of intense moments, but thanks to you, I learned how to approach research, deliver effective presentations, and write impactful publications. Despite my spontaneous and straightforward use of language, you taught me how to properly frame questions and generate meaningful discussions in a clear and precise way to avoid misinterpretation. Although at the beginning I could only grasp a small part of our discussions, over time I grew to follow your ideas and carve out my own scientific path. I also had the privilege of getting to know you beyond the academic strict environment at conferences and symposiums—drinking Guinness together comes to mind! I'll never forget learning from you that the peak of the Alps can be found in the Netherlands, and you inspired me to bring the peak of Ben Nevis to our group's museum as well. Thank you for sharing your knowledge, insights and many interesting scientific stories, and for showing genuine interest in the scientific aspects of research. Despite our cultural differences, it has truly been an honor and a privilege to be one of the people working and extending the usage of INCS, and share this part of the journey with you. **Nico**, thank you for all the engaging discussions we've had over the years. You often found yourself acting as the referee between me and Martin, though as the true experimentalist, you were usually on the opposing side of us numerical and theoretical enthusiasts! I've also greatly appreciated our conversations about football, politics, and countless other non-academic topics. I genuinely hope that one day when I ask, *'How are you doing today?'* your response will finally be something better than, *'Actually, not so bad today.'*.

I would also like to express my gratitude to all the PIs who had a direct impact on my research career. First, **David**, thank you for the enriching scientific discussions and for providing me with the opportunity to produce significant academic work through collaboration with your group. Working with you has sharpened my sensitivity and specificity in understanding complex concepts and taught me how to diplomatically present my research to deliver a clear and impactful message to my audience. I also had the privilege of getting to know you beyond the academic setting. Our conversations over drinks in conferences, in LA and other informal occasions, discussions on sensitive academic matters, and chats about life and my future plans have been incredibly helpful and meaningful to me. **Verya**, **Rik**, **Guillaume Renaud**, **Paul** and **Guillaume Lajoinie**, thank you all for your kind interactions and valuable contributions to my scientific journey. I deeply appreciate your ability to transform seemingly simple or unimportant concepts into profound insights on topics like microbubble oscillations, multiple scattering, nonlinear acoustics and contrast-enhanced imaging. Your guidance and expertise have been truly invaluable. I would also like to thank the other PIs from the Medical Imaging group—**Frans**, **Sebastian**, and **Qian**. Although not directly involved in my research, their support and daily interactions

have greatly enhanced my PhD journey and contributed to both my personal and academic growth.

A special thanks goes to four remarkable individuals who are responsible for maintaining peace, cohesion, and brightening our days in the Medical Imaging Group. First, **Angela**, thank you so much for all our conversations about mountains, skiing, camping, traveling, and so much more that made my journey in this group lighter and more enjoyable. I'm also grateful for your support with my administrative matters and for organizing events that helped bring the group together. Your role is truly invaluable to all of us. **Annelies**, thank you for always being open to discussion and for your assistance with all the organizational matters. Your help has been greatly appreciated. **Ronald**, you hold a special place in my heart. Thank you for being such a joyful, vibrant, and musically electrified and jazzy spirit. I will truly miss your enthusiastic 'Kalimera' and the energy you brought to every moment. **Henry**, thank you so much for your kind and thoughtful nature. I really enjoyed our conversations about cycling. Unfortunately, we never had the chance to cycle and camp together, but I'm grateful for the moments we shared. I also deeply appreciate how you always offered your help whenever I faced a problem. The four of you truly play a crucial role in making our Medical Imaging group run smoothly and efficiently.

In the academic environment, my mood and energy during our daily interactions were greatly shaped by my wonderful office mates. Thank you, **Martijn**, the first person I shared the office with. I thoroughly enjoyed our discussions during work; we both shared a love for music, and more often than not, our chatty nature led us to discuss much more than just work! **Djalma**, you are the person I spent the most time with at the university. You were there almost every day, and I always had someone to share my thoughts with. Your kindness was evident, as even when you were focused on your own work, you never hesitated to engage with me and answer my random questions, a dialogue in our otherwise quiet working environment. You were always generous in sharing your ideas, both academic and beyond. We never had any issues, whether it was sharing beers and alcohol in our closet or occasionally playing loud music due to my uneasy nature. I'm also glad my football knowledge is very limited, or else we might still be working on our PhDs! **Chih-Hsien**, thank you very much for being there. You supported me when I had a problem, always willing to discuss with me and sit down to enjoy for a coffee or drink beers together in the social gatherings. You always used your ancient Taiwanese nature to help me with things such as patches for back pain and other important matters. Finally, I cannot forget the most recent addition to our office, **Martina**. Although we didn't have the time to interact in the office, your presence was incredibly valuable. You were always ready for a discussion, and your energy ensured the office never felt empty.

Outside my office and meeting everyone in the corridor of the MI, CI groups, I would like to extend my gratitude to my old and new colleagues for our daily interactions over lunches, coffee breaks and MI seminars: **Jack, Ulaş, Alberico, Elango, Boudewine, Xiufeng, Sabiju, Dion, Alina, João, Kathleen, Eleonora, Yidong, Yi, Liam,** and **Min**. A big thanks goes to all the people from the Biomedical Engineering group in Erasmus MC for all the discussions during lunces and conferences. Each one of you holds a special place in my PhD journey.

A special thanks goes to those with whom we shared both lively and quiet moments, whether over drinks or in sober conversations. I truly appreciate your presence, **Djalma, Fabian, Jack, Eszter, Moein, Paulina, Victor, Ayda, Maša, Chih-Hsien**, and **Xiufeng**. **Chiara**, thank you for sharing so many fun moments and drinks with me, always with our Mediterranean temperament. I'm also grateful for your generous hospitality and for being such a warm host and guide during our time in Italy. I deeply appreciate the time spent with your kind family, which felt as natural and welcoming as a Greek family gathering. Although our unfortunately short interaction, I would like to specially thank three people. **Hugues** , I really loved our bouldering sessions, partying, drinking, plans, discussions and every daily interaction. Together with Hugues, **Gabrielle**, you brought a vibrant energy to the group with your French spirit. I also can't forget your partners, **Irene** and **Alister**, whose presence made every outing even more enjoyable. A heartfelt thanks also goes to my dear Orthodox sister, **Martina**, for always being up for outings, parties, and drinks. We shared many meaningful conversations and laughs about sensitive topics. Lastly, thank you both you and Hugues, for being there for me, especially as a psychological support during my iceskating experience.

Finally, within our Delft group, two people certainly outdrank me, but that's not the reason I'm dedicating a separate paragraph to them. **Baptiste**, without you, my life in the Netherlands—both academically and socially—would have been much duller. I'll always remember the great times at your place, watching the sunset at the beach with drinks in hand being an obstacle for the sand-setter vehicles, our cycling races in the Netherlands and in LA (though you were always stronger than me). I also loved your DJ skills—I'll never forget the moment we watched the LA skyline while you were DJing before we went off to a crazy party. I remember your farewell party in David's house and will not forget saying goodbye to you at your place with your family and Rinko. With Baptiste, **Rick**, you two made a formidable and occasionally dangerous duo. I'm grateful to have been part of this group. You're incredibly smart and socially aware, and although you sometimes were annoyed by life, you were always kind and supportive. You were always too strong when it came to drinking, but you were also always there to lend a hand when needed. The parties we shared were unforgettable, and street bouldering was always an adventure—even if we occasionally found ourselves in dangerous situations. One essential moment was when we went ice skating and I got my tibia fracture, and you were such a great support before leaving Netherlands (and as a driver of my wheelchair). I want to thank you not just for being there when I needed assistance, but for all the special and meaningful moments we shared together. Both of you always avoided living in your own bubbles and instead sought to connect with others. The pages I wrote with both of you in my PhD journey will always have a special place in my heart.

I would also like to thank three people who have played a catalytic role, first in my life and second in my academic journey outside Delft. **Gonzalo**, you were the first person I met in the academic environment when I started this PhD. You were instrumental in helping me settle into this new chapter. Thank you for being a great mate throughout it all. I'm grateful for the many pages we've written together in the story of my life. We shared countless drinks, even at conferences, had many

laughs, and I was always comfortable discussing sensitive topics with you. Despite you being an experimentalist, we got along very well, first with **Floris** and later with our collaboration with Nathan. **Nathan** our short interaction was very meaningful to me. Your idiosyncratic humour gave me many laughs and I really enjoyed our experimental collaboration. Both with Gonzalo, you helped me a lot to understand complex topics in microbubble dynamics. **Geraldi**, thank you so much for being such an essential part of this journey. We shared many memorable moments, both in the academic setting with our brief collaborations, and outside the office over drinks, especially at nearly every conference I attended. I always appreciated your positive energy and how you'd repeat funny phrases and behaviors that never failed to make me laugh. Despite my occasionally critical and cynical nature, you never got upset with me. Together, we brought the Ben Nevis peak to the Netherlands and walked countless kilometers through different cities, creating unforgettable memories along the way. I gave a cutting promise so I am still waiting to see if Europe is better than USA. I am truly grateful to have met each of you, and I will miss every one of you individually. I sincerely hope you all have fulfilling lives and successful careers, and that our paths cross again either sceduled or unexpectedly at a future occassion.

Although my PhD journey is complete and I was able to write my PhD dissertation, these last 5 pages are the most important to me. Thank you every one individually for being part in this PhD journey. I would not manage to write my conclusion without you.

About the author

Agisilaos Matalliotakis was born on September 10, 1993, in Heraklion, Crete, Greece. He commenced his mechanical engineering studies at Aristotle University of Thessaloniki in 2012. During his third-year internship, he received university recognition for developing an algorithm using the open-source Python-based software FEniCS to compute the production rate of brain cancer cells for glioblastoma. In his fourth year, he specialized in aeronautical engineering, focusing on advanced fluid mechanics in a two-year master's program. For his master's thesis, he created a computational fluid mechanics model describing blood flow in the human carotid bifurcation using fluid-structure interaction (FSI). This model had applications in scenarios involving air fighters experiencing high positive or negative gravitational forces. His main supervisor, Anestis Kalfas, awarded a grade of 10/10. He graduated third in his class with a grade of 8.29/10, ranking in the top 2% of the overall mechanical engineering graduates. Subsequently, he completed a 9-month mandatory military service in the artillery division in Rhodes, Greece in September 2018. From October 8, 2019, to March 15, 2024, he conducted research on modeling nonlinear acoustics for medical ultrasound applications, with a specific focus on contrast-enhanced ultrasound, as part of his Ph.D. at Delft University of Technology, the Netherlands.

Propositions

accompanying the dissertation

Nonlinear propagation of ultrasound in microbubble populations: Exploring collective dynamics

by

Agisilaos Matalliotakis

1. Monodispersity enhances efficiency, while polydispersity enriches the population's dynamics. (this thesis).
2. Focusing on a problem from two directions enhances specificity and sensitivity in understanding.
3. Parameter optimization is simpler when adjusting one variable at a time.
4. Reaching a local minimum presents an opportunity to find the global maximum.
5. Life becomes increasingly nonlinear with the addition of more exciting events.
6. Stability is achieved through iteratively converging dialogue in a multiparty parliament.
7. Research skills are not necessary to climb the academic ladder.
8. The destruction of natural environment is the clearest footprint of a corrupted government.
9. Time planning in academia is like waiting for a bus in Greece: slow and seemingly endless.
10. Simulations are never truly noiseless.

These propositions are regarded as opposable and defendable, and have been approved as such by the promotors Dr. ir. M. D. Verweij and Prof. dr. ir. N. de Jong.

Invitation

You are cordially invited to
attend the public defence of
the PhD dissertation entitled:

Nonlinear propagation of ultrasound in microbubble populations

The defence will take place
on Thursday 19 December 2024
at 13:00h in the Senaatszaal
of the Aula Congress Centre,
Delft University of Technology,
Melkweg 5, Delft.

Prior to the defence, at 12:30h,
I will give a brief presentation
about my research.

Agisilaos Matalliotakis
a.matalliotakis@tudelft.nl